



Universiteit
Leiden

The Netherlands

Pushing the characterization of exoplanet atmospheres down to temperate rocky planets in the era of JWST

Zieba, S.

Citation

Zieba, S. (2024, June 25). *Pushing the characterization of exoplanet atmospheres down to temperate rocky planets in the era of JWST*. Retrieved from <https://hdl.handle.net/1887/3765836>

Version: Publisher's Version

License: [Licence agreement concerning inclusion of doctoral thesis in the Institutional Repository of the University of Leiden](#)

Downloaded from: <https://hdl.handle.net/1887/3765836>

Note: To cite this publication please use the final published version (if applicable).

Pushing the Characterization of Exoplanet Atmospheres Down to Temperate Rocky Planets in the Era of JWST

Proefschrift

ter verkrijging van
de graad van doctor aan de Universiteit Leiden,
op gezag van rector magnificus prof.dr.ir. H. Bijl,
volgens besluit van het college voor promoties
te verdedigen op dinsdag 25 juni 2024
klokke 12:30 uur

door
Sebastian Zieba

geboren te Salzburg, Oostenrijk

in 1995

Promotores:

Prof. dr. L. Kreidberg MPIA, Heidelberg

Prof. dr. I.A.G. Snellen

Promotiecommissie:

Dr. M.A. Kenworthy

Prof. dr. B.R. Brandl

Dr. A.A. Vidotto

Prof. dr. M. Gillon Université de Liège

Prof. dr. L.D. Deming University of Maryland

ISBN: 9789090386959

Frontcover and backcover: *Brianna Zawadzki*

Copyright © 2024 *Sebastian Zieba*.

I've never been a natural,
all I do is try, try, try.

Taylor Swift

Contents

1	Introduction	1
1.1	Exoplanet Population	1
1.1.1	Rocky exoplanets	2
1.1.2	Ultra-short-period planets	4
1.1.3	Lava planets	8
1.2	Observing techniques of atmospheres	8
1.2.1	Transmission spectroscopy	9
1.2.2	Emission spectroscopy	10
1.2.3	Phase curves	12
1.3	Notable Planets and Systems	13
1.3.1	55 Cnc e	13
1.3.2	Kepler-10 b	14
1.3.3	LHS 3844 b	15
1.3.4	TRAPPIST-1	15
1.4	Facilities	17
1.5	This thesis	19
2	<i>K2</i> and <i>Spitzer</i> phase curves of the rocky ultra-short-period planet K2-141 b hint at a tenuous rock vapor atmosphere	23
2.1	Introduction	25
2.2	Observations and data reduction	28
2.2.1	<i>Spitzer</i> photometry	28
2.2.2	<i>K2</i> photometry	30
2.3	Light curve fits	31
2.3.1	<i>Spitzer</i> only fit	33
2.3.2	Goodness of <i>Spitzer</i> only fit	36
2.3.3	Joint <i>Spitzer</i> and <i>Kepler</i> fit	36
2.3.4	Goodness of joint <i>Spitzer</i> and <i>Kepler</i> fit	42
2.3.5	Improved ephemerides	42
2.3.6	Results	42
2.4	Atmospheric constraints	43
2.4.1	Pseudo-2D rock vapor model	43
2.4.2	1D turbulent boundary layer model	45
2.4.3	Comparison of the models	47
2.4.4	Comparison between the models and the data	47

2.5	Discussion	50
2.5.1	Evidence against a thick atmosphere	50
2.5.2	Evidence for a thin rock vapor atmosphere	50
2.6	Summary and conclusions	51
	Appendices	55
2.A	Updated ephemeris for K2-141 c	55
2.B	Additional tables	58
2.B.1	Rescaling of uncertainties	58
2.B.2	Parameters of the fit models	59
2.C	Additional plots	62
2.C.1	Systematics	62
2.C.2	<i>Spitzer</i> pointings	65
2.C.3	<i>Spitzer</i> BLISS maps	66
2.C.4	<i>Spitzer</i> Allan deviation plots	67
2.C.5	<i>Spitzer</i> fit: Sinusoidal ($\phi = 0$)	68
2.C.6	<i>Spitzer</i> fit: Sinusoidal (ϕ free)	69
2.C.7	<i>Spitzer</i> fit: two temperature model	70
2.C.8	Joint (<i>K2</i> and <i>Spitzer</i>) fit: toy model ($F = 0$)	71
2.C.9	Joint (<i>K2</i> and <i>Spitzer</i>) fit: toy model (F free)	72
2.C.10	Joint (<i>K2</i> and <i>Spitzer</i>) fit: two temperature model	73
3	PACMAN: A pipeline to reduce and analyze Hubble Wide Field Camera 3 IR Grism data	75
3.1	Statement of need	77
3.2	Outline of the pipeline steps	77
3.3	Dependencies	79
3.4	Documentation	81
3.5	Future work	81
4	No thick carbon dioxide atmosphere on the rocky exoplanet TRAPPIST-1 c	83
4.1	Introduction	85
4.2	Observations	85
4.3	Data reduction and analysis	85
4.4	Discussion	86
4.4.1	Comparison to emission models	86
4.4.2	Water inventory	90
	Appendices	92
4.A	<i>JWST</i> MIRI Observations	92
4.B	Data Reduction	93
4.B.1	Data Reduction SZ	96
4.B.2	Data Reduction ED	96
4.B.3	Data Reduction MG	98
4.B.4	Data Reduction PT	99
4.C	Data Analysis	99
4.C.1	Data Analysis SZ	99

4.C.2	Data Analysis ED	100
4.C.3	Data Analysis MG	101
4.C.4	Data Analysis PT	103
4.D	Brightness Temperature Calculation	104
4.E	Emission modelling for TRAPPIST-1 c	104
4.E.1	Bare Rock	105
4.E.2	Simple 1+D O ₂ /CO ₂ Mixtures	106
4.E.3	Coupled Climate-Photochemical Venus-like Atmospheres	106
4.F	Atmospheric Escape models	107
4.G	Interior structure model	108
4.H	Stellar Properties	108
4.I	Eclipse Timing Variations	110
5	A Hubble WFC3 infrared look at the transmission spectrum of the hot, inflated sub-Saturn KELT-11 b	115
5.1	Introduction	117
5.2	Observations and Data Reduction	118
5.3	Light Curve Analysis	121
5.3.1	<i>HST</i> /WFC3 White Light Transit	121
5.3.2	<i>HST</i> /WFC3 Spectroscopic Transit	127
5.4	Discussion	132
5.4.1	Systematic bias from divide-white fitting technique	132
5.4.2	Comparison of G141 to other hot inflated sub-Saturns	132
5.4.3	Shape of G102	133
5.5	Summary	135
	Appendices	137
5.A	Best fitting white light curve model	137
5.B	Spectroscopic light curve fits	144
6	The β Pictoris b Hill sphere transit campaign - II. Searching for the signatures of the β Pictoris exoplanets through time delay analysis of the δ Scuti pulsations	151
6.1	Introduction	153
6.2	The β Pictoris system	154
6.2.1	The star	154
6.2.2	The planets: β Pictoris b and c	154
6.3	Observations	156
6.3.1	BRITe-Constellation	158
6.3.2	bRing	158
6.3.3	ASTEP	159
6.3.4	TESS	159
6.4	Theory and methodology	160
6.4.1	δ Scuti stars	160
6.4.2	The ephemeris equation	161
6.4.3	Frequency modulation and phase modulation: The state of the art	161

6.4.4	Time delays	162
6.4.5	Phase modulation method: Methodology	164
6.4.6	Intrinsic amplitude and phase variations	167
6.4.7	Light curve reduction	167
6.5	Results	168
6.5.1	Frequency stability between the different observations . . .	168
6.5.2	Simulation based on Kepler data	168
6.5.3	Time delay analysis of the photometry	170
6.5.4	Detection limits for β Pictoris	173
6.5.5	Analysis of pulsational stability using TESS data	174
6.5.6	Comparison to KIC 7917485	176
6.6	Conclusions	178
	Appendices	181
6.A	TESS frequency analysis	181
6.A.1	Frequency list	181
6.A.2	Gaussian high-pass filter	182
	Bibliography	183
	English summary	207
	Nederlandse samenvatting	215
	Deutsche Zusammenfassung	223
	Publications	229
	Curriculum Vitae	233
	Acknowledgements	236

1

INTRODUCTION

1.1 Exoplanet Population

The story of this thesis starts in the year 1995: By detecting a periodic shift in the spectral lines of the sun-like star 51 Pegasi, Michel Mayor and Didier Queloz concluded that the star was being orbited by a Jupiter-mass planet (Mayor & Queloz 1995). The most surprising aspect of this discovery was the orbital period of the planet; 51 Pegasi b orbited its host star every 4.2 days. This is far shorter than the period for any Solar System planet. The first gas giant as seen from the Sun, Jupiter, needs approximately a thousand times longer to complete one revolution around our Sun. For this discovery, the two astronomers were eventually awarded with the Nobel Prize in Physics in 2019.

Since this first discovery of an exoplanet around a Sun-like star nearly 30 years ago, the field has progressed considerably. Based on data retrieved from the NASA Exoplanet Archive at the end of 2023, over 5500 exoplanets were detected to this day (see Figure 1.1). Main findings of the past few decades include: (a) small planets being a common outcome of planet formation (see Chapter 1.1.1), (b) the prediction and discovery of the so-called Radius Valley, a lack of planets with approximately two times the Earth’s radius, and (c) the existence of planets on “ultra-short-orbits” (< 1 day) (see Chapter 1.1.2). In this Introduction, I will present these various planet populations focusing on smaller exoplanets. With the advent of *JWST*, we can characterize rocky exoplanets in detail like never before. In fact, 35 of the 116 transiting exoplanets that will be observed in Cycles 1 and 2 of *JWST* are small planets ($< 2 R_{\oplus}$, with R_{\oplus} being Earth’s radius) to study their atmospheres or surfaces. In Chapter 1.2, I explain the main techniques to characterize transiting exoplanets. Some noteworthy systems and planets are presented in Chapter 1.3. The space-based workhouse facilities for the study of small exoplanets are discussed in Chapter 1.4. Finally, in Chapter 1.5, I introduce the individual scientific chapters of this thesis and their main conclusions.

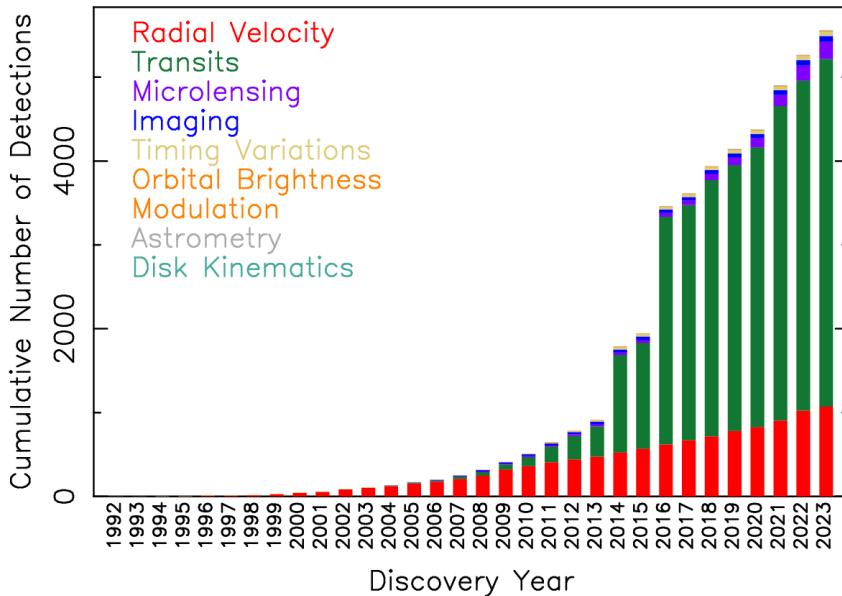


Figure 1.1: Plot showing the cumulative number of detected exoplanets as a function of time. From the first detection of planets around a pulsar (Wolszczan & Frail 1992), progressing to the detection of a hot Jupiter orbiting a solar-like star in 1995 (Mayor & Queloz 1995), and the multitude of transiting exoplanets unveiled during the early 2010s by NASA’s *Kepler Space Telescope* (Borucki et al. 2010), we know of more than 5500 exoplanets to date. Retrieved from the NASA Exoplanet Archive in December 2023.

1.1.1 Rocky exoplanets

Thanks to the many dedicated exoplanet missions of the past, like NASA’s *Kepler Space Telescope*, which has discovered approximately half of all the exoplanets known today, we know that planets are ubiquitous in our Galaxy (Dressing & Charbonneau 2015; Fulton et al. 2017; Zhu & Dong 2021). The formation of planets commonly yields small exoplanets, and they are even more prevalent around smaller stars (Rogers 2015; Fulton et al. 2017). By measuring their masses and radii, we learned that planets smaller than $1.6 R_{\oplus}$ are most likely terrestrial (i.e., rocky) in composition (Weiss & Marcy 2014; Rogers 2015; Wolfgang & Lopez 2015). In Figure 1.2, mass and radius measurements of exoplanets are shown compared to a range of compositional scenarios (Wordsworth & Kreidberg 2022). Smaller planets usually fall into two bounding cases that characterize rocky planets: those composed of 100% iron and those made up of 100% silicates (MgSiO_3). All of the terrestrial Solar System planets can be found between these two extremes, with Earth showing a composition of approximately 30% iron and 70% silicates. Above $1.6 R_{\oplus}$, exoplanets show a bigger spread in radii for a given mass and deviate from this rocky regime. These planets need a significant fraction of their mass in gas or volatiles, like hydrogen (H_2) or water (H_2O). Even a small amount of hydrogen - just 1% by mass - in the atmosphere of a small planet,

leads to a significant increase in its radius of $2 R_{\oplus}$ (Valencia et al. 2010; Lopez & Fortney 2014). Their envelope then contributes a significant fraction to the size of the planet. Thinner atmospheres are not expected as they are very vulnerable to escape processes and easily lost by stellar wind. Furthermore, planets with 1% of their mass in a hydrogen-dominated envelope, are not expected to have solid, rocky surfaces. Due to the high pressures and temperatures, their surfaces are expected to be molten (Lopez & Fortney 2014; Chachan & Stevenson 2018). All of this is essentially why we typically do not consider these planets with primordial, hydrogen atmospheres to be rocky. Another major observation made by data collected by the *Kepler* mission is the drought of planets ranging between 1.5 and 2.0 Earth radii. The phenomenon, referred to as the radius valley or radius gap, is likely attributed to the rapid increase in planet size when a thick gaseous atmosphere persisted (Fulton et al. 2017; Van Eylen et al. 2018).

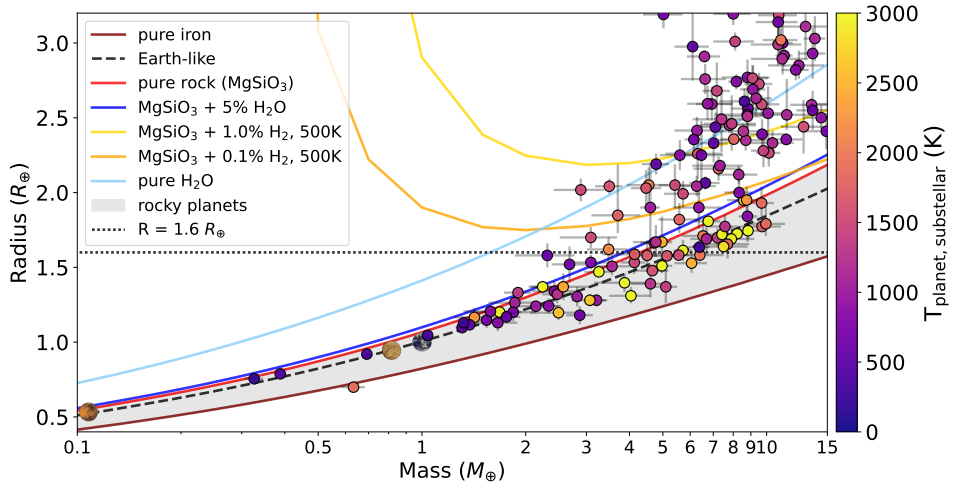


Figure 1.2: A mass-radius diagram comparing discovered exoplanets compared to a suite of compositional models. The gray shaded area shows the region in the mass-radius parameter space which is typically identified as being rocky. It is enclosed by two compositional lines: the 100% iron (Fe) model (brown solid line) and the pure rock or silicate line (100% MgSiO_3 in solid red). The Earth-like compositional line consists of 32.5% iron and 67.5% silicates. Other models with various amounts of volatiles are also shown. The horizontal dotted line depicts a radius of 1.6 Earth Radii (R_{\oplus}), above which planets are predicted to retain a substantial hydrogen atmosphere (Rogers 2015). The confirmed planets are color-coded by their substellar temperatures defined by $T_{\text{subst}} = T_{\text{eff}} / \sqrt{a/R_s}$, with T_{eff} being the effective temperature of the host star and a/R_s the semi-major-axis to stellar radius ratio. We also show the images of the Solar System planets Mars, Venus, and Earth in the plot in their corresponding positions in this mass-radius plot. For clarity, we only show discovered exoplanets, which have at least a 5σ mass and radius detection. The plot was adapted and updated from Wordsworth & Kreidberg (2022). The planetary parameters were accessed from the NASA Exoplanet Archive in December 2023. The compositional lines were taken from Zeng et al. (2019).

Even though we have discovered many small exoplanets to this day, and we expect them to be rocky in composition based on their measured bulk densities, we still only have little knowledge about the makeup of their atmospheres (for a recent review on rocky exoplanet atmospheres see Wordsworth & Kreidberg 2022). Our solar system already exhibits a diverse range of atmospheres for rocky bodies (see Figure 1.3): Venus with its thick (93 bar) CO₂ dominated atmosphere, Saturn’s moon Titan with an N₂ dominated one at 1.5 bar, Earth with its 1 bar atmosphere predominantly composed out of N₂ and O₂, and Mars with its thinner (0.006 bar) CO₂-dominated atmosphere (for a review on these thicker Solar System atmospheres see Encrenaz & Coustenis 2018). Our Solar system also contains planets with thin, tenuous atmospheres: Pluto and Neptune’s moon Triton have N₂ as their main atmospheric species and a surface pressure of the order of 10 microbars caused by the sublimation of ices. Jupiter’s moon Io has an SO₂ nanobar atmosphere generated by sublimation and vulcanism. Mercury is too close to the Sun to hold onto any significant atmosphere. Its exosphere is created by captured solar wind particles and by meteors hitting the planetary surface. It has a thickness of approximately 1 picobar (10^{-12} bars) and is mainly composed of hydrogen, helium, oxygen, sodium, potassium, and calcium (Domingue et al. 2007) (for a review of these tenuous solar system atmospheres see Lellouch 2018).

The theoretical prediction of an atmosphere on small planets also remains challenging due to numerous unknown factors, which can affect its composition and thickness, such as atmospheric escape, outgassing from volcanism, the delivery of volatiles by comets, rainout, and the existence of plate tectonics (e.g., Raymond et al. 2004; Kite et al. 2009; Wordsworth 2015; Luger & Barnes 2015; Bolmont et al. 2017; Moore & Cowan 2020). The spectral type of the host star may also strongly influence a planet’s atmosphere. M-dwarf stars provide their planets with a completely different environment than Sun-like stars. These stars undergo prolonged pre-main sequence phases marked by heightened luminosity (Luger & Barnes 2015) and also show increased starspot activity leading to increased XUV radiation (France et al. 2016; McDonald et al. 2019). Additionally, M-dwarfs exhibit heightened coronal-mass-ejection activity than their solar-like counterparts (Crosley & Osten 2018; Odert et al. 2020). Despite all of that, planets around M dwarfs remain the easiest to study. Their proximity to their host stars results in a greater transit probability and the relatively high planet-to-star radius ratio leads to a higher signal-to-noise of the planet’s atmospheric features making them easiest to be studied. Therefore, M dwarfs, being the most prevalent type of stars in the galaxy, offer a large sample of planets with high signal-to-noise exoplanets to characterize. These advantageous aspects are commonly referred to in the exoplanet community as the “M-dwarf opportunity”.

1.1.2 Ultra-short-period planets

After the discovery of 51 Pegasi b on its 4.2 day orbit, even more extreme planets were discovered. In 2009, the *CoRoT* (Convection, Rotation and Transits) telescope detected CoRoT-7 b, a planet with a radius of $1.7 R_{\oplus}$ and an orbital period of just 20 hours (Léger et al. 2009). At the time of its discovery, it was the small-

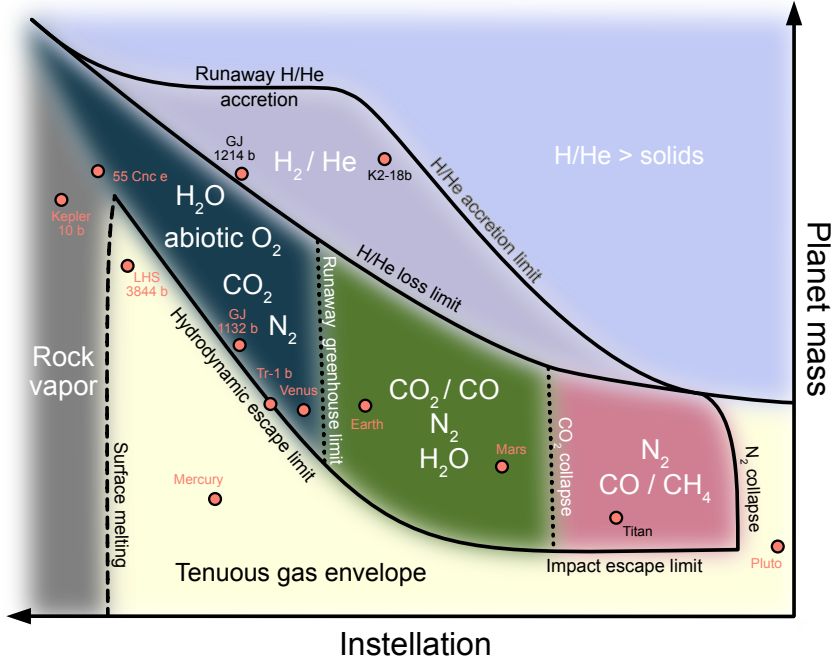


Figure 1.3: A regime plot showing various atmospheric scenarios for a range of stellar instellations and planetary masses. Planets with high masses are expected to have retained their hydrogen/helium-dominated atmospheres (we typically do not consider them as being “rocky”). Low-mass planets and more irradiated planets suffer from atmospheric escape and might be bare rocks (e.g., Mercury in the Solar System). Very high irradiated planets (lava planets) are expected to develop a rock vapor atmosphere. Substantial high-mean-molecular weight atmospheres (e.g., CO_2 , H_2O , O_2 , N_2) can be found in the dark blue, green, and pink areas. Various exoplanets and Solar System planets are marked as red dots in the plot for comparison. Figure taken from Lichtenberg et al. (2023).

est planet found up to that point and had the shortest period. By convention, we call these exoplanets with orbital periods shorter than a day “ultra-short-period” planets (also known as “USPs”) (for a review on these USPs, see Winn et al. 2018). The majority of these strongly irradiated worlds are smaller than $2.0 R_\oplus$ (Sanchis-Ojeda et al. 2014; Jontof-Hutter 2019). Being on these tight orbits, the tidal forces experienced by the planet translate into a very short circularization time scale leading to quick attenuation of any non-zero eccentricity and also giving it a permanent dayside and nightside (Winn et al. 2018). From theoretical and empirical work on these USPs we can therefore assume that they are tidally locked (Lyu et al. 2023).

USPs, just like hot Jupiters, are not common in the Milky Way (Cumming et al. 2008; Wright et al. 2012; Winn et al. 2018). By determining the occurrence rate of USPs, Sanchis-Ojeda et al. (2014) found that only one out of 200 G-type stars have

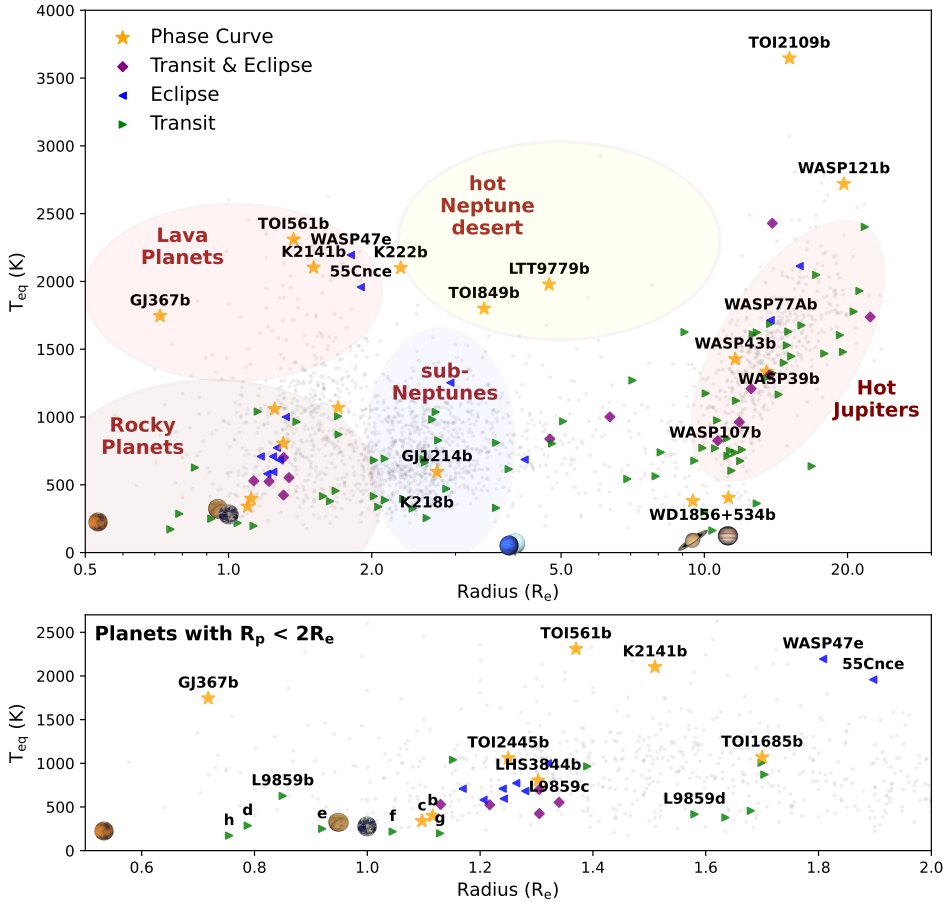


Figure 1.4: The exoplanet “zoo” showing the equilibrium temperature of all confirmed planets (gray dots) as a function of their radius. The equilibrium temperature T_{eq} assumes perfect reradiation of heat and a Bond albedo of zero: $T_{\text{eq}} = T_{\text{eff}} / \sqrt{2 a/R_s}$, with T_{eff} being the effective host star temperature and a/R_s the semi-major-axis to stellar radius ratio. We mark the rough location of prominent exoplanet populations and show the images of the Solar System planets in the plot in their corresponding positions in this temperature-radius plot (Mercury with approximately $0.4 R_{\oplus}$ is not shown). The names of noteworthy exoplanets, discussed in any scientific chapters, or well-studied planets, have been positioned above the corresponding dots on the plot. Planets observed by *JWST* in Cycle 1 or 2 are additionally highlighted: those set for phase curve observations with a yellow star (\star), eclipse observations with a blue left-pointing triangle (\blacktriangleleft), transit observations with a green right-pointing triangle (\blacktriangleright), and both with purple diamonds (\blacklozenge). The lower panel provides a zoom-in to the population of smaller exoplanets but is otherwise identical to the upper panel.

a planet on such a tight orbit (see also Bryson et al. 2020; Zhu & Dong 2021). For comparison, one in five G-type stars are estimated to have an Earth-sized planet

in the habitable zone around their stars (Kunimoto & Matthews 2020). The origin of these USPs is still being highly studied and the dominant formation mechanism is generally unknown.

USPs are typically small: of the 132 planets discovered to this date with an orbital period shorter than a day and a measured radius, 113 (i.e., 86%) are smaller than 2 Earth radii. For comparison, only 37% (1562 of 4180) of all planets with radii are $< 2 R_{\oplus}$. It was originally thought that these small USPs might have been Hot Jupiters (HJs) which underwent photoevaporation due to the proximity to their host star (Jackson et al. 2013; Valsecchi et al. 2015; Königl et al. 2017; Winn et al. 2018). However, two observations have emerged, suggesting otherwise. Firstly, it is well known that HJs are typically found around metal-rich stars (Petigura et al. 2018). This strong correlation with metallicity is not seen for small USP planets (Winn et al. 2017). If HJs would have been the progenitors of USPs then they also have to orbit the same type of stars. Secondly, HJs are typically found alone and rarely have other planets in their systems. This is in strong contrast to USPs which often have other companions in the system (Sanchis-Ojeda et al. 2014; Adams et al. 2017; Petrovich et al. 2019). This still leaves sub-Neptunes as a possible progenitor. In this scenario, small USPs would be exposed cores of sub-Neptunes (planets with approximately $2.0 - 3.9 R_{\oplus}$) instead which underwent photoevaporation or Roche overflow (Lundkvist et al. 2016; Lee & Chiang 2017; Winn et al. 2018). This would then be also consistent with hot-sub Neptunes not showing a strong correlation with host star metallicity like USPs (Winn et al. 2018). In this scenario, the progenitors might have initially formed at greater separations and then migrated to their current orbits due to gravitational interactions with the disk (Ida & Lin 2004; Schlaufman, Lin & Ida 2010; Terquem 2014) or tidal dissipation (Petrovich et al. 2019; Pu & Lai 2019). As the planets would have formed further out then, they would consist of water-rich material (making them “wet”).

Another hypothesis is the formation of these small planets on their tight orbits (also known as “in-situ” formation) (Chiang & Laughlin 2013). A planet that formed that closely to its host star would be expected to lack volatiles and be “dry”. Some models predict that only the most refractory elements (i.e., elements which only condense at high temperatures of approximately 1400 K; Wang et al. 2019) would be available as planetary building blocks, leading to the formation of relatively low density, core-less worlds dominated by Calcium and Aluminium (Dorn et al. 2019).

Additional measurements of the radii and masses of USPs, along with discovering more of these planets, will contribute to our understanding of how this population is formed. Certain models offer predictions about their origin, impacting the presence of water they might contain. *JWST* could then be used to characterize the atmospheres of these worlds to search for water. Moreover, models, such as the low eccentricity tidal dissipation scenario (Pu & Lai 2019), make specific predictions about the existence of unseen planets, providing testable hypotheses for future observations.

1.1.3 Lava planets

If the temperature on the dayside of a small, rocky exoplanet reaches a temperature of approximately 1300 K, silicates will start melting leading to a molten surface (see Chao et al. 2021, and references within). Between this temperature and the silicate liquidus temperature of approximately 2000 K the magma will consist of a viscous mix of liquid and solid compounds (Hirschmann 2000; Wordsworth & Kreidberg 2022). It is worth noting here that no solar system body experiences temperatures like this caused by solar irradiation with the substellar temperatures of Mercury and Venus being well below 1000 K (Chao et al. 2021). By further increasing the dayside temperature, the planet’s surface magma ocean will outgas a thin rock vapor atmosphere (Schaefer & Fegley 2009; Léger et al. 2011; Miguel et al. 2011; Ito et al. 2015; Kite et al. 2016). At 1500 K the outgassed atmosphere will be very tenuous at a surface pressure of 10^{-7} bar. This further increases exponentially reaching 10^{-3} bar at 2000 K and 10^{-2} bar at 2500 K (Zilinskas et al. 2022). Depending on the temperature of the planet, various species will dominate the atmospheric composition like Na, O, O₂, SiO, SiO₂, MgO, and FeO (Schaefer & Fegley 2009; Miguel et al. 2011; Chao et al. 2021; Zilinskas et al. 2022). Of these, the silicon oxides, SiO and SiO₂ are of particular interest as they have spectral features, which should be detectable by the MIRI/LRS instrument on *JWST*: by observing the planet’s emission spectrum, SiO₂ should cause a lowered emission around 7 μm and SiO will be in emission leading to an increased emission compared to a black body around 9 μm (Zilinskas et al. 2022). Observing these features would lead to the first detection of a rocky vapor atmosphere outgassed from a magma ocean. Thankfully, the archetypal lava world K2-141 b will be observed in two separate *JWST* programs during Cycle 1 of its mission: program GO2347 by Dang et al. (2021) and GO2159 by Espinoza et al. (2021).

1.2 Observing techniques of atmospheres

In the following, several techniques for the characterization of transiting exoplanets will be discussed (there are many in-depth reviews on exoplanet atmospheres characterization methods and their results; see e.g., Deming & Seager 2017; Kreidberg 2018; Deming et al. 2019; Madhusudhan 2019). Some techniques like direct imaging of exoplanet atmospheres or high-resolution Doppler spectroscopy will not be covered here as the current instruments do not have the needed precision to detect the faint signal caused by rocky exoplanet atmospheres. This is typically because the star outshines its companion by several orders of magnitude, making it challenging to detect the planetary signature. It is however worth noting that high-resolution Doppler spectroscopy on a ground-based extremely large telescope (ELT) might be able to be used in the future to detect an atmosphere on the non-transiting, potentially habitable exoplanet Proxima b (Snellen et al. 2013, 2015; Wang et al. 2017; Birkby 2018). Currently being studied, space-based missions, which would be able to characterize potentially habitable exoplanets include NASA’s *Habitable Worlds Observatory* (*HWO*) (National Academies of Sciences, Engineering, and Medicine 2021) and ESA’s *Large Interferometer For Exoplanets*

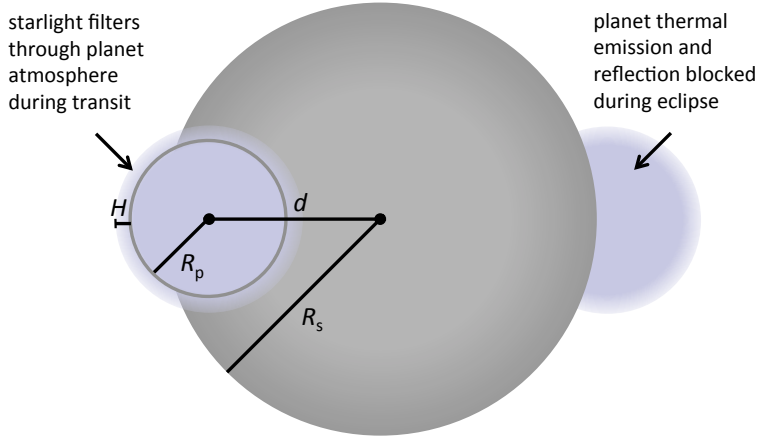


Figure 1.5: Geometry of the exoplanetary system when observing a transmission or emission spectrum. When the planet passes between the observer and its host star we observe a transit. Stellar light then travels through the planetary atmosphere, which leads to feature sizes in the transmission spectrum that are proportional to the scale height of the planet $H = k_B T_{\text{eq}}/(\mu g)$, where k_B is the Boltzmann constant, T_{eq} the equilibrium temperature of the planet, μ the mean molecular weight and g the planetary surface gravity. Approximately, half an orbital period later, the planet disappears behind its star and we observe the eclipse. Figure adapted from Robinson (2017) and Kreidberg (2018).

(*LIFE*) mission (Quanz et al. 2022b,a).

1.2.1 Transmission spectroscopy

When a planet transits between us (the observer) and its host star, the stellar light will pass through the planetary atmosphere at the day-night terminator (see Fig. 1.5). At the moment of transit (also known as primary eclipse) we see absorptions caused by the planet's spectrum superimposed with the stellar spectrum. By taking the difference between the spectrum we observe during transit and the one out of transit, we receive the transmission spectrum of the exoplanet. Molecules or atomic species will then leave absorptions in the transmission spectrum, making them detectable. This technique led to the first detection of an exoplanetary atmosphere on the hot Jupiter HD 209458 using the Space Telescope Imaging Spectrograph (STIS) onboard the *Hubble Space Telescope* (HST) by looking at the absorption by neutral Sodium in the optical (Charbonneau et al. 2002) and atomic Hydrogen in the UV (Lyman α) (Vidal-Madjar et al. 2003).

The size of the planet's transmission spectrum is proportional to the planet's scale height, $H = k_B T_{\text{eq}}/(\mu g)$, where k_B is the Boltzmann constant, T_{eq} the equilibrium temperature of the planet, μ the mean molecular weight and g the planetary surface gravity. This explains why the best planets for transmission spectroscopy will have high temperatures, low surface gravities, and a low mean

molecular weight atmosphere, e.g., hydrogen-dominated atmospheres. Commonly detected species in transmission spectroscopy include molecules in the infrared wavelengths, like H_2O (e.g., Kreidberg et al. 2015), or now with *JWST* CO_2 (*JWST* Transiting Exoplanet Community Early Release Science Team et al. 2023) and CH_4 (Bell et al. 2023b). Furthermore, the alkali metals Na and K can be detected in the visible due to their strong absorptions in the visible (e.g., Charbonneau et al. 2002; Feinstein et al. 2023).

Clouds can also strongly affect the observed transmission spectrum of a planet caused by the slant viewing geometry through the planet’s atmosphere during transit (Fortney 2005; Sing et al. 2016). They effectively make a planet appear bigger and therefore completely mute or weaken spectral features in the transmission spectrum (see e.g., Deming et al. 2013; Kreidberg et al. 2014a; Knutson et al. 2014; Kreidberg et al. 2015). Due to Rayleigh scattering, condensates can also lead to a strong increase in transit depths at shorter wavelengths, causing a so-called scattering slope (see e.g., Pont et al. 2008; Lecavelier Des Etangs et al. 2008; Sing et al. 2011b). Clouds do not weaken planetary features in emission (see Chapter 1.2.2) as much as they do in transmission due to the long slant paths at the limb the photons travel through in the latter technique.

The heterogeneity of the stellar disk can strongly affect a transmission spectrum and has to be considered (Sing et al. 2011b; Rackham et al. 2017, 2018; Pinhas et al. 2018; Rackham et al. 2023). In particular, an unocculted starspot (cool areas on the stellar photosphere) will make the star effectively redder during transit, as more area of the star is cooler than compared to out of transit. This reddening will lead to an increasing slope towards shorter wavelengths in the planetary spectrum McCullough et al. (2014). On the other side, faculae, which are hot spots on a star, will lead to a decrease in transit depth with shorter wavelengths. Additionally, the existence of molecules (like water, Wallace et al. 1995), in a cool star spot can lead to wrongly attributing the molecular features to the planet’s atmosphere (Kreidberg 2018). This effect is known as the transit light source (TLS) effect and is caused by the fact that the transit chord might not be representative of the stellar disk as a whole (Rackham et al. 2018). This is particularly a problem for planets orbiting M dwarfs which are typically more active and have a higher star coverage (Rackham et al. 2018). The TLS effect does not affect emission spectroscopy because the planet does not cross the stellar disk during this kind of observation. The only way to disentangle the planetary and stellar signals is by monitoring the star and determining its activity by studying its photometry variability or comparing to activity indicators (e.g., Nikolov et al. 2014).

1.2.2 Emission spectroscopy

Approximately half an orbital period after the transit, we observe the (secondary) eclipse of the planet. The exact timing of the eclipse depends on the eccentricity of the planet and the argument of periastron (for a review on secondary eclipses see Alonso 2018). During the eclipse, we only observe the spectrum of the star because the planet is hidden behind its host star providing us with the measurement of the baseline. Right before and after the eclipse, we see the combined planetary

dayside and stellar spectrum. By taking the difference between these two cases we yield our dayside emission spectrum of the planet which is the spectrum, reflected or emitted by the dayside of the planet. Compared to the transmission spectrum, we now probe the dayside compared to the limb or terminator of the planet.

A planetary emission spectrum will have two contributions: reflection and emission. Reflection typically dominates at optical wavelengths where exoplanet host stars typically reach the peak of their stellar spectrum. Thermal emission on the other side usually dominates in the infrared wavelengths due to the lower temperatures of the exoplanets. The majority of dayside observations have been performed in the infrared as with longer wavelengths the host star is fainter as in the optical, increasing the planet-to-star contrast and making the planet more observable.

The planet’s albedo plays an important role when observing an eclipse: in reflected light which is typically the dominating source of emission coming from a planet in the optical wavelengths, the amount of reflectivity is typically described by the geometric albedo, A_g . It is basically a measurement of the reflection efficiency of the planet as a function of wavelength at full illumination (i.e., at a phase angle of zero) (Seager 2010; Roberge & Seager 2018). High geometric albedos might be indicative of reflective clouds in the atmosphere, surface ices, or highly reflective lava (see e.g., Mansfield et al. 2019). The thermal emission on the other hand depends on the planet’s temperature. Temperature is connected to the planet’s heat redistribution efficiency and the planet’s Bond albedo A_B . The Bond albedo measures the fraction of stellar radiation that is absorbed by the planet at all wavelengths and is therefore wavelength independent (Seager 2010; Deming & Seager 2017; Alonso 2018).

The first eclipse observations were observed with the *Spitzer Space Telescope* in the infrared for hot Jupiters (Deming et al. 2005; Charbonneau et al. 2005). For both planets, temperatures were derived by measuring the depth of the eclipse. Furthermore, the timing of the eclipse constrained the eccentricity of the planets. In the following years, *Spitzer* continued to detect many more eclipses of exoplanets in the infrared. The IRAC photometry centered around 3.6 and 4.5 μm became the powerhouse of space-based eclipse and phase curve observations until the telescope’s shutdown in 2020.

The emerging planetary emission spectrum will depend on the chemical composition of the planetary atmosphere and its temperature gradient (Kreidberg et al. 2014b; Stevenson et al. 2014b). A temperature profile with a temperature decreasing with altitude will lead to an absorption feature. For example, a cloud and haze-free, CO_2 dominated atmosphere will show strong absorption in its planetary emission spectrum at 15 μm . This is because the CO_2 molecule exhibits a “bending” mode at this wavelength (Catling & Kasting 2017) leading to the gas preventing us from probing the low, hot surface and we only see the cold, top layer of the atmosphere at this wavelength¹. If the temperature gradient is reversed, the temperature increases with altitude, we will see the CO_2 in emission. This can for example happen if the atmosphere has hazes that absorb stellar radiation in the

¹The effective absorption of infrared radiation by CO_2 is also why it is such an effective greenhouse gas in the Earth’s atmosphere (Catling & Kasting 2017).

upper layers of the atmosphere. This will lead to an effective heating of the top atmospheric layer and a cooling of the lower ones. This process is called “thermal inversion” and it is also observed in our solar system: for example, on Earth due to ozone absorbing UV in the stratosphere and on Saturn’s moon Titan due to photochemical hazes (Lellouch 2018; Encrenaz & Coustenis 2018).

Eclipse measurements also give strong constraints on the global climate and heat transport on an exoplanet. In the case of a thick atmosphere, winds can transport heat from the dayside over to the nightside, effectively cooling the dayside and heating the nightside. We therefore get an estimate of the surface pressure by measuring the dayside temperature (Selsis et al. 2011; Koll et al. 2019a). The full picture of a planet’s climate can be revealed by observing the planet’s emission at all planetary phases by observing a so-called “phase curve”.

1.2.3 Phase curves

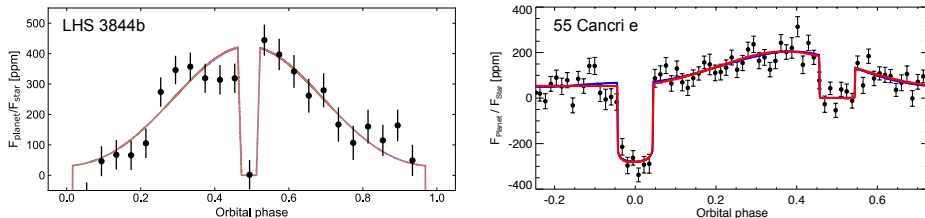


Figure 1.6: Thermal phase curves of small ($< 2 R_{\oplus}$) exoplanets as observed by *Spitzer*. Left: The symmetric phase curve of the rocky exoplanet LHS 3844 b ($1.3 R_{\oplus}$) reveals no indication of a hotspot offset, suggesting that the planet is devoid of any atmosphere and resembles a bare rock. Right: The peak emission occurs before the eclipse for the phase curve of 55 Cnc e ($1.9 R_{\oplus}$). This hot spot offset is indicative of heat transport in a moderate mean molecular weight (CO or N_2) atmosphere with a surface pressure of a few bars. In this scenario, a super-rotating jet could transport energy away from the substellar point (Kite et al. 2016; Hammond & Pierrehumbert 2017; Angelo & Hu 2017). The hotspot offset could however not be confirmed by a reanalysis of the data by Mercier et al. (2022). Figures taken from Kreidberg et al. (2019a); Demory et al. (2016a); Wordsworth & Kreidberg (2022).

When we observe a planet for a whole planetary orbit, we will measure the planet’s spectrum from the different sides (or phases) of the planet (for a review on phase curves and mapping exoplanets with them, see Parmentier & Crossfield 2018; Cowan & Fujii 2018). By measuring the emission coming from the various longitudes of the planet, we measure the day-to-night temperature contrast informing us about the heat transport on the planet. We essentially measure an emission spectrum at various phases of the planet, giving us information on the abundances and temperatures all around the planet Sing et al. (2016).

The planets that are typically being studied with phase curves are on short orbital orbits of a few days or hours and due to the strong tidal forces they experience most likely tidally locked. Eclipses, which give us a measurement of the

stellar flux alone, provide us with a baseline. Therefore, phase curve observations usually start shortly before an eclipse and end right after the following eclipse, one orbital period later (e.g., Mikal-Evans et al. 2022). As this observational setup also covers at least one transit, we additionally observe a transmission spectrum.

The first successful photometric phase curve was measured by Knutson et al. (2007) for the hot Jupiter HD 189733 b with the *Spitzer Space Telescope* at 8 μm . The peak brightness did not occur at the substellar point but right before the eclipse, indicating an eastward offset of the hotspot. These observations were in agreement with predictions made by 3D global circulation models (GCMs), which were developed to explain the observed thermal hot Jupiter phase curves. These models predict the existence of an eastward equatorial jet transporting heat eastwards away from the substellar point (Showman et al. 2008, 2009). The first spectroscopic phase curve was then taken by Stevenson et al. (2014b) with *HST*/WFC3 for the hot Jupiter WASP-43 b (Kreidberg 2018). The observations were able to constrain the planet’s temperature-pressure profile as a function of longitude, the hotspot offset as a function of wavelength, and with all that unveiling the substantial information content stored in a spectroscopic phase curve observation. Phase curve observations of smaller planets have been also possible thanks to *Spitzer* and *JWST* (see 1.3.1 and 1.3.3).

1.3 Notable Planets and Systems

In the following, I will discuss a selection of small exoplanets, that had a successful eclipse measurement in either other optical or infrared, giving us constraints on the planet’s reflectivity or temperature.

1.3.1 55 Cnc e

55 Cnc is a bright ($V = 6$ mag, $K_s = 4$ mag), nearby (12.6 pc), Sun-like star hosting five exoplanets (for a review on the system, see Fischer 2018). Only the most inner one planet, 55 Cnc e is known to be transiting with an ultra-short-period of 18 hours (McArthur et al. 2004; Fischer et al. 2008). The short orbital period leads to an equilibrium temperature of approximately $T_{\text{eq}} = 1950$ K (Bourrier et al. 2018) (assuming a Bond albedo of zero and perfect heat redistribution). Transits of the planet were discovered around the same time with the Microvariability and Oscillations of Stars (*MOST*) telescope (Winn et al. 2011) and the *Spitzer Space Telescope* (Demory et al. 2011). The planet’s bulk density ($R_p = 1.9 R_{\oplus}$, $M_p = 8.6 M_{\oplus}$) is inconsistent with an Earth-like interior composition but rather with a pure silicate (MgSiO_3) composition, a composition with a significant amount of volatiles or a composition dominated by Al and Ca without any iron core (Crida et al. 2018b; Zeng et al. 2019; Dorn et al. 2019).

The phase curve captured by the *Spitzer Space Telescope*, which was the first one taken for a small exoplanet, revealed a surprisingly large eastward offset of the planet’s hotspot ($41 \pm 12^\circ$) (see Fig. 1.6) (Demory et al. 2016a). This phase curve offset was initially attributed to a moderate mean molecular weight (CO or N_2)

atmosphere with a surface pressure of a few bars featuring a super-rotating jet, which transports energy away from the substellar point (Kite et al. 2016; Hammond & Pierrehumbert 2017; Angelo & Hu 2017). However, a recent reassessment conducted by Mercier et al. (2022) indicated that this hotspot offset might be an artifact of the data reduction process, revealing a negligible offset instead. The eclipse depth of the planet was also found to vary by a factor of 3.7 between 2012 and 2013, corresponding to dayside brightness temperatures ranging from 1300 K up to 2800 K (Demory et al. 2016b). The authors suggested that the observed changes might be attributed to volcanic activity, giving rise to plumes that raise opacity within the *Spitzer* bandpass (Demory et al. 2016b; Tamburo et al. 2018). A recently published optical phase curve of 55 Cnc e observed by *CHEOPS* (CHaracterising ExOPlanet Satellite) detects a phase-curve amplitude and offset that varies in time, potentially attributing it to a dust torus around the star (Meier Valdés et al. 2023).

Even after all the monitoring, the planet’s atmospheric and interior composition is still unclear. The search for escaping hydrogen from the planet led to a non-detection of hydrogen-atmosphere (Ehrenreich et al. 2012). A recent study did also not discover any Helium atmosphere (Zhang et al. 2021b). Both studies together make it unlikely that 55 Cnc e has any H/He-rich primordial atmosphere. The search for various atomic and ionized species that might have originated from a silicate-vapor atmosphere in high-resolution spectroscopy also only led to non-detections (Keles et al. 2022; Rasmussen et al. 2023). A low-resolution *HST*/WFC3 transmission spectrum by Tsiaras et al. (2016a) hinted at an HCN absorption feature in a likely hydrogen-rich atmosphere. High-resolution transit spectroscopy by Deibert et al. (2021) however ruled out the most likely models presented in Tsiaras et al. (2016a). To shed light on 55 Cnc e, two *JWST* programs were approved in Cycle 1 which will characterize the planet’s atmosphere and planetary rotation period (see Fig. 1.4) (Hu et al. 2021; Brandeker et al. 2021).

1.3.2 Kepler-10 b

Kepler-10 is an old, fainter ($V = 11$ mag, $K_s = 9$ mag) Sun-like star with two transiting (Kepler-10 b and c) and one non-transiting planet (Kepler-10 d) (Bonomo et al. 2023). Kepler-10 b is a lava world with a bulk density consistent with Earth ($R_p = 1.5 R_\oplus$, $M_p = 3.3 M_\oplus$) and an ultra-short orbital period of just 20 hours leading to an equilibrium temperature of $T_{\text{eq}} = 2170$ K. The planet was the first rocky planet discovered by the *Kepler* mission (Batalha et al. 2011). Eclipse observations of the planet by *Kepler* showed a relatively deep eclipse depth that suggests a high geometric albedo of 0.60 ± 0.09 for the planet (Batalha et al. 2011; Sheets & Deming 2014). This comes as a surprise as small exoplanets ($1.0 - 2.0 R_\oplus$), are typically very dark showing upper values in the geometric albedos of 0.11 ± 0.06 (note that Kepler-10 b is removed from this statistical albedo analysis because it significantly increases the average of the *Kepler* small planet sample) (Sheets & Deming 2017). A high reflectivity like that for Kepler-10 b might be due to clouds or due to unusually reflective lava (Rouan et al. 2011; Essack et al. 2020). How-

ever, recently Zieba et al. (2022) suggested that the high emission in the optical would not be due to a highly reflective surface but rather due to emission features of Sodium and Potassium indicating a silicate atmosphere, which would be consistent with the planet’s bulk density and high dayside temperature. Further spectroscopic follow-up of the planet in these optical wavelengths could confirm this hypothesis.

1.3.3 LHS 3844 b

LHS 3844 b was discovered by the Transiting Exoplanet Survey Satellite (*TESS*) and has an orbital period of just 11 hours (Vanderspek et al. 2019). The small planet ($R_p = 1.3 R_\oplus$) has a equilibrium temperature of $T_{\text{eq}} = 805$ K and is orbiting an M dwarf ($V = 15$ mag, $K_s = 9$ mag). The planet was observed for over 100 hours continuously with *Spitzer* at $4.5 \mu\text{m}$ to collect its thermal phase curve (Kreidberg et al. 2019a). The phase curve was symmetric showing no hint of a hotspot offset (see Fig. 1.6), a large day-nightside contrast, and no significant flux emitted by the planet’s nightside. All that is consistent with the planet being a bare rock and the modelling presented in Kreidberg et al. (2019a) ruled out any thick (> 10 bar) atmosphere on the planet. Thinner atmospheres would have been eroded by the stellar irradiation over the planet’s lifetime. Ground-based transmission spectra are also consistent with no significant atmosphere on the planet (Diamond-Lowe et al. 2020).

The planet is in a sweet spot for surface characterization with the highest expected thermal emission signal among terrestrial planets below 1000 K, without reaching temperatures that would cause surface melting (Mansfield et al. 2019). By comparing the eclipse depth measured by *Spitzer* with emission spectra corresponding to various surface compositions (ultramafic, feldspathic, basaltic, and granitoid), it was determined that the observations are most consistent with a pure dark basaltic surface (Kreidberg et al. 2019a). A surface like this is similar to the lunar mare and Mercury, possibly arising from widespread extrusive volcanic activity. MIRI/LRS eclipse observations scheduled for *JWST* Cycle 1 will measure the infrared emission spectrum of the planet between 5 and $12 \mu\text{m}$ and search for trace amounts of SO_2 which might arise from volcanic activities (Kreidberg et al. 2021b). A *JWST* phase curve of the planet will be also studied by Zieba et al. (2023a) with NIRSpec/G395H ($2.87 - 5.14 \mu\text{m}$), to study the emission as a function of longitude.

1.3.4 TRAPPIST-1

A particularly interesting system for the characterization of rocky exoplanets is TRAPPIST-1 (for a short review on the TRAPPIST survey and TRAPPIST-1, see Burdanov et al. 2018; Gillon et al. 2020). Seven approximately Earth-sized planets orbit the nearby (12 pc) ultra-cool-dwarf ($M_s = 0.09 M_\odot$, $R_s = 0.12 R_\odot$) TRAPPIST-1, with orbital periods ranging from 1.5 days (for planet b) to 18.8 days (for planet h) (Gillon et al. 2016, 2017; Agol et al. 2021). The planets allow us to do comparative planetology between all seven transiting planets in this system

(Morley et al. 2017). Up to four of the planets (d, e, f, g) are also in the temperature zone around their star where liquid water could exist on the planet’s surface, making this system particularly interesting for the study of its habitability (Kasting et al. 1993; Kopparapu et al. 2013, 2014; Wilson et al. 2021). There are several factors contributing to the potential challenges faced by the TRAPPIST-1 planets in retaining their atmospheres, rendering them comparatively less hospitable for life: late M-dwarfs like TRAPPIST-1 have prolonged pre-main sequence phases (Baraffe et al. 1998, 2015), which can take billions of years, where they highly luminous leading to extreme water loss (Luger & Barnes 2015; Bolmont et al. 2017). They are also known to show frequent flares and coronal mass ejections further leading to atmospheric escape (Roettenbacher & Kane 2017; Paudel et al. 2018; Tilley et al. 2019; Airapetian et al. 2020).

The system was observed by *Spitzer* continuously for approximately 20 days in 2016. Due to the compact nature of the system, the system experiences transit-timing variations (TTVs): the planetary transits do not occur in a constant interval but vary due to gravitational interactions between the different planets. The delay or early arrival of a transit depends on the masses of the other planets in the system. This technique was then used to measure the masses and radii of all of the planets in the system to high precision (Yee et al. 2017). The masses are two orders of magnitude more accurate than what current radial velocity (RV) capabilities can achieve (Agol et al. 2021). The planets do all fall onto the same rocky mass-radius relationship which is slightly depleted in iron compared to the Earth, 21% for the TRAPPIST-1 planets compared to 32% for the Earth. Also consistent would be the planets having an Earth-like composition, which is enriched in lighter elements, like water (Agol et al. 2021).

The transmission spectra of all planets in the TRAPPIST-1 system have been collected with *HST*/WFC3 and *Spitzer* but were only able to rule out hydrogen-dominated atmospheres. The observations are all consistent with cloudy atmospheres, high mean-molecular weight atmospheres (e.g., CO_2 , H_2O), or no atmospheres at all (de Wit et al. 2016, 2018; Zhang et al. 2018; Ducrot et al. 2018; Garcia et al. 2022). All of the planets will be studied by *JWST* in Cycle 1 in transmission and the two most inner planets, b and c, in emission. The first *JWST* transmission spectrum of a TRAPPIST-1 planet was published in Lim et al. (2023), which used *JWST*/NIRISS (0.6 – 2.8 μm) to observe planet b in two visits. The shape of the transmission spectra between the two visits differs significantly from each other which is explained by unocculted starspots in the first visit and unocculted faculae in the second. The observations were able to rule out hydrogen-rich atmospheres confirming previous studies, but could not determine the atmospheric composition. The study shows how stellar contamination dominates over the transmission spectrum and that the stellar contribution has to be accurately disentangled from the planetary signature. As discussed in Section 1.2.2, emission spectroscopy does not suffer from stellar contamination like transmission, because the planet does not move across the stellar disk as seen by the observer, therefore not occulting any star inhomogeneities. The photometric emission studies of TRAPPIST-1 b (Greene et al. 2023) and TRAPPIST-1 c (Zieba et al. 2023b) with *JWST* showed deep eclipses at 15 μm . They are inconsistent with cloud-free, CO_2 dominated

atmospheres as the CO_2 in their atmospheres would lead to low brightness temperatures at $15\text{ }\mu\text{m}$ and therefore shallow eclipses. TRAPPIST-1 b is consistent with a dark, bare rock surface, whereas TRAPPIST-1 c is more consistent with thin CO_2 atmospheres are slightly non-zero albedo surfaces (Greene et al. 2023; Zieba et al. 2023b). Observations in other wavelengths (outside of the CO_2 band at $12.8\text{ }\mu\text{m}$ for planet b, Lagage & Bouwman 2017) and a phase curve (at $15\text{ }\mu\text{m}$ for planet b and c, Gillon et al. 2023) are planned and will give us a more complete picture of the atmospheres of the planets and their heat redistribution.

1.4 Facilities

The majority of detections mentioned in the previous chapters have been primarily focused on the characterization efforts performed with space-based observatories, in particular, *HST*, *Spitzer*, and *JWST*. Ground-based atmospheric characterization has several disadvantages: it for example suffers from turbulence in Earth’s atmosphere. There are also wavelengths in particular in the UV and infrared (due to the water absorption bands) where the Earth’s atmosphere is mostly opaque and does not let the majority of radiation reach the surface. The thermal background is also higher on Earth than in a thermally stable environment like the Earth-Sun Lagrange point, L2 (where *JWST* is located). On the other side, however, ground-based telescopes are theoretically not space-constrained, unlike space telescopes, which must conform to the dimensions of the launch rocket fairing. Ground telescopes have detected, for example, Na and K in the optical wavelengths (e.g., Redfield et al. 2008; Snellen et al. 2008; Sing et al. 2011a), Helium (e.g., Allart et al. 2019; Zhang et al. 2022), water (e.g., Birkby et al. 2013) or various carbon and nitrogen-bearing species (e.g., Jacobbe et al. 2021).

Figure 1.7 shows a selection of space-based instruments for the study of exoplanets. Of these the powerhouse facilities of atmospheric characterization in the past decade were *HST* with its WFC3 (Wide Field Camera 3, covering the near-infrared) (McCullough & MacKenty 2012; Deming et al. 2013) and STIS (Space Telescope Imaging Spectrograph, covering the optical and UV) (Ehrenreich et al. 2015; Sing et al. 2016) instruments and *Spitzer* with its photometric Infrared Array Camera (IRAC) Channel 1 and 2 centered around 3.6 and $4.5\text{ }\mu\text{m}$ (Fazio et al. 2004). The WFC3 G141 grism (1.1 and $1.7\text{ }\mu\text{m}$) covers a strong water absorption feature around $1.4\text{ }\mu\text{m}$, which leads to dozens of detections of water in the atmospheres of hot Jupiters, Neptune-sized planets, and sub-Neptunes (e.g., Deming et al. 2013; Huitson et al. 2013; McCullough et al. 2014; Fraine et al. 2014; Kreidberg et al. 2014b, 2015; Benneke et al. 2019). By observing eclipses, *HST* also detected the same water feature in emission in the atmosphere of some exoplanets (e.g., Crouzet et al. 2014; Kreidberg et al. 2014b). G102, the bluer grism on *HST*/WFC3 was used to detect Helium in the atmosphere of WASP-107 at 1083 nm (Spake et al. 2018). Finally, STIS has led to many Na (577 nm) and K (779 nm) detections in the atmospheres of transiting hot Jupiters (Sing et al. 2016; Madhusudhan 2019). Additionally to the high precision spectroscopy by *HST*, the *Spitzer* Space Telescope has been able to provide us with near-continuous pho-

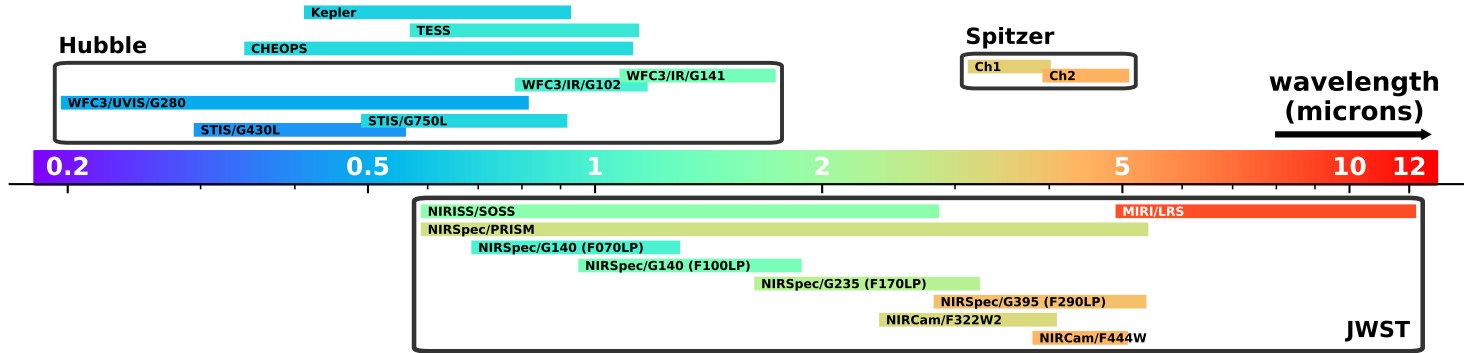


Figure 1.7: Figure showing current (*JWST*, *HST*, *TESS*, and *CHEOPS*) and past (*Kepler* and *Spitzer*) space-based instruments and telescopes for the observation of exoplanets and their coverage of the electromagnetic spectrum. Other observational modes of *HST* or *Spitzer* are not depicted, as they were either only used on a handful of planets (e.g., Channel 3 and 4 on *Spitzer*, which were operational in the telescope’s “cold phase”) or generated not reproducible results (e.g., the NICMOS instrument on *HST*). Next to *JWST*’s MIRI/LRS instrument (low-resolution spectrograph; approximately 5 – 12 μm), MIRI also has nine broadband filters for photometric imaging with their center wavelength ranging from 5.6 to 25.5 μm . See Zieba et al. (2023b) i.e., scientific chapter 4, for an application of MIRI filter F1500W (centered around 15 μm) to observe an exoplanet. There is also a prospect of using MIRI/MRS (medium-resolution spectrograph; ranging from approximately 5 to 28 μm) for transiting exoplanets (Deming et al. 2021). Only *JWST* and *HST* have spectrographs. *Kepler*, *TESS*, *CHEOPS*, and *Spitzer*’s IRAC Channels 1 and 2 are photometric. Figure adapted from Kreidberg (2018).

tometry observations in its “warm phase” (after its coolant ran out) until it shut down in 2020, leading for example to phase curve observations of rocky exoplanets or the characterization of the TRAPPIST-1 planets (for a review of the scientific highlights of *Spitzer*, see Deming & Knutson 2020).

Following the deployment of the *James Webb Space Telescope (JWST)* on December 25th, 2021, followed by the start of scientific data collection, a state-of-the-art space telescope has been introduced, enhancing our observational capabilities. The advantages of *JWST* are immense, most importantly (1) *JWST* collecting area is approximately 6 times greater than *HST*’s collecting area, and (2) the various instruments cover a great wavelength range from the optical at 0.6 μm up to 28 μm (although the longest wavelengths might not be usable for transiting exoplanets) (see Fig. 1.7). In the short time of its operations, it has already delivered major discoveries for transiting exoplanets including the first detection of CO_2 (JWST Transiting Exoplanet Community Early Release Science Team et al. 2023), CH_4 (Bell et al. 2023b), and SO_2 (JWST Transiting Exoplanet Community Early Release Science Team et al. 2023; Rustamkulov et al. 2023; Alderson et al. 2023) in an exoplanet atmosphere, the first detection of photochemistry following the observation of SO_2 (Tsai et al. 2023), and the first detection of thermal emission coming from temperate rocky exoplanets (Greene et al. 2023; Zieba et al. 2023b). Anticipating a propellant lifespan of 20 years or beyond for *JWST*, it is expected that its observations will lead to numerous groundbreaking discoveries that will improve our understanding of exoplanets and their atmospheres (Rigby et al. 2023).

1.5 This thesis

The work in this thesis revolves around the characterization of exoplanets through the analysis of primarily space-based data. Even though I do not spatially resolve the planet from the star in any of these following works, the combined stellar and planetary light informs us about the properties of the exoplanet like its radius, atmospheric composition, reflectivity, and heat redistribution. The photometric and spectroscopic observations were taken with a range of telescopes like *Kepler*, *Spitzer*, *HST*, and *JWST*.

In **Chapter 2** we characterize a lava world called K2-141 b with an ultra-short orbital period of just 6.7 hours. Discovered by *Kepler* during its second-light K2 mission, the planet showed a strong eclipse signal in the optical wavelengths of *Kepler*. By only having this one emission measurement, however, we have a degeneracy: we do not know how much of this emission is due to reflection and how much is due to thermal emission. We therefore study approximately 70 hours of *Spitzer* photometry of the planet in the infrared at 4.5 μm . With these continuous observations, we are able to take its phase curve and measure a hot dayside and cold nightside, consistent with no thick atmosphere redistributing heat. We also break the degeneracy by combining the optical data of *Kepler* and the infrared data of *Spitzer* and show that the high emission in the optical is either due to a reflective surface or emission features caused by a rock-vapor atmosphere. We also

suggest that the latter process might explain the high observed emission seen for Kepler-10 b rather than a reflective surface.

In **Chapter 3** we published an open-source `Python` code called `PACMAN`. It is an end-to-end pipeline for *Hubble Space Telescope* (*HST*) data taken by either of the infrared grisms on the Wide-Field-Camera 3 (WFC3). It includes spectral extraction and light curve fitting to receive a planetary transmission or emission spectrum. Covering a strong water absorption feature at 1.4 μm and its high stability and precision, which has been also used to observe phase curves of exoplanets, *HST* remains a valuable telescope for atmospheric characterization even in the era of *JWST*. In Chapter 5, we present the analysis of *HST*/WFC3 data for a hot, sub-Saturn mass planet using `PACMAN`.

In **Chapter 4** we present one of the first studies using data from the long-awaited *James Webb Space Telescope* (*JWST*). We use the Mid-Infrared Instrument (MIRI) on *JWST* combined with the 15 μm filter to observe the thermal emission coming from the temperate planet TRAPPIST-1 c. Our measured brightness temperature is disfavoured a thick, CO_2 -rich cloud-free atmosphere on the planet. The observations are able to rule out cloud-free O_2/CO_2 mixtures with surface pressures ranging from 10 bar (with 10 ppm CO_2) to 0.1 bar (pure CO_2). Thinner atmospheres or bare-rock surfaces are consistent with our measured planet-to-star flux ratio. The absence of a thick, CO_2 -rich atmosphere on TRAPPIST-1 c suggests a relatively volatile-poor formation history, for the planet. If all planets in the system formed in the same way, this would indicate a limited reservoir of volatiles for the potentially habitable planets in the system. Shortly before the publication of our work, the innermost planet TRAPPIST-1 b was observed in the same observational mode revealing a deep eclipse consistent with the planet being a dark, bare rock. More data for both planets is needed to paint a more complete picture of them, but already these first observations are presenting *JWST* capabilities to characterize temperate rocky exoplanets and push down to planets in temperature and size to the inner solar system bodies.

In **Chapter 5** we analyze *HST*/WFC3 data of the hot, low-density, sub-Saturn called KELT-11 b. Previous work on the planet using the G141 grisms data (1.1 – 1.7 μm) reveals a low-amplitude water feature that was several orders of magnitude below the anticipated levels predicted by planet formation models on our solar system. In this chapter, we analyze unpublished *HST*/WFC3 G102 (0.8 – 1.1 μm) spectroscopic grism data and also perform a reanalysis of the *HST*/WFC3 G141 data. We show that the previously seen low metallicity might be due to the `divide-white` technique which assumes that systematics do not change with wavelength. The transit depth of our G102 spectrum decreases toward shorter wavelengths, suggesting the presence of faculae on the stellar photosphere influencing our spectrum. This is commonly observed for late-type M-dwarfs but not for earlier-type stars like KELT-11, which is a retired A star. This suggests that stellar inhomogeneities should also be taken into consideration for earlier type stars.

Finally, in **Chapter 6** we work on the β Pictoris system, a near planetary system with gas giant planets, an edge-on circumstellar disk, and transiting exocomets. The star, exhibiting stellar pulsations, particularly δ Scuti pulsations,

offers the potential for indirect detection of gas giant planets through time delays in the pulsational signals. Analysis of multi-year δ Scuti pulsations using BRITE-Constellation, bRing, ASTEP, and *TESS* data reveals significant pulsations, but the study fails to detect expected signals for β Pictoris b and c. The limitations are attributed to inherent pulsational mode drifts and insufficient sensitivity in combined datasets for detecting timing drifts. Future work might show possible detection limits of other planets in the system.

With this we finish the introduction, covering the exoplanet zoo, detection methods, notable planets, and a short summary of the individual chapters of the thesis. Thanks to the launch of *JWST* and the construction of the ELTs, we will further characterize rocky worlds and compare our solar system to other exoplanetary systems. Of particular interest is also the observation of lava worlds with molten daysides, as the cover temperature regimes which are not accessible in our Solar System. Studying their atmospheres will also further inform us about the interior composition of these worlds. Rocky bare rocks also give us the possibility to study their surface compositions and learn about their geophysical history. Even though we will have to be very lucky to even detect biosignatures in one of the most observable exoplanets, the chances are good in the next few decades with the advent of the ELTs, the *HWO*, or *LIFE*.

2

K2 AND *SPITZER* PHASE CURVES OF THE ROCKY ULTRA-SHORT-PERIOD PLANET K2-141 B HINT AT A TENUOUS ROCK VAPOR ATMOSPHERE

Sebastian Zieba, Mantas Zilinskas, Laura Kreidberg, T. Giang Nguyen, Yamila Miguel, Nicolas B. Cowan, Raymond T. Pierrehumbert, Ludmila Carone, Lisa Dang, Mark Hammond, Tom Loudon, Roxana E. Lupu, Luca Malavolta, and Kevin B. Stevenson

Published in Astronomy & Astrophysics, 2022.

Abstract

K2-141 b is a transiting, small ($1.5 R_{\oplus}$) ultra-short-period (USP) planet discovered by the *Kepler Space Telescope* orbiting a K-dwarf host star every 6.7 hours. The planet’s high surface temperature of more than 2000 K makes it an excellent target for thermal emission observations. Here we present 65 hours of continuous photometric observations of K2-141 b collected with *Spitzer*’s Infrared Array Camera (IRAC) Channel 2 at $4.5 \mu\text{m}$ spanning ten full orbits of the planet. We measured an infrared eclipse depth of $f_p/f_* = 142.9^{38.5}_{39.0}$ ppm and a peak to trough amplitude variation of $A = 120.6^{42.3}_{43.0}$ ppm. The best fit model to the *Spitzer* data shows no significant thermal hotspot offset, in contrast to the previously observed offset for the well-studied USP planet 55 Cnc e. We also jointly analyzed the new *Spitzer* observations with the photometry collected by *Kepler* during two separate *K2* campaigns. We modeled the planetary emission with a range of toy models that include a reflective and a thermal contribution. With a two-temperature model, we measured a dayside temperature of $T_{p,d} = 2049^{362}_{359}$ K and a night-side temperature that is consistent with zero ($T_{p,n} < 1712$ K at 2σ). Models with a steep dayside temperature gradient provide a better fit to the data than a uniform dayside temperature ($\Delta\text{BIC} = 22.2$). We also found evidence for a nonzero geometric albedo $A_g = 0.282^{0.070}_{-0.078}$. We also compared the data to a physically motivated, pseudo-2D rock vapor model and a 1D turbulent boundary layer model. Both models fit the data well. Notably, we found that the optical eclipse depth can be explained by thermal emission from a hot inversion layer, rather than reflected light. A thermal inversion may also be responsible for the deep optical eclipse observed for another USP, Kepler-10 b. Finally, we significantly improved the ephemerides for K2-141 b and c, which will facilitate further follow-up observations of this interesting system with state-of-the-art observatories such as *JWST*.

2.1 Introduction

The field of exoplanetary science started off with the surprising discovery of planets with short orbital periods. The formation of these planets has been well studied and still remains a puzzle to this day (see e.g., Dawson & Johnson 2018). Ultra-short-period (USP) planets are an extreme subgroup of this population with orbital periods shorter than one day (for a review of USPs see e.g., Winn et al. 2018). The majority of these planets have been found to be smaller than $2 R_{\oplus}$ (Sanchis-Ojeda et al. 2014; Lundkvist et al. 2016).

One early theory was that these small USP planets could be remnant bare cores of hot Jupiters that lost their envelopes due to photoevaporation, Roche overflow, or other processes (Jackson et al. 2013). It was however shown that the well-known planet-metallicity correlation (Fischer & Valenti 2005) is not observed for USP planets (Winn et al. 2017). USP planets are therefore probably not evaporated hot Jupiters, but there is still no consensus about whether they are born rocky or whether they once had a modest hydrogen envelope (Van Eylen et al. 2018; Lopez 2017). As USPs and sub-Neptunes (planets between $2 R_{\oplus}$ and $4 R_{\oplus}$) generally orbit stars with similar metallicities, sub-Neptunes might be possible progenitors. Most USPs have Earth-like densities (Dai et al. 2019), but a few (55 Cnc e; Crida et al. 2018b,a) (WASP-47e; Vanderburg et al. 2017) have lower densities consistent with a low iron fraction or a small volatile envelope. Direct observations of the planet’s atmospheres are needed to distinguish between these scenarios.

55 Cnc e (Fischer et al. 2008; Dawson & Fabrycky 2010; Winn et al. 2011; Demory et al. 2011), is one of the best-studied small USP planets and shows evidence for a thick atmosphere (Demory et al. 2016a; Angelo & Hu 2017). It is one of the very few small planets ($< 2 R_{\oplus}$) for which thermal emission was observed in the infrared (others include LHS 3844 b by Kreidberg et al. (2019a) and K2-141 b in this work). Most other USP planets have been observed in the visible light with missions such as *CoRoT* (Auvergne et al. 2009), *Kepler* (Borucki et al. 2010), *K2* (Howell et al. 2014), or more recently *TESS* (Ricker et al. 2014). Numerous observations of 55 Cnc e with *Spitzer* have shown some surprising results: a large hotspot offset, where the hottest region of the planet is significantly offset from the substellar point (Demory et al. 2016a). This phase curve offset could be explained by a thick atmosphere with a super-rotating jet that advects energy away from the substellar point (Kite et al. 2016; Hammond & Pierrehumbert 2017; Angelo & Hu 2017). Demory et al. (2016b) furthermore reported varying observed dayside temperatures for 55 Cnc e ranging from 1300 K to 2800 K. The authors propose that these observed changes were possibly caused by volcanic activity, leading to plumes which increase the opacity in the *Spitzer* bandpass. Tamburo et al. (2018) reanalyzed the *Spitzer* observations and conclude that the changing eclipse depths were best modeled by a year-to-year variability model. They also suggest that the dayside of the planet is intermittently covered with reflective grains obscuring the hot surface, possibly originating from volcanic activity or cloud variability. Despite the numerous observations of 55 Cnc e, its composition and structure still remains puzzling. Dorn et al. (2019) suggest that the low observed density of 55 Cnc e ($6.4 \pm 0.3 \text{ g/cm}^3$) might be explained by the planet being a part of a new

class of Super-Earths which formed from high-temperature condensates. Planets similar to this would have no core and have enhancements in Ca, Al rich minerals leading to a lower overall bulk density compared to an Earth-like (30% Fe and 70% MgSiO_3) or a pure MgSiO_3 composition.

Recent observations of 55 Cnc e with *TESS* also showed a tentative deep optical eclipse, which could be caused by a nonzero albedo if confirmed (Kipping & Jansen 2020). Other observations of 55 Cnc e in the optical by the *Microvariability and Oscillations in Stars (MOST)* telescope (Winn et al. 2011) showed a quasi-sinusoidal modulation of flux with the same period as the planet. The amplitude of the signal was, however, too large to be reflected light or thermal emission alone and its origin remained unclear in that study. Additional MOST observations spanning several weeks between 2011 and 2015 by Sulis et al. (2019) confirmed this optical modulation. The amplitude and phase of the signal were variable which the authors suggested might be due to some star-planet interaction or the presence of a transiting circumstellar dust torus. They also did not detect the secondary eclipse of the planet which led to an upper value for the geometric albedo of 0.47 (2σ). Furthermore, recently Morris et al. (2021) presented *CHEOPS* observations of the planet showing a large phase variation but they do not detect a significant secondary eclipse of the planet. The authors suggest that the origin of the signal might be from circumstellar or circumplanetary material modulating the flux of the system. This is just another example of the challenges to determine the nature of 55 Cnc e.

Another surprising discovery came with Kepler-10 b (Batalha et al. 2011), the first rocky planet detected by the *Kepler* mission. The planet showed a deep secondary eclipse that suggested an unusually high reflectivity in the *Kepler* bandpass (Batalha et al. 2011; Rouan et al. 2011; Sheets & Deming 2014). A high albedo for planets that are highly irradiated by their stars could be explained by the creation of calcium- and aluminum-rich surfaces on their dayside (Léger et al. 2011; Rouan et al. 2011; Kite et al. 2016; Modirrousta-Galian et al. 2021). A subset of planets detected by *Kepler* showed comparably high albedos in the optical wavelengths (Demory 2014). Most notably, both Kepler-10 b and Kepler-78 b (Sanchis-Ojeda et al. 2013) have albedos of 0.4-0.6 (Sheets & Deming 2014). Hu et al. (2015) re-analyzed the *Kepler* data of Kepler-10 b and did not detect any phase curve offset. They found that any model with a Bond albedo greater than 0.8 fits the visible phase curve well regardless of whether asymmetric reflection exists.

Due to the high irradiation small USP planets receive from their host stars, they are more susceptible to atmospheric loss (Lopez 2017). LHS 3844 b (Vanderspek et al. 2019), an USP planet orbiting an M-type star, was clearly shown to lack a thick atmosphere using observations by the *Spitzer Space Telescope* and is therefore likely a bare rock (Kreidberg et al. 2019a). The 100 hour continuous phase curve of the planet showed no hotspot offset ruling out the possibility of a thick atmosphere, and any less-massive atmospheres would be unstable to erosion by stellar wind. Some planets might however retain an atmosphere by the evaporation of surface lava oceans leading to a silicate rich atmosphere (Schaefer & Fegley 2010; Miguel et al. 2011) or might have other thick, high mean-molecular-weight atmospheres (Demory et al. 2016a).

Here we present *Spitzer* observations of the USP K2-141 b (EPIC 246393474 b). The planet was discovered in 2018 by Malavolta et al. (2018) and independently by Barragán et al. (2018) using observations of the *Kepler* telescope during its “second light” mission, *K2* (Howell et al. 2014). The planet has a radius of $R_p = 1.51 \pm 0.05 R_\oplus$ and orbits its K-dwarf host star every 0.28 days (6.7 hours). Observations of the star by the high-precision spectrograph HARPS-N measured a mass for the planet ($M_p = 5.08 \pm 0.41 M_\oplus$). With a density of $\rho = (8.2 \pm 1.1) \text{ g/cm}^3$, K2-141 b is mostly consistent with an Earth-like iron-silicate composition. The radial velocity observations furthermore confirmed another companion K2-141 c, which is in radius and upper mass more likely to be a Neptune-like planet than a rocky planet or a HJ, orbiting further out with an orbital period of 7.7 days.

The *Kepler* observations also revealed the optical phase curve and secondary eclipse with a depth of $23 \pm 4 \text{ ppm}$. The equilibrium temperatures of K2-141 b, Kepler-10 b and 55 Cnc e are 2150K, 2170K and 1950K in case of full atmospheric heat redistribution and 2745K, 2775K and 2490K for instant reradiation, respectively¹. K2-141 b is therefore a perfect target to compare to other well studied USPs (see also Table 2.1). Its host star is also bright enough ($V = 11.5 \text{ mag}$, $K = 8.4 \text{ mag}$) to conduct follow-up observations of the planet’s emission in the infrared as previously done with 55 Cnc e ($V = 6.0 \text{ mag}$, $K = 4.0 \text{ mag}$) (Demory et al. 2016a,b). K2-141 b and 55 Cnc e are therefore the only two currently known small USPs which are accessible in both the optical and infrared which invites comparison between the two planets. We note, however, the difference in densities for the planets: While K2-141 b’s density is consistent with an Earth-like composition (30% Fe), 55 Cnc e is inconsistent with an Earth-like composition at over 4σ .²

Recently, Nguyen et al. (2020) modeled the atmosphere of K2-141 b assuming the planet has a thin rock vapor atmosphere which arises from the evaporation of the surface on the dayside. This leads to a flow that is maintained by the pressure gradient between the nightside and dayside on the planet. This flow is however not able to transport enough heat to the nightside to create a considerable thermal hotspot offset nor to heat the nightside. Previous studies of transit spectroscopy of lava planets focused on more volatile species such as Na or K (Castan & Menou 2011; Kite et al. 2016). Nguyen et al. (2020) compared different atmospheric compositions expected for a rock vapor atmosphere (Na, SiO and SiO₂) and found that an SiO₂ atmosphere may be easier to observe due to the extreme geometry of this system. Nguyen et al. (2020) also noted that due to the proximity of K2-141 b to its host star ($a/R_* = 2.292$), the night side (the area of the planet which never receives any incident flux) is only about a third of the planet, rather than a hemisphere. The terminator for K2-141 b is located approximately 115° from the substellar point, leading to a hemisphere-integrated night side temperature of approximately 400K for the planet³. Therefore, the regions probed during a transit range from $\sim 65^\circ$ to $\sim 115^\circ$ from the substellar point. If the planet is further away

¹Calculated using $T_{\text{eq}} = T_*/\sqrt{a/R_*} (1 - A_B)^{1/4} f^{1/4}$ while assuming Bond albedo $A_B = 0$. The heat redistribution factor, f , is $f = 1/4$ in case of uniform redistribution (if the planet has a thick atmosphere able to redistribute heat) and $f = 2/3$ for instant reradiation (if the planet is a bare rock) (Koll et al. 2019a).

²Calculations based on the Mass-Radius tables from Zeng et al. (2019).

³Calculations based on Kopal (1954) and Nguyen et al. (2020)

Table 2.1: Selection of USPs and their properties.

Planet	P (days)	R_p (R_\oplus)	M_p (M_\oplus)	ρ_p (g/cm^3)	a/R_*
⁽¹⁾ K2-141 b	0.28	1.51(5)	5.1(4)	8.2(1.1)	2.29
⁽²⁾ 55 Cnc e	0.74	1.95(4)	8.6(4)	6.4(0.3)	3.52
⁽³⁾ Kepler-10 b	0.84	1.47(3)	3.3(5)	5.5(0.9)	3.46
⁽⁴⁾ LHS 3844 b	0.46	1.30(2)	—	—	7.11

Planet	$T_{\text{eq}}^{f=1/4}$ (K)	$T_{\text{eq}}^{f=2/3}$ (K)	T_* (K)	K (mag)	V (mag)
⁽¹⁾ K2-141 b	2150	2745	4599	8.4	11.5
⁽²⁾ 55 Cnc e	1950	2490	5172	4.0	6.0
⁽³⁾ Kepler-10 b	2170	2775	5708	9.5	11.0
⁽⁴⁾ LHS 3844 b	805	1030	3036	9.1	15.2

References. ⁽¹⁾ Malavolta et al. (2018); ⁽²⁾ Bourrier et al. (2018), Crida et al. (2018a); ⁽³⁾ Dumusque et al. (2014); ⁽⁴⁾ Vanderspek et al. (2019)

from the star the region probed during a transit is approximately 90° from the substellar point. This effect is so small, however, that the flux emitted from the night side would not be detectable within the measurement precision of our data. We therefore adopt a night hemisphere in this paper.

The paper is structured as follows: Section 2.2 describes the data reduction of the *K2* and *Spitzer* observations used in this paper. Section 2.3 discusses the different models which were fit to the *K2* and *Spitzer* data to extract information on the reflective and thermal emission coming from the planet. Section 2.4 compares the observations to two different atmospheric models: a pseudo-2D rock vapor model and a 1D turbulent boundary layer model, the latter being recently published in Nguyen et al. (2020) and further improved in Nguyen et al. (2022). In Section 2.5 we discuss our findings and summarize our conclusions in Section 2.6.

2.2 Observations and data reduction

2.2.1 *Spitzer* photometry

We observed the K2-141 system with the *Spitzer* InfraRed Array Camera (IRAC; Fazio et al. 2004) for about 65 hours between October 09 and October 11, 2018 (Program 14135, Kreidberg et al. 2018c). We used Channel 2 on IRAC (equivalent to a photometric bandpass of $4 - 5 \mu\text{m}$) with a two-second exposure time. The observations began with a 30-minute burn-in to allow for the telescope to thermally settle. Following this procedure, we placed the target on the “sweet spot”, a pixel

Table 2.2: Observations with *Kepler* and *Spitzer* used in this work.

Observation	AORKEY	Start Date	End Date	Exp. time (s)
K2 C12	—	2016-12-21 22:41:48	2017-03-04 12:56:44	1800
K2 C19	—	2018-09-08 02:48:49	2018-09-15 03:00:18	60
<i>Spitzer</i> AOR1	66695168	2018-10-09 01:52:12	2018-10-09 13:41:46	2
<i>Spitzer</i> AOR2	66694912	2018-10-09 13:47:34	2018-10-10 01:37:08	2
<i>Spitzer</i> AOR3	66694656	2018-10-10 01:42:56	2018-10-10 13:32:30	2
<i>Spitzer</i> AOR4	66694400	2018-10-10 13:38:18	2018-10-11 01:27:52	2
<i>Spitzer</i> AOR5	66694144	2018-10-11 01:33:40	2018-10-11 13:23:14	2
<i>Spitzer</i> AOR6	66693632	2018-10-11 13:29:02	2018-10-11 18:28:51	2

on the detector which is known to have a minimal intra-pixel sensitivity variation.

We split the observations into six sequential datasets (AORs, Astronomical Observation Requests) which we downloaded from the *Spitzer* Heritage Archive⁴ (see Table 2.2 for the start and end time of each individual AOR). We reduced the Basic Calibrated Data (BCD, provided by the *Spitzer* Science Center) with the Photometry for Orbits, Eclipses, and Transits (POET) pipeline (which is available open-source on GitHub⁵) developed by Stevenson et al. (2012) and Cubillos et al. (2013). It performs centroiding on each frame by fitting a 2D Gaussian profile to the stellar image (Lust et al. 2014) in each *Spitzer* exposure after upsampling by a factor of five in each spatial direction (Harrington et al. 2007). The target remains centered near the sweet spot for the entire AOR in each observation, with the majority of the exposures being well within of 0.1 pixels from the sweet spot (see plots in Section 2.C.2). POET then identifies and flags bad pixels using an iterative sigma-clipping procedure along the time axis and then sums the flux in each fixed aperture. We have chosen a grid of apertures with radii ranging from two to four pixels in 0.25 pixel steps for every AOR and used the aperture which minimizes the residual noise in each of the extracted light curves (a list of the apertures can be found in Table 2.3). For the median background flux estimation, we used an annulus with an inner radius of 7 pixels and outer radius of 15 pixels.

The dominant systematics for the 4.5 μm *Spitzer* channel are intrapixel sensitivity variations (Charbonneau et al. 2005; May & Stevenson 2020). We therefore fit for them by using the BiLinearlyInterpolated Subpixel Sensitivity (BLISS) map technique introduced by Stevenson et al. (2012) (see plots in Section 2.C.3 to see the determined intrapixel sensitivity variations across the detector). We determined the pixel bin size used for the map for every AOR and listed it in Table 2.3.

We visually inspected the data and removed three short segments of data (two in AOR3 and one in AOR5) making up approximately 5% of the observations that showed strong correlated noise in the residuals. After visually inspecting the individual frames during the discarded segment in AOR5 it was able to attribute

⁴<https://sha.ipac.caltech.edu/applications/Spitzer/SHA/>

⁵<https://github.com/kevin218/POET>

Table 2.3: Parameters used for the data reduction of every *Spitzer* AOR determined by minimizing the Bayesian Information Criterion (BIC).

AOR	aper. size	bin size	ramp model	PRF-FWHM
1	3.00	0.013	constant	Y_1
2	3.00	0.013	linear	X_3
3	3.00	0.015	constant	X_1
4	3.00	0.013	constant	X_3
5	3.25	0.011	constant	X_1, Y_3
6	3.00	0.012	constant	X_3, Y_3

Notes. aper. size: aperture size given in pixels; bin size: the optimal resolution for BLISS mapping; ramp model: the optimal ramp model $R(t)$ for the AOR (see Equation 2.1); PRF-FWHM: the complexity of the PRF fit $G(X, Y, t)$. The latter is described by the dimension (X or Y) and the degree of the fit (1 for linear, 2 for quadratic and 3 for cubic).

this event to a strong cosmic ray hit on the detector (see Fig. 2.16). The other segment in AOR3 showed no noticeable trends in PRF width or other parameters (see Fig. 2.15). Similar outliers were also observed in previous observations using *Spitzer*’s IRAC Channel 2 (e.g., Kreidberg et al. 2019a; Challener et al. 2021). For the majority of the observations, the target fell well within 0.5 pixels around the sweet spot. We removed an additional 0.3% of exposures in the third AOR because these exposures had a centroid position shifted by a whole pixel in the x-dimension.

2.2.2 K2 photometry

Campaign 12

K2’s campaign 12 (C12) was carried out by the *Kepler Space Telescope* from December 15, 2016, to March 04, 2017. The photometric data were taken in the long cadence sampling rate (~ 30 minutes) over a timespan of about 79 days. The data extraction and reduction is described in Malavolta et al. (2018) and was reused for this analysis.

Campaign 19

K2’s campaign 19 (C19) was carried out from August 30, 2018 to September 26, 2018 and marked the last observations taken by the *Kepler Space Telescope* before running out of fuel. C19’s field-of-view overlapped with C12 leading to a reobservation of K2-141⁶. The fuel shortage on the spacecraft, however, led to

⁶The star was proposed to be observed in short cadence mode in *K2* Campaign 19 from the following *K2* General Observer programs: GO19027, A. Vanderburg; GO19065, C. Dressing

a shorter campaign. These last data taken by *Kepler* span only about a month and suffer from erratic pointing at the beginning and end of the campaign. We removed approximately 54% of the data leaving us with approximately 7 days of observations with a photometric precision comparable to other *K2* Campaigns. Approximately 8.5 days at the beginning of the observations were removed because the boresight of the telescope was off-nominal leading to K2-141 being completely out of the pixel stamp. We also removed the final 11 days of the observations where the boresight and roll of *Kepler* fluctuated erratically⁷. In contrast to C12, the observations of K2-141 in C19 were taken in the short cadence mode with a sampling rate of about one minute. Due to this higher temporal resolution, there is no need to oversample the C19 data.

The photometry was accessed with the python package `lightkurve` (Lightkurve Collaboration et al. 2018), which retrieves the data from the MAST archive⁸. We downloaded the Simple Aperture Photometry (SAP) data and removed every measurement with a nonzero “quality” flag, which indicates events like thruster firings or cosmic ray hits.

We used the self-flat-fielding (SFF) procedure described in Vanderburg & Johnson (2014) and Vanderburg et al. (2016), which is implemented in `lightkurve`, to correct for the systematic flux variations of the *K2* data caused by thruster firings every six hours. In addition to the six hour back and forth movement throughout the *K2* mission, there was also transverse spacecraft drift on timescales longer than 10 days (Vanderburg et al. 2016). We therefore subdivided the 8 days of data into two “windows” and performed the SFF independently in each of them. To remove outliers, we fit a cubic spline to the data and performed an iterative sigma clipping with respect to the median to mask outliers at 5σ below and 3σ above the light curve, which removed 0.3% of the remaining C19 data. We then normalized the data by dividing by the median of the flux.

To remove the stellar variability ($P_{rot} \sim 14$ days, Malavolta et al. 2018), we fit a linear function of time to the out-of-transit data for each orbit (eclipse to eclipse) while masking the transits following Sanchis-Ojeda et al. (2013). For each orbit, the linear function was then subtracted from the data and unity was added. The observations contain 25 full phases (eclipse to eclipse) of the planet around the star. The C19 observations also contain one transit of K2-141 c which we removed from our analysis, but use in Appendix 2.A to improve the ephemeris of K2-141 c.

2.3 Light curve fits

We considered fits to the *Spitzer* data alone (see Section 2.3.1), and to the joint *Spitzer* and *Kepler* dataset (see Section 2.3.3). For every model described in the following section we performed a differential evolution Markov chain Monte Carlo (MCMC) (Ter Braak 2006) analysis to estimate parameter uncertainties. We rescaled the uncertainties for every data point by a constant factor so that

⁷see the Data Release Notes for *K2* Campaign 19 for further information: https://archive.stsci.edu/missions/k2/doc/drn/KSCI-19145-002_K2-DRN29_C19.pdf

⁸https://archive.stsci.edu/k2/data_search/search.php

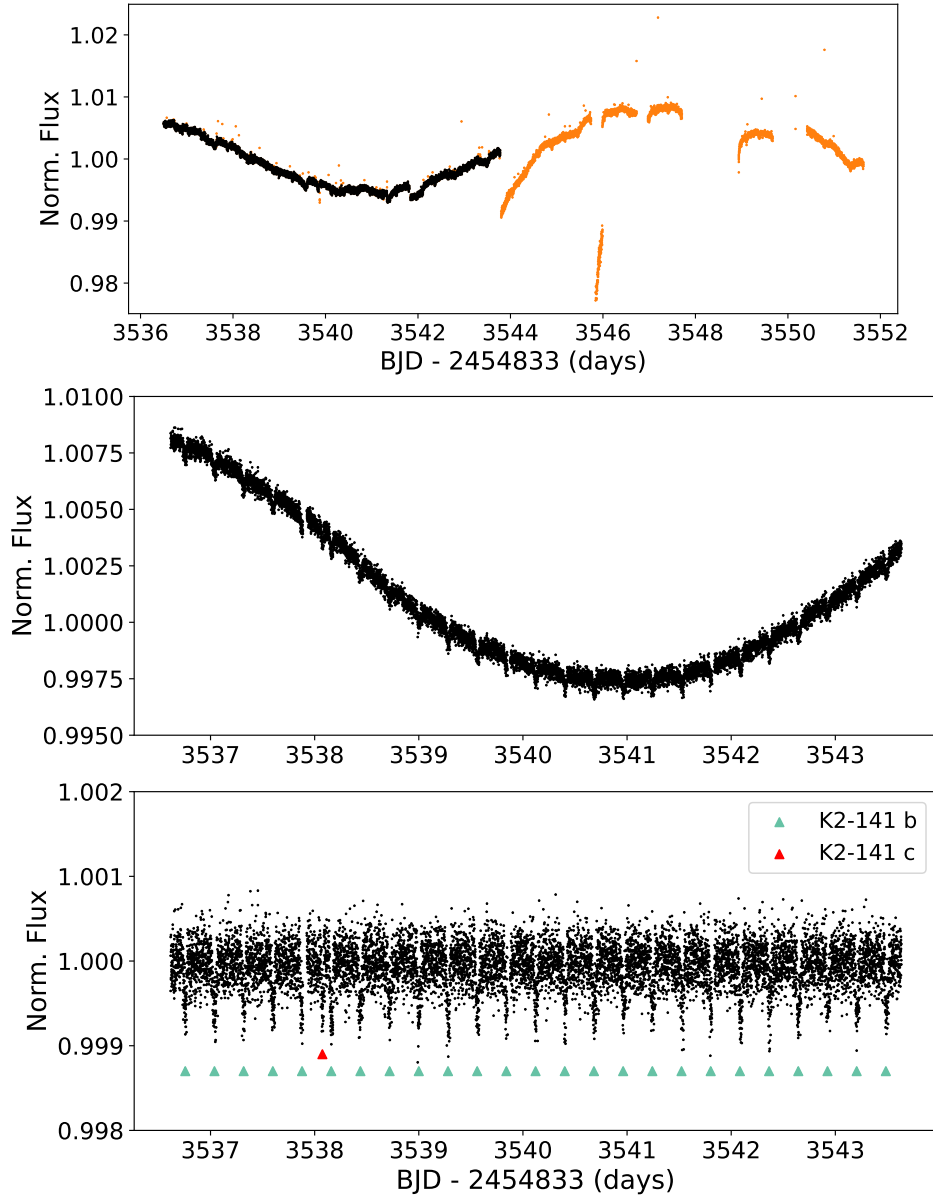


Figure 2.1: *K2* Campaign 19 data of K2-141. *Upper panel:* The full *K2* Campaign 19 observations. We removed outliers and data suffering from decreased photometric precision due to *Kepler* running out of fuel (marked in orange). *Middle panel:* *K2* C19 data with instrumental systematics removed using the SFF algorithm. *Lower panel:* The *K2* C19 observations after removal of the stellar variability. The 25 transits by K2-141 b have been marked in green. An additional transit by K2-141 c is denoted in red.

the reduced chi-squared is unity and we get realistic uncertainties for the fit parameters. The chi-squared values before rescaling based on the final best fitting model in our analysis can be found in Table 2.9. We ran the MCMC until all free parameters of four initialized chains converged to within 1% of unity according to the Gelman-Rubin statistic (Gelman & Rubin 1992). Each chain consisted out of 10000 steps and we discarded the first 50% of the MCMCs as burn-in. This leaves us with a total of 20000 steps for each run. We include plots of the resulting posterior distributions in the Appendix (2.C.5 to 2.C.10).

The transit model implemented in **batman** (Kreidberg 2015) which was used in every fit, consists of the time of central transit t_0 , the radius of planet in units of stellar radii R_p/R_* , the orbital period P , semi-major axis in units of stellar radii a/R_* and the cosine of the inclination $\cos i$. We fixed the eccentricity ecc and the argument of periastron ω to zero. This is justified due to the very short circularization time scale of these USPs. Following equation 3 from Adams & Laughlin (2006), the circularization time scale for K2-141 b is only about $\tau_{circ} = 3.1$ Myrs assuming a tidal quality factor of $Q_P = 10^6$. We used the **ExoCTK** limb darkening calculator (Batalha et al. 2017) and the stellar parameters given in Malavolta et al. (2018) to determine and fix the linear and quadratic limb-darkening coefficients u_1 and u_2 . They are $u_1 = 0.105$ and $u_2 = 0.119$ in the *Spitzer* IRAC Channel 2 bandpass and $u_1 = 0.666$ and $u_2 = 0.062$ in the *Kepler* bandpass.

2.3.1 *Spitzer* only fit

We model the full *Spitzer* light curve, $F(x, y, X, Y, t)$, as:

$$F(x, y, X, Y, t) = F_s R(t) M(x, y) T(t) E(t) P(t) G(X, Y), \quad (2.1)$$

where F_s is the constant out-of-transit flux (i.e., the stellar flux), $R(t)$ is the ramp model, $M(x, y)$ is the BLISS map with (x, y) describing the position of the star on the detector, $T(t)$ is the Mandel & Agol (2002) transit model implemented in **batman** (Kreidberg 2015), $E(t)$ is the eclipse model implemented in **batman** and $P(t)$ the phase variation in **SPIDERMAN** (Louden & Kreidberg 2018) or **POET** Cubillos et al. (2013) (depending on which specific model was used). $G(X, Y)$ is a term fitting for variations in the pixel response function (PRF) using a 2D cubic (i.e., PRF-FWHM detrending, see e.g., Lanotte et al. 2014; Mendonça et al. 2018; May & Stevenson 2020) and has the following form:

$$G(X, Y) = X_1 s_x + X_2 s_x^2 + X_3 s_x^3 + Y_1 s_y + Y_2 s_y^2 + Y_3 s_y^3 + 1, \quad (2.2)$$

where X_1 (Y_1), X_2 (Y_2), and X_3 (Y_3) are the linear, quadratic and cubic coefficients in the X (Y) dimension, respectively, and s_x and s_y the Gaussian widths of the pixel response function in the X (Y) dimension, respectively. The optimal resolution for BLISS mapping, the ramp model $R(t)$ (either a constant or linear ramp) and the order of the PRF fit $G(X, Y)$ were independently determined by minimizing the Bayesian Information Criterion (BIC) for every AOR and are listed in Table 2.3.

Equation 2.1 describes the general model which was fit to the *Spitzer* data. For this model, the orbital period P was fixed to the literature value reported in

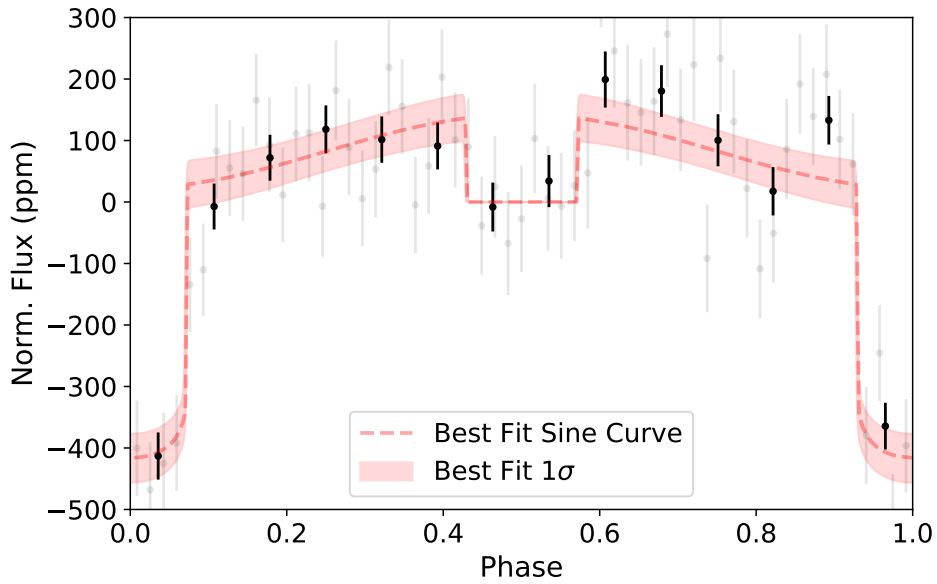


Figure 2.2: Phase curve of K2-141 b after phase folding the complete *Spitzer* observations. The eclipse is at phase = 0.5. The best fitting model shown in red describes the observed thermal emission from the planet as a sinusoidal function. Each bin in black (gray) consists out of 7200 (1800) *Spitzer* 2-second exposures. The pairs plot for this model can be found in the Appendix, Section 2.C.5.

Malavolta et al. (2018). For parameters which are more precisely determined by the *K2* data, namely t_0 , R_p/R_* , a/R_* and $\cos i$, we used Gaussian priors in our analysis based on the literature values.

We fit three different phase variation models $P(t)$ to the *Spitzer* data. First, a sinusoid with amplitude A multiplied by an eclipse model with eclipse depth f_p/f_* and including a phase offset ϕ of the hotspot. Second, same as above but without a phase offset. Third, a two temperature model for the planet with a constant temperature on the dayside, $T_{p,d}$, and on the nightside, $T_{p,n}$. A list of the free parameters for every model is listed in the Appendix (see Table 2.10).

A commonly approach for model selection in the exoplanet literature is using the Bayesian Information Criterion (BIC, Schwarz 1978; Kass & Raftery 1995; Liddle 2007). It approximates the evidence E and has the following form:

$$\begin{aligned} \ln E &\approx -\frac{1}{2}\text{BIC} = \ln \mathcal{L}_{max} - \frac{1}{2}k \ln N \\ \implies \text{BIC} &= -2 \ln \mathcal{L}_{max} + k \ln N, \end{aligned} \quad (2.3)$$

where \mathcal{L}_{max} is the maximum likelihood of the model, k the number of free parameters of the model and N the number of data points. The BIC therefore penalizes models with more free parameters and the best-fitting model is the one with the lowest BIC (i.e., the largest evidence). We compare models by calculating ΔBIC :

$$\Delta\text{BIC}_i = \text{BIC}_i - \text{BIC}_{\min}, \quad (2.4)$$

with BIC_{\min} being the smallest BIC of the set of models being compared. By taking the difference of BIC_i and BIC_{\min} , several constants cancel out and we are left with: $\text{BIC} = \chi^2 + k \ln N$, which now includes the χ^2 value of the model. When comparing two models, Kass & Raftery (1995) lists a $\Delta\text{BIC} > 3.2$, $\Delta\text{BIC} > 10$, $\Delta\text{BIC} > 100$ as being a substantial, strong, decisive evidence for the model with the lower BIC, respectively.

The symmetric sinusoidal model with no hotspot offset is statistically substantially preferred with $\Delta\text{BIC} > 8.8$ (see Table 2.3.3) compared to a sinusoid with an offset. We therefore find the data are consistent with the peak brightness occurring at the substellar point, in contrast to the prominent USP planet 55 Cnc e which has an eastward offset of $41^\circ \pm 12^\circ$ (Demory et al. 2016a). When we include an offset as a free parameter, we obtain $\phi = -34.5^{15.3}_{-14.6}$ (the negative sign denotes an offset westward from the substellar point). We measure an eclipse depth in the *Spitzer* bandpass $f_p/f_* = 142.9^{38.5}_{-39.0}$ ppm and an amplitude variation $A = 120.6^{42.3}_{-43.0}$ ppm. We note that the reflected light contribution at $4.5 \mu\text{m}$ has not been subtracted from the brightness temperature computation. Table 2.3.3 lists all best fit parameters and their uncertainties. A comparison of the BIC between the models showed that the sinusoidal model with no hotspot offset fits best to the *Spitzer* data. We show the best fitting model with the *Spitzer* observations in Fig. 2.2.

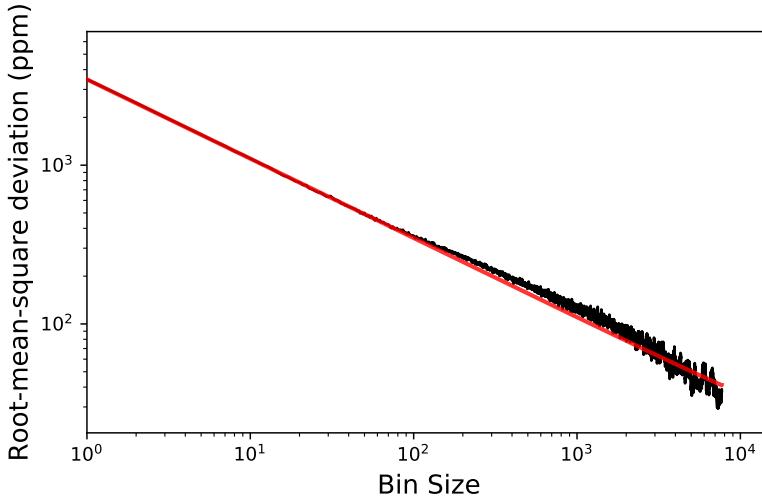


Figure 2.3: Allan deviation plot of the *Spitzer* data: root-mean-square (rms) of the fit residuals of the *Spitzer* data using the sinusoidal model without a hotspot offset (black curve) as a function of the number of data points per bin. A bin size of one depicts no binning at all. The red line shows the expected rms for Gaussian noise following the inverse square root law.

2.3.2 Goodness of *Spitzer* only fit

We tested for the presence of red noise by comparing the root-mean-square (rms) of the binned residuals of the light curve with the predictions from white noise. If the data are uncorrelated (white) in time, the rms of the residuals is expected to decrease with \sqrt{N} , where N is the number of data in a bin. A bin size of one, therefore, denotes no binning at all. We combined all six datasets and subtracted the best fitting model. Figure 2.3 shows that the residuals of the *Spitzer* data agree well with the expectations from uncorrelated noise. The same figures for each individual *Spitzer* AOR can be found in Appendix 2.C.4.

2.3.3 Joint *Spitzer* and *Kepler* fit

The phase variation $P(t)$ for the joint fit consists of a thermal $P_{\text{therm}}(t)$ and a reflective $P_{\text{refl}}(t)$ contribution, with $P(t) = P_{\text{therm}}(t) + P_{\text{refl}}(t)$. For the reflected light component $P_{\text{refl}}(t)$, we assumed a uniform Lambertian reflector (Seager 2010):

$$P_{\text{refl}}(t) = A_g \frac{\sin z(t) + (\pi - z(t)) \cos z(t)}{\pi}, \quad (2.5)$$

where A_g is the geometric albedo and the orbital phase $z(t)$ is described by:

$$z(t) = \arccos \left(-\sin i \cos \left(2\pi \frac{t - t_0}{P} \right) \right). \quad (2.6)$$

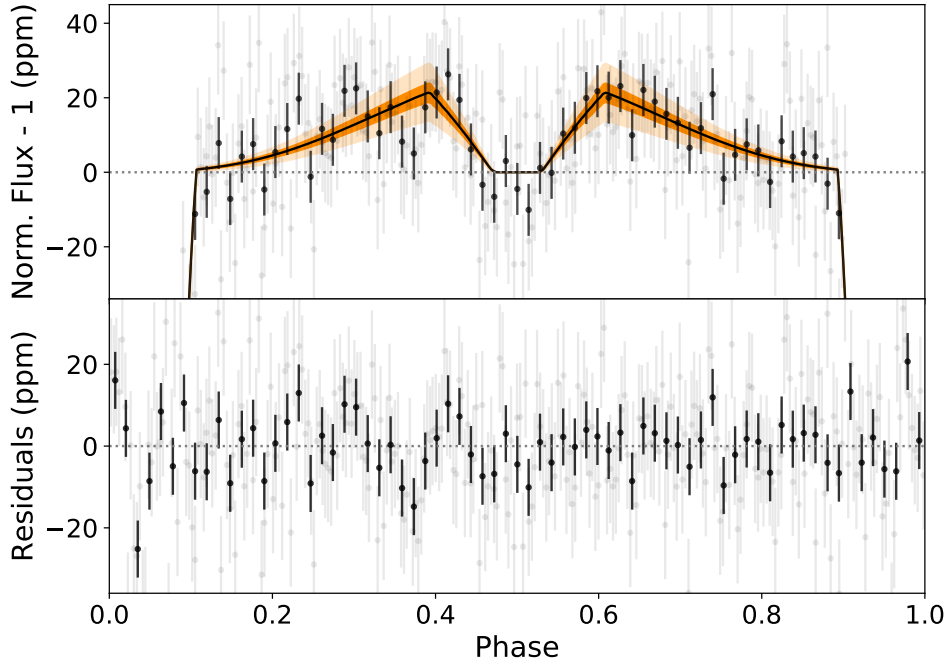


Figure 2.4: Phase curve of K2-141 b as seen by *Kepler* during Campaign 12 and 19. *Upper panel:* The solid black line shows the phase curve based on the values in our best fit model (toy model without heat redistribution for the thermal emission and a uniform Lambertian reflector for the reflected light contribution). The dark orange and light orange areas around the best fitting model are the 1σ and 3σ uncertainties, respectively. We binned the Campaign 19 data that was collected in short cadence mode (~ 1 minute) into bins of 29.4 minutes to have the same temporal resolution as the Campaign 12 data. We then phase folded the *Kepler* observations and binned the data for clarity. Each bin in black (gray) consists out of 180 (45) *Kepler* exposures. *Lower panel:* The residuals of the *Kepler* observations to the best fitting model.

Table 2.4: All models fit to the *Spitzer* data alone.

Parameter	Units	Prior	Model Name		
			Sinusoidal ($\phi = 0$)	Sinusoidal (ϕ free)	Two Temp.
t_0	BJD _{TDB} - 2457744.0 d	$\mathcal{N}(0.07160, 0.00022)$	$0.07191^{0.00019}_{-0.00019}$	$0.07189^{0.00020}_{-0.00021}$	$0.07191^{0.00019}_{-0.00020}$
R_p/R_*	—	$\mathcal{N}(0.02037, 0.00046)$	$0.02038^{0.00041}_{-0.00042}$	$0.02041^{0.00041}_{-0.00041}$	$0.02035^{0.00039}_{-0.00040}$
a/R_*	—	$\mathcal{N}(2.292, 0.056)$	$2.278^{0.040}_{-0.038}$	$2.277^{0.041}_{-0.040}$	$2.278^{0.039}_{-0.040}$
$\cos i$	—	$\mathcal{N}(0.064532, 0.064)$	$0.068^{0.042}_{-0.039}$	$0.066^{0.045}_{-0.038}$	$0.070^{0.044}_{-0.040}$
A	ppm	$\mathcal{U}(0, 400)$	$120.6^{42.3}_{-43.0}$	$142.2^{42.7}_{-43.1}$	—
f_p/f_*	ppm	$\mathcal{U}(0, 400)$	$142.9^{38.5}_{-39.0}$	$144.7^{39.4}_{-39.0}$	—
ϕ	degrees	$\mathcal{U}(-180^\circ, 180^\circ)$	—	$-34.5^{15.3}_{-14.6}$	—
T_*	K	$\mathcal{N}(4599, 79)$	—	—	4602^{76}_{-78}
$T_{p,n}$	K	$\mathcal{U}(0, 4599)$	—	—	909^{497}_{-560}
$T_{p,d}$	K	$\mathcal{U}(0, 4599)$	—	—	2233^{330}_{-335}
ΔBIC			0	8.8	9.6

Notes. The Gaussian priors on $t_0, R_p/R_*, a/R_*, \cos i$ and T_* are based on the values reported in Malavolta et al. (2018). The orbital period P was fixed in these runs to $P = 0.2803244$ days (Malavolta et al. 2018). \mathcal{N} and \mathcal{U} denote a Gaussian and uniform prior, respectively.

We fit three thermal emission models to the combined *Spitzer* and *K2* dataset. First, a toy model described in Kreidberg & Loeb (2016) with the planet’s heat redistribution F as a free parameter. Second, same as above but with the redistribution fixed to zero leading to a nightside temperature of 0 K. Third, a two temperature model with a constant temperature on the dayside, $T_{p,d}$, and on the nightside, $T_{p,n}$. A list of the free parameters for every model is listed in the Appendix (see Table 2.11). The toy heat redistribution model described in Kreidberg & Loeb (2016) expresses the temperature of the planet $T(z)$ as a function of the zenith angle z using the following form:

$$\sigma T(z)^4 = \begin{cases} S(1 - A_B)F/2, & \text{nightside} \\ S(1 - A_B)(F/2 + (1 - 2F)\cos z), & \text{dayside} \end{cases} \quad (2.7)$$

where σ is the Stefan-Boltzmann constant, $S = \sigma \frac{T_{\text{eff}}^4}{(a/R_*)^2}$ the insolation, A_B the Bond albedo, z the zenith angle and $0 < F < 0.5$ the heat redistribution parameter. For $F = 0$ no heat is being distributed and the nightside has a temperature of 0K. If $F = 0.5$, half of the energy received by the dayside is being transported to the nightside and the whole planet is isothermal.

With the full *Spitzer* and *Kepler* dataset, we now also fit for the orbital period P . We use Gaussian priors for T_* and a/R_* based on values reported in Malavolta et al. (2018): The prior for the stellar temperature is $T_* = (4599 \pm 79)$ K and for semi-major axis in units of the stellar radius we use $a/R_* = 2.36 \pm 0.06$, which we derive from the stellar density $\rho_* = (2.244 \pm 0.161)\rho_\odot$ following $a/R_* \propto (\rho_* P^2)^{1/3}$.

The *K2* data in Campaign 12 was collected in the long cadence mode with a sampling rate of approximately 30 minutes. We oversample the data by a factor of 11 as in Malavolta et al. (2018) to account for the long exposure time. The data from Campaign 19 has a shorter sampling rate of about a minute and we therefore do not oversample this data set.

The insolation parameter S for the toy model was calculated at every step in a self-consistent way, assuming $S \propto T_{\text{eff}}^4/(a/R_*)^2$. We fit for the stellar temperature in the toy model, to take into account its uncertainty in the calculation of the insolation. In every step of the MCMC, we calculate a Kurucz model (Kurucz 1993) for the host star using the priors on the stellar temperature and stellar properties from Malavolta et al. (2018).

We tested using separate geometric albedos for the *Kepler* and the *Spitzer* dataset ($A_{g,K2}$ and $A_{g,Spitzer}$), but obtained a uniform posterior distribution for $A_{g,Spitzer}$, indicating that the *Spitzer* data are not able to constrain the albedo at $4.5 \mu\text{m}$ (where thermal emission dominates). We therefore used a wavelength-independent geometric albedo A_g in all subsequent fits.

The toy model includes the Bond albedo as a parameter to regulate the radiation balance of the planet. Since we assume Lambertian reflection in our analysis, the Bond albedo A_B and the geometric albedo A_g are related by: $A_B = 3/2 A_g$. While Lambertian reflectance is not an accurate model for the rocky bodies in the Solar System (Mayorga et al. 2016), this simplifying assumption is appropriate given the precision of our data and the unknown surface properties of K2-141 b.

Table 2.5: Derived parameters for K2-141 b from the best fitting model (Toy Model with $F=0$) presented in Table 2.3.4.

Parameter	Unit	Value
i	$^\circ$	85.2 ± 2.7
R_p	R_\oplus	1.53 ± 0.04
ρ_p	g/cm^3	7.82 ± 0.90
$f_p/f_{*,K2}$	ppm	$26.4^{3.5}_{-2.5}$
T_{14}	hours	$0.939^{0.005}_{-0.004}$
$(R_p/R_*)^2$	ppm	$424.8^{8.1}_{-5.2}$

Notes. The calculations use the measured stellar radius and planetary mass reported in Malavolta et al. (2018).

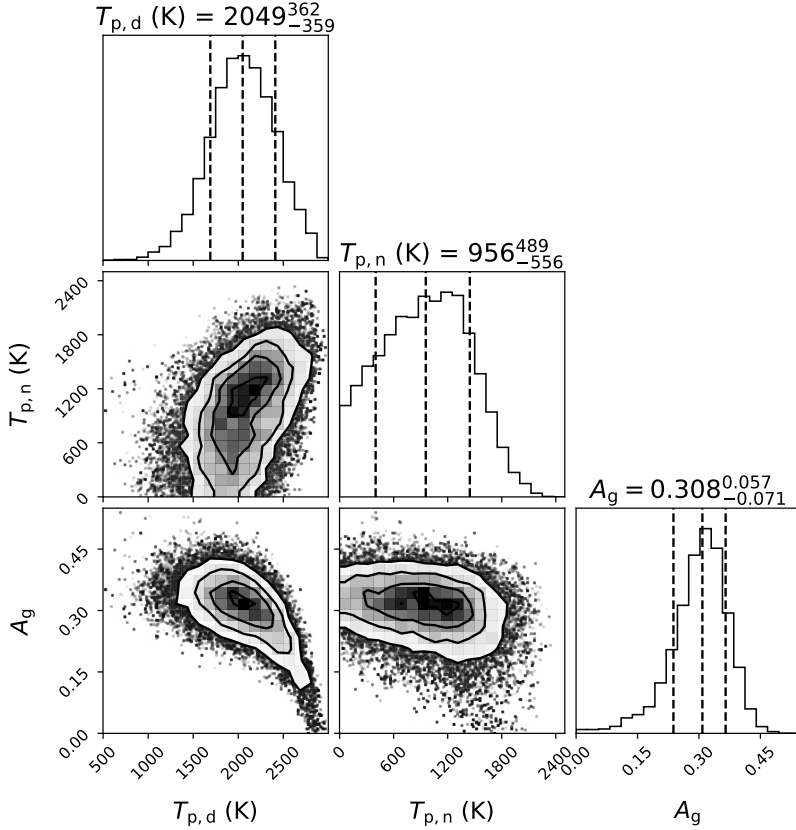


Figure 2.5: Corner plot of the best fitting model to the joint *K2* and *Spitzer* dataset for the dayside temperature $T_{p,d}$, the nightside temperature $T_{p,n}$ and the geometric albedo A_g .

Table 2.6: All models fit to the joint *Spitzer* and *K2* dataset.

Parameter	Unit	Prior	Model Name		
			⁽¹⁾ Toy Model ($F=0$)	Toy Model (F free)	Two Temp. Model
P	P - 0.2803 d	$\mathcal{U}(1.690\text{e}-5, 3.190\text{e}-5)$	$2.4956\text{e}-5^{+0.0067\text{e}-5}_{-0.0065\text{e}-5}$	$2.4957\text{e}-5^{+0.0068\text{e}-5}_{-0.0069\text{e}-5}$	$2.4955\text{e}-5^{+0.0068\text{e}-5}_{-0.0066\text{e}-5}$
t_0	BJD _{TDB} - 2457744.0 d	$\mathcal{U}(0.07094, 0.07226)$	$0.071508^{+0.000103}_{-0.000103}$	$0.071505^{+0.000106}_{-0.000103}$	$0.071505^{+0.000108}_{-0.000101}$
R_p/R_*	—	$\mathcal{U}(0.01807, 0.02267)$	$0.02061^{+0.00020}_{-0.00013}$	$0.02065^{+0.00020}_{-0.00015}$	$0.02064^{+0.00021}_{-0.00015}$
a/R_*	—	$\mathcal{N}(2.36, 0.06)$	$2.365^{+0.032}_{-0.052}$	$2.354^{+0.037}_{-0.050}$	$2.356^{+0.037}_{-0.055}$
$\cos i$	—	$\mathcal{U}(0, 0.36975)$	$0.083^{+0.048}_{-0.047}$	$0.095^{+0.044}_{-0.048}$	$0.093^{+0.047}_{-0.052}$
F	—	$\mathcal{U}(0, 0.5)$	0 (fixed)	$0.156^{+0.141}_{-0.098}$	—
T_*	K	$\mathcal{N}(4599, 79)$	4593^{+80}_{-81}	4603^{+80}_{-79}	4604^{+77}_{-81}
$T_{p,n}$	K	$\mathcal{U}(0, 4599)$	—	—	956^{+489}_{-556}
					(<1712K 2σ , <2085K 3σ)
$T_{p,d}$	K	$\mathcal{U}(0, 4599)$	—	—	2049^{+362}_{-359}
					(<2635 2σ , <2857K 3σ)
A_g	—	$\mathcal{U}(0, 1)$	$0.282^{+0.070}_{-0.078}$	$0.298^{+0.062}_{-0.068}$	$0.308^{+0.057}_{-0.071}$
ΔBIC			0	12.0	22.2

Notes. The uniform priors on $P, t_0, R_p/R_*, \cos i$ are based on the 5σ confidence interval of these parameters reported in Malavolta et al. (2018). The Gaussian prior for T_* and a/R_* are also from Malavolta et al. (2018). We derived the Gaussian prior for a/R_* from the stellar density $\rho_* = (2.244 \pm 0.161)\rho_o$ following $a/R_* \propto (\rho_* P^2)^{1/3}$. \mathcal{N} and \mathcal{U} denote a Gaussian and uniform prior, respectively.

⁽¹⁾ The Toy model without any redistribution ($F = 0$) provides the best fit to our data. We therefore recommend using the planetary parameters ($P, t_0, R_p/R_*, a/R_*, \cos i$) used in this column.

2.3.4 Goodness of joint *Spitzer* and *Kepler* fit

As in Section 2.3.2 we took the observations and subtracted the best fitting model to compare the rms of the fit residuals with the expected rms for Gaussian noise. The *Spitzer* data agrees again well with the expectations from uncorrelated noise and looks very similar to Figure 2.3. Figure 2.6 shows the Allan deviation plots for the two *K2* Campaigns.

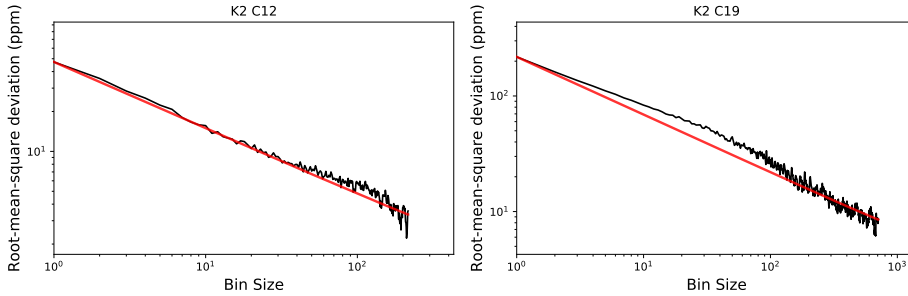


Figure 2.6: Allan deviation plot for *K2* C12 in the *left panel* and *K2* C19 in the *right panel*.

2.3.5 Improved ephemerides

Having a precise ephemeris is crucial to schedule follow-up observations of a planet. *K2*-141 b is an exciting target to be observed with observatories such as *JWST*. In fact, Cycle 1 of *JWST* includes two programs to observe the planet (Dang et al. 2021; Espinoza et al. 2021). We improved the orbital period P and the transit time t_0 significantly in our joint analysis using the three different datasets: the long cadence *K2* C12 observations used in the discovery papers (Malavolta et al. 2018; Barragán et al. 2018), new short cadence observations during Campaign 19 of *K2* and new *Spitzer* observations. The updated parameters for P and t_0 are listed in Table 2.7. They are based on our joint fit using the toy model (Kreidberg & Loeb 2016) with the heat redistribution F set to zero as the resulting fit agrees best with our data. With the additional data, the 3σ uncertainty on the predicted transit time in 2024 decreases from about an hour to just 2.7 minutes. We also used the one transit of *K2*-141 c observed in *K2* C19 (see Figure 2.1) to improve the ephemeris of the planet. Future observers can use the updated P and t_0 of *K2*-141 c to avoid scheduling conflicts with planet b. The analysis for *K2*-141 c can be found in Appendix 2.A.

2.3.6 Results

We performed three different fits for the *Spitzer* data and for the joint dataset. We measured the eclipse depth in the *Spitzer* bandpass $f_p/f_* = 142.9^{38.5}_{-39.0}$ ppm and an amplitude variation (peak to trough) $A = 120.6^{42.3}_{-43.0}$ ppm. The best fit is a two temperature model for the planet without a hotspot offset ϕ . When we,

Table 2.7: Updated ephemeris for K2-141 b and the 3σ uncertainty on the predicted transit time in 2022 and 2024.

K2-141 b	⁽¹⁾ Discovery	Updated
P (d)	0.2803244 ± 0.0000015	$0.280324956^{6.7e-08}_{-6.5e-08}$
⁽²⁾ t_0	7744.07160 ± 0.00022	$7744.071508^{0.000103}_{-0.000103}$
$3\sigma_{2022}$	42 minutes	1.9 minutes
$3\sigma_{2024}$	59 minutes	2.7 minutes

Notes. The same analysis for K2-141 c can be found in the Appendix (see Table 2.8).

⁽¹⁾ Based on Malavolta et al. (2018)

⁽²⁾ Expressed as $\text{BJD}_{\text{TDB}} - 2450000.0$ d

however, let ϕ vary, we find a value of $\phi = -34.5^{15.3}_{-14.6}$, which is at a 3.9σ level strongly inconsistent with the value obtained for 55 Cnc e of $41^\circ \pm 12^\circ$ (Demory et al. 2016a). For the joint analysis (*Spitzer* observations and the two *K2* Campaigns) we find that a toy heat redistribution model from Kreidberg & Loeb (2016) without heat redistribution is most preferred. We measure a geometric albedo of $A_g = 0.282^{0.070}_{-0.078}$, a dayside temperature of $T_{p,d} = 2049^{362}_{-359}\text{K}$ and a nightside temperature of $T_{p,n} = 956^{489}_{-556}\text{K}$ ($<1712\text{K}$ at 2σ). We found an eclipse depth in the *Kepler* bandpass of $f_p/f_* = 26.4^{3.5}_{-2.5}$ ppm which is consistent with the value reported in the discovery paper (23 ± 4 ppm, Malavolta et al. 2018). We therefore robustly detect emission coming from the dayside of K2-141 b in the optical light. As a comparison, 55 Cnc e’s secondary eclipse detection was only seen in the *TESS* observations at a significance of 3σ (Kipping & Jansen 2020). We show the best fitting model to the joint data set with the *Kepler* observations in Fig. 2.4.

2.4 Atmospheric constraints

In addition to the toy models presented in Section 3, here we compare the data to physically motivated models. K2-141 b is expected to have a molten surface with a thin rock vapor atmosphere. To model the atmosphere, we used two different approaches: (1) a pseudo 2-D model that includes radiative transfer for plausible chemical species, and (2) 1D turbulent boundary layer model that includes mass transfer between the planet’s surface and the atmosphere.

2.4.1 Pseudo-2D rock vapor model

We calculated pseudo-2D models for the atmosphere by dividing the planet into concentric rings in 10 degree radial increments starting at the substellar point and finishing at a zenith angle of 80° (for angles $> 80^\circ$ the outgassed atmosphere becomes too tenuous resulting in numerical instabilities).

This modeling approach is accurate in the limit that each column of atmosphere equilibrates locally with the magma ocean, without any influence of heat

or mass transport from neighboring columns. For each increment, we calculated the outgassed chemistry and temperature-pressure structure of a gas-melt equilibrium atmosphere. Our outgassed elemental budget and atmospheric pressure are determined by the results of the melt-gas equilibrium code **MAGMA** (Fegley & Cameron 1987; Schaefer & Fegley 2004). This is done for a volatile-free komatiite⁹ composition with no fractional vaporization (removal of vapor from the atmosphere) (Schaefer & Fegley 2004; Miguel et al. 2011). The outgassed chemistry and pressure are consistently adjusted for a surface temperature computed using radiative-transfer models, which are described below. We note that possible melt compositions for exoplanets are currently not known. Our choice of komatiite is based on early Earth (Miguel et al. 2011). Different melt compositions or evaporated atmospheres may result in chemistry and thermal structure changes (Zilinskas et al. 2022).

Equilibrium gas chemistry in the atmosphere is computed using a thermochemical equilibrium model **FastChem**¹⁰ (Stock et al. 2018). The chemistry considered includes over 30 different species for elements: O, Na, Si, Fe, Mg, K, Ti, Al, Ca and does not include ions. We do not consider the possible temporal evolution of chemistry through disequilibrium processes such as photochemistry or atmospheric mixing.

The temperature profile of the atmosphere is modeled in a radiative-convective equilibrium using a radiative transfer code **HELIOS**¹¹ (Malik et al. 2017; Malik et al. 2019b). As absorbers we include Na and SiO, for which we use a sampling wavelength resolution of $\lambda/\Delta\lambda = 1000$ and a range of 0.06 – 200 μm . Na opacity is computed using Vienna Atomic Line Database (VALD3) line list (Ryabchikova et al. 2015). We use the Voigt profile approximation for all, but the 0.6 μm doublet. The doublet is instead fit using unified line-shape theory of Rossi & Pascale (1985) and Allard et al. (2007a,b). The opacity of SiO is constructed using the EBJT (Barton et al. 2013) line list for ground state transitions and the Kurucz (Kurucz 1992) line list for shortwave bands. For simplicity we assume null surface albedo and blackbody stellar irradiation, which may slightly overestimate incident shortwave flux. As with chemistry, temperature profiles, including the surface temperature, are consistently adjusted depending on the outgassed material. The temperature-pressure profiles of K2-141 b at different zenith angles for this model are shown in Figure 2.8. All zenith angles show a thermal inversion due to short-wavelength Na absorption, with a sharp increase in temperature starting at a few millibar. The amount of heating is sensitive to the UV spectrum of the star, which is unknown; however, in general thermal inversions should be expected in rock vapor atmospheres (Zilinskas et al. 2021). Future UV characterization of K2-141 would refine the theoretical predictions of the temperature structure.

To simulate emission spectra for each radial segment we use the radiative-transfer code **petitRADTRANS**¹² (Mollière et al. 2019) with the same wavelength

⁹Komatiites are magnesium-rich, ultramafic lavas which formed on Earth during the Archaean (3.8 – 2.5 billion years ago) when the Earth had higher surface temperatures (McEwen et al. 1998; Schaefer & Fegley 2004).

¹⁰<https://github.com/exoclime/FastChem>

¹¹<https://github.com/exoclime/HELIOS>

¹²<https://gitlab.com/mauricemolli/petitRADTRANS>

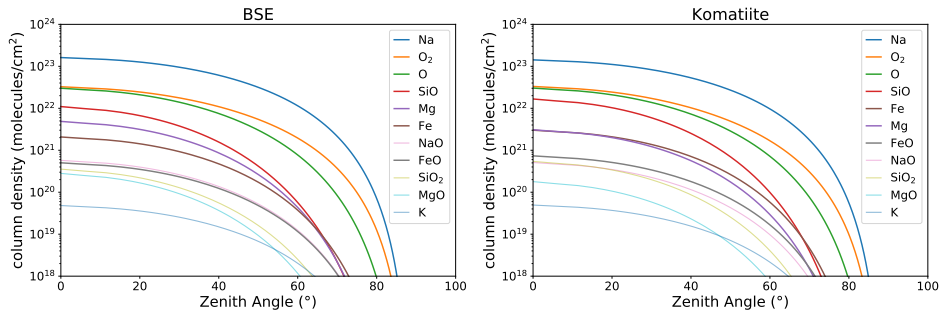


Figure 2.7: Column density of various species as a function of the zenith angle of the planet for a Bulk-Silicate-Earth composition (*left panel*) and a komatiite composition (*right panel*) based on calculations in Miguel et al. (2011). The temperature as a function of zenith angle assumed for this plot is based on our best fit model presented in Kreidberg & Loeb (2016) without heat redistribution ($F = 0$). It assumes that the temperature at the substellar point is $T_{\text{substellar}} = \left(\frac{S(1-A_B)}{\sigma}\right)^{1/4} = \frac{T_{\text{eff}}}{\sqrt{a/R_*}}(1 - A_B)^{1/4}$ and $T_{\text{terminator}} = 0$ K at a zenith angle of $z = 90^\circ$, with S being the insolation, A_B the Bond albedo and σ the Stefan–Boltzmann constant. The species in the legend are sorted by the column density at the substellar point in descending order.

resolution and opacities as for the T-P profile calculation. We sum the fluxes weighted by the area of each concentric ring to calculate the total flux from the planet. Finally, we divide the planet flux by a PHOENIX stellar spectrum (Husser et al. 2013) to determine the planet-to-star contrast.

Equilibrium gas chemistry in the atmosphere leads to a decreasing surface pressure with zenith angle. Figure 2.7 shows the column density as a function of zenith angle for different species expected at the temperatures of K2-141 b based on calculations in Miguel et al. (2011). We show the densities for a Bulk-Silicate-Earth composition and a komatiite composition which show similar results with Na being the most abundant in both of them.

2.4.2 1D turbulent boundary layer model

In addition to the pseudo-2D model described above, we also computed an atmospheric circulation model following Nguyen et al. (2020) and Castan & Menou (2011). The model calculates the steady-state flow induced by constant evaporation on the dayside and condensation on the nightside. Being tidally locked, we can impose symmetry across the substellar-antistellar axis by neglecting Coriolis forces. By assuming a turbulent boundary layer (TBL), we can marginalize over the vertical dimension and further reduce the problem to 1D: distance from the substellar point.

This model assumes a boundary layer that is: hydrostatically-bound and behaves like a continuous fluid (atmosphere does not escape K2-141 b and we can apply fluid dynamic equations), turbulent (for vertically-constant wind speeds), and optically thin (no radiative transfer necessary). With these assumptions, we

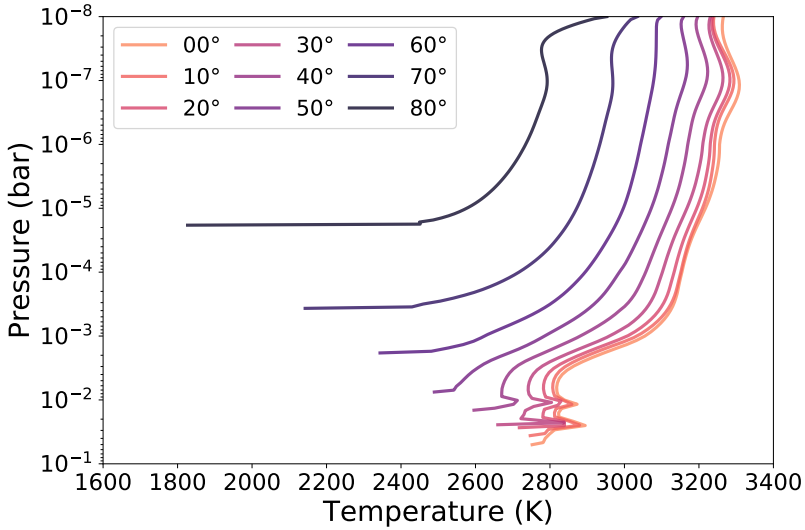


Figure 2.8: T-P profile of K2-141 b based on the pseudo-2D rock vapor model as described in Section 2.4.1 at different angles from the substellar point.

can construct a system of differential equations similar to the shallow-water equations which calculate the atmospheric pressure, wind velocity, and temperature at the boundary layer. We can only reduce the vertical dependence by assuming a vertical temperature profile.

The model itself describes the conservation of mass, momentum, and energy and their interactions: the atmospheric flow is being pushed by the pressure-gradient (momentum balance) driven by the uneven evaporation and condensation (mass balance), bringing with it sensible heating and cooling (energy balance) across the planet’s surface which in turns affect the evaporation/condensation. A solution is found when the pressure, temperature, and wind speed obey the conservation of mass, momentum, and energy and a steady-state flow exists.

Recent progress in these types of model have been made by including radiative transfer, in a three-band scheme (UV, optical and IR), for an SiO-dominated atmosphere (Nguyen et al. 2022). SiO absorbs strongly in the UV, which causes upper-level atmospheric heating, possibly leading to a temperature inversion (Ito et al. 2015). Therefore, the updated TBL model tests different vertical temperature profiles: adiabatic, isothermal, and inverted. Finally, coupling the radiative budgets of the atmosphere and surface, we can calculate emission spectra and phase variations for K2-141 b.

The different temperature profiles lead to significant changes to the dynamics. Making the lapse rate negative (temperature increases with height) increases the horizontal pressure gradient force which induces stronger winds. However, the energy budget is unchanged as incoming stellar flux does not depend on the temperature profile used. Therefore, the atmosphere reacts to the increased kinetic energy by lowering its thermal energy, leading to overall cooler temperatures.

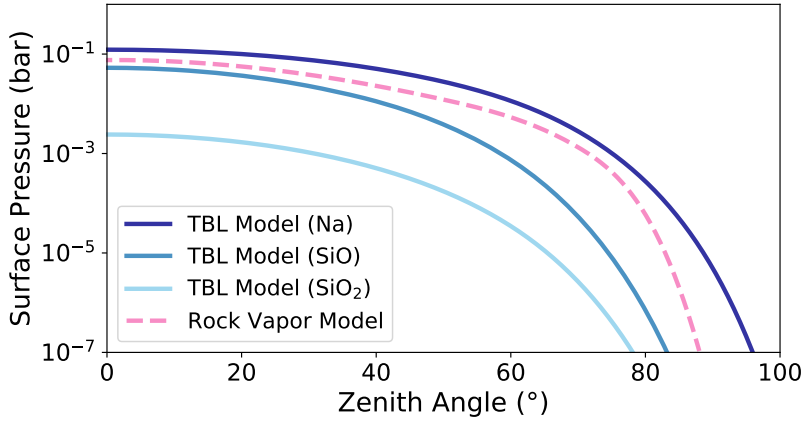


Figure 2.9: Surface pressure as a function of the zenith angle for the two different models used in this paper. The dashed pink line is based on the pseudo-2D rock vapor model and the blue lines are based on the 1D TBL model for a Na, SiO and SiO₂ atmosphere. Although, the TBL models shown in this plot are based on Nguyen et al. (2020) and lack radiative transfer, this would introduce little to no changes to the surface pressure. Na is the most volatile possible component of rock vapor atmosphere, so a pure Na atmosphere has the highest surface pressure (Schaefer & Fegley 2004).

2.4.3 Comparison of the models

We calculated the surface pressure for both models as a function of zenith angle and show the results in Figure 2.9. One can see that due to the lack of atmospheric circulation in the pseudo-2D rock vapor model the surface pressure does not drop off as quickly with zenith angle as in the 1D turbulent boundary layer (TBL) model. This indicates that the pseudo-2D rock vapor model a reasonably good approximation to the 1D TBL model due to the overall atmospheric circulation being low.

2.4.4 Comparison between the models and the data

We compared both the physically motivated models and the toy models to the measured dayside emission spectrum and the full phase curves. The thermal emission spectrum of K2-141b consists of the two broad photometric bands for *K2* and *Spitzer* IRAC Channel 2, as shown in Fig. 2.10. The two photometric band measurements are both consistent within two sigma with the pseudo-2D rock vapor atmosphere model and the best-fit toy model to the joint dataset, where the planet was modeled by a two temperature model and a Lambertian reflective law. As illustrated in Fig. 2.10, both models produce a larger eclipse depth at optical wavelengths than a single temperature blackbody. In the case of the toy model, this eclipse depth is due to reflected light from a moderately high albedo ($A_g = 0.282^{+0.070}_{-0.078}$). For the rock vapor model, the eclipse depth in the *K2* band-pass is dominated by thermal emission from a high-temperature inversion layer

in the atmosphere. We note that the blackbody spectra in the Figure have been divided by a Kurucz stellar spectrum (Kurucz 1993); any features in the black body spectra are therefore originating from the host star. As noted by Ito et al. (2015) for 55 Cnc e, the strong UV heating of the atmosphere, combined with relatively weak IR radiative cooling, leads to an inversion that extends all the way to the ground, suppressing convection. This is a potentially important feature for interpreting infrared emission data for lava planets because the inversion makes the atmosphere considerably hotter than the planet’s surface. There are strong absorption features from Na in the optical, and SiO in the infrared, so the emission in both of our photometric bands largely comes from the atmosphere rather than the surface.

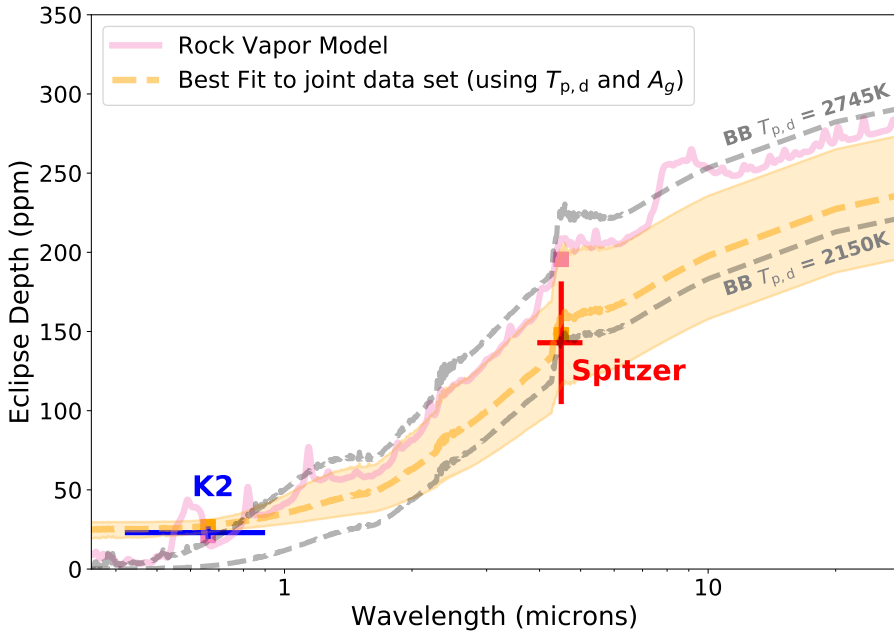


Figure 2.10: Eclipse depths measured in the *Kepler* and *Spitzer* bandpasses compared to different emission spectra of the planet: the pink solid line was calculated using the pseudo-2D rock vapor model and shows thermal emissions in the optical due to Na. The dashed orange line uses the best fit dayside temperature $T_{p,d}$ and geometric albedo A_g values using the joint dataset (*Spitzer* & *K2*). The orange shaded area is due to the uncertainties in $T_{p,d}$ and A_g . We also show black body (BB) emission spectra in gray for two exemplary dayside temperatures of K2-141 b assuming a geometric albedo of $A_g = 0$: $T_{p,d} = 2150\text{K}$ that corresponds to a full redistribution of heat on the planet (whole planet is isothermal) and $T_{p,d} = 2745\text{K}$ in case of instant reradiation of incoming energy (nightside temperature is zero). Any features in the black body spectra are originating from the host star because we divide the black body spectrum of the planet with a Kurucz stellar spectrum (Kurucz 1993). The pink (orange) boxes show the *Spitzer* and *K2* bandpass integrated eclipse depth for the rock vapor model (sum of the thermal and reflective emission from the best fit to the joint data set).

We also compared the measured phase curves to a range of models. For the 1D TBL model, we computed three different phase curves assuming an adiabatic, an isothermal, and a temperature inversion case. We furthermore used the Open Source package **SPIDERMAN** (Louden & Kreidberg 2018) to convert the emitted flux coming from each concentric ring in the pseudo-2D rock vapor model and generated a phase curve. Figure 2.11 shows the comparison of the *Spitzer* data to these different phase curves. The adiabatic TBL model and rock vapor model both compare well to the data with the adiabatic model agreeing best. The temperature inversion TBL model provides the worst fit to the data with $\Delta\text{BIC} = 7.3$ relative to the adiabatic model ($\Delta\text{BIC} > 3.2$ (> 10) is a substantial (strong) evidence for the model with the lower BIC; Kass & Raftery 1995). The isothermal TBL and rock vapor model have $\Delta\text{BIC} = 3.3$ and $\Delta\text{BIC} = 2.4$, respectively.

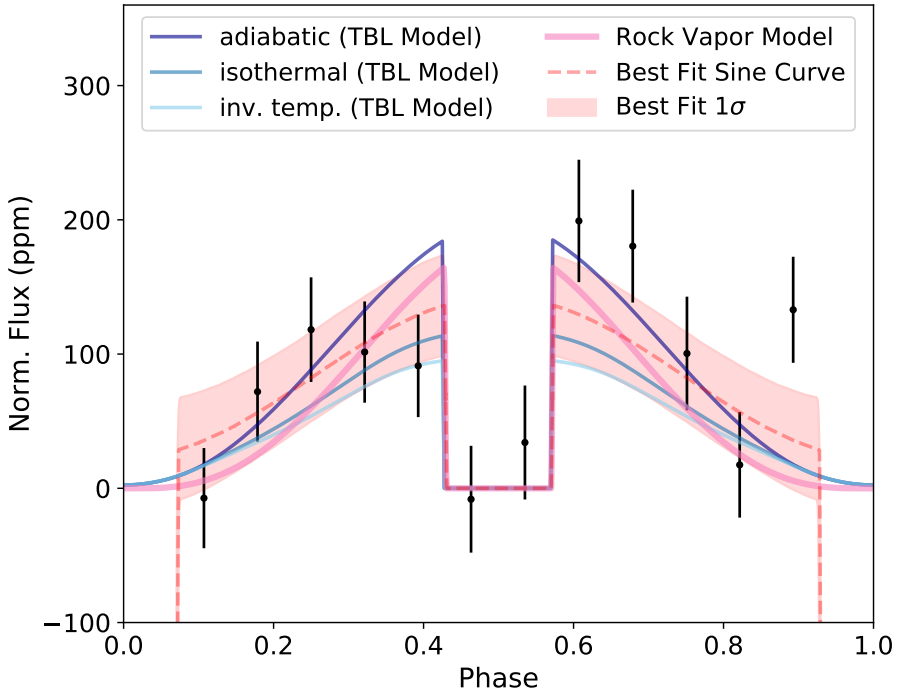


Figure 2.11: Observed *Spitzer* phase curve and the best fit sine curve to the *Spitzer* data (red dashed line with the one sigma uncertainty shaded in red) compared to four theoretical phase curves: The different three blue solid lines are phase curves for the 1D TBL model assuming an adiabatic, an isothermal and an temperature inversion case. We also generated a phase curve out of the pseudo-2D rock vapor model (solid pink line). The adiabatic, isothermal and rock vapor model all fit the observations well and the temperature inversion model provides the worst fit.

2.5 Discussion

What sets K2-141 b apart from previously studied USPs is that it is the first with detected phase variation and secondary eclipse at optical and infrared wavelengths, enabling unique constraints on its atmospheric properties. By comparing the joint *K2* and *Spitzer* datasets with a range of toy and physically-motivated models, we find that a thick atmosphere is disfavored, but a rock vapor atmosphere provides a good explanation to all available data.

2.5.1 Evidence against a thick atmosphere

One noteworthy feature of the data is that the peak brightness occurs at the substellar point. Based on a sinusoidal model fit to the *Spitzer* data, we found no significant offset ($\phi = -34.5^{15.3}_{-14.6}$). The observation of a thermal hotspot has been usually attributed to a super-rotating jet that advects energy on the planet eastward from the substellar point (e.g., Showman & Polvani 2011). Previously, an eastward offset on a small ($< 2R_{\oplus}$) exoplanet was observed for 55 Cnc e using *Spitzer* data. Demory et al. (2016a) analyzed the shape of the thermal phase curve and measured a hotspot offset of $\phi = 41^{\circ} \pm 12^{\circ}$. This offset could be explained by a thick atmosphere and suggests a moderate mean molecular weight atmosphere with a surface pressure of a few bars (Kite et al. 2016; Angelo & Hu 2017; Hammond & Pierrehumbert 2017). By contrast, our measured phase curve for K2-141 b rules out a 55 Cnc e-like offset at the 3.9σ level. The nondetection of a significant offset in our analysis of K2-141 b indicates that the planet does not have a thick, 55 Cnc e-like atmosphere.

This conclusion is further supported by the low observed nightside temperature, $T_{p,n} = 956^{489}_{-556}$ K (< 1712 K at 2σ) compared to the nightside temperature of 1380 ± 400 K observed for 55 Cnc e (Demory et al. 2016a). Nonzero nightside temperatures are commonly also attributed by heat transport from the dayside to the nightside. To check for heat redistribution on the planet, we used a toy model presented in Kreidberg & Loeb (2016) (see equation 2.7) to fit the planet’s thermal emission. The model uses a heat redistribution parameter, F , to regulate how much energy is transported from the dayside to the nightside of the planet. We fit this toy heat redistribution model to the joint (*K2* & *Spitzer*) data set, and found that fixing the heat redistribution parameter to $F = 0$ (i.e., no heat redistribution on the planet) is statistically preferred compared to letting F vary free at $\Delta\text{BIC} = 12.0$ which is strong evidence for the model with no heat redistribution (Kass & Raftery 1995). Taken together, the absence of a hotspot offset and atmospheric heat redistribution support a scenario where the planet has little-to-no atmosphere.

2.5.2 Evidence for a thin rock vapor atmosphere

While a thick atmosphere is disfavored by the data, thinner atmospheres are a possibility. Thin gas-melt equilibrium atmospheres are expected for USPs (e.g., Miguel et al. 2011). These atmospheres have much weaker heat circulation, but may be sufficiently optically thick that they have detectable spectral features (e.g.,

Ito et al. 2015). To evaluate this possibility, we compared the dayside emission spectrum of K2-141 to two different models (see Figure 2.10). The first is a toy model based on the joint fit from Section 3.2 (a blackbody plus a reflected light component). The second model is the physically-motivated, pseudo-2D rock vapor spectrum described in Section 4.1. We focused on the dayside spectrum alone because a full 3D model with realistic radiative transfer is beyond the scope of this paper.

Both the model spectra fit the observed eclipse depths well (within 2σ), but they have different implications for the nature of the planet’s atmosphere. Both models have a larger optical eclipse depth than expected from a single-temperature blackbody. In the toy model, the eclipse depth in the *Kepler* bandpass is fit by a high geometric albedo ($A_g = 0.282^{+0.070}_{-0.078}$). By contrast, in the rock vapor model, the large optical eclipse depth is due to thermal emission from a hot inversion layer in the upper atmospheres, which is probed by strong absorbers at optical wavelengths. A priori, it is challenging to say whether thermal emission or reflected light is more physically plausible. Recent lab experiments by Essack et al. (2020) have shown that lava worlds like K2-141 b are expected to have low albedos ($A_g < 0.1$). In light of those results, a thermal inversion in a rock vapor atmosphere may be a more plausible explanation for the data. Alternatively, it is also possible that highly reflective clouds could form in a rock vapor atmosphere; this possibility merits further theoretical investigation. Either way, whether the optical eclipse depth is due to a thermal inversion or reflective clouds, both explanations point to a thin rock vapor atmosphere rather than a reflective surface.

These results shed new light on another well-known USP, Kepler-10 b (Batalha et al. 2011), discovered by *Kepler*. Kepler-10 b also showed a surprisingly deep optical eclipse depth attributed to a highly reflective lava (Léger et al. 2011; Rouan et al. 2011). We find that the eclipse depth may also be explained by a thermal inversion layer. Figure 2.12 shows our pseudo-2D rock vapor atmosphere model adjusted for the planetary and stellar parameters of Kepler-10 b compared to the measured eclipse depth by Sheets & Deming (2014). Emission features due to the thermal inversion of Na at approximately 0.6 and 0.8 μm increase the observed emission in the *K2* bandpass. The spectrum agrees well with the originally published eclipse depth. Subsequent analysis suggested that the eclipse depth may be even higher (Sheets & Deming 2014; Singh et al. 2022). The thermal inversion model agrees with these values to within 2.4 and 3.6σ , respectively. Depending on the exact approach used for the data analysis, a thermal inversion can explain all or part of the observed signal. Thermal inversions are thus important to consider when interpreting the optical eclipse depths for USPs.

2.6 Summary and conclusions

We analyzed new *Spitzer* observations of K2-141 b spanning 65 hours and detected the thermal emission of the planet at 3.7σ confidence with an eclipse depth of $f_p/f_* = 142.9^{+38.5}_{-39.0}$ ppm. We fit several models to the *Spitzer* data alone, and to the joint *Spitzer* and *Kepler* dataset. By fitting a sinusoid to the *Spitzer* data we found

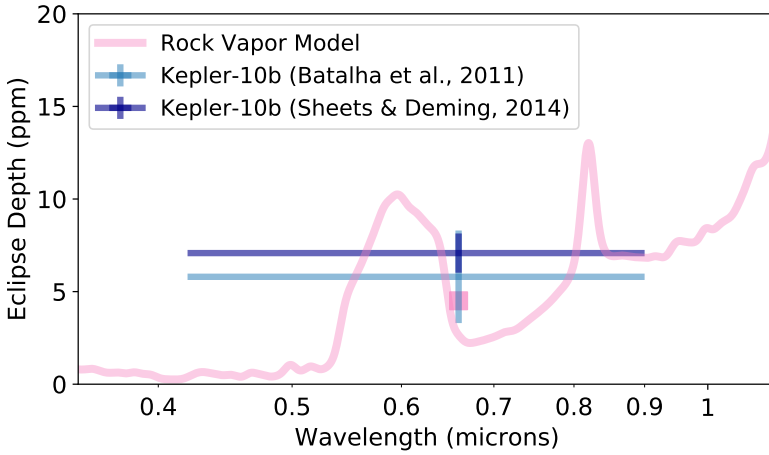


Figure 2.12: Eclipse depth of Kepler-10 b measured in the *Kepler* bandpass compared to a pseudo-2D rock vapor model in pink showing emission features caused by thermal emission. The pink square is the predicted bandpass integrated eclipse depth assuming the rock vapor atmosphere model for the planet.

no evidence for a hotspot offset. Our results on the hotspot offset are inconsistent with the *Spitzer* observations of 55 Cnc e at a 3.9σ level, the only other small USP planet with temperatures high enough to melt rock observed with *Spitzer*. Combining the *Spitzer* observations which are dominated by thermal emission with the *Kepler* observations dominated by optical emission we are able to break the degeneracy between these two emission sources. We fit a toy model described in Kreidberg & Loeb (2016) with the planet’s heat redistribution F as a free parameter and find that fixing $F = 0$ is statistically preferred. We find a nonzero geometric albedo of $A_g = 0.282^{0.070}_{-0.078}$, a dayside temperature of $T_{p,d} = 2049^{362}_{-359}$ K and a nightside temperature of $T_{p,n} = 956^{489}_{-556}$ K (<1712 K at 2σ).

The planetary system containing the two confirmed planets was discovered using *Kepler* observations collected in the *K2* Campaign 12 (Malavolta et al. 2018; Barragán et al. 2018). Since then, the system has been reobserved during *K2* Campaign 19 and with *Spitzer*. We were able to significantly improve the ephemerides of K2-141 b and K2-141 c. The 3σ uncertainty on the predicted transit time in 2024 decreased from about an hour to just 2.7 minutes for planet b and from 5.2 hours to 16 minutes planet c compared to Malavolta et al. (2018). This will help in the future to schedule observations of K2-141 b and avoid transits or eclipses of planet c.

We compare the data to physically motivated models, including a pseudo-2D rock vapor atmosphere model and a 1D turbulent boundary layer (TBL) model. We found that the TBL model with an adiabatic temperature pressure profile and the rock vapor model both agree well to the observed phase curve with *Spitzer*. With TBL model with an isothermal T–P profile agrees worse with a $\Delta\text{BIC} = 3.3$ and the TBL model with a temperature inverted T–P profile has substantial

disagreement with the observations $\Delta\text{BIC} = 7.3$.

The moderately high albedo (roughly 0.3) may be due to a reflective surface, or a thermal inversion in a rock vapor atmosphere. The previous high albedo measurement for Kepler-10 b can be also partially explained by such an inversion. A high optical emission also for other rocky planets might therefore be explained by a thermal inversion in a rock vapor atmosphere.

The negligible hotspot offset for K2-141 b contrasts with the large offset previously observed for 55 Cnc e. This suggests that the atmospheres have different properties. 55 Cnc e was suggested to have a moderate mean molecular weight atmosphere of a few bars (Hammond & Pierrehumbert 2017; Angelo & Hu 2017). K2-141 b either has a high mean molecular weight and low surface pressure or no atmosphere at all.

Future observations of ultra-short-period planets will give more insight on the nature of these extreme planets. In fact, the *James Webb Space Telescope* (*JWST*) will observe several small ($< 2 R_{\oplus}$) USP planets during its Cycle 1 General Observers program:

- LHS 3844 b with $R = 1.3 R_{\oplus}$, $P = 11.1\text{h}$, $T_{\text{eq}} = 805\text{K}$
 - three eclipses with MIRI/LRS (Kreidberg et al. 2021b)
- GJ 367 b with $R = 0.72 R_{\oplus}$, $P = 7.7\text{h}$ and $T_{\text{eq}} = 1350\text{K}$
 - phase curve with MIRI/LRS (Zhang et al. 2021a)
- 55 Cnc e with $R = 1.9 R_{\oplus}$, $P = 17.7\text{h}$, $T_{\text{eq}} = 1950\text{K}$
 - one eclipse with NIRCam/GRISMR+F444W (Hu et al. 2021)
 - one eclipse with MIRI/LRS (Hu et al. 2021)
 - four eclipses with NIRCam/GRISMR+F444W (Brandeker et al. 2021)
- K2-141 b with $R = 1.51 R_{\oplus}$, $P = 6.9\text{h}$ and $T_{\text{eq}} = 2150\text{K}$.
 - phase curve with NIRSpec/G395H+F290LP (Espinoza et al. 2021)
 - phase curve with MIRI/LRS (Dang et al. 2021)

Of these four planets observed in Cycle 1, only K2-141 b and 55 Cnc e are hot enough to have a molten dayside. *JWST*'s sensitivity and spectroscopic range is perfectly suited to study the thermal emission coming from these highly irradiated exoplanets. These planets might have detectable Na, SiO or SiO₂ in their atmospheres due to the evaporation of their surfaces. For example, SiO has broad features at 4 and 9 μm (Ito et al. 2015). The large wavelength coverage of the MIRI/LRS instrument (~ 5 to 12 μm) is especially suited for probing in and out of the SiO band to determine the presence of an extended atmosphere. With *JWST* observations already planned for K2-141 b during Cycle 1, additionally information about the atmosphere is forthcoming. Espinoza et al. (2021) will use the NIRSpec G395H+F290LP instrument with a resolution of $R = 1900 - 3700$ to

observe a phase curve in the near infrared ($2.87 - 5.18 \mu\text{m}$). The planned mid-infrared observations by Dang et al. (2021) will use MIRI’s LRS mode ($5 - 12 \mu\text{m}$) at a resolution of $R \sim 100$. All of these *JWST* observations, combined with the available data collected in the optical by *K2* and in the infrared by *Spitzer* will paint an unprecedented picture for a lava planet.

Acknowledgements

L.C. acknowledges support from the DFG Priority Programme SP1833 Grant CA 1795/3. R.L. acknowledges support from the NASA ROSES XRP grant NNX17AC02G. This research made use of Lightkurve, a Python package for Kepler and TESS data analysis (Lightkurve Collaboration, 2018). This paper includes data collected by the Kepler mission and obtained from the MAST data archive at the Space Telescope Science Institute (STScI). Funding for the Kepler mission is provided by the NASA Science Mission Directorate. STScI is operated by the Association of Universities for Research in Astronomy, Inc., under NASA contract NAS 5–26555. This work is based on observations made with the Spitzer Space Telescope, which was operated by the Jet Propulsion Laboratory, California Institute of Technology under a contract with NASA. This research has made use of the NASA/IPAC Infrared Science Archive, which is funded by the National Aeronautics and Space Administration and operated by the California Institute of Technology. We gratefully acknowledge the packages and tools that made this work possible: `numpy` (Harris et al. 2020), `matplotlib` (Hunter 2007a), `scipy` (Virtanen et al. 2020), `astropy` (Astropy Collaboration et al. 2013, 2018), `ipython` (Perez & Granger 2007), `batman` (Kreidberg 2015), `SPIDERMAN` (Louden & Kreidberg 2018), `POET` (Cubillos et al. 2013), `corner` (Foreman-Mackey 2016), `dynesty` (Speagle 2020), `MAGMA` (Fegley & Cameron 1987; Schaefer & Fegley 2004), `FastChem` (Stock et al. 2018), `HELIOS` (Malik et al. 2017; Malik et al. 2019b), `petitRADTRANS` (Mollière et al. 2019). Finally, we thank the anonymous referee for a detailed report, which helped us to improve the quality of this paper.

Appendix

2.A Updated ephemeris for K2-141 c

We used the one transit of K2-141 c which occurred in the continuous 8 days of K2 C19 (see Figure 2.1) to improve the ephemeris of the planet. Our total model uses the transit model implemented in **batman** (Kreidberg 2015) multiplied by a constant. The fit model has 5 free parameters: the orbital period P , the time of central transit t_0 , the radius of planet in units of stellar radii R_p/R_* , the semi-major axis in units of stellar radii a/R_* , the cosine of the inclination $\cos i$ and a constant c . We fixed the eccentricity ecc and the argument of periastron ω to zero. We used the same values for the limb-darkening coefficients u_1 and u_2 as in our analysis of K2-141 b (see Section 2.3). The Parameters and their uncertainties were estimated using the Nested Sampling package **dynesty** (Speagle 2020). We used Gaussian priors based on the values reported in Malavolta et al. (2018) for P , a/R_* and $\cos i$. The final fit and the pairs plot of the posteriors can be found in Figure 2.13 and Figure 2.14, respectively. The resulting t_0 was used to recalculate the orbital period P following the following approach:

$$\frac{t_{0,new} - t_{0,Lit.}}{P_{Lit.}} = n_{old} \quad (2.8)$$

$$n_{old} \approx n_{new}, \text{ with } n_{new} \in \mathbb{Z} \quad (2.9)$$

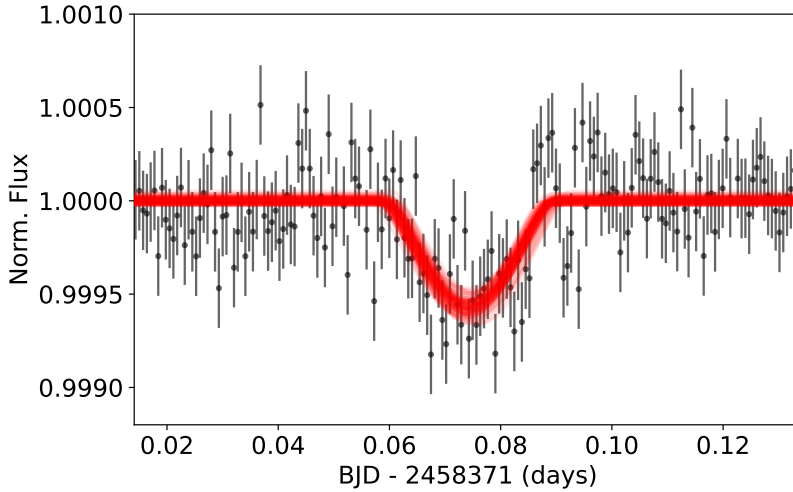
$$(t_{0,Lit.} - t_{0,new}) * n_{new} = P_{new}. \quad (2.10)$$

Firstly, we take the difference between our newly determined transit time $t_{0,new}$ and the value $t_{0,Lit.}$ reported in Malavolta et al. (2018) and divide this value by the orbital period (see Equation 2.8). This equals the number of elapsed orbits between the two transit times and be a number n_{old} really close to a full integer n_{new} (see Equation 2.9). Finally, we can use the newly determined n_{new} to update the orbital period (see Equation 2.10). Our updated ephemeris for K2-141 c is listed in Table 2.8. We could improve the uncertainties on the orbital period on the transit time for the planet, so that the 3σ uncertainty on the predicted transit time in 2024 was reduced from 5.2 hours to 16 minutes compared to Malavolta et al. (2018). This will make it especially easier in the future to schedule observations of K2-141 b and avoid transits or eclipses of planet c.

We only fit for the single transit which occurred in K2 C19. This lead to a better ephemeris, but we were not able to improve other orbital parameters like a/R_* , $\cos i$ or the planet's size R_p/R_* . Our resulting radius of K2-141 c in units of stellar radii R_p/R_* is consistent with the value reported in Malavolta et al. (2018). It is, however, strongly correlated with the cosine of the inclination $\cos i$ due to the grazing transit geometry of the planet. This can be also seen in Figure 2.13 as the duration of the transit is short and V-shaped.

Table 2.8: Updated ephemeris for K2-141 c and the 3σ uncertainty on the predicted transit time in 2022 and 2024.

K2-141 c	⁽¹⁾ Discovery	Updated
P (d)	7.74850 ± 0.00022	$7.7489943^{+1.48e-05}_{-1.49e-05}$
⁽²⁾ t_0 (d)	7751.1546 ± 0.0010	$8371.07415^{+0.000632}_{-0.000652}$
$3\sigma_{2022}$	3.7 hours	10 minutes
$3\sigma_{2024}$	5.2 hours	16 minutes

Notes.⁽¹⁾ Based on Malavolta et al. (2018)⁽²⁾ Expressed as $\text{BJD}_{\text{TDB}} - 2450000.0$ d**Figure 2.13:** The transit of K2-141c in C19 with 100 random draws from the posterior in red.

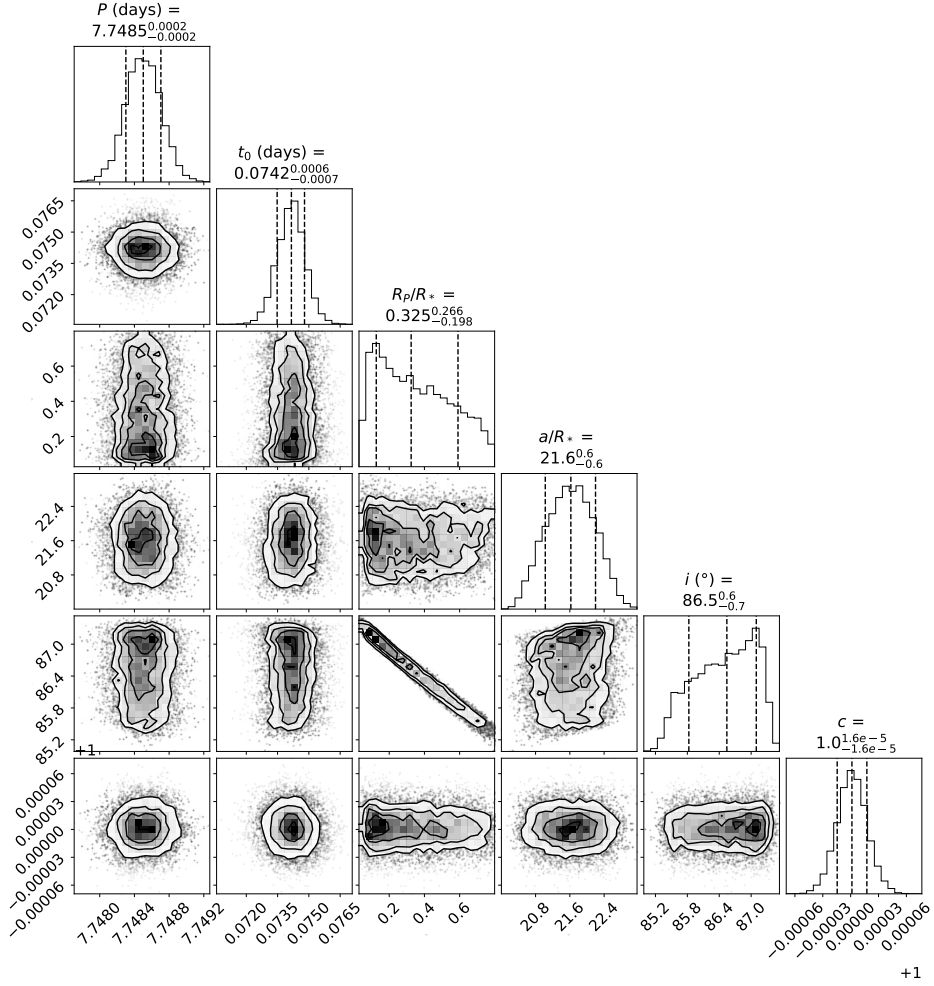


Figure 2.14: Corner plot of the fit transit model based on the single transit of K2-141 c in K2 C19 to update the ephemeris of the planet. Gaussian Priors were used on P , a/R_* and $\cos i$ based on the values reported in Malavolta et al. (2018) who only used the observations in C12. We used the resulting transit time t_0 to recalculate the orbital period P . The transit time in this plot is expressed as $\text{BJD}_{\text{TDB}} - 2458371.0$ d.

2.B Additional tables

2.B.1 Rescaling of uncertainties

Table 2.9: χ^2 values for each *Spitzer* AOR before rescaling them to unity.

AOR	χ_{old}^2	rms _{obs} (ppm)	rms _{phot} (ppm)	β
1	1.155	3477	3236	1.129
2	1.082	3463	3330	0.996
3	1.103	3471	3306	1.369
4	1.106	3466	3296	1.184
5	1.098	3485	3327	0.976
6	1.102	3452	3288	0.927
All	—	3471	—	1.132

Notes. The values in this table are based on the residuals of the full dataset (*Spitzer* and *Kepler*) and the Toy model without redistribution fit. The photon noise-limited root-mean-square (rms) was calculated like the following: $\text{rms}_{\text{phot}} = \text{rms}_{\text{obs}} / \sqrt{\chi_{\text{old}}^2}$, where rms_{obs} is the rms of the residuals. β describes the ratio between the achieved standard deviation (rms_{obs}) of the binned residuals and the standard deviation in absence of red noise. It was calculated using the “time-averaging” method (Pont et al. 2006; Winn et al. 2007, 2008) by calculating median values of this ratio for binnings around the transit duration. The Allan deviation plots for each AOR can be found in Section 2.C.4.

2.B.2 Parameters of the fit models

Table 2.10: All free parameters used in the models which were fit to the *Spitzer* data alone.

Model	Free Parameters	ΔBIC
Sinusoidal Model ($\phi = 0$)	$t_0, R_p/R_*, a/R_*, \cos i$ $A, f_p/f_*,$ $c_{\text{AOR}1}, v_{\text{AOR}2}, c_{\text{AOR}2}, c_{\text{AOR}3}, c_{\text{AOR}4}, c_{\text{AOR}5}, c_{\text{AOR}6},$ $Y_1, \text{AOR}1, X_3, \text{AOR}2, X_1, \text{AOR}3, X_3, \text{AOR}4, X_1, \text{AOR}5, Y_3, \text{AOR}5, X_3, \text{AOR}6, Y_3, \text{AOR}6$	0
Sinusoidal Model (ϕ free)	$t_0, R_p/R_*, a/R_*, \cos i$ $A, f_p/f_*, \phi,$ $c_{\text{AOR}1}, v_{\text{AOR}2}, c_{\text{AOR}2}, c_{\text{AOR}3}, c_{\text{AOR}4}, c_{\text{AOR}5}, c_{\text{AOR}6},$ $Y_1, \text{AOR}1, X_3, \text{AOR}2, X_1, \text{AOR}3, X_3, \text{AOR}4, X_1, \text{AOR}5, Y_3, \text{AOR}5, X_3, \text{AOR}6, Y_3, \text{AOR}6$	8.8
Two Temp. Model	$t_0, R_p/R_*, a/R_*, \cos i,$ $T_*, T_{p,n}, T_{p,d},$ $c_{\text{AOR}1}, v_{\text{AOR}2}, c_{\text{AOR}2}, c_{\text{AOR}3}, c_{\text{AOR}4}, c_{\text{AOR}5}, c_{\text{AOR}6},$ $Y_1, \text{AOR}1, X_3, \text{AOR}2, X_1, \text{AOR}3, X_3, \text{AOR}4, X_1, \text{AOR}5, Y_3, \text{AOR}5, X_3, \text{AOR}6, Y_3, \text{AOR}6$	9.6

Table 2.11: All free parameters used in the models which were fit to the joint *Kepler* and *Spitzer* dataset.

Model	Free Parameters	ΔBIC
Toy Model ($F = 0$)	$t_0, R_p/R_*, a/R_*, \cos i, P,$ $T_*, A_g,$ $\mathcal{CAOR1}, \mathcal{VAOR2}, \mathcal{CAOR2}, \mathcal{CAOR3}, \mathcal{CAOR4}, \mathcal{CAOR5}, \mathcal{CAOR6}, \mathcal{CK2C12}, \mathcal{CK2C19},$ $Y_1, \text{AOR1}, X_3, \text{AOR2}, X_1, \text{AOR3}, X_3, \text{AOR4}, X_1, \text{AOR5}, Y_3, \text{AOR5}, X_3, \text{AOR6}, Y_3, \text{AOR6}$	0
Toy Model (F free)	$t_0, R_p/R_*, a/R_*, \cos i, P,$ $T_*, F, A_g,$ $\mathcal{CAOR1}, \mathcal{VAOR2}, \mathcal{CAOR2}, \mathcal{CAOR3}, \mathcal{CAOR4}, \mathcal{CAOR5}, \mathcal{CAOR6}, \mathcal{CK2C12}, \mathcal{CK2C19},$ $Y_1, \text{AOR1}, X_3, \text{AOR2}, X_1, \text{AOR3}, X_3, \text{AOR4}, X_1, \text{AOR5}, Y_3, \text{AOR5}, X_3, \text{AOR6}, Y_3, \text{AOR6}$	12.0
Two Temp. Model	$t_0, R_p/R_*, a/R_*, \cos i, P,$ $T_*, T_{p,d}, T_{p,n}, A_g,$ $\mathcal{CAOR1}, \mathcal{VAOR2}, \mathcal{CAOR2}, \mathcal{CAOR3}, \mathcal{CAOR4}, \mathcal{CAOR5}, \mathcal{CAOR6}, \mathcal{CK2C12}, \mathcal{CK2C19},$ $Y_1, \text{AOR1}, X_3, \text{AOR2}, X_1, \text{AOR3}, X_3, \text{AOR4}, X_1, \text{AOR5}, Y_3, \text{AOR5}, X_3, \text{AOR6}, Y_3, \text{AOR6}$	22.2

Table 2.12: Best fit systematic parameters for all six models.

Parameter	Model Name					
	Sin. M. ($\phi = 0$)	Sin. M. (ϕ free)	Two Temp.	Toy Model ($F = 0$)	Toy Model (F free)	Two Temp. Model
CAOR1	75412^{+386}_{-391}	75414^{+400}_{-396}	75430^{+392}_{-415}	75427^{+389}_{-385}	75420^{+421}_{-420}	75414^{+396}_{-398}
VAOR2	$-130.8^{+29.3}_{-30.1}$	$-120.7^{+29.9}_{-29.5}$	$-131.8^{+30.0}_{-29.2}$	$-128.5^{+29.2}_{-29.3}$	$-133.8^{+29.1}_{-29.7}$	$-128.8^{+29.8}_{-29.7}$
CAOR2	$1.601e + 05^{+19730}_{-19270}$	$1.5344e + 05^{+19420}_{-19630}$	$1.6074e + 05^{+19190}_{-19600}$	$1.586e + 05^{+19180}_{-19180}$	$1.6209e + 05^{+19610}_{-19090}$	$1.5883e + 05^{+19470}_{-19590}$
CAOR3	77386^{+435}_{-445}	77296^{+465}_{-448}	77397^{+483}_{-470}	77407^{+467}_{-445}	77393^{+448}_{-422}	77381^{+461}_{-472}
CAOR4	$74910.5^{+123.5}_{-120.8}$	$74905.4^{+122.5}_{-121.3}$	$74921.8^{+123.5}_{-125.4}$	$74917.1^{+124.9}_{-123.2}$	$74932.3^{+122.2}_{-129.8}$	$74912.4^{+123.1}_{-117.8}$
CAOR5	80275^{+268}_{-270}	80249^{+275}_{-264}	80278^{+276}_{-276}	80248^{+277}_{-275}	80260^{+263}_{-263}	80265^{+290}_{-271}
CAOR6	75321^{+243}_{-243}	75299^{+253}_{-243}	75312^{+243}_{-242}	75330^{+244}_{-240}	75348^{+230}_{-235}	75324^{+240}_{-249}
CK2C12	—	—	—	$1^{+1.481e-06}_{-1.485e-06}$	$0.99999^{+1.465e-06}_{-1.459e-06}$	$0.99999^{+1.513e-06}_{-1.498e-06}$
CK2C19	—	—	—	$0.99999^{+2.54e-06}_{-2.44e-06}$	$0.99999^{+2.5e-06}_{-2.49e-06}$	$0.99999^{+2.49e-06}_{-2.59e-06}$
Y ₁ , AOR1	$-0.06349^{+0.00869}_{-0.00852}$	$-0.06353^{+0.00881}_{-0.00880}$	$-0.06388^{+0.00924}_{-0.00864}$	$-0.06384^{+0.00855}_{-0.00857}$	$-0.06366^{+0.00936}_{-0.00927}$	$-0.06353^{+0.00884}_{-0.00871}$
X ₃ , AOR2	$-0.094898^{+0.01552}_{-0.01582}$	$-0.09531^{+0.01565}_{-0.01518}$	$-0.09523^{+0.01631}_{-0.01578}$	$-0.09460^{+0.01606}_{-0.01562}$	$-0.09470^{+0.01595}_{-0.01550}$	$-0.09462^{+0.01542}_{-0.01607}$
X ₁ , AOR3	$-0.09822^{+0.01039}_{-0.01005}$	$-0.09612^{+0.01049}_{-0.01077}$	$-0.09847^{+0.01098}_{-0.01114}$	$-0.09872^{+0.01038}_{-0.01076}$	$-0.09836^{+0.00984}_{-0.01034}$	$-0.09809^{+0.01100}_{-0.01063}$
X ₃ , AOR4	$-0.14612^{+0.01114}_{-0.01132}$	$-0.14570^{+0.01115}_{-0.01124}$	$-0.14717^{+0.01156}_{-0.01133}$	$-0.14681^{+0.01134}_{-0.01145}$	$-0.14809^{+0.01193}_{-0.01120}$	$-0.14635^{+0.01083}_{-0.01128}$
X ₁ , AOR5	$-0.14020^{+0.00776}_{-0.00769}$	$-0.13899^{+0.0078}_{-0.00756}$	$-0.14013^{+0.00762}_{-0.00787}$	$-0.13967^{+0.00791}_{-0.00796}$	$-0.14041^{+0.00757}_{-0.00774}$	$-0.14005^{+0.00774}_{-0.0078}$
Y ₃ , AOR5	$-0.06069^{+0.01649}_{-0.01643}$	$-0.06409^{+0.01678}_{-0.01625}$	$-0.06114^{+0.01659}_{-0.01607}$	$-0.06047^{+0.01671}_{-0.01724}$	$-0.05830^{+0.01666}_{-0.01686}$	$-0.060765^{+0.01637}_{-0.01633}$
X ₃ , AOR6	$-0.0893^{+0.0208}_{-0.0207}$	$-0.08745^{+0.0208}_{-0.0211}$	$-0.0884^{+0.0210}_{-0.0214}$	$-0.0899^{+0.0220}_{-0.0213}$	$-0.0894^{+0.0207}_{-0.0205}$	$-0.0888^{+0.0213}_{-0.0221}$
Y ₃ , AOR6	$-0.0836^{+0.0201}_{-0.0201}$	$-0.0839^{+0.0205}_{-0.0200}$	$-0.08393^{+0.0209}_{-0.0204}$	$-0.08447^{+0.02029}_{-0.01994}$	$-0.08561^{+0.01998}_{-0.02042}$	$-0.08352^{+0.01934}_{-0.02018}$

2.C Additional plots

2.C.1 Systematics

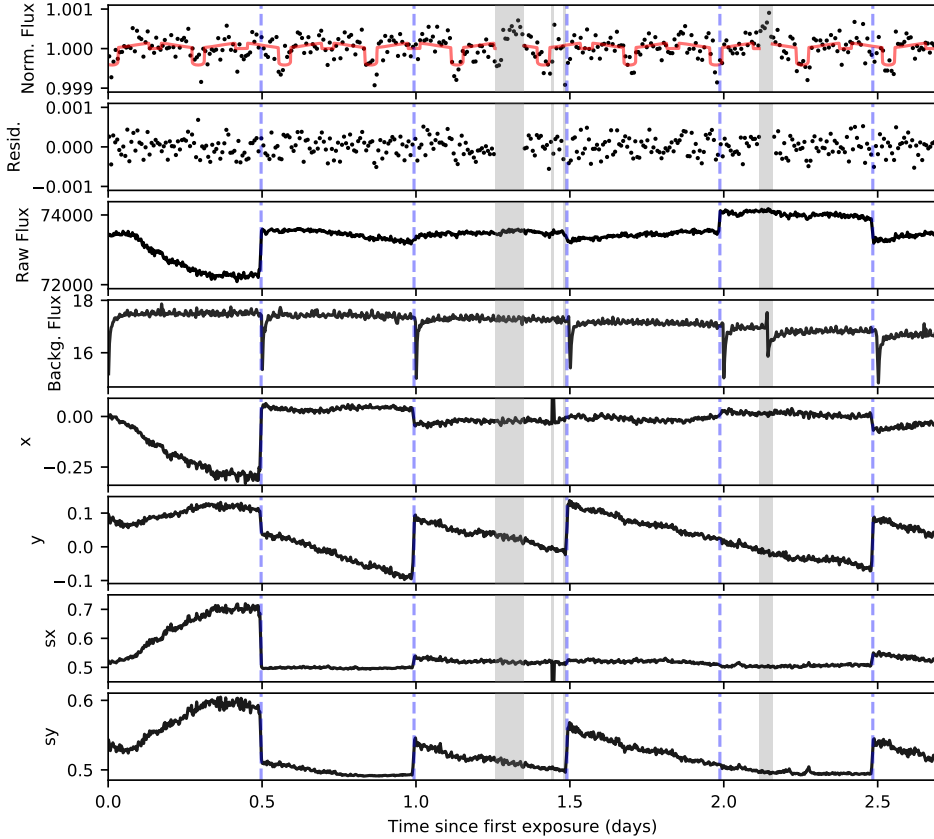


Figure 2.15: Diagnostic plot of the full *Spitzer* observations: The vertical, dashed blue lines indicate the start of a new Astronomical Observation Request (AOR). The data in the vertical, gray shaded regions were removed for the fit due to systematic effects. The red line in the top panel shows the best fit model of the *Spitzer* data. The difference between the model and the normalized flux can be seen in the panel below. The data has been binned down to 10 minutes in the top two panels and to 4 minutes in the lower panels. The observed raw flux in $\mu\text{Jy}/\text{pixel}$ is shown in the third panel. The background flux in the fourth panel is showing changes at the beginning of every AOR as expected due to changes in pointing. An outlier segment in AOR5 which was manually removed from the dataset has been able to be attributed to a strong cosmic ray hit on the detector. The 2D images showing this event can be found in Fig. 2.16. The parameters, x and y are the pixel position of the target relative to the “sweet spot”. Finally, sx and sy describe the Gaussian widths of the star’s point spread function.

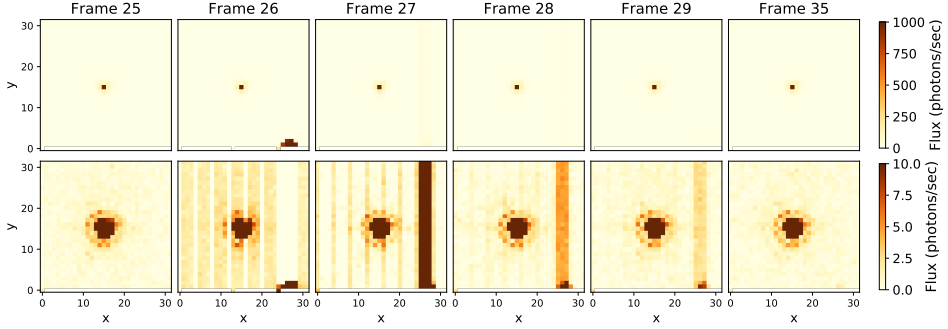


Figure 2.16: *Spitzer* data frames showing strong cosmic ray hit on the *Spitzer* IRAC detector which led to changes in the background flux during AOR5. Each column shows the same Basic Calibrated Data (BCD, provided by the *Spitzer* Science Center) frame but at a different contrast. The star is located in the center of every frame, whereas the cosmic ray hit can be seen in the lower right of the second frame. All frames in this plot have been taken from the same BCD cube which typically consist out of 64 images with 32×32 pixel.

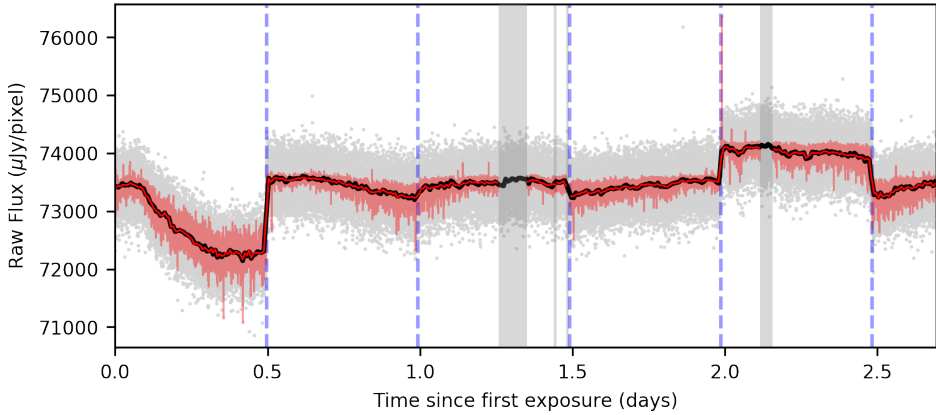


Figure 2.17: Raw, unbinned light curve is shown with gray dots with the best fitting model in light red. The vertical, dashed blue lines indicate the start of a new Astronomical Observation Request (AOR). The data in the vertical, gray shaded regions were removed for the fit due to systematic effects. The solid black (red) line shows the raw light curve (best fitting model) binned down to 10 minutes. The planetary signatures (transit, phase curve variation or eclipse) are too weak to be seen in the raw data. For example, the transit depth of K2-141 b is ~ 425 ppm which leads to a dip of just ~ 30 $\mu\text{Jy/pixel}$.

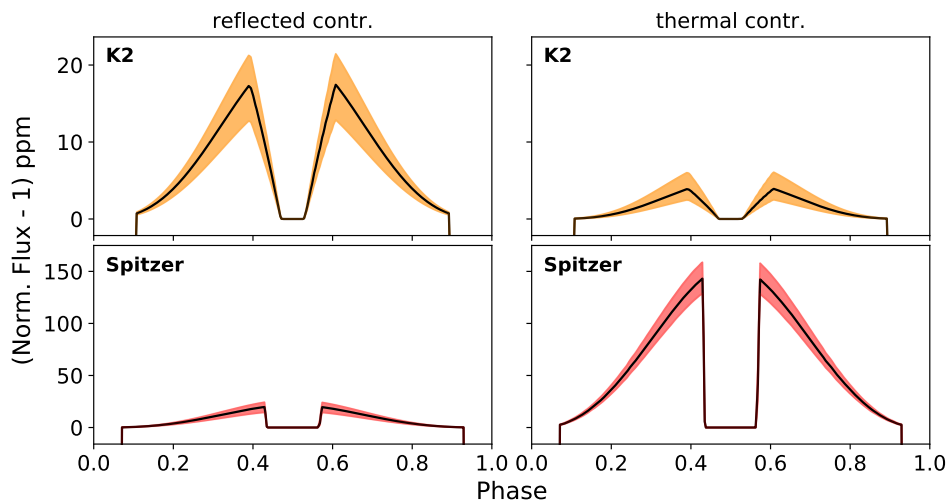


Figure 2.18: Reflected and thermal contributions to the total flux in the *Kepler* and *Spitzer* bandpasses using our best fitting model (toy model without heat redistribution). The shaded areas show the 1σ uncertainties on the best fitting phase curve shape. The *K2* phase curves shown here take the longer exposure time into account (30 minutes for *K2* Campaign 12) which leads to a less steep ingress and egress at the eclipse.

2.C.2 *Spitzer* pointings

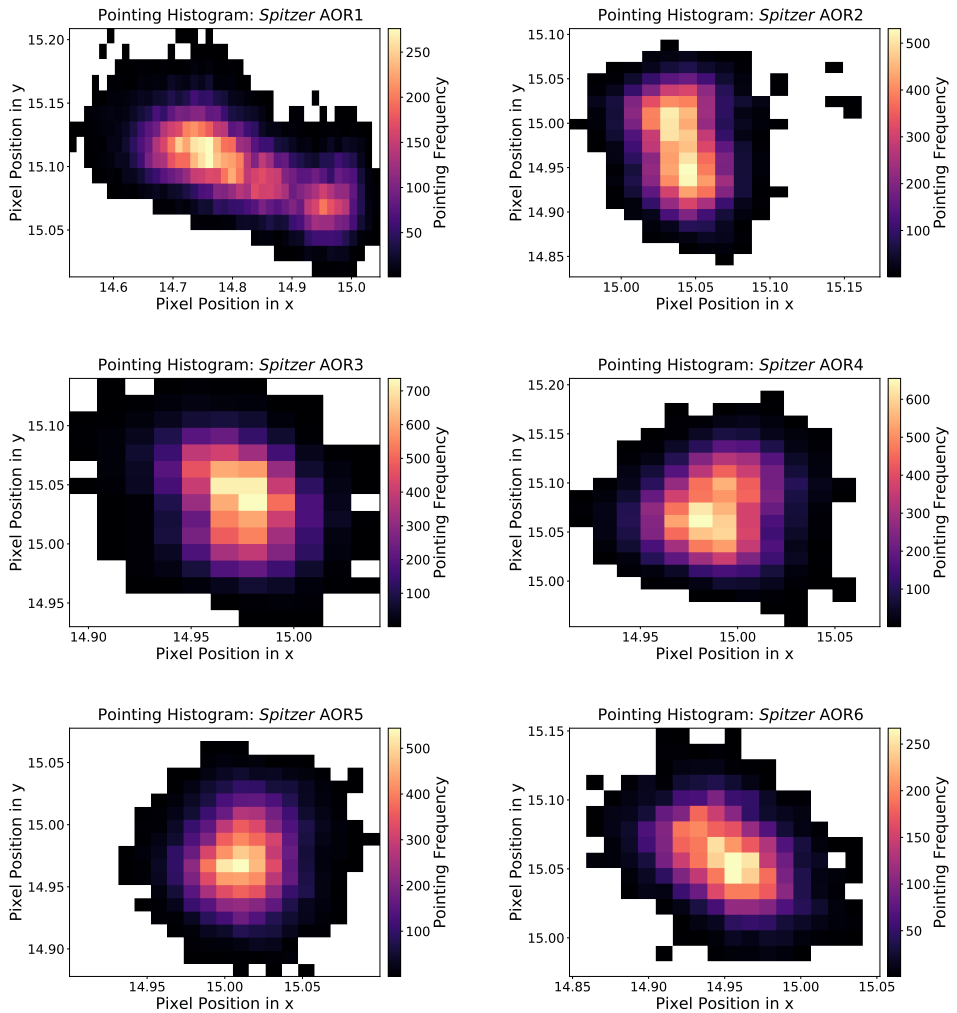


Figure 2.19: Pointing diagrams for all six *Spitzer* AORs. The color map indicates the frequency of exposures for which the centroid of the star hit a certain position.

2.C.3 *Spitzer* BLISS maps

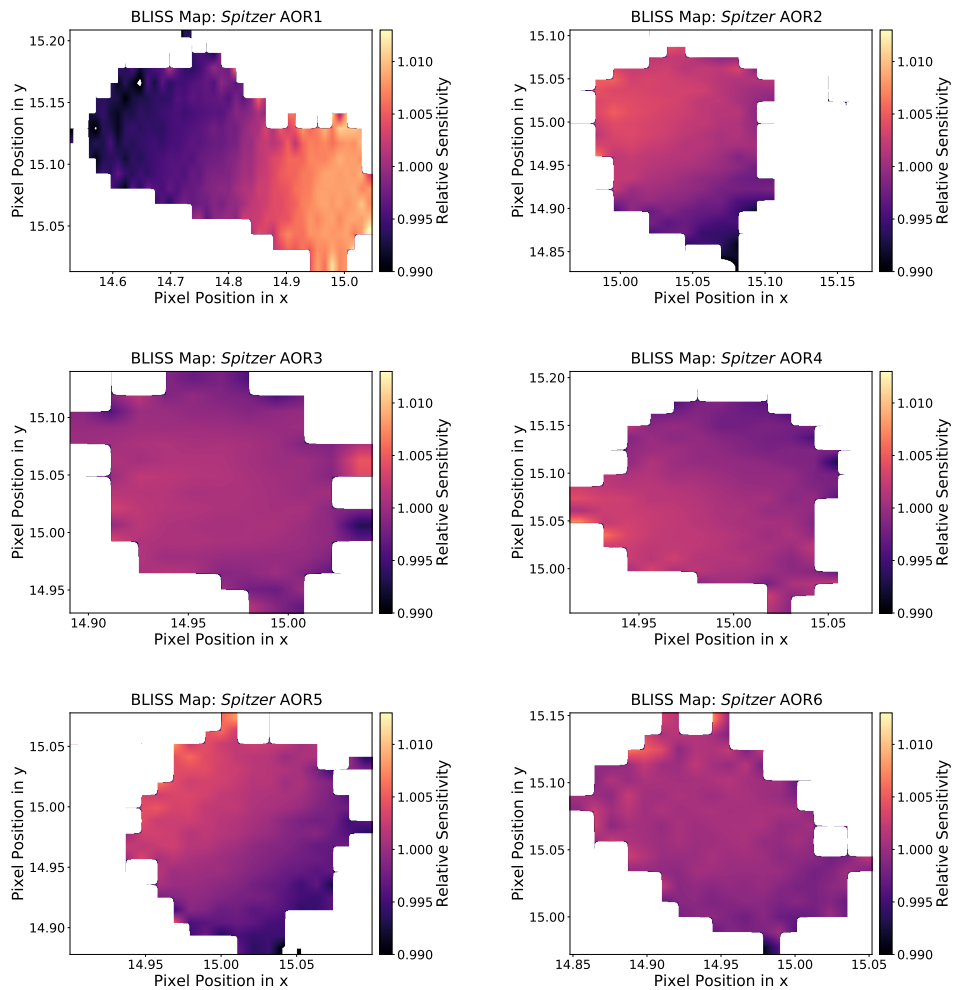


Figure 2.20: BLISS sensitivity maps for all six *Spitzer* AORs.

2.C.4 *Spitzer* Allan deviation plots

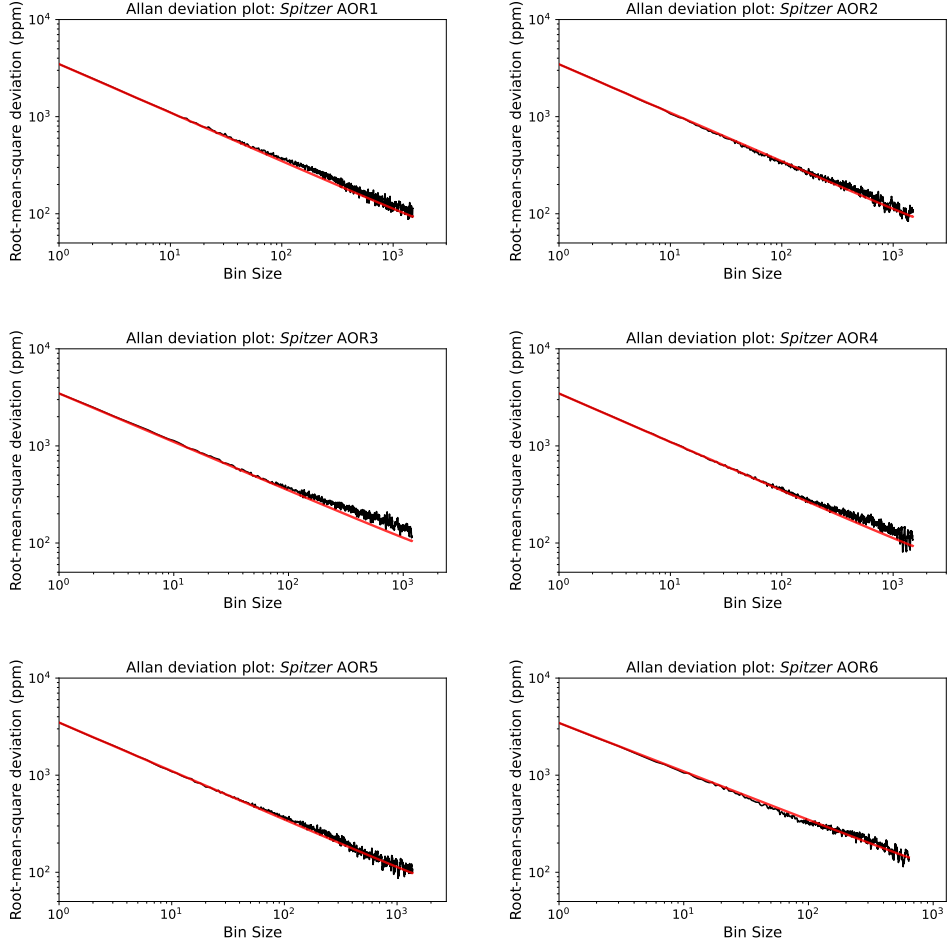


Figure 2.21: Allan deviation plots for all six *Spitzer* AORs. The residuals (black curve) are calculated by taking the difference of the full dataset (*Spitzer* and *Kepler*) and the Toy model without redistribution fit. A bin size of one depicts no binning at all. The red line shows the expected root-mean-square (rms) for Gaussian noise following the inverse square root law.

2.C.5 *Spitzer* fit: Sinusoidal ($\phi = 0$)

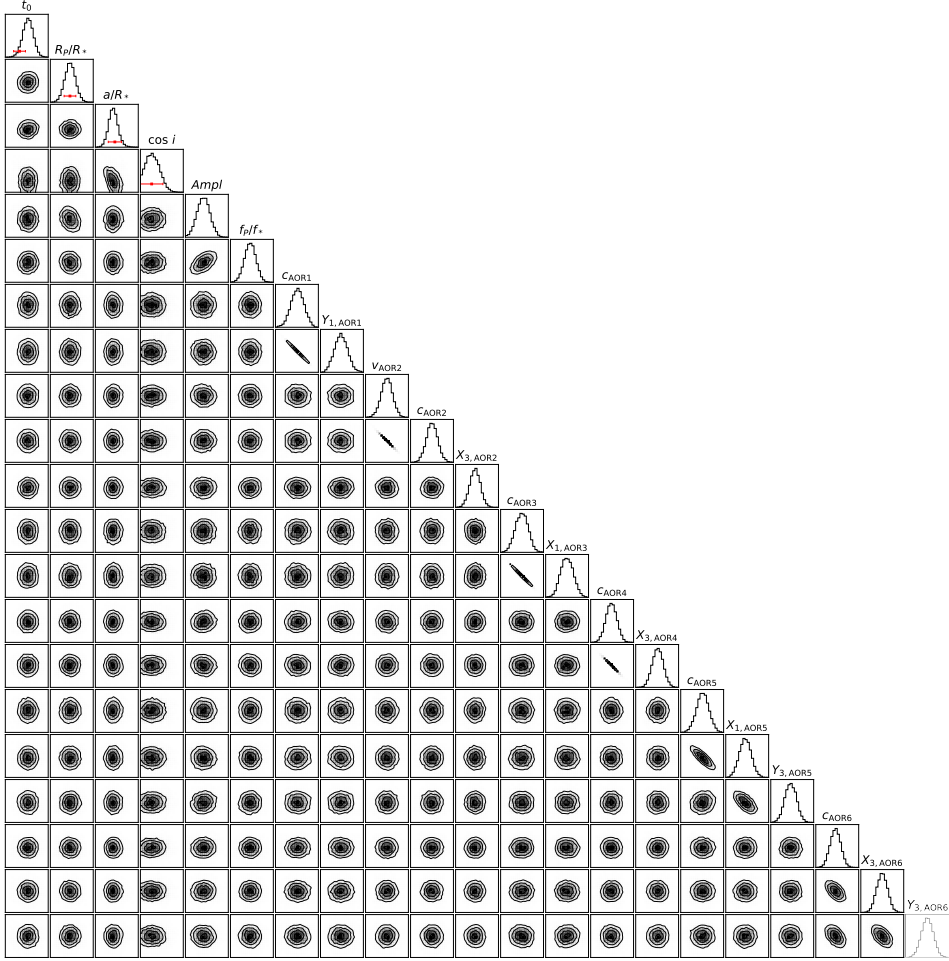


Figure 2.22: MCMC corner plot for the sinusoidal model fit without a hotspot offset ($\phi = 0$) to the *Spitzer* data. The red bars for t_0 , R_p/R_* , a/R_* and $\cos i$ show the Gaussian priors which were used in this fit. The prior values and the best fit values are listed in Table 2.3.3. The resulting values for the systematic parameters are in Table 2.12. A list with all fit parameters can be found in Table 2.10.

2.C.6 *Spitzer* fit: Sinusoidal (ϕ free)

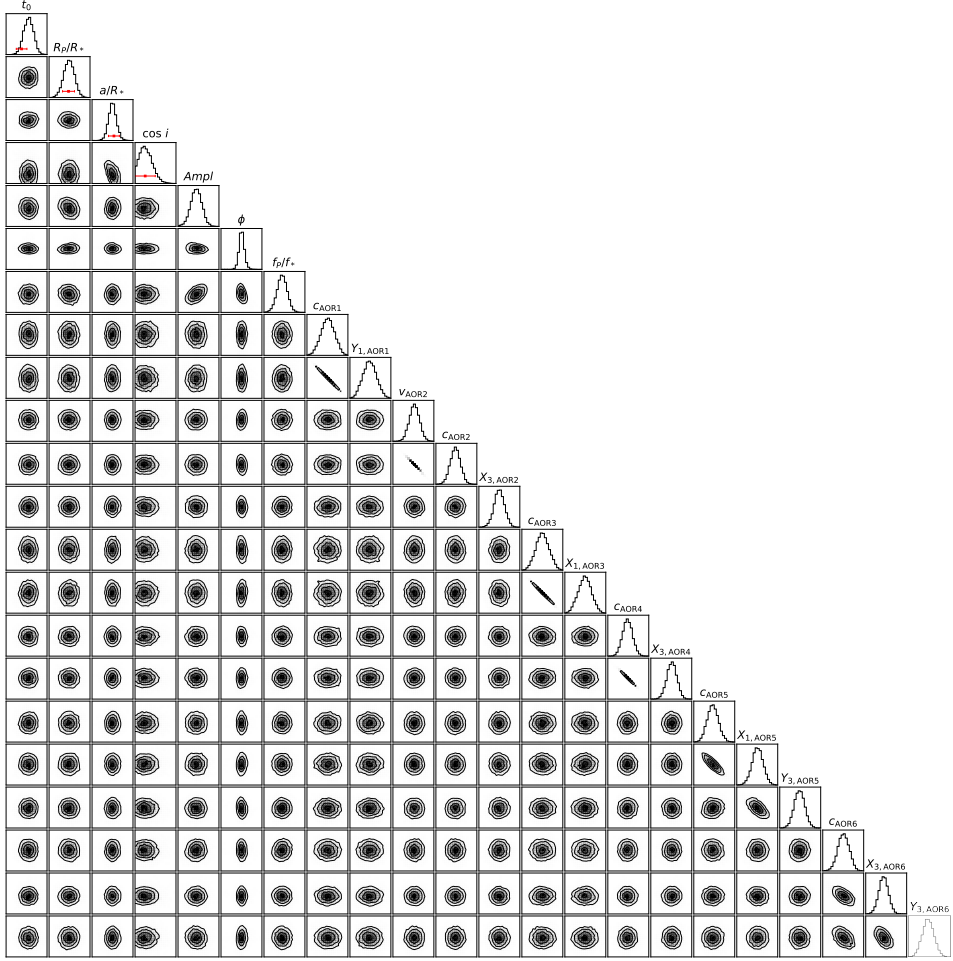


Figure 2.23: MCMC corner plot for the sinusoidal model fit with a hotspot offset (ϕ free) to the *Spitzer* data. The red bars for t_0 , R_p/R_* , a/R_* and $\cos i$ show the Gaussian priors which were used in this fit. The prior values and the best fit values are listed in Table 2.3.3. The resulting values for the systematic parameters are in Table 2.12. A list with all fit parameters can be found in Table 2.10.

2.C.7 *Spitzer* fit: two temperature model

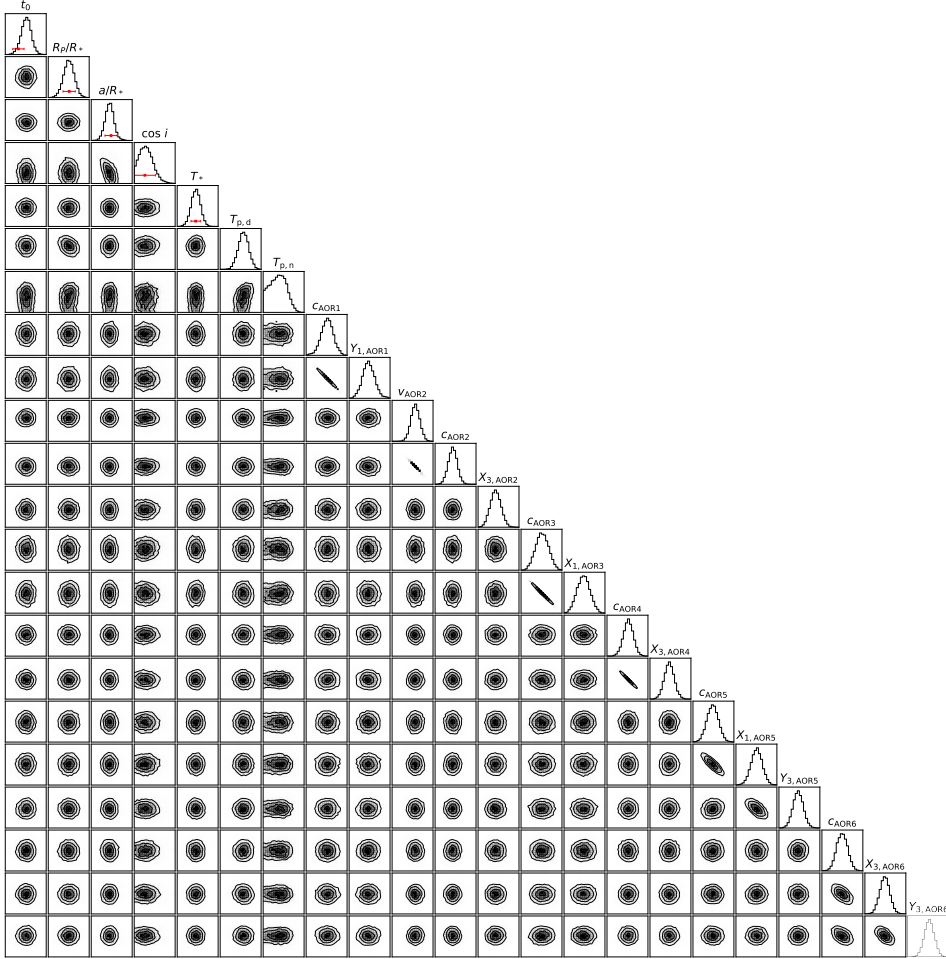


Figure 2.24: MCMC corner plot for the two temperature model fit to the *Spitzer* data. The red bars for t_0 , R_p/R_* , a/R_* , $\cos i$ and T_* show the Gaussian priors which were used in this fit. The prior values and the best fit values are listed in Table 2.3.3. The resulting values for the systematic parameters are in Table 2.12. A list with all fit parameters can be found in Table 2.10.

2.C.8 Joint (*K2* and *Spitzer*) fit: toy model ($F = 0$)

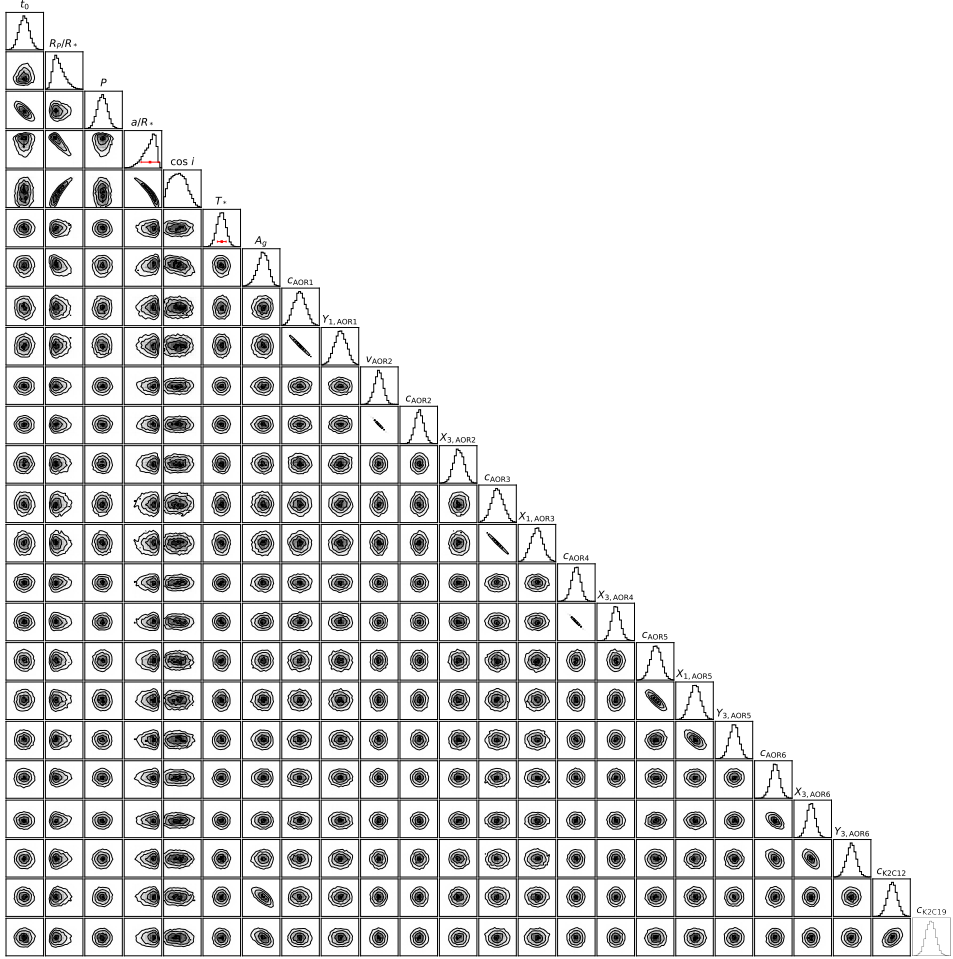


Figure 2.25: MCMC corner plot for the toy model fit without heat redistribution ($F = 0$) to the joint dataset, i.e., *Spitzer* and *K2*. The red bars for a/R_* and T_* show the Gaussian priors which were used in this fit. The prior values and the best fit values are listed in Table 2.3.4. The resulting values for the systematic parameters are in Table 2.12. A list with all fit parameters can be found in Table 2.11.

2.C.9 Joint (*K2* and *Spitzer*) fit: toy model (F free)

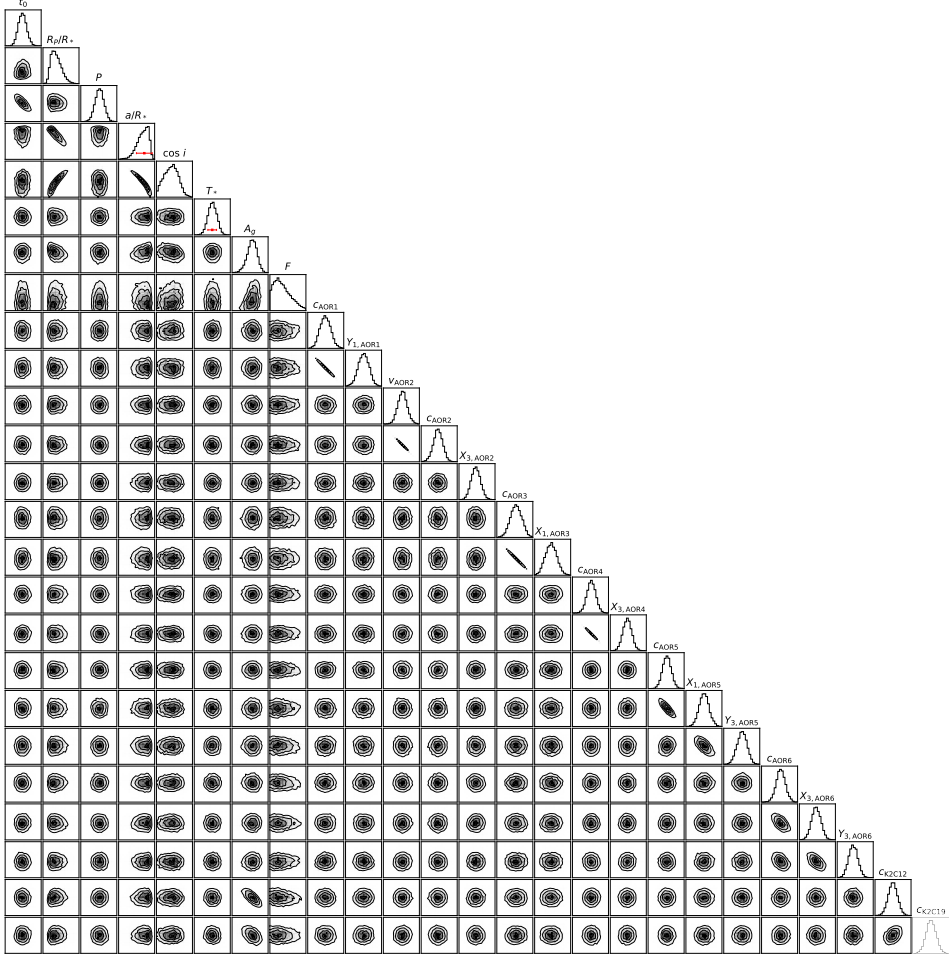


Figure 2.26: MCMC corner plot for the toy model fit with heat redistribution (F free) to the joint dataset, i.e., *Spitzer* and *K2*. The red bars for a/R_* and T_* show the Gaussian priors which were used in this fit. The prior values and the best fit values are listed in Table 2.3.4. The resulting values for the systematic parameters are in Table 2.12. A list with all fit parameters can be found in Table 2.11.

2.C.10 Joint (*K2* and *Spitzer*) fit: two temperature model

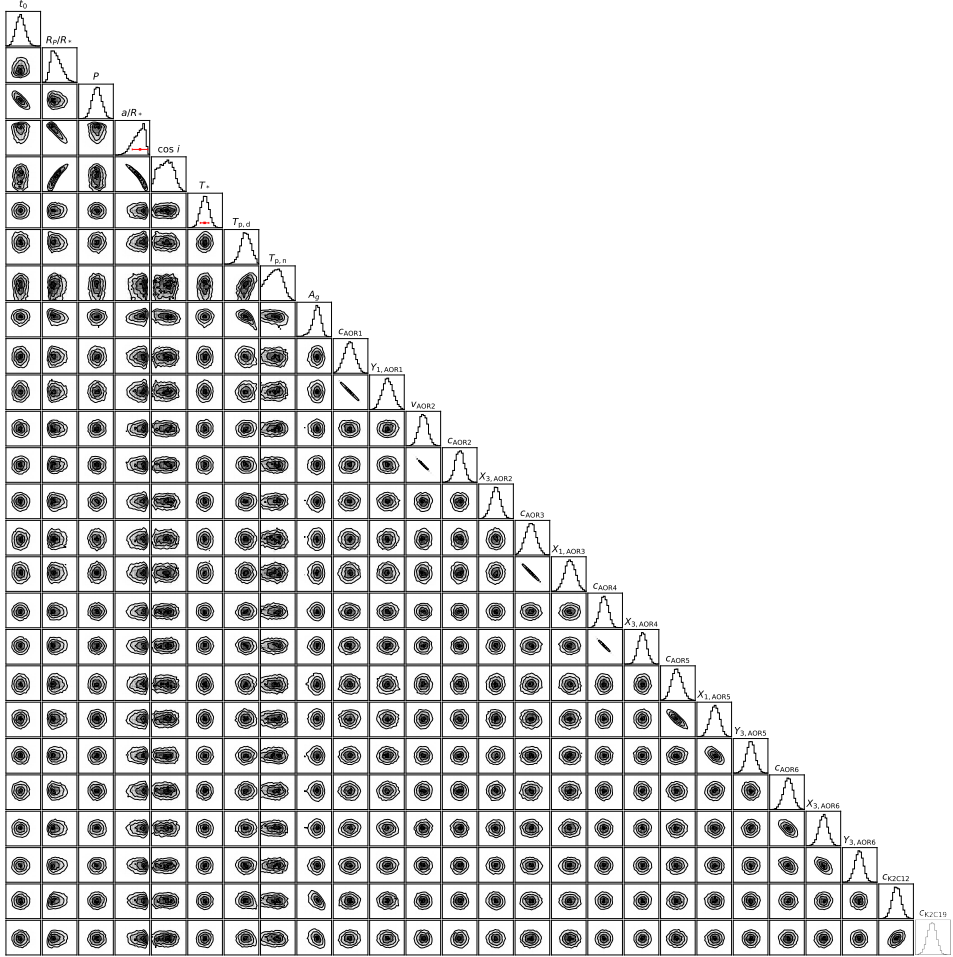


Figure 2.27: MCMC corner plot for the two temperature model fit to the joint dataset, i.e., *Spitzer* and *K2*. The red bars for a/R_* and T_* show the Gaussian priors which were used in this fit. The prior values and the best fit values are listed in Table 2.3.4. The resulting values for the systematic parameters are in Table 2.12. A list with all fit parameters can be found in Table 2.11.

3

PACMAN: A PIPELINE TO REDUCE AND ANALYZE HUBBLE WIDE FIELD CAMERA 3 IR GRISM DATA

Sebastian Zieba and Laura Kreidberg

Published in The Journal of Open Source Software, 2022.

Abstract

The *Hubble Space Telescope* (*HST*) has become the preeminent workhorse facility for the characterization of extrasolar planets. Launched in 1990 and never designed for the observations of exoplanets, the STIS spectrograph on *HST* was used in 2002 to detect the first atmosphere ever discovered on a planet outside of our solar system (Charbonneau et al. 2002).

HST currently has two of the most powerful space-based tools for characterizing exoplanets over a broad spectral range: The Space Telescope Imaging Spectrograph (STIS; installed in 1997) in the UV and the Wide Field Camera 3 (WFC3; installed in 2009) in the Near Infrared (NIR). With the introduction of a spatial scan mode on WFC3 (McCullough & MacKenty 2012; Deming et al. 2012) where the star moves perpendicular to the dispersion direction during an exposure, WFC3 observations have become very efficient due to the reduction of overhead time and the possibility of longer exposures without saturation.

For exoplanet characterization, WFC3 is used for transit and secondary eclipse spectroscopy, and phase curve observations. The instrument has two different grisms: G102 with a spectral range from 800 nm to up to 1150 nm and G141 encompassing 1075 nm to about 1700 nm. The spectral range of WFC3/G141 is primarily sensitive to molecular absorption from water at approximately 1.4 μm . This led to the successful detection of water in the atmosphere of over a dozen of exoplanets (e.g., Deming et al. 2013; Huitson et al. 2013; Fraine et al. 2014; Kreidberg et al. 2014b; Evans et al. 2016). The bluer part of WFC3, the G102 grism, is also sensitive to water and most notably led to the first detection of a helium exosphere (Spake et al. 2018).

Here we present **PACMAN**, an end-to-end pipeline developed to reduce and analyze *HST*/WFC3 data. The pipeline includes both spectral extraction and light curve fitting. The foundation of **PACMAN** has been already used in numerous publications (e.g., Kreidberg et al. 2014a, 2018a) and these papers have already accumulated hundreds of citations.

3.1 Statement of need

Exoplanet spectroscopy with Hubble requires very precise measurements that are beyond the scope of standard analysis tools provided by the Space Telescope Science Institute. The data analysis is challenging, and different pipelines have produced discrepant results in the literature (e.g., Kreidberg et al. 2019b; Teachey & Kipping 2018). To facilitate reproducibility and transparency, the data reduction and analysis software should be open-source. This will enable easy comparison between different pipelines, and also lower the barrier to entry for newcomers in the exoplanet atmosphere field.

What sets **PACMAN** apart from other tools provided by the community, is that it was specifically designed to reduce and fit *HST* data. There are several open-source tools that can fit time series observations of stars to model events like transiting exoplanets, such as **EXOFASTv2** (Eastman et al. 2019), **juliet** (Espinoza et al. 2019), **allesfitter** (Günther & Daylan 2019, 2021), **exoplanet** (Foreman-Mackey et al. 2021b,a), and **starry** (Luger et al. 2019). **PACMAN**'s source code, however, includes fitting models that can model systematics which are characteristic to *HST* data, such as the orbit-long exponential ramps due to charge trapping or the upstream-downstream effect. This removes the need for the user to write these functions themselves. **PACMAN** will also retrieve information from the header of the FITS files, automatically detect *HST* orbits and visits and use this information in the fitting models.

The only other end-to-end open source pipeline specifically developed for the reduction and analysis of *HST*/WFC3 data is **Iraclis**¹ (Tsiaras et al. 2016b). Another open-source pipeline that has been for example used as an independent check of recent results presented in Mugnai et al. (2021) and Carone et al. (2021) is **CASCADE**² (Calibration of trAnsit Spectroscopy using CAusal Data). For a more detailed discussion of **CASCADE** see Appendix 1 in Carone et al. (2021).

3.2 Outline of the pipeline steps

The pipeline starts with the *ima* data products provided by the Space Telescope Science Institute that can be easily accessed from **MAST**³. These files created by the WFC3 calibration pipeline, **calwf3**, have already several calibrations applied (dark subtraction, linearity correction, flat-fielding) to each readout of the IR exposure.

In the following we highlight several steps in the reduction and fitting stages of the code which are typical for *HST*/WFC3 observations:

- **Wavelength calibration:** We create a reference spectrum based on the throughput of the respective grism (G102 or G141) and a stellar model. The user can decide if he or she wants to download a stellar spectrum from **MAST** or use a black body spectrum. This template is used for the wavelength

¹<https://github.com/ucl-exoplanets/Iraclis>

²<https://jbouwman.gitlab.io/CASCADE/>

³<https://mast.stsci.edu/search/hst>

calibration of the WFC3 spectra. We also determine the position of the star in the direct images which are commonly taken at the start of *HST* orbits to create an initial guess for the wavelength solution using the known dispersion of the grism. Using the reference spectrum as a template, we determine a shift and scaling in wavelength-space that minimizes the difference between the template and the first spectrum in the visit. This first exposure in the visit is then used as the template for the following exposures in the visit.

- **Optimal extraction and outlier removal:** PACMAN uses an optimal extraction algorithm as presented in Horne (1986) which iteratively masks bad pixels in the image. We also mask bad pixels that have been flagged by *calwf3* with data quality $DQ = 4$ or 512^4 .
- **Scanning of the detector:** The majority of exoplanetary *HST*/WFC3 observations use the spatial scanning technique (McCullough & MacKenty 2012) which spreads the light perpendicular to the dispersion direction during the exposure enabling longer integration times before saturation. The *ima* files taken in this observation mode consist of a number of nondestructive reads, also known as up-the-ramp samples, each of which we treat as an independent subexposure. Figure 3.1 (left panel) shows an example of the last subexposure when using spatial scanning together with the expected position of the trace based on the direct image.
- **Fitting models:** PACMAN contains several functions to fit models which are commonly used with *HST* data. The user can fit models like in Equation 3.1 to the white light curve or to spectroscopic light curves. An example of a raw spectroscopic light curve and fitting Equation 3.1 to it, can be found in Figure 3.2. Here are some examples of the currently implemented models for the instrument systematics and the astrophysical signal:
 - systematics models:
 - * visit-long polynomials
 - * orbit-long exponential ramps due to charge trapping: NIR detectors like *HST*/WFC3 can trap photoelectrons (Smith et al. 2008), which will cause the number of recorded photoelectrons to increase exponentially, creating typical hook-like features in each orbit
 - astrophysical models:
 - * transit and secondary eclipse curves as implemented in *batman*
 - * sinusoids for phase curve fits
 - * a constant offset that accounts for the upstream-downstream effect (McCullough & MacKenty 2012) caused by forward and reverse scanning

⁴for a list of DQ flags see <https://wfc3tools.readthedocs.io/en/latest/wfc3tools/calwf3.html>

A typical model to fit an exoplanet transit in *HST* data is the following (used, for example, by Kreidberg et al. (2014a)):

$$F(t) = T(t) (c S(t) + k t_v) (1 - \exp(-r_1 t_{\text{orb}} - r_2)), \quad (3.1)$$

with $T(t)$ being the transit model, c (k) a constant (slope), $S(t)$ a scale factor equal to 1 for exposures with spatial scanning in the forward direction, and s for reverse scans, r_1 and r_2 are parameters to account for the exponential ramps. t_v and t_{orb} are the times from the first exposure in the visit and in the orbit, respectively.

- **Parameter estimation:** The user has different options to estimate best fitting parameters and their uncertainties:
 - least squared: `scipy.optimize`
 - MCMC: `emcee` (Foreman-Mackey et al. 2013a)
 - nested sampling: `dynesty` (Speagle 2020)
- **Multi-visit observations**
 - PACMAN has also an option to share parameters across visits.
- **Binning of the light spectrum:** The user can freely specify the bin numbers or locations. Figure 3.1 (right panel) shows the resulting 1D spectrum and a user-defined binning.

Figure 3.1 and 3.2 show some figures created by PACMAN during a run using three *HST* visits of GJ 1214 b collected in GO 13201⁵ (Bean 2012). An analysis of all 15 visits was published in Kreidberg et al. (2014a). The analysis of three visits here using PACMAN, is consistent with the published results.

3.3 Dependencies

PACMAN uses typical dependencies of astrophysical Python codes: `numpy` (Harris et al. 2020), `matplotlib` (Hunter 2007a), `scipy` (Virtanen et al. 2020) and `astropy` (Astropy Collaboration et al. 2013, 2018, 2022). Other dependencies required for the fitting stage depending on the model and sampler being run are: `batman` (Kreidberg 2015), `emcee` (Foreman-Mackey et al. 2013a), `dynesty` (Speagle 2020), and `corner` (Foreman-Mackey 2016). For the barycentric correction, PACMAN accesses the API to JPL’s Horizons system⁶. If the user decides to use a stellar spectrum for the wavelength calibration, PACMAN will download the needed fits file from the “REFERENCE-ATLASES” high level science product⁷ hosted on the MAST archive (STScI Development Team 2013).

⁵https://archive.stsci.edu/proposal_search.php?id=13021&mission=hst

⁶https://ssd-api.jpl.nasa.gov/obsolete/horizons_batch.cgi.html

⁷<https://archive.stsci.edu/hlsps/reference-atlases/cdbs/grid/>

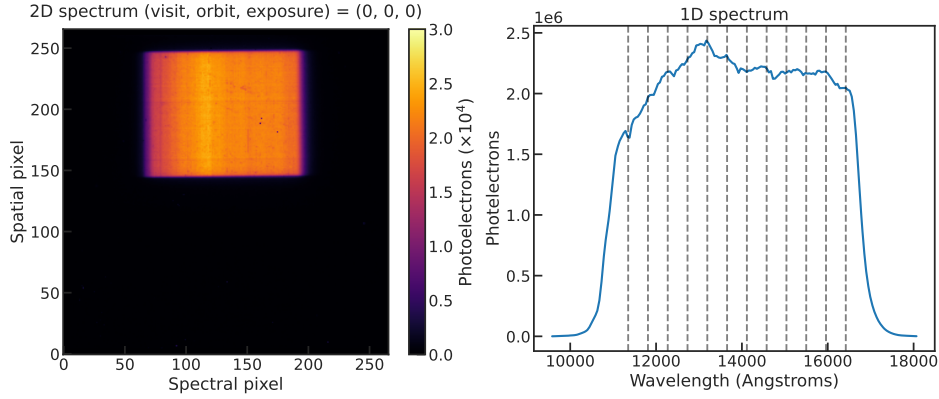


Figure 3.1: *Left panel:* a typical single exposure showing the raw 2D spectrum. *Right panel:* 1D spectrum after the use of optimal extraction including vertical dashed lines showing the user-set binning to generate spectroscopic light curves.

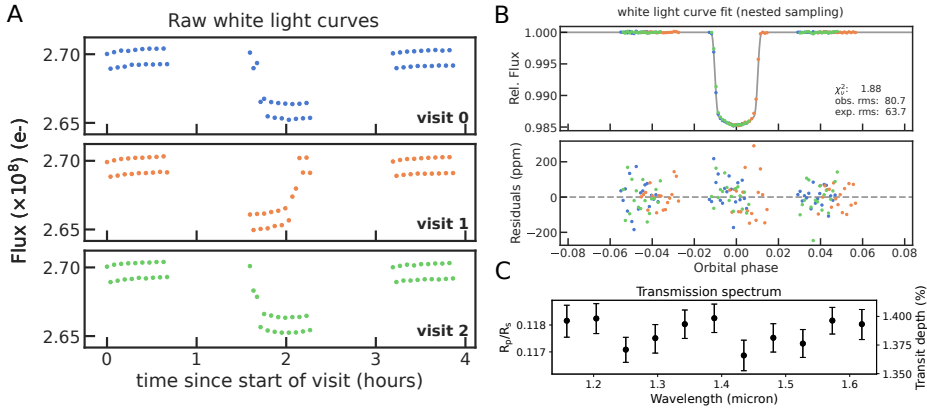


Figure 3.2: *panel A:* raw white light curves for each of the three visits. One can clearly see the constant offset between two adjacent exposures due to the spatial scanning mode. *panel B:* white light curve with the best astrophysical model fit using Equation 3.1. *panel C:* the transmission spectrum after fitting 11 spectroscopic light curves revealing the flat spectrum of GJ 1214 b as published in Kreidberg et al. (2014a).

3.4 Documentation

The documentation for PACMAN can be found at `pacmandocs.readthedocs.io`⁸ hosted on ReadTheDocs⁹. It includes most notably, a full explanation of every parameter in the *pacman control file* (pcf), the API, and an example of how to download, reduce and analyze observations of GJ 1214 b taken with *HST*/WFC3/G141.

3.5 Future work

The following features are planned for future development:

- The addition of fitting models like phase curves using the open-source Python package SPIDERMAN (Louden & Kreidberg 2018).
- Orbit-long ramp fitting using the RECTE systematic model¹⁰.
- Limb darkening calculations for users wanting to fix limb darkening parameters to theoretical models in the fitting stage.
- Extension to WFC3/UVIS data reduction.

Acknowledgements

We acknowledge B. Zawadzki for the creation of the PACMAN logo. We also acknowledge the comments and contributions by I. Momcheva to PACMAN.

⁸<https://pacmandocs.readthedocs.io/en/latest/>

⁹<https://readthedocs.org/>

¹⁰<https://recte.readthedocs.io/en/latest/>

4

NO THICK CARBON DIOXIDE ATMOSPHERE ON THE ROCKY EXOPLANET TRAPPIST-1 C

Sebastian Zieba, Laura Kreidberg, Elsa Ducrot, Michaël Gillon, Caroline Morley, Laura Schaefer, Patrick Tamburo, Daniel D. B. Koll, Xintong Lyu, Lorena Acuña, Eric Agol, Aishwarya R. Iyer, Renyu Hu, Andrew P. Lincowski, Victoria S. Meadows, Franck Selsis, Emeline Bolmont, Avi M. Mandell, and Gabrielle Suissa

Published in Nature, 2023.

Abstract

Seven rocky planets orbit the nearby dwarf star TRAPPIST-1, providing a unique opportunity to search for atmospheres on small planets outside the Solar System (Gillon et al. 2017). Thanks to the recent launch of the James Webb Space Telescope (*JWST*), possible atmospheric constituents such as carbon dioxide (CO_2) are now detectable (Morley et al. 2017; Lincowski et al. 2018). Recent *JWST* observations of the innermost planet TRAPPIST-1 b showed that it is most probably a bare rock without any CO_2 in its atmosphere (Greene et al. 2023). Here we report the detection of thermal emission from the dayside of TRAPPIST-1 c with the Mid-Infrared Instrument (MIRI) on *JWST* at $15\text{ }\mu\text{m}$. We measure a planet-to-star flux ratio of $f_p/f_* = 421 \pm 94$ parts per million (ppm) which corresponds to an inferred dayside brightness temperature of $380 \pm 31\text{ K}$. This high dayside temperature disfavors a thick, CO_2 -rich atmosphere on the planet. The data rule out cloud-free O_2/CO_2 mixtures with surface pressures ranging from 10 bar (with 10 ppm CO_2) to 0.1 bar (pure CO_2). A Venus-analogue atmosphere with sulfuric acid clouds is also disfavoured at 2.6σ confidence. Thinner atmospheres or bare-rock surfaces are consistent with our measured planet-to-star flux ratio. The absence of a thick, CO_2 -rich atmosphere on TRAPPIST-1 c suggests a relatively volatile-poor formation history, with less than $9.5^{+7.5}_{-2.3}$ Earth oceans of water. If all planets in the system formed in the same way, this would indicate a limited reservoir of volatiles for the potentially habitable planets in the system.

4.1 Introduction

Little is known about the compositions of terrestrial exoplanet atmospheres, or even whether atmospheres are present at all. The atmospheric composition depends on many unknown factors, including the initial inventory of volatiles, outgassing resulting from volcanism, and possible atmospheric escape and collapse (see e.g., Wordsworth & Kreidberg 2022). Atmospheric escape may also depend on the spectral type of the host star: planets around M dwarfs may be particularly vulnerable to atmospheric loss during the long pre-main sequence phase (Luger & Barnes 2015). The only way to robustly determine whether a terrestrial exoplanet has an atmosphere is to study it directly, through its thermal emission, reflected light, or transmission spectrum. The tightest constraints on atmospheric properties so far have come from observations of the thermal emission of LHS 3844 b, GJ 1252 b, and TRAPPIST-1 b. The measurements revealed dayside temperatures consistent with no redistribution of heat on the planet and no atmospheric absorption from carbon dioxide (Kreidberg et al. 2019a; Crossfield et al. 2022; Greene et al. 2023). These results motivate observations of cooler planets, which may be more likely to retain atmospheres.

4.2 Observations

We observed four eclipses of TRAPPIST-1 c with MIRI on *JWST* in imaging mode. The observations took place on 27 October, 30 October, 6 November, and 30 November 2022 as part of General Observer programme 2304. Each visit had a duration of approximately 192 minutes, covering the 42-minute eclipse duration of TRAPPIST-1 c as well as out-of-eclipse baseline to correct for instrumental systematic noise. The observations used the MIRI F1500W filter, a 3 μm -wide bandpass centred at 15 μm , which covers a strong absorption feature from CO_2 . Across the four visits, we collected 1,190 integrations in total using the FULL subarray. See Methods for further details on the design of the observations.

4.3 Data reduction and analysis

We performed four independent reductions of the data using the publicly available **Eureka!** code (Bell et al. 2022) as well as several custom software pipelines. Each reduction extracted the light curve of TRAPPIST-1 using aperture photometry (see Methods and Table 4.2). We then fitted the light curves with an eclipse model and a range of different parameterizations for the instrumental systematics, including a polynomial in time, exponential ramps, and decorrelation against the position and width of the point spread function (PSF). For the different analyses, the scatter of the residuals in the fitted light curves had a root mean square (rms) variability ranging from 938 – 1,079 ppm, within 1.06 – 1.22 times the predicted

photon noise limit when using a corrected gain value (Bell et al. 2023a). We estimated the eclipse depths using Markov chain Monte Carlo (MCMC) fits to the data, which marginalized over all the free parameters in the analysis. The resulting eclipse depths from the four data analyses are consistent and agree to well within 1σ (see Table 4.3). The phase-folded light curve from one of the reductions can be seen in Figure 4.1. To determine the final eclipse depth, we took the mean value and uncertainty from the different reductions. To account for systematic error owing to differences in data reduction and modelling choices, we also added an additional 6 ppm to the uncertainty in quadrature, which corresponds to the standard deviation in the eclipse depth between the four analyses. The resulting eclipse depth is $f_p/f_* = 421 \pm 94$ ppm.

4.4 Discussion

From the measured eclipse depth, we derive a brightness temperature of 380 ± 31 K for TRAPPIST-1 c. The innermost planet in the system, TRAPPIST-1 b, was found to have a brightness temperature of 503^{+26}_{-27} K (Greene et al. 2023). Compared with previous detections of thermal emission from small ($R_p < 2 R_\oplus$) rocky planets (see Fig. 4.5) these temperatures are more than 500 K cooler (the previous lowest measured brightness temperature was $1,040 \pm 40$ K for LHS 3844 b (Kreidberg et al. 2019a)). TRAPPIST-1 c is the first exoplanet with measured thermal emission that is comparable with the inner planets of the Solar System; Mercury and Venus have equilibrium temperatures of 440 K and 227 K, respectively, assuming uniform heat redistribution and taking the measured Bond albedo values ($A_{B,\text{Mercury}} = 0.068$, $A_{B,\text{Venus}} = 0.76$) from Moroz et al. (1985); Mallama et al. (2002). Our measured temperature for TRAPPIST-1 c is intermediate between the two limiting cases for the atmospheric circulation for a zero-albedo planet: zero heat redistribution (430 K; expected for a fully absorptive bare rock), versus global heat redistribution (340 K; expected for a thick atmosphere). This intermediate value hints at either a moderate amount of heat redistribution by an atmosphere ($\varepsilon = 0.66^{+0.26}_{-0.33}$) or a non-zero Bond albedo for a rocky surface ($A_B = 0.57^{+0.12}_{-0.15}$) (following the parameterization described in Cowan & Agol (2011)).

4.4.1 Comparison to emission models

To further explore which possible atmospheres are consistent with the data, we compared the dayside flux with a grid of cloud-free, O_2 -dominated models with a range of surface pressures (0.01 bar – 100.0 bar) and CO_2 contents (1 ppm – 10,000 ppm). Also, we generated cloud-free, pure CO_2 atmospheres using the same surface pressures. The models account for both atmospheric heat redistribution and absorption by constituent gasses (Koll et al. 2019a; Morley et al. 2017; Kreidberg et al. 2019a) and assume a Bond albedo of 0.1 (see Methods). O_2/CO_2 mixtures are expected for hot rocky planets orbiting late M-type stars as the planet’s H_2O

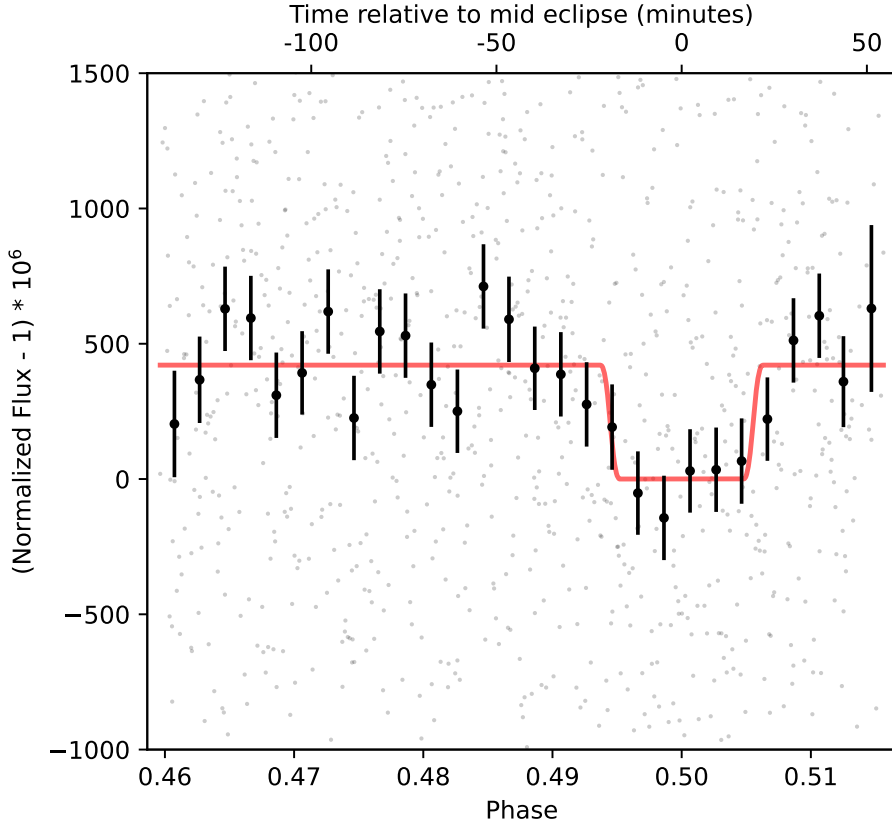


Figure 4.1: Eclipse light curve of TRAPPIST-1 c taken with MIRI F1500W. The phase-folded secondary eclipse light curve of TRAPPIST-1 c, measured with the *JWST*/MIRI imager at 15 μm . The eclipse is centred at orbital phase 0.5 and has a measured depth of $f_p/f_* = 421 \pm 94$ ppm. The light curve includes four visits (that is, four eclipses), each spanning approximately 3.2 hours. To make the eclipse more easily visible, we binned the individual integrations (grey points) into 28 orbital phase bins (black points with 1σ error bars). The light curve was normalized and divided by the best-fit instrument systematic model. The best-fit eclipse model is shown with the solid red line. The data and fit presented in this figure are based on the SZ reduction, one of the four independent reductions we performed in this work.

photodissociates and escapes over time, leaving a desiccated atmosphere dominated by O_2 (Luger & Barnes 2015; Schaefer et al. 2016; Bolmont et al. 2017). Substantial CO_2 (up to about 100 bar) is expected to accumulate from outgassing and does not escape as easily as H_2O (Dorn et al. 2018; Kane et al. 2020). For these mixtures, the predicted eclipse depth decreases with increasing surface pressure and with increasing CO_2 abundance, owing to the strong CO_2 absorption feature centred at 15 μm . Strong inversions for a planet in this parameter space are not expected (Malik et al. 2019a). With our measured eclipse depth, we rule out all thick atmospheres with surface pressures $P_{\text{surf}} \geq 100$ bar (see Fig. 4.2). For the conservative assumption that the CO_2 content is at least 10 ppm, we rule out $P_{\text{surf}} \geq 10$ bar. For cloud-free, pure CO_2 atmospheres we can rule out surface pressures $P_{\text{surf}} \geq 0.1$ bar. As the TRAPPIST-1 planets have precisely measured densities, interior-structure models can give constraints on the atmospheric surface pressures, that is, higher surface pressures would decrease the observed bulk density of the planet. Our findings here agree with these models, which put an upper limit of 160 bar (80 bar) on the surface pressure at a 3σ (1σ) level (Acuña et al. 2021).

We also compared the measured dayside brightness with several physically motivated forward models inspired by Venus. The insolation of TRAPPIST-1 c is just 8% greater than that of Venus (Delrez et al. 2018), so it is possible that the two planets could have similar atmospheric chemistry. We used a coupled climate-photochemistry model to simulate an exact Venus-analogue composition (96.5%, CO_2 3.5% N_2 , and Venus lower atmospheric trace gases), both with and without H_2SO_4 aerosols (Lincowski et al. 2018) (see Methods). The assumed surface pressure was 10 bar, which would produce similar results to a true 93 bar Venus-analogue, because for both cases, the emitting layer and cloud deck lie at similar pressures. We find that these cloudy and cloud-free Venus-like atmospheres are disfavoured at 2.6σ and 3.0σ , respectively (see Fig. 4.3 for the 10 bar cloudy Venus spectrum). The cloudy case is marginally more consistent with the data because the SO_2 aerosols locally warm the atmosphere, providing a warmer emission temperature within the core of the 15 μm band, and therefore a larger secondary eclipse depth.

Finally, we compared the measured flux with bare-rock models with a variety of surface compositions, including basaltic, feldspathic, Fe-oxidized (50% nanophase haematite, 50% basalt), granitoid, metal-rich (FeS_2), and ultramafic compositions (Hu et al. 2012). We also considered space weathering for these models, as TRAPPIST-1 c should have been substantially weathered owing to its proximity to the host star. On the Moon and Mercury, space weathering darkens the surface by means of the formation of iron nanoparticles (Hapke 2001). On TRAPPIST-1 c, this process would similarly darken the surface and therefore increase the eclipse depth. We find that all bare-rock surfaces are consistent with the data (see Fig. 4.3 for an unweathered ultramafic surface and Fig. 4.9 for all surfaces that we considered). Overall, fresh low-albedo surfaces (for example basalt) or weathered surfaces are all compatible with the data, comparable with

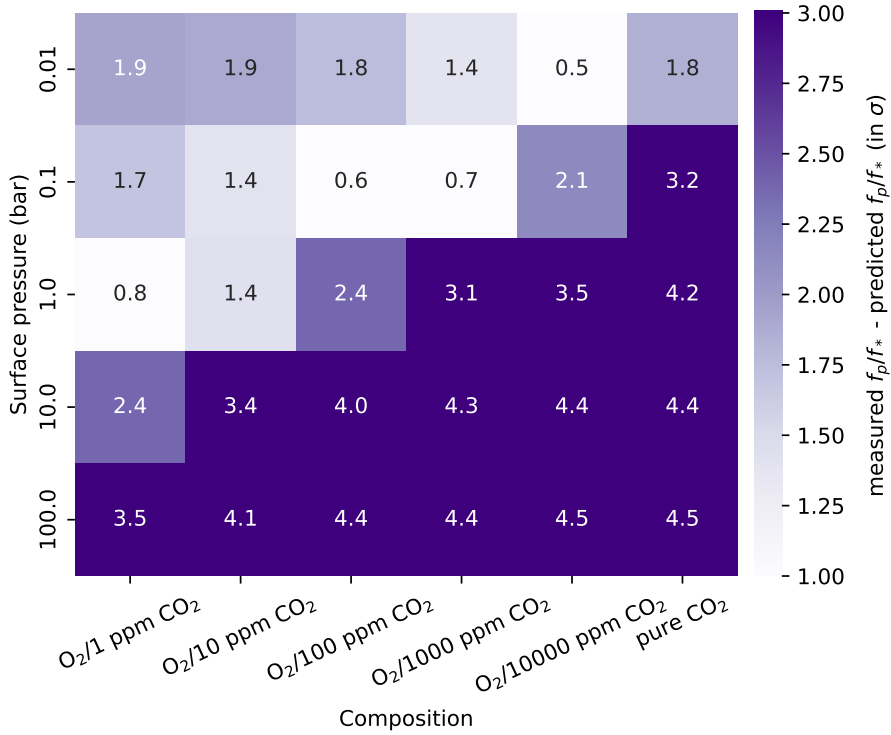


Figure 4.2: Grid plot comparing a suite of atmospheric models to the measured eclipse depth. Comparison between the measured eclipse depth and a suite of different O₂/CO₂, cloud-free atmospheres for TRAPPIST-1 c with varying surface pressures and compositions. Darker grid cells indicate that we more significantly rule out this specific atmospheric scenario. The number in each cell is the absolute difference between each model and the observations in units of sigma. The lower the modelled atmosphere is in the grid, the higher its surface pressure. The rightmost column shows pure CO₂ atmospheres. The other columns are O₂-dominated atmospheres with different amounts of CO₂ ranging from 1 ppm (= 0.0001%) to 10,000 ppm (= 1%).

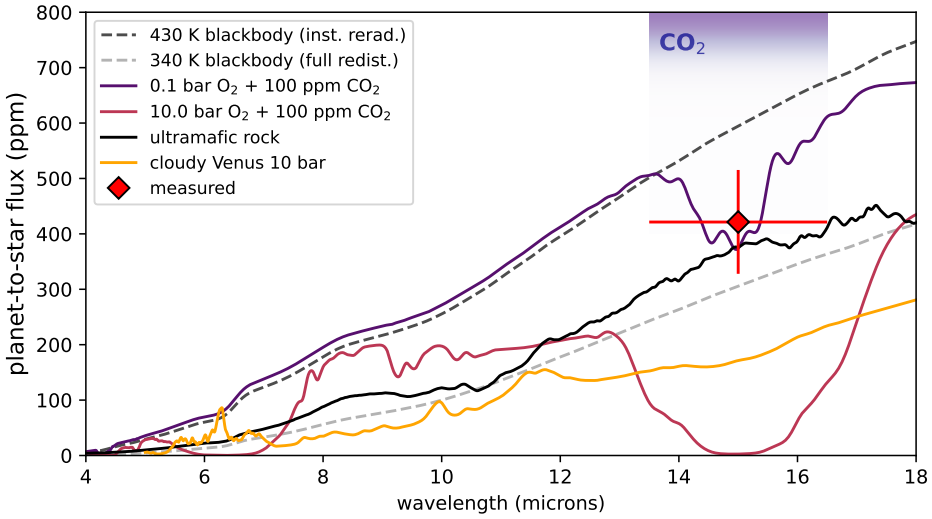


Figure 4.3: Observed flux of TRAPPIST-1 c and various emission models. Simulated emission spectra compared with the measured eclipse depth of TRAPPIST-1 c (red diamond, with the vertical error bar representing the 1σ uncertainty on the measured eclipse depth). The CO_2 feature overlaps directly with the MIRI F1500W filter used for these observations. The two limiting cases for the atmospheric circulation for a zero-albedo planet (zero heat redistribution, that is, instant reradiation of incoming flux and global heat redistribution) are marked with dashed lines. Two cloud-free, O_2/CO_2 mixture atmospheres are shown with purple and red solid lines. They show decreased emission at $15\ \mu\text{m}$ owing to CO_2 absorption. A bare-rock model assuming an unweathered ultramafic surface of the planet with a Bond albedo of 0.5 is shown by the solid black line (see text for more information on weathering, including a full comparison of our measurement to a suite of surfaces in Fig. 4.9). The cloudy Venus forward model with a surface pressure of 10 bars is shown with a solid yellow line.

the likely bare-rock exoplanet LHS 3844 b (Kreidberg et al. 2019a). The highest albedo models, unweathered feldspathic and granitoid surfaces, are a marginally worse fit (consistent at the 2σ level).

4.4.2 Water inventory

To put our results into context with the formation history of the planet, we ran a grid of atmospheric evolution models over a range of initial water inventories ($0.1 - 100$ Earth oceans) and extreme ultraviolet (XUV) saturation fractions for the host star ($10^{-4} - 10^{-2}$) (see Fig. 4.4). The model incorporates outgassing, escape of water vapour and oxygen, and reaction of oxygen with the magma ocean (Schaefer et al. 2016). For an XUV saturation fraction of 10^{-3} being a typical value for a low-mass star (Chadney et al. 2015), we find that the final surface pressure of oxygen could range over several orders of magnitude ($0.1 - 100$ bar),

depending on the initial water inventory (see Fig. 4.4). Our measured eclipse depth disfavours surface pressures at the high end of this range (greater than 100 bar) for conservative CO_2 abundances, implying that TRAPPIST-1 c most likely formed with a relatively low initial water abundance of less than $9.5^{+7.5}_{-2.3}$ Earth oceans. For higher CO_2 abundances (> 10 ppm), we rule out surface pressures greater than 10 bars, implying that the planet formed with less than $4^{+1.3}_{-0.8}$ Earth oceans. Our result suggests that rocky planets around M-dwarf stars may form with a smaller volatile inventory or experience more atmospheric loss than their counterparts around Sun-like stars. This finding motivates further study of the other planets in the TRAPPIST-1 system to assess whether a low volatile abundance is a typical outcome, particularly for the planets in the habitable zone.

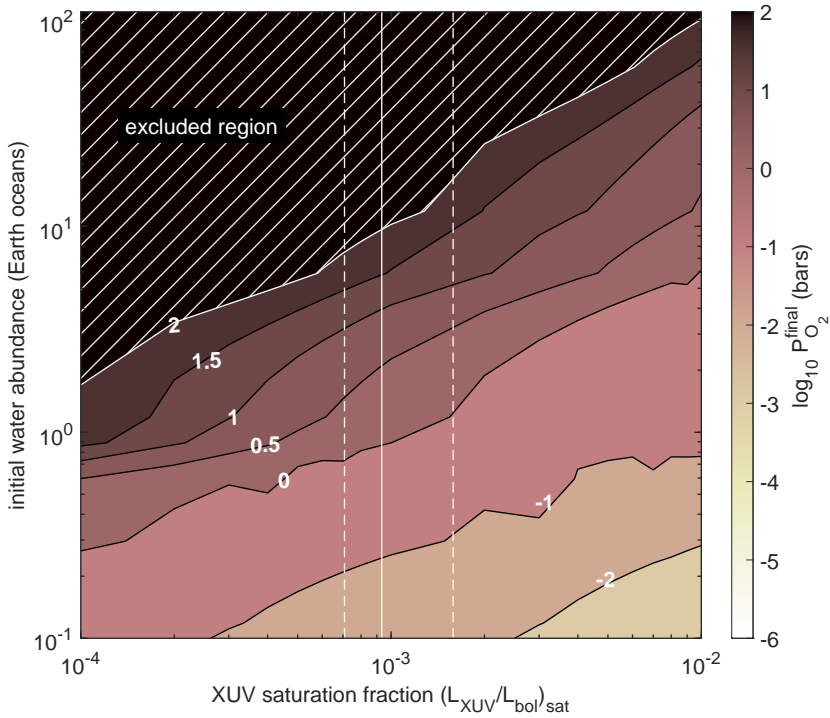


Figure 4.4: Final oxygen atmospheric pressure for TRAPPIST-1 c after 7.5 Gyr of energy-limited escape. We explore different initial planetary water abundances and the amount of XUV the planet receives during the star’s saturated activity period (Luger & Barnes 2015), described as a fraction of its total bolometric luminosity. The vertical lines represent the nominal XUV saturation fraction of $\log_{10}(L_{\text{XUV}}/L_{\text{bol}}) = -3.03^{+0.23}_{-0.12}$ as estimated by Fleming et al. (2020). We assume an escape efficiency of 0.1. The white numbers are the contour values for the logarithm of the atmospheric pressure in bars. Our upper limit on surface pressure of 10 – 100 bars implies an initial water abundance of approximately 4 – 10 Earth oceans.

Appendix

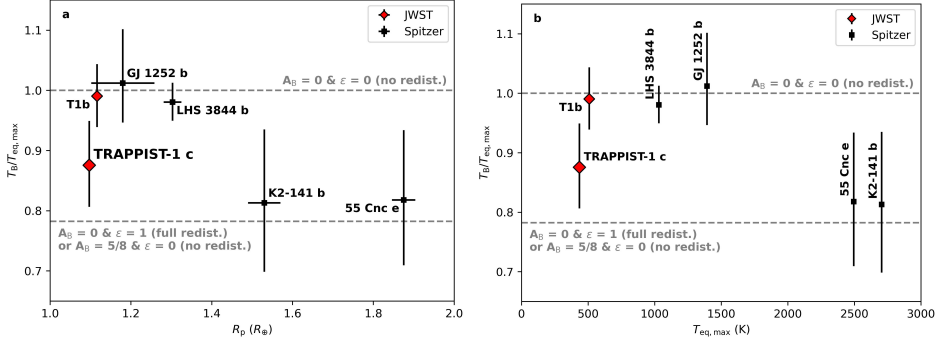


Figure 4.5: Comparison of small exoplanets with measured infrared emission. Following Crossfield et al. (2022), we show the normalized dayside brightness temperature for super-Earths ($R_p < 2R_\oplus$) with measured thermal emission, as a function of planet size (a) and maximum equilibrium temperature (b). The brightness temperatures are normalized relative to predictions for a bare rock with zero albedo and zero heat redistribution, $T_{\text{eq,max}}$. The thermal emission of TRAPPIST-1c has been detected in this work at $15\ \mu\text{m}$. The other planets are TRAPPIST-1b (T1b in plot; also at $15\ \mu\text{m}$) and planets that have been observed with *Spitzer*’s IRAC Channel 2 at $4.5\ \mu\text{m}$. The uncertainties on the radius for the planets in the TRAPPIST-1 system are smaller than the marker symbol. Error bars show 1σ uncertainties.

Table 4.1: Summary of the observations in JWST program GO 2304.

	visit 1	visit 2	visit 3	visit 4
date	27. Oct. 2022	30. Oct. 2022	6. Nov. 2022	30. Nov. 2022
start time	14:08:35	00:09:07	06:32:33	11:49:52
end time	17:21:29	03:21:23	09:44:49	15:02:47
duration (hours)	3.21	3.19	3.19	3.21
Nint	298	297	297	298
Nggroups/int	13	13	13	13
stability rms x (pixel)	0.0032	0.0040	0.0034	0.0031
stability rms y (pixel)	0.0059	0.0074	0.0062	0.0051

4.A JWST MIRI Observations

As part of JWST General Observer (GO) program 2304 (principal investigator (PI): L. Kreidberg) (Kreidberg et al. 2021a), we observed four eclipses of the planet TRAPPIST-1c (see Table 4.1). They were taken on 25 October, 27 October, 30

October, and 6 November 2022 with *JWST*’s MIRI instrument using the F1500W filter. The observations used the FULL subarray with FASTR1 readout and 13 groups per integration. Each visit had a duration of approximately 3.2 hours. We did not perform target acquisition for any of the visits because it was not enabled for MIRI imaging observations during cycle 1. However, the blind pointing precision of *JWST* was perfectly sufficient to place the target well centered on the field of view of the full array (74" x 113"). Figure 4.6 shows one of the integrations with the FULL array.

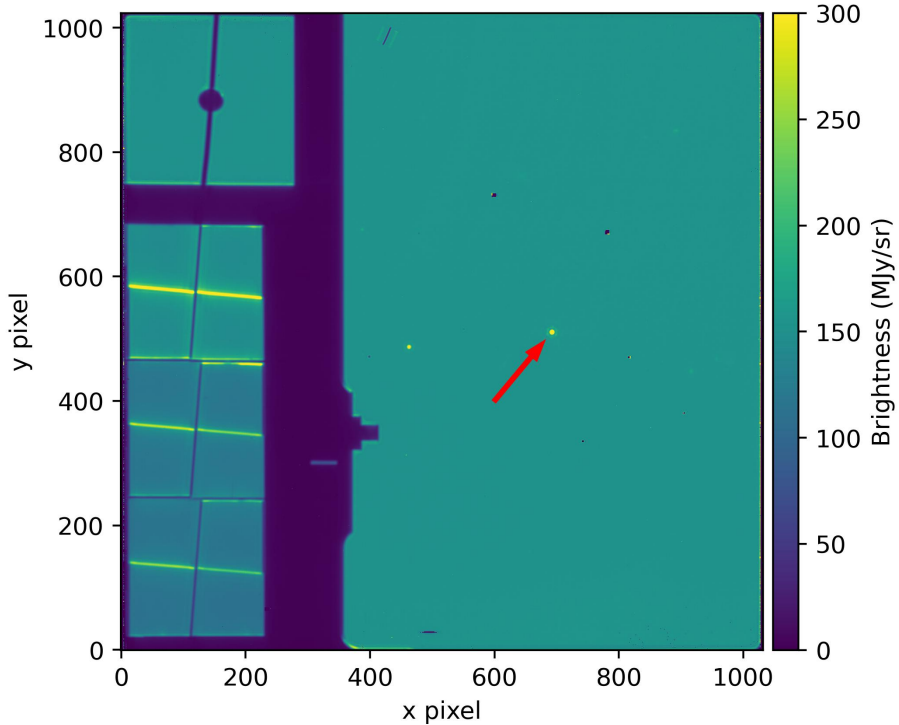


Figure 4.6: Example of a MIRI integration using the FULL array. An integration taken during our observations showing the MIRI imager focal plane. The majority of the FULL array is taken up by the imager field of view on the right side. TRAPPIST-1 is centred on the imager highlighted by the red arrow. The left side of the imager was not used in our analysis and consists out of the Lyot coronagraph (top left) and the three 4-quadrant phase masks coronagraphs (lower left).

4.B Data Reduction

We performed four different reductions of the data collected for *JWST* program GO 2304. The assumptions made by the reductions are listed in Table 4.2. In the following, we describe the individual reductions.

Table 4.2: Details of the four different data reductions.

Step/Parameter	SZ reduction	ED reduction	MG reduction	PT reduction
Stage 1 Run?	Yes	Yes	Yes	-
Jump correction	Jump rejection threshold of 7.0, 6.0, 7.0, 5.0 sigma	No jump correction	No jump correction	-
ramp weighting	default	uniform	uniform	-
Stage 2 Run?	Yes	Yes	Yes	-
photom step	skipped	skipped	skipped	-
Stage 3 notes	-	-	-	Used Calibration Level 2 data directly from MAST
centroid position determination method	2D Gaussian fit to target	2D Gaussian fit to target	2D Gaussian fit to target	2D Gaussian fit to target
target aperture shape	circle	circle	circle	circle
aperture radius	4.0, 4.0, 4.0, 4.0 pixels around the centroid	3.7, 4.0, 3.6, 3.8 pixels around the centroid	3.6, 3.6, 3.5, 3.4 pixels around the centroid	4.4, 4.1, 3.9, 3.5 pixels around the centroid
partial pixels treatment	pixels were supersampled using a bilinear interpolation	pixels were supersampled using a bilinear interpolation	used daophot/phot routine in IRAF ^a	-
background region shape	annulus around the centroid	annulus around the centroid	annulus around the centroid	annulus around the centroid
background aperture size	25 – 41 for each visit	20 – 35 for each visit	20 – 35 for each visit	30 – 45 for each visit
background subtraction method	subtracted the median calculated within the annulus from the whole frame	subtracted the median calculated within the annulus from the whole frame	Computation of the mode of the sky pixel distribution using the mean and median, after 3-sigma clipping of outliers.	mean of sigma-clipped pixel values within the annulus was subtracted from the whole frame (4-sigma clipping threshold)

Table 4.2: Continued.

Details of outlier rejection/ time series clipping	No outliers removed with sigma clipping. First 10 integrations removed	sigma clipping set to 4, no exposure removed	5-Sigma clipping with 20-min moving median. 5, 14, 6, and 4 integrations removed	No outliers removed with sigma clipping. First exposure removed from each visit
---	---	---	--	--

Notes. ^asee <https://iraf.net/irafdocs/apspec.pdf>, page 15

Table 4.3: Details of the four data analyses. See Methods for more details on the individual fits. The uncertainties on the eclipse depth f_p/f_* are 1σ .

Step/Parameter	SZ reduction	ED reduction	MG reduction	PT reduction
Fitting method	emcee (MCMC)	trafit (MCMC-MH)	trafit (MCMC-MH)	emcee (MCMC)
Details for fitting method	150,000 steps, 128 walkers, 30,000 as burn-in. Ran sampler for 80 times the autocorrelation length	1 chain of 50,000 steps for error correction followed by 2 chains of 100,000 steps	2 chains of 100,000 steps, with first 20% of chains as burn-in. Convergence checked with Gelman-Rubin statistical test.	50,000 steps, 64 walkers, 5,000 as burn-in
total number of free parameters in the joint fit	32	35	33	18
number of free systematic parameters	14 (in time) + 8 (decorr.) + 4 (uncertainty multiplier)	14 (in time) + 11 (decorr.)	12 (in time) + 5 (decorr.)	11 (in time)
number of free astrophysical parameters	6 ($4 f_p/f_*, e, \omega$)	10 ($f_p/f_*, b, 4$ TTVs, $M_*, R_*, T_{\text{eff}}, [\text{Fe}/\text{H}]$)	16 ($f_p/f_*, 7$ TTVs, $\log \rho_*, \log M_*, T_{\text{eff}}, [\text{Fe}/\text{H}], \cos i, (R_p/R_*)^2, \sqrt{e} \cos \omega, \sqrt{e} \sin \omega$)	7 ($f_p/f_*, P_{\text{orb}}, i, a/R_*, e, \omega, t_{\text{sec}}$)
rms of joint fit residuals	1020 ppm	961 ppm	938 ppm	1079 ppm
f_p/f_*	431^{+97}_{-96} ppm	423^{+97}_{-95} ppm	414 ± 91 ppm	418^{+90}_{-91} ppm

4.B.1 Data Reduction SZ

For our primary data reduction and data analysis we used the open-source **Python** package **Eureka!** (Bell et al. 2022) which is an end-to-end pipeline for time series observations performed with *JWST* or the *Hubble Space Telescope (HST)*. We started our reduction with the raw uncalibrated (“uncal”) FITS files which we downloaded from the Mikulski Archive for Space Telescopes (MAST) and followed the multi-stage approach of **Eureka!** to generate a light curve for TRAPPIST-1 c. **Eureka!** has been previously successfully used to reduce and analyse the first *JWST* observations of exoplanets (JWST Transiting Exoplanet Community Early Release Science Team et al. 2023; Ahrer et al. 2023; Alderson et al. 2023; Rustamkulov et al. 2023; Lustig-Yaeger et al. 2023).

Stages 1 and 2 of **Eureka!** serve as a wrapper of the **jwst pipeline** (Bushouse et al. 2022) (version 1.8.2.). Stage 1 converts groups to slopes and applies basic detector-level corrections. We used the default settings for all steps in this stage but determined a custom ramp-jump detection threshold for each visit by minimizing the median absolute deviation (MAD) of the final light curves. This step detects jumps in the up-the-ramp signal for each pixel by looking for outliers in each integration that might be caused by events such as cosmic rays. We determined a best jump detection threshold of 7σ , 6σ , 7σ and 5σ for visits 1, 2, 3, and 4, respectively, compared with the default value of 4σ set in the **jwst pipeline**. In stage 2, we only skipped the **photom** step to leave the data in units of DN/s and not convert into absolute fluxes. In stage 3 of **Eureka!**, we first masked pixels in each visit that were flagged with an “DO NOT USE” data quality entry, indicating bad pixels identified by the *JWST* pipeline. Next, we determined the centroid position of the star by fitting a 2D Gaussian to the source. *JWST* remained very stable during our observations of TRAPPIST-1 c and our target stayed well within a 0.01-pixel area (see Table 4.1 and Fig. 4.7). We recorded the centroid position in x and y and the width of the 2D Gaussian in x and y over time to be used in the fitting stage. Next, we determined the best target and background apertures by minimizing the rms of the final light curve. We therefore determined a target aperture of 4 pixels and a background annulus from 25 to 41 pixels from the centroid for each visit. The light curves show a ramp-like trend at the beginning of the observations, which has already been observed in previous *JWST* MIRI observations and is most likely caused by charge trapping (see, for example, Bell et al. 2023a). We decided to remove the first 10 integrations from each visit, corresponding to approximately 6 minutes or 3% of the data per visit, so that we do not have to also model this initial ramp. Finally, we checked for significant outliers in the final light curves by performing an iterative 5σ outlier clipping procedure. However, no integrations were removed during this process, leaving us with 288, 287, 287, and 288 integrations for the four visits, respectively.

4.B.2 Data Reduction ED

For the second data reduction, we also used the **Eureka!** pipeline (Bell et al. 2022) for stages 1 to 5. We also started from the uncal.fits files and used the default **jwst pipeline** settings with the exception of the ramp-fitting weighting

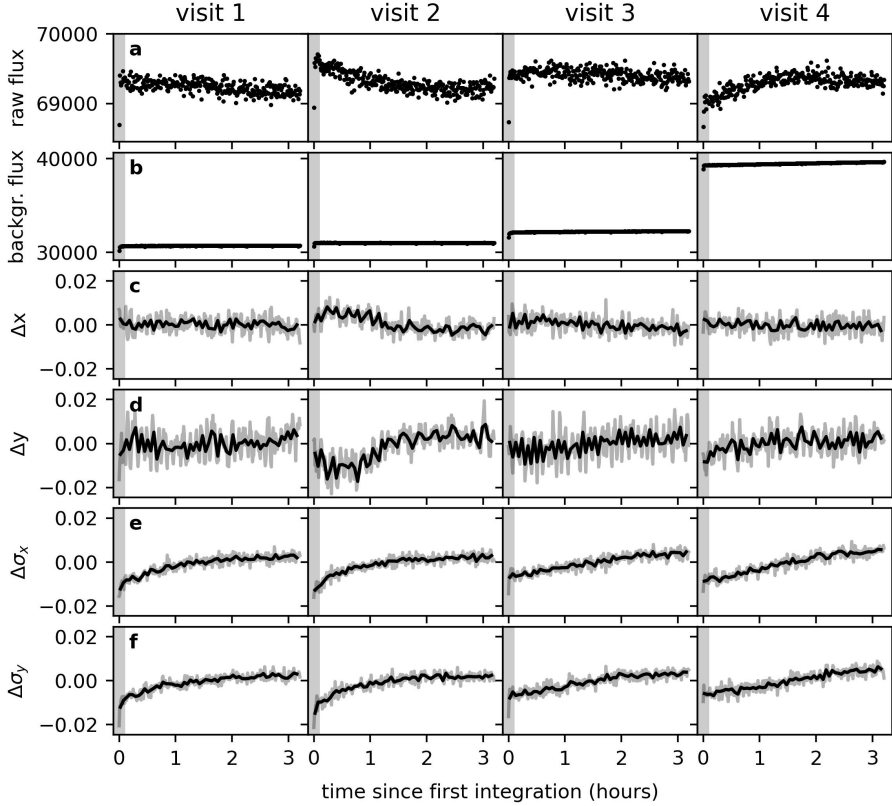


Figure 4.7: Diagnostic plot of all four visits taken during *JWST* program GO 2304 based on the SZ reduction. Every column corresponds to a visit. **a** and **b**. The top and second rows show the raw and background flux in units of electrons per integration per pixel, respectively. The raw flux is referring to the flux level within the target aperture before the subtraction of the background flux. **c** – **f**. The following rows are depicting the properties of the centroid over time. We fitted a 2D Gaussian distribution to the target at every integration to determine its x and y positions on the detector. $\Delta\sigma_x$ and $\Delta\sigma_y$ describe change in the width of the 2D Gaussian with time. The integrations were taken approximately every 40 seconds. The lower four rows were additionally binned to 5 minutes (= 8 integrations) shown with the solid black lines. Due to stronger systematics, we excluded the first 10 integrations in the SZ reduction shown by the grey region at the beginning of each visit.

parameters in stage 1 that we set to uniform instead of default, as it slightly improved the rms of our residuals. This improvement can be explained by the fact that the default ramp-fitting algorithm uses a weighting of the ramp that gives additional weight to the first and last groups of the ramp, which can be problematic when the number of groups is small, such as for TRAPPIST-1 c (only 13 groups). Indeed, the first and last groups can be affected by effects such as the reset switch charge decay or saturation. Thus, to ensure that we fit the ramp correctly, we used an unweighted algorithm that applies the same weight to all groups. Furthermore, in stage 2 we turned off the `photom` step. Then, in stage 3, we defined a subarray region ([632, 752],[450, 570]), masked the pixels flagged in the DQ array, interpolated bad pixels and performed aperture photometry on the star with an aperture size that minimized the rms of the residuals for each visits. For each integration, we recorded the centre and width of the PSF in the x and y directions after fitting a 2D Gaussian. We computed the background on an annulus of 20 to 35 pixel (centred on the target) and subtracted it. We note that the choice of the background annulus has little impact on the light curve. We did not remove any integrations a priori but, in stage 4 we sigma clipped 4σ outliers compared with the median flux calculated using a 10-integrations-width boxcar filter. Then, for each visit for aperture photometry, we chose the aperture radius that led to the smaller rms. These radii were 3.7, 4.0, 3.6, and 3.8 pixels, respectively (see Table 4.2).

4.B.3 Data Reduction MG

We reduced the data using the following methodology. Starting from the `uncal.fits` files, we calibrated them using the two first stages of the **Eureka!** pipeline (Bell et al. 2022). We performed a systematic exploration of all the combinations of all **Eureka!** stage 1 options, and we selected the combination resulting in the most precise light curves. Our selected combination corresponds to the default **jwst pipeline** settings, except for (1) the ramp-fitting weighting parameter set to uniform, and (2) the deactivation of the jump correction. The rest of the reduction was done using a pipeline coded in **IRAF** and **Fortran 2003**. It included for each calibrated image (1) a change of unit from MJy/sr to recorded electrons, (2) the fit of a 2D Gaussian function on the profile of the star to measure the subpixel position of its centroid and its full width at half maximum (FWHM) in both directions, and (3) the measurement of the stellar and background fluxes using circular and annular apertures, respectively, with **IRAF/DAOPHOT** (Stetson 1987). Finally, the resulting light curves were normalized and outliers were discarded from them using a 5σ clipping with 20-min moving median algorithm. For each visit, the radius of the circular aperture used to measure the stellar flux was optimized by minimizing the standard deviation of the residuals. For each stellar flux measurement, the corresponding error was computed taking into account the star and background photon noise, the readout noise, and the dark noise, and assuming a value of 3.1 el/ADU for the gain (E. Ducrot, private communication). See Table 4.2 for more details.

4.B.4 Data Reduction PT

We performed an additional analysis using the level 2 (flux-calibrated) “calints” science products as processed by the Space Telescope Science Institute and hosted on the MAST archive. We determined centroid positions and average seeing FWHM values in the x and y dimensions with a 2D Gaussian fit to the star. We performed fixed-aperture photometry with circular apertures centred on the source centroids, with radii ranging from 3.2–5.0 pixels in 0.1-pixel increments. We also performed variable-aperture photometry using circular apertures with radii set to c times a smoothed time series of the measured FWHM values, where c ranged from 0.75–1.25 in increments of 0.05. We smoothed the FWHM values using a 1D Gaussian kernel with a standard deviation of 2. For both fixed-aperture and variable-aperture photometry, we measured the background using a circular annulus with an inner radius of 30 pixels and an outer radius of 45 pixels. We subtracted the sigma-clipped mean of the pixel values within this annulus from the source counts in each frame, using a clipping level of 4σ . Finally, we recorded the values of a grid of background-subtracted pixels interior to the average photometric aperture size surrounding the source centroid in each frame. We used normalized time series of these pixel values to test whether pixel-level decorrelation (PLD) methods developed for minimizing intrapixel effects in *Spitzer Space Telescope* data (Deming et al. 2015) are warranted in the analysis of *JWST*/MIRI time-series data.

We excluded the first integration of each visit from our analysis as the measured source flux in this exposure was found to be significantly lower than the remainder of the time series for each of the four visits. We checked for outliers in each visit by performing sigma clipping with a threshold of 4σ , but no exposures were flagged with this step. We then selected the aperture size and method (fixed or variable) that minimized the out-of-eclipse scatter for each visit for use in our analysis. We found that fixed-aperture photometry provided the best performance in each case, with optimal radii of 4.4, 4.1, 3.9, and 3.5 pixels for the four visits, respectively.

4.C Data Analysis

We fitted each of the reductions to extract an eclipse depth value. The different assumptions for the four global fits are listed in Table 4.3.

4.C.1 Data Analysis SZ

We fitted the eclipse light curve using the open-source python MCMC sampling routine **emcee** (Foreman-Mackey et al. 2013b). Our full fitting model, $F(t)$, was the product of a **batman** (Kreidberg 2015) eclipse model, $F_{\text{eclipse}}(t)$ and a systematic model, $F_{\text{sys}}(t)$. We fit the systematics of *JWST* with a model of the following form:

$$F_{\text{sys}}(t) = F_{\text{polynom}}(t) F_x(t) F_y(t) F_{\sigma_x}(t) F_{\sigma_y}(t), \quad (4.1)$$

where F_{polynom} is a polynomial in time and $F_x(t)$, $F_y(t)$, $F_{\sigma_x}(t)$, and $F_{\sigma_y}(t)$ detrend the light curve against a time series of the centroid in x and y and the width of

the PSF in x and y , respectively. Before fitting the full light curve consistent out of the four visits, we first determined the best systematic model for each visit by minimizing the Bayesian Information Criterion (BIC) (Schwarz 1978; Kass & Raftery 1995; Liddle 2007). We tried a range of polynomials ranging from zeroth order to third order and detrended for the shift in x - and y -pixel positions or for the change in the width of the PSF in time. The best final combination of polynomials and detrending parameters for each visit are listed in Table 4.3. Our eclipse model used the predicted transit times from Agol et al. (2021) which accounts for the transit-timing variations (TTVs) in the system and we allowed for a non-zero eccentricity. We also accounted for the light travel time, which is approximately 16 seconds for TRAPPIST-1 c, that is, its semi-major-axis is about 8 light-seconds. We fixed the other parameters of the planet and system, such as the ratio of the semi-major axis to stellar radius a/R_* , the ratio of the planetary radius to stellar radius R_p/R_* , and the inclination i , to the values reported in Agol et al. (2021). We decided to also supersample the light curve by a factor of 5 in our fitting routine because the sampling of the data (\approx every 40 seconds) is comparable with the ingress/egress duration of 200 seconds (Agol et al. 2021). Our global fit consisted of 32 free parameters: 6 physical (the eccentricity, the argument of periastron, and an eclipse depth for each visit), 22 parameters to fit for the systematics, and 4 free parameters that inflated the uncertainties in the flux for each visit. These four free parameters are necessary because the current gain value on the Calibration References Data System (CRDS) has been empirically shown to be wrong for MIRI data (Bell et al. 2023a). For our global MCMC, we used 128 walkers (= 4 times the number of free parameters), 150,000 steps, and discarded the first 20% of steps (= 30,000 steps) as burn-in. This corresponds to approximately 80 times the autocorrelation length. After calculating a weighted average of the four eclipse depths, we get an eclipse depth of $f_p/f_* = 431^{+97}_{-96}$ ppm for this reduction. Figure 4.8 shows the Allan deviation plots of the residuals for each of the visits and the global fit. The rms of the residuals as a function of bin size follows the inverse square root law, which is expected for Gaussian noise.

4.C.2 Data Analysis ED

Once we obtained the light curve for each visit from stage 4 of the **Eureka!** pipeline we used the **Fortran** code **trafit** which is an updated version of the adaptive MCMC code described in Gillon et al. (2010, 2012, 2014). It uses the eclipse model of Mandel & Agol (2002) as a photometric time series, multiplied by a baseline model to represent the other astrophysical and instrumental systematics that could produce photometric variations. First, we fit all visits individually. We tested a large range of baseline models to account for different types of external sources of flux variations/modulations (instrumental and stellar effects). This includes polynomials of variable orders in time, background, PSF position on the detector (x , y) and PSF width (in x and y). Once the baseline was chosen, we ran a preliminary analysis with one Markov chain of 50,000 steps to evaluate the need for rescaling the photometric errors through the consideration of a potential underestimation or overestimation of the white noise of each measurement and

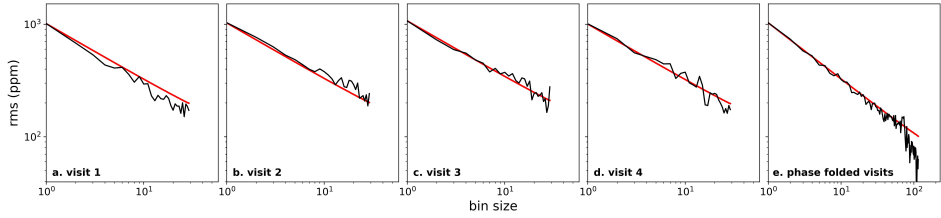


Figure 4.8: Allan deviation plots. a – d. Allan deviation plots of the individual visits: root-mean-square (rms) of the best-fit residuals from data reduction SZ as a function of the number of data points per bin shown in black. **e.** The same, but for the combined dataset. A bin size value of one corresponds to no binning. The red line shows the expected behaviour if the residuals are dominated by Gaussian noise. The absolute slope of this line is $1/\sqrt{\text{bin size}}$, following the inverse square root. The rms of our residuals closely follow this line, showing that our residuals are consistent with uncorrelated photon shot noise.

the presence of time-correlated (red) noise in the light curve. After rescaling the photometric errors, we ran two Markov chains of 100,000 steps each to sample the probability density functions of the parameters of the model and the physical parameters of the system, and assessed the convergence of the MCMC analysis with the Gelman & Rubin statistical test (Gelman & Rubin 1992). For each individual analysis, we used the following jump parameters with normal distributions: M_* , R_* , $T_{\text{eff},*}$, $[\text{Fe}/\text{H}]$, t_0 , b all priors were taken from Ducrot et al. (2020) except for the transit timings, which were derived from the dynamical model predictions by Agol et al. (2021). We fixed P , i and e to the literature values given in Ducrot et al. (2020); Agol et al. (2021). The eclipse depth that we computed for each visit individually were 445 ± 193 ppm, 418 ± 173 ppm, 474 ± 158 ppm, and 459 ± 185 ppm, respectively.

We then performed a global analysis with all four visits, using the baseline models derived from our individual fits for each light curve. Again, we performed a preliminary run of one chain of 50,000 steps to estimate the correction factors that we then apply to the photometric error bars and then a second run with two chains of 100,000 steps. The jump parameters were the same as for the individual fits except for the fact that we fixed t_0 and allowed for transit timing variations (TTV) to happen for each visit (each transit TTV has an unconstrained uniform prior). We used the Gelman & Rubin statistic to assess the convergence of the fit. We measure an eclipse depth of 423^{+97}_{-95} ppm from this joint fit.

4.C.3 Data Analysis MG

Our data-analysis methodology was the same as that used by ED, that is, we used the **Fortran** 2003 code **trafit** to perform a global analysis of the four light curves, adopting the Metropolis-Hasting MCMC algorithm to sample posterior probability distributions of the system’s parameters. Here too, we tested for each light curve a large range of baseline models, and we adopted the ones minimizing the BIC. They were (1) a linear polynomial of time for the first visit, (2) a cubic

polynomial of time and a linear polynomial of the y position for the second visit, (3) a linear polynomial of time and of the x position for the third visit, and (4) a cubic polynomial of time and of the y position for the fourth visit. We also performed a preliminary analysis (composed of one Markov Chain of 10,000 steps) to assess the need to rescale the photometric errors for white and red noise. We then performed two chains of 500,000 steps each (with the first 20% as burn-in). The convergence of the analysis was checked using the Gelman & Rubin statistical test (Gelman & Rubin 1992). The jump parameters of the analysis, that is, the parameters perturbed at each step of the MCMC chains, were (1) for the star, the logarithm of the mass, the logarithm of the density, the effective temperature, and the metallicity, and (2) for the planet, the planet-to-star radius ratio, the occultation depth, the cosinus of the orbital inclination, the orbital parameters $\sqrt{e} \cos \omega$ and $\sqrt{e} \sin \omega$ (with e the orbital eccentricity and ω the argument of pericentre), and the timings of the transits adjacent to each visit. We assumed normal prior distributions for the following parameters based on the results from reference Agol et al. (2021): $M_* = 0.0898 \pm 0.023$, $R_* = 0.1192 \pm 0.0013$, $T_{\text{eff}} = 2566 \pm 26$ K, and $[\text{Fe}/\text{H}] = 0.05 \pm 0.09$ for the star; $(R_p/R_*)^2 = 7123 \pm 65$ ppm, $b = 0.11 \pm 0.06$, $e = 0 + 0.003$ (semi-gaussian distribution) for the planet. We also tested the assumption of a circular orbit and obtained similar results. For each visit, we considered for the timings of the two adjacent transits normal prior distributions based on the predictions of the dynamical model of reference Agol et al. (2021). At each step of the MCMC, the orbital position of the planet could then be computed for each time of observation from the timings of the two adjacent transits and from e and ω , and taking into account the approximately 16s of light-travel time between occultation and transit. This analysis led to the value of 414 ± 91 ppm for the occultation, and to an orbital eccentricity of $0.0016^{+0.0015}_{-0.0008}$ consistent with a circular orbit. Under the assumption of a circular orbit, our analysis led to an occultation depth of 397 ± 92 ppm, in excellent agreement with the result of the analysis assuming an eccentric orbit.

We also performed a similar global analysis, but allowing for different occultation depths for each visit. The resulting depths were 400 ± 163 ppm, 374 ± 184 ppm, 421 ± 187 ppm, and 403 ± 202 ppm, i.e. they were consistent with a stable thermal emission of the planet's dayside (at this level of precision). Similar to data reduction SZ, we also did create Allan deviation plots for this particular data reduction. The best-fit residuals as a function of bin size from each visit do generally follow the inverse square root law (see Fig. 4.8 for the Allan deviation plots of data reduction SZ).

Finally, we computed the brightness temperature of the planet at $15 \mu\text{m}$ from our measured occultation depth using the following methodology. We measured the absolute flux density of the star in all the calibrated images, using an aperture of 25 pixels large enough to encompass the wings of its PSF. We converted these flux densities from MJy/sr to mJy, and computed the mean value of 2.559 mJy and the standard deviation of 0.016 mJy. We added quadratically to this error of around 0.6% a systematic error of 3%, which corresponds to the estimated absolute photometric precision of MIRI (P.-O. Lagage, private communication). It resulted in a total error of 0.079 mJy. Multiplying the measured flux density

by our measured occultation depth led to a planetary flux density of 1.06 ± 0.23 μJy . Multiplying again this result by the square of the ratio of the distance of the system and the planet's radius, and dividing by π , led to the mean surface brightness of the planet's dayside. Applying Planck's law, we then computed the brightness temperature of the planet, while its error was obtained from a classical error propagation. Our result, for this specific reduction, was 379 ± 30 K, to be compared with an equilibrium temperature of 433 K computed for a null-albedo planet with no heat distribution to the nightside.

It is also worth mentioning that applying the same computation on the star itself led to a brightness temperature of 1867 ± 55 K, which is significantly lower than its effective temperature.

4.C.4 Data Analysis PT

We began our analysis by determining which time-series regressors (if any) should be included for fitting systematics in the photometry on the basis of the BIC. Our total model is the product of a **batman** eclipse model (F_{eclipse}) and a systematics model (F_{sys}) to the data, which has a general form of

$$F_{\text{sys}}(t) = F_{\text{polynom}}(t) F_x(t) F_y(t) F_{\text{FWHM}}(t) F_{\text{ramp}}(t) F_{\text{PLD}}(n, t). \quad (4.2)$$

Here, F_{polynom} is a polynomial in time, $F_x(t)$ and $F_y(t)$ are time series of the target centroids in x and y , $F_{\text{FWHM}}(t)$ is the time series of average FWHM values for the source determined with a 2D Gaussian fit, and F_{ramp} is an exponential function that accounts for ramp-up effects. $F_{\text{PLD}}(n, t)$ is the linear combination of n basis pixel time series, and it has a form of

$$F_{\text{PLD}}(n, t) = \sum_{i=1}^n C_i \hat{P}_i(t) \quad (4.3)$$

Here, $\hat{P}_i(t)$ is the normalized intensity (from 0–1) of pixel i at time t and C_i is the coefficient of pixel i determined in the fit. PLD was developed to mitigate systematic intrapixel effects in *Spitzer*/Infrared Array Camera (IRAC) data (Deming et al. 2015), in which the combination of source PSF motion and intrapixel gain variations introduced percent-level correlated noise in time-series data (e.g., Ingalls et al. 2012).

In our analysis, we tested forms of F_{polynom} ranging from degree 0–3 and different sets of PLD basis pixels including the brightest 1, 4, 9, 16, 25, and 36 pixels. For each visit, we explored grids of every possible combination of the components of $F_{\text{sys}}(t)$. For each combination, we first initialized the coefficients of each component using linear regression. We then used **emcee** to perform an MCMC fit of the total eclipse and systematic model to the visit data. We ran $2\nu+1$ walkers for 10,000 steps in each fit, in which ν represents the number of free parameters in the total model. The first 1,000 steps of these chains were discarded as burn-in. We fit for seven physical parameters in our calculation of F_{eclipse} , these being the orbital period, a/R_* , orbital inclination, eccentricity, longitude of periastron, eclipse depth, and time of secondary eclipse. Gaussian priors were assigned to

these parameters with means and standard deviations set by their measurements reported in Agol et al. (2021). We also placed Gaussian priors on the coefficients of the components of F_{syst} , with means set by the linear regression fit and standard deviations set to the absolute value of the square root of those values.

We calculated the BIC of the best-fitting model that resulted from the MCMC analysis, and then selected the form of F_{syst} that minimized the BIC. The form of F_{syst} that we determined for each visit with this approach consisted of only an F_{polynom} component. The first visit was best fit by a linear polynomial, whereas the remaining three were best fit by a quadratic polynomial.

With the form of $F_{\text{syst}}(t)$ determined for each visit, we then performed a joint fit of all four eclipses. This fit included 18 total free parameters: 7 physical and 11 for fitting systematics (see Table 4.3). We ran this fit with 64 chains for 50,000 steps, discarding the first 5,000 steps for burn-in. We measured a resulting eclipse depth of 418^{+90}_{-91} ppm from this fit.

4.D Brightness Temperature Calculation

The following analysis was based on stage 0 (.uncal) data products pre-processed by the *JWST* data processing software version number 2022_3b, and calibrated with **Eureka!** as described above in the “Data Reduction MG” section. We computed the brightness temperature of the planet at 15 μm from our measured occultation depth using the following methodology. We measured the absolute flux density of the star in all the calibrated images, using an aperture of 25 pixels large enough to encompass the wings of its PSF. We converted these flux densities from MJy/sr to mJy, and computed the mean value of 2.559 mJy and the standard deviation of 0.016 mJy. We added quadratically to this error of about 0.6% a systematic error of 3%, which corresponds to the estimated absolute photometric precision of MIRI (P.-O. Lagage, private communication). It resulted in a total error of 0.079 mJy. Multiplying the measured flux density by our measured occultation depth led to a planetary flux density of 1.06 ± 0.23 μJy . Multiplying again this result by the square of the ratio of the distance of the system and the planet’s radius, and dividing by π , led to the mean surface brightness of the planet’s dayside. Applying Planck’s law, we then computed the brightness temperature of the planet, whereas its error was obtained from a classical error propagation. Our result, for the MG reduction, was 379 ± 30 K, to be compared with an equilibrium temperature of 433 K computed for a null-albedo planet with no heat distribution to the night side. It is also worth mentioning that applying the same computation on the star itself led to a brightness temperature of 1867 ± 55 K, which is significantly lower than its effective temperature.

4.E Emission modelling for TRAPPIST-1 c

We generated various emission spectra for TRAPPIST-1 c to compare them to our measured eclipse depth at 15 μm . These models include (1) bare-rock spectra, (2) O_2/CO_2 mixture atmospheres and pure CO_2 atmospheres, and (3) coupled

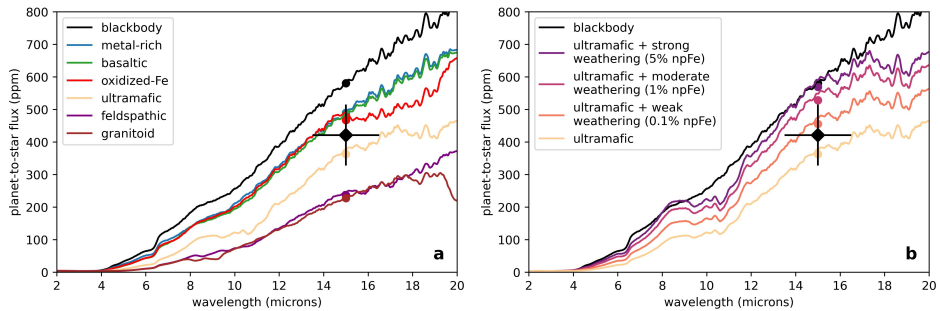


Figure 4.9: Measured eclipse depth compared to a suite of simulated bare-rock emission spectra. **a.** Secondary eclipse spectra for various fresh surface compositions, assuming that TRAPPIST-1 c is a bare rock. High-albedo feldspathic and granitoid surfaces are cool and fit the data moderately poorly (2σ), as does a low-albedo and hot blackbody surface (1.7σ). **b.** Space weathering via formation of iron nanoparticles (npFe) lowers the albedo at short wavelengths, thereby increasing the surface’s temperature and its secondary eclipse depth. An intermediate-albedo fresh ultramafic surface would fit the data well, but the fit becomes marginal after taking into account the influence of strong space weathering (1.6σ , or about 90% confidence). The vertical error bar on our 15 μm measurement represents the 1σ uncertainty on the observed eclipse depth.

climate-photochemical forward models motivated by the composition of Venus. In the following, we describe each of these models.

4.E.1 Bare Rock

Our bare-rock model is a spatially resolved radiative transfer model and computes scattering and thermal emission for a variety of surface compositions. For each composition, the surface’s radiative equilibrium temperature is computed on a 45×90 latitude-longitude grid, assuming TRAPPIST-1 c is tidally locked. Surface reflectance and emissivity data are from Hu et al. (2012), which were derived from reflectance spectra of rock powders or minerals measured in the laboratory combined with an analytical radiative-transfer model (Hapke 2002). These data have previously been used to model surface albedos and emission spectra of bare-rock exoplanets (Hu et al. 2012; Mansfield et al. 2019; Kreidberg et al. 2019a). Here we consider six compositions as well as a blackbody: basaltic, feldspathic, Fe-oxidized (50% nanophase haematite, 50% basalt), granitoid, metal-rich (FeS_2), and ultramafic (see Fig. 4.9). Given the uncertainty in the measured eclipse depth, we assume a Lambertian surface with isotropic scattering and emission, and neglect the angular dependency of the surface reflectance and emissivity, which would depend on the surface roughness and regolith particle size (Hu et al. 2012). Sensitivity tests show that these surface-model assumptions are indistinguishable within the current precision of the TRAPPIST-1 c measurements (not shown).

Furthermore, albedos and spectra of bare rocks in the Solar System are modified by space weathering, so we also consider the impact of space weathering on

TRAPPIST-1 c. The timescale for lunar space weathering through exposure to the solar wind has been estimated to range from $\sim 10^5$ years to $\sim 10^7$ years (Hapke 1977; Keller & Berger 2017). We extrapolate from the lunar value to TRAPPIST-1 c using scaling relations from a stellar-wind model (Johnstone et al. 2015). We find that the space-weathering timescale for TRAPPIST-1 c is significantly shorter than the lunar value, about $10^2 - 10^3$ years, largely because of the planet’s small semi-major axis. An exposed surface on TRAPPIST-1 c should therefore have been substantially weathered. To simulate the impact of space weathering on un-weathered surfaces, we incorporate the same approach as that in Hapke (2001, 2012). The surface composition is modelled as a mixture of a fresh host material (described above) and nanophase metallic iron using Maxwell-Garnett effective medium theory. The refractive index of metallic iron is taken from Polyanskiy (2016).

4.E.2 Simple 1+D O₂/CO₂ Mixtures

We construct a grid of O₂-dominated model atmospheres with a range of surface pressures and mixing ratios of CO₂. These are broadly representative of a plausible outcome of planetary atmosphere evolution, in which water in the atmospheres of terrestrial planets orbiting late-type M dwarfs is photolysed and the H is lost, leaving a large O₂ reservoir (Wordsworth 2015; Schaefer et al. 2016). The atmosphere models we construct are 1D models following the approach presented in Morley et al. (2017), with adiabatic pressure-temperature profiles in the deep atmosphere and isothermal pressure-temperature profiles above 0.1 bar (for thicker atmospheres, $P > 0.1$ bar) or the skin temperature (for thinner atmospheres). This approach uses DISORT (Stamnes et al. 1988, 2000) to calculate radiative transfer in 1D through the atmosphere to generate emission spectra.

We do consider how an atmosphere can transport heat to the nightside. To include heat transport to the nightside, we implement the analytic approach of Koll et al. (2019a); we use the redistribution factor f calculated in equation (3) of that work for each of the models in the grid. We assume that both the surface Bond albedo and the top-of-the-atmosphere Bond albedo are 0.1. We construct a grid of O₂-dominated model atmospheres with surface pressures from 0.01 to 100 bar (in 1-dex steps) and CO₂ mixing ratios from 1 ppm to 10,000 ppm (in 1-dex steps). We also generate pure CO₂ atmospheres with the same surface pressures. For the thicker atmospheres ($P_{\text{surf}} \geq 1$ bar) we set the thermopause (in which the atmosphere transitions from adiabatic to isothermal) to 0.01 bar.

4.E.3 Coupled Climate-Photochemical Venus-like Atmospheres

We use a 1.5D coupled climate-photochemical forward model (Robinson & Crisp 2018; Lincowski et al. 2018; Lincowski 2020, VPL Climate) that explicitly models day and night hemispheres with layer-by-layer, day-night advective heat transport driven by simplified versions of the 3D primitive equations for atmospheric transport, to simulate plausible atmospheric states for TRAPPIST-1 c for cloudy Venus-like scenarios. VPL Climate uses SMART (Meadows & Crisp 1996) with

DISORT (Stamnes et al. 1988, 2000) for spectrum-resolving radiative transfer for accuracy and versatility for both the climate modelling and the generation of the resulting planetary spectra. The model has been validated for Earth (Robinson et al. 2011) and Venus (Arney et al. 2014), but is capable of modelling a range of atmospheric states.

Due to the early luminosity evolution of the star, TRAPPIST-1 c would have been subjected to very high levels of radiation (Baraffe et al. 2015), and so we would anticipate evolved atmospheres that had undergone atmospheric and possibly ocean loss (Luger & Barnes 2015). We start with the self-consistently coupled climate-photochemical Venus-like atmospheres generated for an evolved TRAPPIST-1 c from Lincowski et al. (2018), with 96.5% CO₂ and 3.5% N₂ and assume Venus lower atmospheric trace gases and self-consistent generated sulfuric acid aerosols. We use these atmospheres as a starting point for 1.5D clear-sky Venus-like atmospheres (0.1, 1, 10 bars) and 1.5D cloudy Venus-like atmospheres (10 bars) with sulfuric acid haze. Note that 10 bar Venus-like atmospheres will produce similar results to a 93 bar Venus-like atmosphere due to the emitting layer being above or at the cloud deck, which is at a similar pressure for the 10 bar and 93 bar cases. All the modelled clear-sky Venus atmospheres produce 15 μm CO₂ features with depths spanning 134–143 ppm, with the cloudy 10 bar Venus centered at 181 ppm. Because H₂SO₄ aerosols are likely to condense in the atmosphere of a Venus-like planet at TRAPPIST-1 c’s orbital distance (Lincowski et al. 2018), we show the dayside spectrum for the 10 bar cloudy Venus for comparison with the data in Figure 4.3. The emitting layer (cumulative optical depth 1) for the cloud aerosols occurs at 7 mbars in this atmosphere, although the 15 μm CO₂ absorption is sufficiently strong that it emits from a comparable pressure level in the core of the band. The observations rule out a self-consistent Venus-like atmosphere for TRAPPIST-1 c to 2.6 sigma.

4.F Atmospheric Escape models

We use energy-limited atmospheric escape models (Schaefer et al. 2016; Luger & Barnes 2015) from a steam atmosphere to explore the amount of atmospheric escape that TRAPPIST-1 c may have experienced over its lifetime. The model assumes that escape occurs in the stoichiometric ratios of H/O in water vapour, allows for escape of oxygen, and reaction of oxygen with the magma ocean. The model transitions from magma ocean to passive stagnant-lid outgassing when surface temperatures drop below the silicate melting point. Escape continues throughout all tectonic stages. In Figure 4.4, we show the final amount of O₂ gas left in the atmosphere after 7.5 Gyr of evolution for a range of planetary water abundances and XUV saturation fractions. For typical saturation fractions of 10^{-3} (Wright et al. 2018; Fleming et al. 2020), our observations suggest that the planet likely had a relatively low starting volatile abundance. We note that these models are likely upper limits on thermal escape and more detailed models of escape, especially incorporating other gases such as CO₂ and N₂, are needed in the future to confirm these results. We also estimate total ion-driven escape fluxes due to

stellar wind interactions of a minimum of 1-3 bars over the planet’s lifetime, assuming constant stellar wind over time (Dong et al. 2018). We also considered the extended pre-main sequence for a star like TRAPPIST-1. We used the stellar evolution models of Baraffe et al. (2015) for a $0.09 M_{\odot}$ star to approximate the pre-main sequence evolution of the star.

4.G Interior structure model

We use an interior-structure model to perform an MCMC retrieval on the planetary mass and radius of TRAPPIST-1 c, and the possible stellar Fe/Si of TRAPPIST-1. The estimated Fe/Si mole ratio of TRAPPIST-1 is 0.76 ± 0.12 (Unterborn et al. 2018), which is lower than the Solar value, $\text{Fe/Si} = 0.97$ (Sotin et al. 2007). Our interior-structure model solves a set of differential equations to compute the density, pressure, temperature, and gravity as a function of radius in a one-dimensional grid (Brugger et al. 2016, 2017). The interior model presents two distinct layers: a silicate-rich mantle and an Fe-rich core. On top of the mantle, we couple the interior model with an atmospheric model to compute the emission and the Bond albedo. These two quantities enable us to solve for radiative-convective equilibrium, find the corresponding surface temperature at the bottom of the atmosphere, and find the total atmospheric thickness from the surface up to a transit pressure of 20 mbar (Mousis et al. 2020; Acuña et al. 2021). We consider a H_2O -dominated atmosphere, with 99% H_2O and 1% CO_2 . Our 1D, k-correlated atmospheric model prescribes a pressure-temperature profile comprised of a near-surface convective layer and an isothermal region on top. In the regions of the atmosphere where the temperature is low enough for water to condense and form clouds, we compute the contribution of these to the optical depth and their reflection properties as described in Marcq (2012); Marcq et al. (2017).

The posterior distribution function of the surface pressure retrieved by our MCMC indicates a 1σ confidence interval of 40 ± 40 bar for TRAPPIST-1 c. Surface pressures between 0 and 120 bar would be compatible with our probability density function within 2σ (Acuña et al. 2023). Oxygen is more dense than H_2O . Consequently, for a similar surface pressure, an O_2 -rich atmosphere would be less extended than the H_2O -dominated envelope we consider in our coupled interior-atmosphere model. This means that the density of TRAPPIST-1 c could be reproduced with an oxygen-rich atmosphere with a lower surface pressure as low as our H_2O upper limit, 80 bar.

4.H Stellar Properties

The stellar properties of TRAPPIST-1 have been constrained with observations of the total luminosity of the star, $L_* = 4\pi D_*^2 F_{bol}$ (based on broadband photometry to obtain the bolometric flux of the star, F_{bol} , and a distance measured with *Gaia*, D_*), a mass-luminosity relation (Mann et al. 2019) to obtain the stellar mass, $M_*(L_*)$, with uncertainty, as well as a precise stellar density, ρ_* , thanks to modelling of the seven transiting planets (Van Grootel et al. 2018; Ducrot et al.

2020; Agol et al. 2021). These combine to give the stellar radius and effective temperature, R_* and $T_{\text{eff},*}$,

$$R_* = \left(\frac{3M_*}{4\pi\rho_*} \right)^{1/3} \propto M_*^{1/3}, \quad (4.4)$$

$$T_{\text{eff}} = \left(\frac{L_*}{4\pi R_*^2 \sigma} \right)^{1/4} \propto M_*^{-1/6}. \quad (4.5)$$

The planets' properties have also been measured precisely in relation to the star using the depths of transit, yielding R_p/R_* , and transit-timing variations, yielding M_p/M_* (Agol et al. 2021). To convert the secondary eclipse depth, $\delta = F_p/F_*$, into a brightness temperature of the planet requires an estimate of the brightness temperature of the star:

$$\delta = \frac{I_{b,p}}{I_{b,*}} \frac{R_p^2}{R_*^2}, \quad (4.6)$$

or

$$I_{b,p} = I_{b,*} \delta \frac{R_*^2}{R_p^2}, \quad (4.7)$$

in which $I_{b,*}$, $I_{b,p}$ are the mean surface brightness of the star and planet in the MIRI band at full phase (that is, secondary eclipse), respectively. The ratio R_p/R_* is well constrained from the transit depth, whereas the brightness temperature of the star can be measured with an absolute calibration of the stellar flux in the MIRI band, F_* (e.g., Ducrot et al. 2020). The stellar intensity may then be computed as:

$$I_{b,*} = \frac{F_*}{\Omega_*} = \frac{F_* D_*^2}{\pi R_*^2}, \quad (4.8)$$

in which Ω_* is the solid angle of the star. Because our estimate of R_* is proportional to $M_*^{1/3}$, this means that $I_{b,*} \propto M_*^{-2/3}$. For a given value of R_* , this surface brightness can be translated into a brightness temperature, $T_{b,*}$, and with the equation 4.7 above, we can compute the intensity and therefore the surface brightness of the planet, $T_{b,p}$ to be 380 ± 31 K using the eclipse depth and the stellar flux density. We also estimate the stellar brightness temperature in the MIRI band with an atmospheric model for the star relating $T_{b,*}$ in the MIRI band to the T_{eff} , as $\alpha = T_{b,*}/T_{\text{eff},*}$. We have accomplished this with the state-of-the-art SPHINX model for low-temperature stars (Iyer et al. 2023) and assumed $T_{\text{eff}} = 2566$ K (Agol et al. 2021), yielding $\alpha = 0.72$ at $14.87 \mu\text{m}$. We also compute the α from *JWST* spectrophotometric observations with a flux of 2.599 ± 0.079 mJy at $14.87 \mu\text{m}$, yielding $\alpha = 0.71 \pm 0.02$. The MIRI images are flux-calibrated (with an internal error of 3%). We measure the stellar flux in all images within an aperture large enough to encompass the whole PSF, and then compute the mean and the standard deviation. We compute the total error on the measurement to be the 3% larger than this standard deviation. As the unit of flux in MIRI images is given in Jy/str, we multiply the measured fluxes by the angular area covered by a pixel in str to yield units of Jy.

The stellar brightness temperature scales linearly with effective temperature and metallicity in the MIRI wavelength range, and scales inversely with surface

Table 4.4: Measured eclipse times. Eclipse times (in BJD_{TDB}) determined by the four different reductions by fitting an eclipse model to each visit. An offset of 2459880.0 days was subtracted from each of the values in the table.

	visit 1	visit 2	visit 3	visit 4
SZ	$0.1872^{+0.0043}_{-0.0074}$	$2.6209^{+0.0021}_{-0.0022}$	$9.8782^{+0.0038}_{-0.0077}$	$34.0940^{+0.0053}_{-0.0021}$
ED	$0.1894^{+0.0452}_{-0.0164}$	$2.6197^{+0.0051}_{-0.0110}$	$9.8722^{+0.0038}_{-0.0040}$	$34.0930^{+0.0166}_{-0.0057}$
MG	0.1899 ± 0.0022	2.6202 ± 0.0018	$9.8792^{+0.0033}_{-0.0069}$	$34.0928^{+0.0018}_{-0.0030}$
PT	$0.1887^{+0.0106}_{-0.0086}$	$2.6211^{+0.0014}_{-0.0021}$	$9.8735^{+0.0087}_{-0.0047}$	$34.0949^{+0.0051}_{-0.0019}$

gravity of the star. The effective temperature, however, scales as $T_{\text{eff}} \propto M_*^{-1/6}$ (or $R_*^{-1/2}$), with stellar mass (or radius) relative to the estimate based on the measured flux. The estimate of α , therefore, may have a significant imprecision given the possible heterogeneity of the stellar atmosphere, as well as the inherent uncertainties involved in modelling late-type stellar atmospheres. Both the synthetically derived α and those from observations match within 2σ uncertainty, lending credence to empirical mass-luminosity relations and synthetic atmosphere-model-derived stellar brightness temperatures. Note, however, that the mass-luminosity relation is only calibrated with a handful of low-mass stars in binaries (Mann et al. 2019), and hence its applicability to TRAPPIST-1 may be tenuous; this may thus be the weakest link in determining the stellar parameters. Assumption-driven deviations between synthetic models for late-type stars and empirically calibrated methods both still remain a significant challenge in truly understanding these hosts.

4.I Eclipse Timing Variations

Dynamical modelling of the TRAPPIST-1 system (Agol et al. 2021) gives a precise forecast of the times of transit and eclipse for all seven planets. These have been used in the planning of the observations, and can also be compared with the measured times.

The times of eclipse can be offset from the mid-point between the times of transit due to four different effects: 1) the light-travel time across the system (Fabrycky 2010), 2) non-zero eccentricity (Winn 2010), 3) non-uniform emission from an exoplanet (Agol et al. 2010)¹, and 4) eclipse-timing variations due to perturbations by other planets in the system. Of these three effects, the second effect is typically the largest, which can be used to constrain one component of the eccentricity vector of the transiting planet (Winn 2010).

In Table 4.4 we list the measured eclipse times from the four different reductions and in Figure 4.10 we compare them with the forecast from Agol et al. (2021). To make the forecast, we used the posterior probability of the timing model to compute the times of transit and eclipse, and then we calculate the time of eclipse

¹This does not change the mid-point of the eclipse, but it does change the shape of ingress/egress, and can lead to an artificial time offset if not accounted for in the modelling.

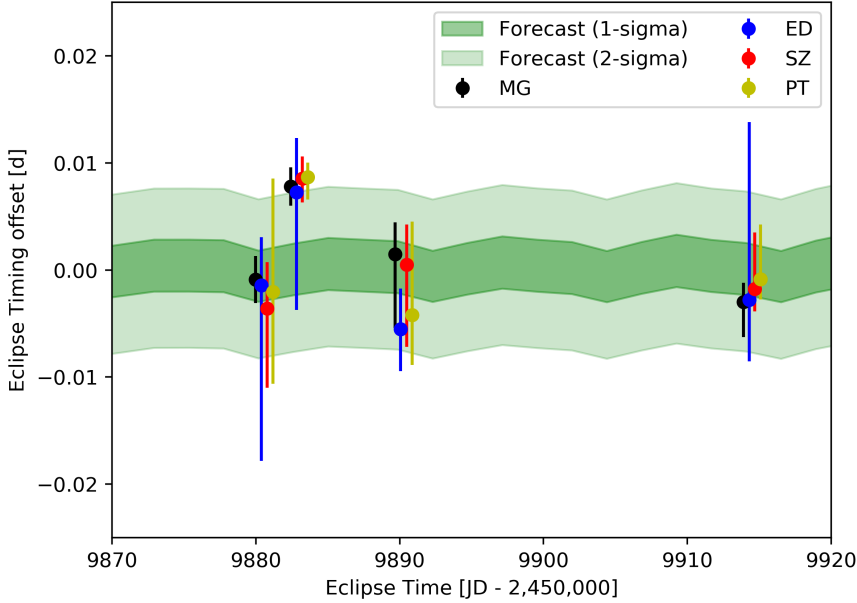


Figure 4.10: Measured eclipse times compared with the predicted eclipse times. The points show the measured eclipse timing offsets (defined as the time of eclipse minus the mean of the two adjacent transit times of planet c) from four different analyses. The error bars correspond to the 16th and 84th percentiles of the eclipse time posterior. The dark (light) green shaded region shows the 1-(2)-sigma confidence intervals forecast from the transit-timing analysis from Agol et al. (2021).

minus the mean of the two adjacent transits of planet c to derive an “Eclipse timing offset”. This offset should be zero for a circular, unperturbed orbit with negligible light-travel time (which is about 16 seconds, or 1.8×10^{-4} days for TRAPPIST-1 c). The dynamical modelling is constrained by the times of transit, which place some constraint on the eccentricity of the orbit of planet c (in particular, the mean or free eccentricity could be non-zero). The uncertainty on the eccentricity leads to uncertainty on the times of secondary eclipse. Our forecast models for the eclipse timing offset have a 1σ uncertainty of ~ 3.5 minutes at the measured times of eclipse (approximately 0.0024 days).

The measured times were taken from four analyses (by SZ, PT, ED, and MG) in which a broad prior was placed on the times of transit, whereas the duration and depth were constrained to the measured values of the four eclipses. The times of each eclipse were then free to vary, and the posterior times of transit were inferred using MCMC (ED/MG/PT) or nested sampling (SZ). The four analyses give good agreement on the values, but have significant differences between the uncertainties.

Overall, the forecast eclipse timing offsets agree well with the measured times, within $1\text{--}2\sigma$ offsets. The uncertainties on the measured times are comparable with the forecast uncertainties, and so, in future work, we hope to use these measured eclipse times to further constrain the eccentricity vector of the orbit of planet c. This may help to constrain tidal damping models of planet c, but it may also constrain tidal damping of *all* of the planets as the free eccentricity vector of planet c is tightly correlated with those of the other planets due to the “eccentricity-eccentricity” degeneracy present in transiting planet systems (Lithwick et al. 2012).

Acknowledgements

This work is based in part on observations made with the NASA/ESA/CSA James Webb Space Telescope. The data were obtained from the Mikulski Archive for Space Telescopes at the Space Telescope Science Institute, which is operated by the Association of Universities for Research in Astronomy, Inc., under NASA contract NAS 5-03127 for JWST. These observations are associated with program #2304. MG is F.R.S.-FNRS Research Director, and acknowledges support from the Belgian Federal Science Policy Office BELSPO BRAIN 2.0 (Belgian Research Action through Interdisciplinary Networks) for the project PORTAL n° B2/212/P1/PORTAL (PhOtotrophy on Rocky habiTable pLanets). VM and AL are part of the Virtual Planetary Laboratory Team, which is a member of the NASA Nexus for Exoplanet System Science, and funded via NASA Astrobiology Program Grant 80NSSC18K0829. AI acknowledges support from the NASA FINESST Grant 80NSSC21K1846.

Author Contributions

SZ, LK, MG, PT, ED, AL, VM, DK, CM, LS, EA, LA, and GS contributed significantly to the writing of this manuscript. SZ, ED, PT, and MG provided a data reduction and data analysis of the four visits for this work and contributed an eclipse depth value. CM, DK, XL, RH, AL, and VM ran theoretical models for the planet’s atmosphere and surface. LA ran models on the planet’s interior structure. AI and EA modeled the stellar spectrum. LS modeled the atmospheric escape for the planet. LK, MG, VM, DK, RH, CM, LS, EA, FS EB, and AM contributed to the observing proposal.

Data availability

The data used in this work were collected by *JWST* as part of GO program 2304 and will be publicly accessible after the default proprietary period of one year. The most recently taken visit will therefore be publicly accessible on the Mikulski Archive for Space Telescopes (MAST) on Dec, 1st. 2023.

Code availability

We used the following codes, resources, and `python` packages to reduce, analyze and interpret our *JWST* observations of TRAPPIST-1c: `numpy` (Harris et al. 2020), `matplotlib` (Hunter 2007a), `astropy` (Astropy Collaboration et al. 2022), `batman` (Kreidberg 2015), `Eureka!` (Bell et al. 2022), `jwst` (Bushouse et al. 2022), `emcee` (Foreman-Mackey et al. 2013b), `trafit` (Gillon et al. 2010, 2012, 2014), `dynesty` (Speagle 2020; Koposov et al. 2023a), `SMART` (Meadows & Crisp 1996), `VPL Climate` (Robinson & Crisp 2018; Lincowski et al. 2018; Lincowski 2020), `DISORT` (Stamnes et al. 1988, 2000), `IRAF/DAOPHOT` (Stetson 1987). We can share the code used in the data reduction or data analysis upon request.

Competing Interests

The authors declare no competing interests.

5

A HUBBLE WFC3 INFRARED LOOK AT THE TRANSMISSION SPECTRUM OF THE HOT, INFLATED SUB-SATURN KELT-11 B

Sebastian Zieba, Knicole D. Colón, Luis Welbanks, Laura Kreidberg, Kevin B. Stevenson, Dana R. Louie, Daniel Angerhausen, Thomas Barclay, Thomas Beatty, Jonathan J. Fortney, David J. James, Michael R. Line, Eric D. Lopez, Nikku Madhusudhan, Avi Mandell, Erin May, Joseph E. Rodriguez, and Keivan G. Stassun

In Preparation, 2024.

Abstract

The high equilibrium temperature (1703K), low density (nine times less than Saturn), and bright host star ($V = 8$ mag) make KELT-11 b a perfect target for atmospheric characterization via transmission spectroscopy. Here, we present a new transmission spectrum for this hot, inflated sub-Saturn taken by the *Hubble Space Telescope* (*HST*) using its Wide Field Camera 3 (WFC3). We analyze unpublished *HST*/WFC3 G102 ($0.8 - 1.1 \mu\text{m}$) spectroscopic grism data collected in December 2020 and also perform a reanalysis of the *HST*/WFC3 G141 ($1.1 - 1.7 \mu\text{m}$) data collected in April 2018, previously published in Colón et al. (2020). We perform a thorough study of the systematic effects observed in the dataset and lay out how different model assumptions change the final transmission spectrum. We find that the commonly used **divide-white** technique can lead to systematic bias in the transmission spectrum in cases where the systematic noise varies with wavelength (e.g. Sun-like stars). The unusual transmission shape in the G141 grism seen by Colón et al. (2020) is most likely caused by the choice of the **divide-white** technique. Our G141 spectrum shows smaller transit depths at the red edge of the detector, similar to other hot, inflated sub-Saturns previously studied with WFC3 G141, like WASP-39 b and WASP-107 b. The transit depth of our G102 spectrum decreases toward shorter wavelengths, which is indicative of faculae on the stellar photosphere contaminating our spectrum.

5.1 Introduction

KELT-11 b was detected in photometric ground-based and radial velocity data (Pepper et al. 2017) and later also observed by the *Spitzer Space Telescope* at 3.6 μm (Beatty et al. 2017). The planet orbits a bright ($V = 8.04$ mag, $H = 6.25$ mag, $K_s = 6.12$ mag), evolved subgiant (KELT-11, HD 93396) (Pepper et al. 2017). With an exceptionally low planetary density of just $0.08 \pm 0.02 \text{ g/cm}^3$ (compare to $\rho_{\text{Saturn}} = 0.687 \text{ g/cm}^3$), the planet is part of the population of hot inflated Saturns (Colón et al. 2020) (see Fig. 5.1 and Table 5.1). The planet also has a short orbital period of 4.7361 days (Beatty et al. 2017), leading to a high equilibrium temperature of approximately 1700 K (following Koll et al. 2019b, assuming $A_B = 0$ and uniform redistribution). Taken together, the planet’s low surface gravity, high equilibrium temperature, and bright host star make KELT-11 b an excellent target for atmospheric follow-up using transmission spectroscopy.

Another member of the group of hot inflated Saturns is WASP-39 b (Faedi et al. 2011), which was recently extensively studied as part of *JWST*’s Early Release Science (ERS) program (JWST Transiting Exoplanet Community Early Release Science Team et al. 2023; Ahrer et al. 2023; Alderson et al. 2023; Rustamkulov et al. 2023; Feinstein et al. 2023; Tsai et al. 2023). The planet was found to have a strong CO_2 absorption feature, expected in chemical equilibrium for $\sim 10\times$ solar composition (Mollière et al. 2015), which is comparable to Saturn’s metallicity (Atreya et al. 2022). This measurement for WASP-39 b is therefore in agreement with the metallicity-mass trend observed for the solar system gas giants, which shows that a planet’s mass is indirectly proportional to its atmospheric metallicity (Kreidberg et al. 2014b; Welbanks et al. 2019). For KELT-11 b, however, the *HST*’s Wide Field Camera 3 (WFC3) G141 observations published in Colón et al. (2020) showed a different picture of the planet: the observed water abundance of the planet was determined to be orders of magnitude lower than previously expected from planet formation models. Depending on the chosen model, the data also showed hints of carbon- and oxygen-bearing species (HCN, TiO, and AlO) (Colón et al. 2020). The presence of a lower-than-anticipated water abundance in the sub-Saturn KELT-11 b, from the perspective of planet formation, is intriguing. Models predict that the atmospheric metal enrichment for sub-Saturns, ranges from 10 – 100 times the solar composition, regardless of whether these planets form interior or exterior to the water ice line (Fortney et al. 2013; Mordasini et al. 2016). Interior structure models, derived from the observed masses and radii of gas giant exoplanets, also indicate a metal enrichment of approximately 10 times the solar composition for planets within the sub-Saturn mass range (Thorngren et al. 2016). However, Colón et al. (2020) atmospheric retrievals for KELT-11 b resulted in a sub-solar water abundance (0.01 – 0.1 times solar), significantly lower than the anticipated values by several orders of magnitude.

In this paper, we reanalyze the *HST*/WFC3 G141 observations originally published in Colón et al. (2020) and present a planetary transmission spectrum, which is inconsistent with the previously published transmission spectrum. We also analyze new observations taken by the G102 grism. In Section 5.2 and 5.3, we describe the observations, data reduction, and light curve fitting. We discuss our G141 and

G102 transmission spectra in Section 5.4.1 and 5.4.3. In Section 5.4.2 we compare our G141 spectrum with some other planets with similar properties. Finally, we summarize our findings in Section 5.5.

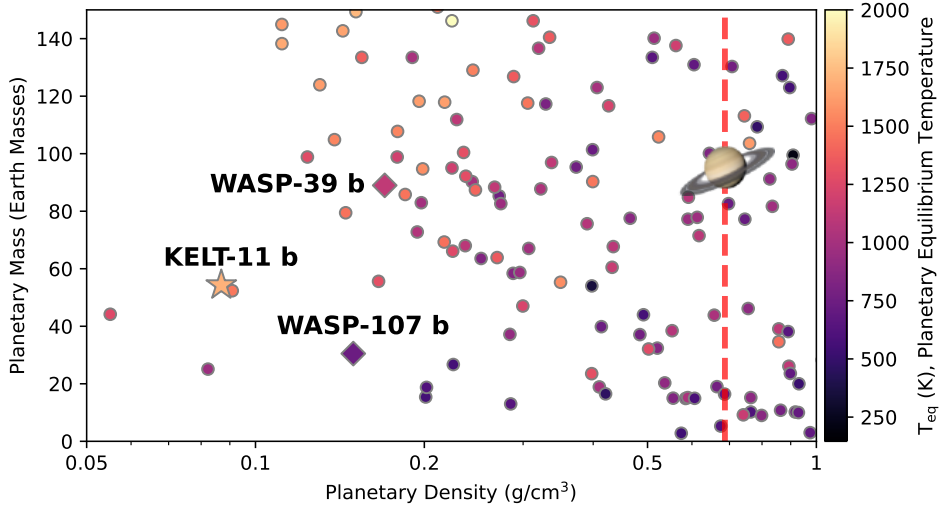


Figure 5.1: Exoplanets with low densities, highlighting KELT-11 b (star symbol), the *JWST* ERS target WASP-39 b (diamond symbol), and WASP-107 b (diamond symbol). These three planets have some of the lowest densities while having (sub-)Saturn-like masses. We only show planets with bright host stars ($K_s < 12$ mag) and well-characterized planetary masses and radii ($> 5\sigma$). A list of properties for the highlighted planets is listed in Table 5.1. Data were taken from the NASA Exoplanet Archive in December 2023.

5.2 Observations and Data Reduction

We observed two transits of KELT-11b with *HST*’s Wide Field Camera 3 (WFC3) as part of the General Observer (GO) Programs 15255 (Colon 2017) and 15926 (Colon et al. 2019) (see Table 5.2 for a summary of the observations). The first transit was taken with the G141 grism (1.1 – 1.7 μm) on 2018 April 18 and originally published in Colón et al. (2020). Here, we conduct a reanalysis of this data. The second transit was taken with the G102 grism (0.8 – 1.1 μm) on 2020 December 28. Both observations consisted of 9 consecutive *HST* orbits and were taken in round-trip spatial scan mode, where we alternated between forward and reverse scans (McCullough & MacKenty 2012; Deming et al. 2013). With this setup, the stellar light is spread over more pixels by slewing the telescope in the cross-dispersion direction. This effectively increases the exposure time and duty cycle of the observations without reaching saturation, but leads to a constant offset between forward and reverse scans, which we will correct for in the fitting stage.

Both observations used an identical observational setup: the data were taken

Table 5.1: A selection of planets, which are part of the hot, inflated (sub-)Saturn population. References: KELT-11 b: Beatty et al. (2017); WASP-39 b: Faedi et al. (2011); WASP-107 b: Anderson et al. (2017); Piaulet et al. (2021)

Planet	$R_p(R_J)$	$M_p(M_J)$	ρ_p (g/cm ³)	P_{orb} (d)	T_{eq} (K)	$R_*(R_s)$	[Fe/H] _* (dex)
KELT-11 b	1.35 ± 0.10	0.171 ± 0.015	0.092 ± 0.022	4.74	1703	2.7	0.17 ± 0.07
WASP-39 b	1.27 ± 0.04	0.280 ± 0.030	0.182 ± 0.026	4.06	1118	0.9	0.01 ± 0.09
WASP-107 b	0.94 ± 0.02	0.096 ± 0.005	0.154 ± 0.013	5.72	733	0.7	0.02 ± 0.10
Saturn	0.83	0.30	0.687				

Table 5.2: Summary of the two *HST*/WFC3 observations analyzed in this work, with N_{orb} being the number of orbits and N_{exp} the number of spectroscopic exposures in each program.

Instrument	GO ID	Date (UT)	N_{orb}	N_{exp}
<i>HST</i> /WFC3/G141	15255	2018-04-18	9	234
<i>HST</i> /WFC3/G102	15926	2020-12-28	9	261

with the 512x512 subarray (SQ512SUB) and had a scan rate of 0.96 arcsec/sec (7.4 pixels/sec). We used the SPARS25 read-out mode with NSAMP = 4, resulting in an exposure time of 46.7 seconds for both visits. This led to a scan length of 53.1 arcsec or 395 pixels. We reached a maximum photoelectron count per pixel of approximately 2.9×10^4 electrons per second for G102 and 4.8×10^4 electrons per second for G141, which is below the non-linear regime of the WFC3 detector for both of the observations (Hilbert 2008). We started every *HST* orbit with an undispersed “direct image” of the star using the WFC3 F130N narrow-band filter, which we used to determine the position of the spectroscopic trace (see Fig. 5.2). The direct images were then typically followed by 26 (31) spectroscopic exposures per *HST* orbit, leading to 234 (261) 2D spectra in total for the G102 (G141) observations.

We accessed and downloaded the calibrated intermediate IR multiaccum image (IMA) files¹ which were produced by the `calwf3` pipeline version 3.6.2 from MAST². These files have calibrations like dark subtraction, linearity correction, and flat fielding applied to each individual readout of the exposure. We then reduced this data with the end-to-end open-source pipeline PACMAN³ (Zieba & Kreidberg 2022) which is based on the procedure described in previous works (see e.g., Kreidberg et al. 2014a,b, 2015, 2018a). By observing the star with the spatial scanning technique, each exposure consists of a number of non-destructive reads, which are also called “up-the-ramp samples” (see Fig. 5.2). We treat each of them as an independent subexposure and start by masking bad pixels, which were flagged by the `calwf3` with a data quality flag of either DQ = 4 or 512⁴. Next, we calculated the difference between consecutive non-destructive reads and subtracted the background. We determined the background flux of each difference frame by computing the median flux of the pixels where the stellar light did not fall on the detector. The background flux per pixel was ~ 33 e⁻/sec during the G102 observations increasing at the end of each orbit and ~ 58 e⁻/sec during the G141 observations being highest at the beginning of each orbit (see Fig. 5.3). We then optimally extract each of the background subtracted difference images by following the algorithm presented in Horne (1986). For each of the subexposures, we chose an extraction window that corresponded to ± 20 pixels relative to the upper and lower edges of the spectrum⁵. We then summed up the spectra for all the differenced images to get the final 1D spectrum for each exposure (see Fig. 5.4). Finally, we performed a wavelength calibration on these 1D spectra by cross-correlating them with a reference spectrum. The reference spectrum consisted of the product of the bandpass of the respective grism and a smoothed stellar spectrum following Deming et al. (2013). The chosen stellar spectrum was an ATLAS9 stellar atmosphere model by Castelli & Kurucz (Castelli & Kurucz 2003), which was the closest one to the published stellar parameters in Beatty et al. (2017), i.e.,

¹for more information on the “ima” data products see the WFC3 Data Handbook: <https://hst-docs.stsci.edu/wfc3dnhb/chapter-2-wfc3-data-structure/2-1-types-of-wfc3-files>

²<https://mast.stsci.edu/search/hst>

³for PACMAN’s documentations see: <https://pacmandocs.readthedocs.io/en/latest/>

⁴for an explanation of the various `calwf3` quality flags see <https://wfc3tools.readthedocs.io/en/latest/wfc3tools/calwf3.html#data-quality-initialization-dqicorr>

⁵for more details see <https://pacmandocs.readthedocs.io/en/latest/pcf.html#window>

the stellar model with $T_{\text{eff}} = 5250\text{K}$, $\log(g) = 3.5$ and $[M/H] = +0.2^6$.

5.3 Light Curve Analysis

5.3.1 *HST*/WFC3 White Light Transit

We generated white (i.e., broadband) light curves by summing the flux in the 1D spectra (see Fig. 5.4) for each exposure. The resulting light curves can be seen in Figure 5.3. They exhibit systematics that are typical for *HST*/WFC3 observations like the offset caused by the “upstream/downstream” effect or a ramp-like trend in each *HST* orbit. The latter is caused by charge-trapping in the WFC3 detector (Zhou et al. 2017). We discard the first orbit of the WFC3 observations because they have stronger ramp amplitudes compared to the following orbits, which is common practice (see e.g., Deming et al. 2013; Kreidberg et al. 2014a; Wakeford et al. 2017). We also remove the first exposure of each *HST* orbit due to their strong systematics.

HST/WFC3 observations also typically show visit-long drifts in the baseline level which are typically fitted by low-order time-dependent polynomials, i.e., linear or quadratic trends. Like in Guo et al. (2020), we also explore exponential and logarithmic visit-long trends to describe this drift in flux.

Our final fitting model $F(t)$ consists out of a **batman** (Kreidberg 2015) transit model $F_{\text{transit}}(t)$, the orbit-long systematics $F_{\text{sys,o}}(t)$, and the visit-long systematics $F_{\text{sys,v}}(t)$:

$$F(t) = F_{\text{transit}}(t)F_{\text{sys,o}}(t)F_{\text{sys,v}}(t). \quad (5.1)$$

As in previous work, we model the ramp-like trends in each *HST* orbit with an exponential function, which is commonly also called “model-ramp”:

$$F_{\text{sys,o}}(t) = 1 - \exp(-r_1 t_o - r_2 - D(t)), \quad (5.2)$$

where r_1 describes the rate of the exponential function and r_2 its amplitude. The delay function, $D(t)$, has the value of r_3 for the first orbit and is 0 otherwise. This is an optional parameter, which might be used if the first orbit exhibits a stronger orbit-long ramp than the following orbits (in this case, r_3 would have a negative value). The time elapsed from the first exposure in each orbit is described by t_o .

We compared the following visit-long trends:

$$F_{\text{sys,v}}(t) = \begin{cases} c S(t) + v_1 t_v, & \text{linear} \\ c S(t) + v_1 t_v + v_2 t_v^2, & \text{quadratic} \\ c S(t) + \exp(-e_1 t_v) e_2, & \text{exponent.} \\ c S(t) + \log(t_v + 1/l_1) l_2, & \text{logarith.} \end{cases} \quad (5.3)$$

with t_v being the time elapsed since the first exposure in a visit and c is a normalization constant. The scale function, $S(t)$, accounts for the offset caused by

⁶we accessed the Castelli & Kurucz stellar spectrum from MAST <https://archive.stsci.edu/hlsp/reference-atlases/cdbs/grid/ck04models/>

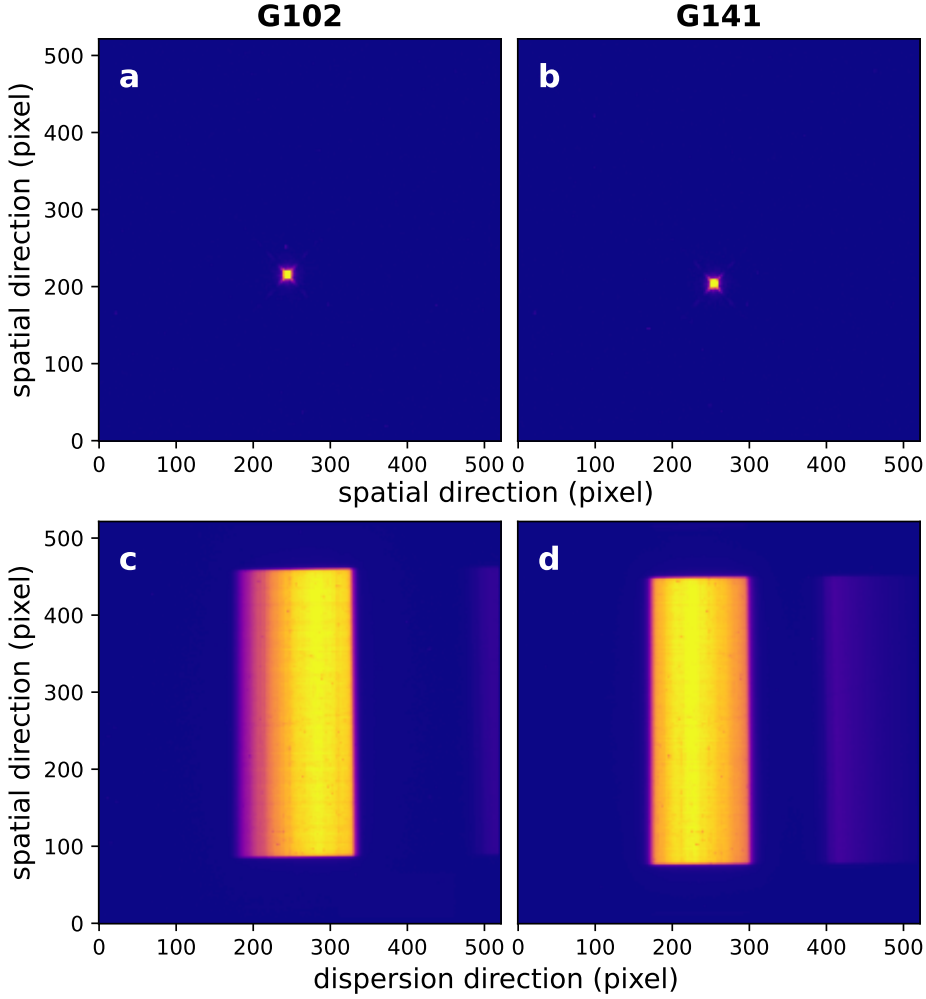


Figure 5.2: Examples of calibrated intermediate IR multiaccum image (IMA) files using the 512x512 subarray (SQ512SUB) on *HST*/WFC3. The top panels show the undispersed “direct images” of KELT-11 taken with the WFC3 F130N narrow-band filter for the G102 (panel a) and G141 (panel b) observations. The bottom panels c and d show first-order 2D spectra for the last up-the-ramp sample (i.e., the last non-destructive read) for a randomly chosen exposure in each observation. The faint second-order spectra (which are not used in this work) can be seen on the right side of the subarray.

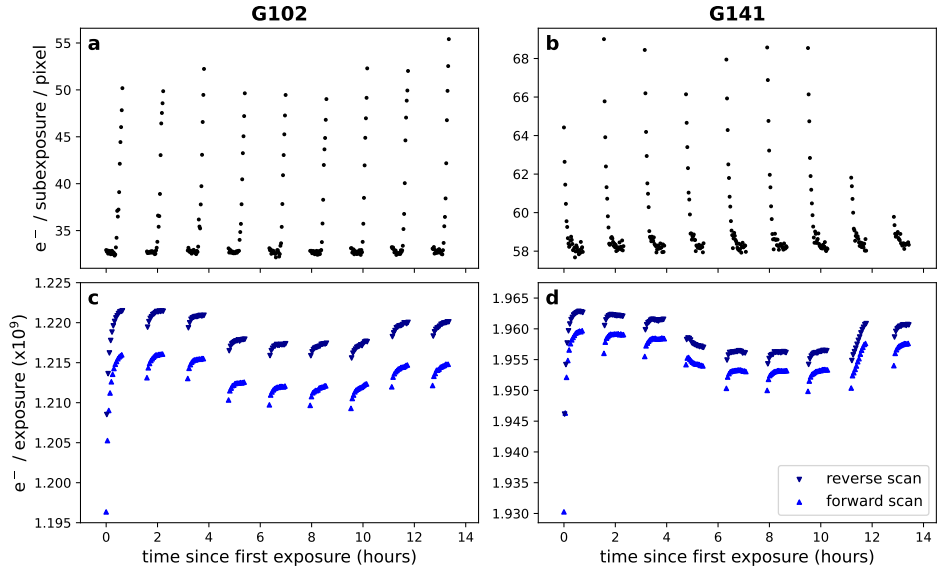


Figure 5.3: Top row: background flux of each up-the-ramp sample (subexposure) per pixel as a function of time. Bottom row: raw white light curves after performing the data reduction described in Section 5.2. The offset caused by the “upstream/downstream” effect can be clearly seen by observing in the round-trip spatial scan mode. This is caused by the total integration time effectively slightly increasing when the scan is “downstream” (“reverse scanning”) because the star will be moved on the detector in the same direction as the readout (McCullough & MacKenty 2012).

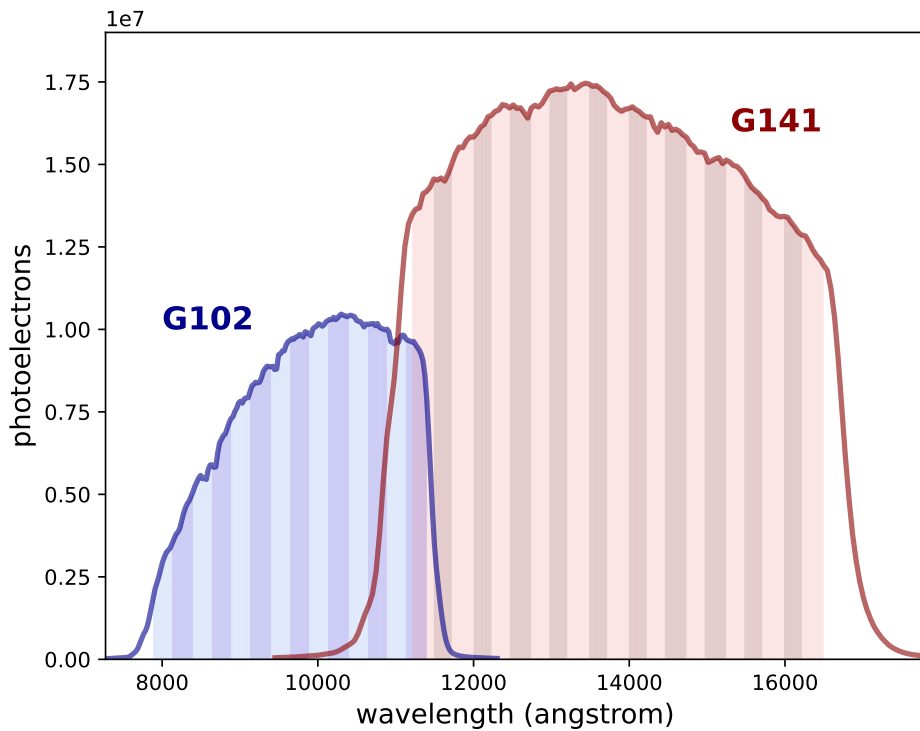


Figure 5.4: Wavelength calibrated 1D spectra of KELT-11 for a random exposure taken during both observations. The alternating colors under the curves depict the chosen binning for the spectroscopic light curves, which was chosen to be $0.025 \mu\text{m}$ for both observations.

the “upstream/downstream” effect and is 1 for exposures taken with a forward scan direction and s for reverse scans. For our observations, this offset is $\sim 0.4\%$ for G102 and $\sim 0.2\%$ for the G141 data. Finally, v_1 , v_2 , e_1 , e_2 , l_1 , and l_2 are free parameters for the respective trends, which describe the shape of the visit-long systematic.

For the transit model, the free parameters were the transit midpoint time t_0 , the planet-to-star radius ratio R_p/R_s , the ratio of semimajor axis to stellar radius a/R_s , the orbital inclination i and the limb darkening. We fixed the orbital period of the planet P_{orb} to a literature value and used normal priors for a/R_s and i based on Beatty et al. (2017) (see Table 5.3). We also fixed the eccentricity to zero as previous studies found that the orbits were all consistent with a circular orbit (Beatty et al. 2017; Pepper et al. 2017; Colón et al. 2020). We tested both a linear limb darkening and a two-parameter limb darkening following the parameterization described in Kipping (2013). The second orbit in a visit is known to sometimes exhibit a stronger orbit-long ramp than the following ones. Due to that, we also test if our fit improves when we use the delay function $D(t)$ on that orbit or if we get a better fit by removing the orbit altogether. We also fit for an uncertainty-multiplier factor σ_{multi} , which scales the error bars of our data, so that the model reaches a reduced chi-squared of one ($\chi^2_{\text{red.}} = 1$), which accounts for any additional not-photon-limited noise in the observations and ensures that we are not underestimating the uncertainties of our fitted parameters.

Table 5.3: Adopted literature values from Beatty et al. (2017) for the white light curve fits in this work.

Parameter	Value
P_{orb} (days)	4.7361
a/R_s	4.98 ± 0.05
i ($^\circ$)	85.3 ± 0.2

We determine the best-fit model by minimizing the Bayesian information criterion (BIC; Schwarz 1978) where we apply the definition that a ΔBIC value greater than 10 shows strong evidence against a given model (Kass & Raftery 1995). A table with all explored models for the G102 and G141 observations and values like the BIC or χ^2 can be found in the Appendix (Table 5.7 and 5.8). We use the dynamic nested sampling approach (Skilling 2004, 2006; Higson et al. 2019) implemented in the open-source python package `dynesty` (Speagle 2020; Koposov et al. 2023b) to estimate our free parameters and their uncertainties (details in Appendix 5.A). For both datasets, we find that the white light curve is best fitted by a quadratic limb darkening law. The best fitting visit long trend for the G102 data is a quadratic function and for G141 an exponential function. We furthermore find that removing the first two orbits for the G102 observations and orbit number one and five for G141 significantly improves the fits. The best white light curve fits for both datasets are shown in Figure 5.5. Our final residuals display

Table 5.4: Free parameters from the *HST*/WFC3 G102 and G141 white light curves. The values correspond to the median of the posterior distribution of the white light curve fits and their 16th and 84th percentiles.

Parameter	Value
G102	
t_0 (BJD _{TBD})	2459212.1374 ± 0.0018
a/R_s	5.00 ± 0.05
i ($^\circ$)	$85.27^{+0.20}_{-0.19}$
R_p/R_s	0.0452 ± 0.0003
$q1$	$0.24^{+0.08}_{-0.07}$
$q2$	$0.05^{+0.09}_{-0.04}$
$u1$ (derived)	$0.05^{+0.07}_{-0.04}$
$u2$ (derived)	$0.44^{+0.10}_{-0.14}$
G141	
t_0 (BJD _{TBD})	$2458227.01495 \pm 0.00008$
a/R_s	4.95 ± 0.02
i ($^\circ$)	$85.17^{+0.16}_{-0.14}$
R_p/R_s	0.04630 ± 0.00009
$q1$	0.167 ± 0.017
$q2$	0.11 ± 0.06
$u1$ (derived)	$0.09^{+0.05}_{-0.04}$
$u2$ (derived)	0.32 ± 0.06

a low amount of scatter. We measure a root-mean-squared (rms) variability of 71.6 ppm for G102 and 37.6 ppm for G141. This is $2.5\times$ and $1.6\times$ the expected Poisson noise. Our G141 residuals show considerably less scatter than the 65ppm ($3\times$ poisson) published in Colón et al. (2020). This is mostly due to removing the fifth orbit which exhibits more scatter and determining that an exponential trend is approximating the visit long systematics better than the quadratic trend used in Colón et al. (2020) (see Tab. 5.8 for all models fitted to the G141 white light curve). Our final results for the white light curve fits for both grisms are listed in Table 5.4.

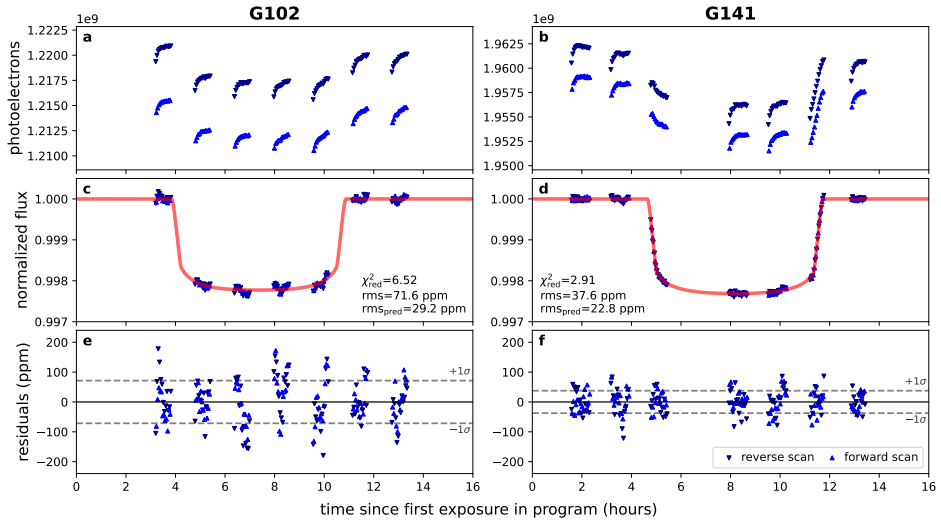


Figure 5.5: Best white light curve fits for the G102 and G141 observations. Top row: Raw white light curve. Orbit 1 and 2 were removed for the G102 data and orbit 1 and 5 for the G141 observations. Middle row: Best white light curve fit with the visit and orbit long trends removed. The red line shows the best fitting **batman** model. Lower row: The residuals from the best fit. The standard deviation of the residuals is shown by dashed lines.

5.3.2 *HST*/WFC3 Spectroscopic Transit

We create spectroscopic light curves by binning each of the observations. The wavelengths we considered are $0.79 - 1.14 \mu\text{m}$ for the G102 grism and $1.125 - 1.650 \mu\text{m}$ for the G141 grism. We chose a bin width of $0.025 \mu\text{m}$ for both datasets, leading to 14 and 21 spectroscopic bins for the G102 and G141 data, respectively. We fit the visit long systematics of each spectroscopic light curve with the best white light curve model, that is, a quadratic trend for G102 and an exponential trend in time for G141. We furthermore fit each light curve with a transit model with a quadratic limb darkening law (u_1, u_2) and exponential ramp for each orbit. We fix the transit time t_0 to the best-fitting values listed in Table 5.4 for each

of the grisms. We also fixed P_{orb} , a/R_s , and i to the values reported in (Beatty et al. 2017) (see Table 5.3). Each spectroscopic light curve fit therefore had 10 free parameters: R_p/R_s , u_1 , u_2 , c , s , r_1 , r_2 , σ_{multi} and two visit long parameters (e_1 and e_2 for G102; v_1 and v_2 for G141). We used the dynamic nested sampling code **dynesty** to sample the posteriors of each of these parameters and used the same setup as for the white light curve fits (see Appendix 5.A).

In Figure 5.14 and 5.15, we show the individual spectroscopic light curve fits. Figure 5.6 shows the transmission spectrum of KELT-11 b after fitting our models to each spectroscopic light curve (the data can be found in Table 5.5 and 5.6). We find that the shape of our G141 spectrum significantly deviates from the transmission spectrum published in Colón et al. (2020) (see Figure 5.7). In particular, our G141 spectrum shows decreasing absorption at longer wavelengths. The Colón et al. (2020) spectrum was comparatively flat between 1.40 and 1.65 μm . The final model chosen in Colón et al. (2020) used the **divide-white** technique, which assumes that the observed systematics are not wavelength-dependent but have the same shape across the detector (Stevenson et al. 2014a; Kreidberg et al. 2014a). For that, each spectroscopic light curve is fit by the astrophysical model (in our case a transit) multiplied by the scaled systematics of the best-fitting white light curve. For a more detailed discussion of the **divide-white** technique, see Section 5.4.1.

We also search for correlated noise in the residuals of our spectroscopic light curve fits. For that, we calculate the rms of the residuals for bins of different sizes. The rms of our light curve residuals decrease with increasing bin size and follow the $1/\sqrt{N}$ line, which is expected if the residuals are dominated by Poisson noise. This suggests that our residuals are uncorrelated in time. See Figure 5.17 for the Allan deviation plots for each of the spectroscopic light curve fits. We list the various properties of our spectroscopic light curve fits like rms and χ^2 in Table 5.9. By calculating the ratio between our achieved residual rms and the predicted rms in the case of the presence of only Poisson noise, we determine that we range from 3% to 34% above the photon limit for the G102 data and 2% below to 51% above it for G141.

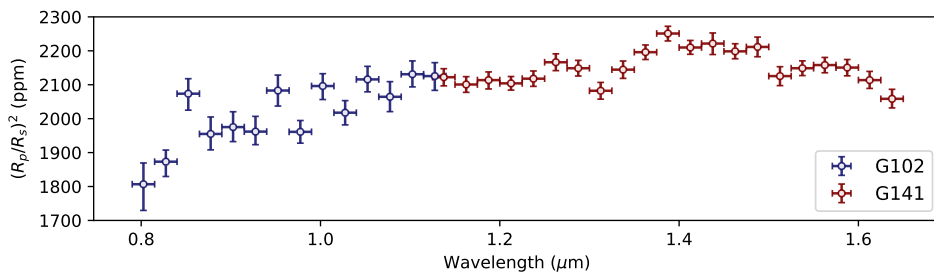


Figure 5.6: The full *HST*/WFC3 transmission spectrum of KELT-11 b using the G102 (midnight blue bins) and G141 (maroon bins) grisms. The data for this figure is listed in Tabel 5.5 and 5.6.

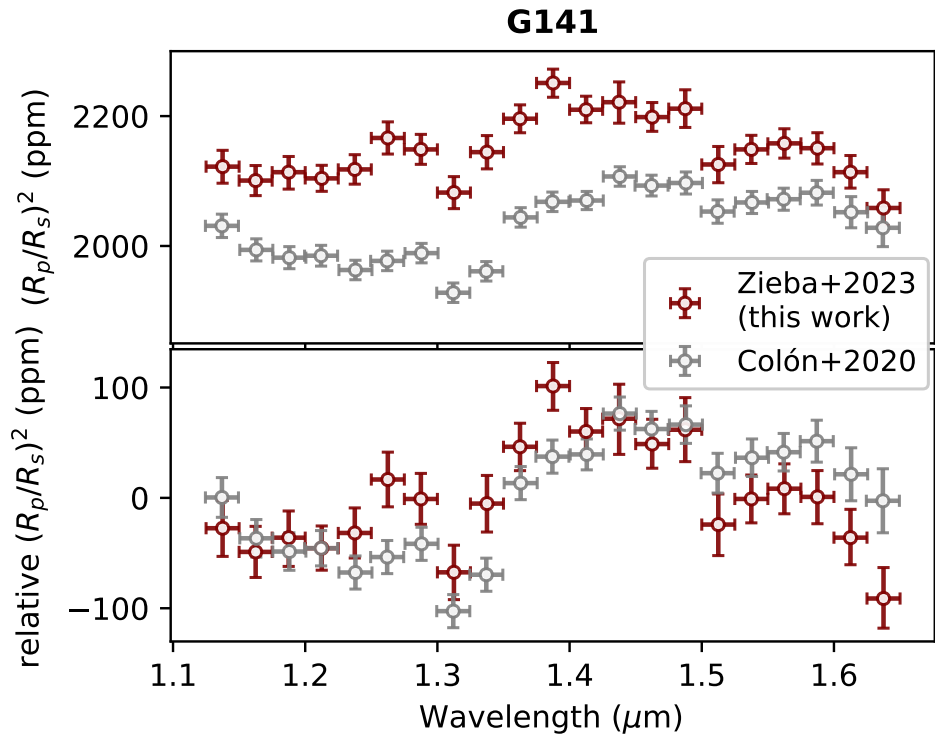


Figure 5.7: Comparison of the G141 transmission spectrum of KELT-11 b presented in this work (maroon bins) compared to the spectrum published in Colón et al. (2020) (gray bins). In the lower panel, we subtracted the mean transit depth from each transmission spectrum.

Table 5.5: Planet-to-star ratio (R_p/R_s) and transit depth $(R_p/R_s)^2$ in ppm for each spectroscopic light curve fit using the G102 grism data. Each of the bins has a half width of 0.0125 μm . So e.g., the 1.1275 μm bin covers the wavelengths 1.115 μm to 1.140 μm . The R_p/R_s values listed in the Table correspond to the median of the posterior distribution and the errorbars to the 14th and 86th percentiles.

$\lambda_{\text{mid}}(\mu\text{m})$	R_p/R_s	$(R_p/R_s)^2$ (ppm)
0.8025	$0.04251^{+0.00074}_{-0.00091}$	1807^{+63}_{-77}
0.8275	$0.04328^{+0.00040}_{-0.00050}$	1873^{+34}_{-44}
0.8525	$0.04554^{+0.00048}_{-0.00053}$	2074^{+44}_{-49}
0.8775	$0.04422^{+0.00057}_{-0.00053}$	1955^{+50}_{-47}
0.9025	$0.04444^{+0.00051}_{-0.00048}$	1975^{+45}_{-43}
0.9275	$0.04429^{+0.00051}_{-0.00044}$	1962^{+45}_{-39}
0.9525	$0.04564^{+0.00050}_{-0.00050}$	2083^{+46}_{-46}
0.9775	$0.04428^{+0.00038}_{-0.00038}$	1961^{+33}_{-33}
1.0025	$0.04578^{+0.00040}_{-0.00043}$	2096^{+36}_{-40}
1.0275	$0.04492^{+0.00040}_{-0.00040}$	2018^{+36}_{-36}
1.0525	$0.04600^{+0.00042}_{-0.00040}$	2116^{+38}_{-37}
1.0775	$0.04544^{+0.00049}_{-0.00048}$	2064^{+45}_{-44}
1.1025	$0.04616^{+0.00043}_{-0.00041}$	2131^{+39}_{-37}
1.1275	$0.04610^{+0.00043}_{-0.00046}$	2126^{+40}_{-42}

Table 5.6: Same as Table 5.5 but for the spectroscopic light curve fits to the G141 grism data.

λ_{mid} (μm)	R_p/R_s	$(R_p/R_s)^2$ (ppm)
1.1375	$0.04607^{+0.00027}_{-0.00028}$	2122^{+25}_{-26}
1.1625	$0.04583^{+0.00025}_{-0.00025}$	2101^{+23}_{-23}
1.1875	$0.04597^{+0.00026}_{-0.00028}$	2114^{+24}_{-26}
1.2125	$0.04587^{+0.00022}_{-0.00022}$	2104^{+20}_{-20}
1.2375	$0.04602^{+0.00025}_{-0.00025}$	2118^{+23}_{-23}
1.2625	$0.04654^{+0.00027}_{-0.00027}$	2166^{+25}_{-25}
1.2875	$0.04635^{+0.00025}_{-0.00025}$	2149^{+23}_{-23}
1.3125	$0.04563^{+0.00027}_{-0.00027}$	2082^{+25}_{-25}
1.3375	$0.04631^{+0.00028}_{-0.00028}$	2145^{+26}_{-26}
1.3625	$0.04686^{+0.00023}_{-0.00023}$	2196^{+21}_{-22}
1.3875	$0.04744^{+0.00022}_{-0.00023}$	2251^{+21}_{-22}
1.4125	$0.04701^{+0.00022}_{-0.00021}$	2210^{+21}_{-20}
1.4375	$0.04713^{+0.00033}_{-0.00034}$	2221^{+31}_{-32}
1.4625	$0.04689^{+0.00024}_{-0.00023}$	2198^{+22}_{-22}
1.4875	$0.04703^{+0.00031}_{-0.00031}$	2211^{+29}_{-29}
1.5125	$0.04610^{+0.00030}_{-0.0003}$	2125^{+28}_{-28}
1.5375	$0.04635^{+0.00023}_{-0.00023}$	2149^{+22}_{-22}
1.5625	$0.04645^{+0.00024}_{-0.00024}$	2158^{+23}_{-23}
1.5875	$0.04637^{+0.00026}_{-0.00026}$	2151^{+24}_{-24}
1.6125	$0.04597^{+0.00028}_{-0.00027}$	2114^{+26}_{-25}
1.6375	$0.04537^{+0.00031}_{-0.00030}$	2058^{+28}_{-27}

5.4 Discussion

5.4.1 Systematic bias from divide-white fitting technique

In Figure 5.7 we compare our reanalyzed G141 transmission spectrum of KELT-11 b with the one previously published in Colón et al. (2020). Notably, our spectrum reveals a distinctive “water bump” around 1.4 μm , a characteristic feature successfully identified in the atmospheres of numerous exoplanets using *HST*/WFC3 G141 (e.g., Deming et al. 2013; Huitson et al. 2013; Fraine et al. 2014; Kreidberg et al. 2014b; Evans et al. 2016). The initial shape of the G141 transmission spectrum, characterized by an unusually flat profile at the red edge of the detector, suggested the presence of another absorber at longer wavelengths, potentially HCN (we refer to Figure 16 in Colón et al. 2020). In Figure 5.16, we demonstrate that the shape of our spectrum remains consistent across different model assumptions (like the choice of limb darkening law or the functional form of the visit-long systematic trend), further reinforcing the robustness of our findings. We also performed a **divide-white** fit to the G141 data in this work and were able to recreate the transmission spectrum published in Colón et al. (2020). In Figure 5.8, we show that the systematic parameters in the spectrum are not constant but reveal substantial variations across the detector. Consequently, we conclude that employing the **divide-white** approach is unsuitable for this dataset.

Kreidberg et al. (2015) noted that the **divide-white** technique might not always be appropriate because the systematics observed for the WFC3 detector are known to depend on the amount of illumination received (Berta et al. 2012; Swain et al. 2013). For our observations, the flux received by the different parts of the detector varies significantly: the spectroscopic bin corresponding to the most illuminated part of the detector receives 400% and 40% more flux than the least illuminated part for G102 and G141, respectively (see Fig. 5.4). The observations taken in Kreidberg et al. (2015) varied by 30%, which was reportedly enough to make **divide-white** an inadequate model choice. This might therefore be important to consider when working on *HST*/WFC3 near-infrared datasets of earlier type stars that exhibit significant brightness variations across wavelengths. Notably, in the two instances where the **divide-white** method substantially influenced the final spectrum shape, the stars in question were of earlier types: KELT-11 (this work) is a retired A star ($T_{\text{eff}} = 5375\text{K}$) and WASP-12 studied in Kreidberg et al. (2015) has a spectral type of G0V ($T_{\text{eff}} = 6300\text{K}$) (Bergfors et al. 2013; Hebb et al. 2009).

5.4.2 Comparison of G141 to other hot inflated sub-Saturns

Like in Colón et al. (2020), we compare our measured G141 spectrum with previously studied hot, inflated sub-Saturns like WASP-39 b (Wakeford et al. 2018) and WASP-107 b (Kreidberg et al. 2018b). Figure 5.9 shows the transmission spectra for KELT-11 b and the other two planets, showing a clear detection of water in the atmospheres for all three planets. The presence of water was also recently confirmed for WASP-39 b (e.g., JWST Transiting Exoplanet Community Early Release Science Team et al. 2023) and WASP-107 b (Dyrek et al. 2023), indicating

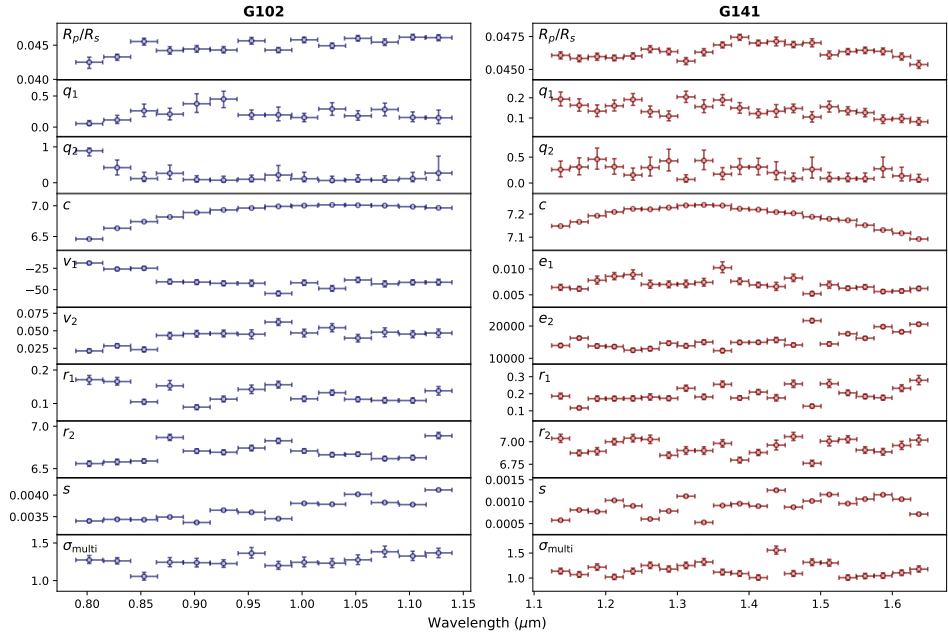


Figure 5.8: All free parameters as a function of wavelength for both datasets. The different parameters are described in Section 5.3.1.

a super-solar metallicity for both planets.

5.4.3 Shape of G102

Our G102 transmission spectrum of KELT-11 b (see Fig. 5.6) shows a decreasing transit depth with shorter wavelengths. This suggests hot faculae on the stellar photosphere, which are brighter areas on a star and are known to contaminate planetary transmission spectra (Pinhas et al. 2018). This has been observed for the mini-Neptune GJ 1214 b and the super-Earth GJ 1132 b. Their optical transmission spectra show lower transit depths compared to the infrared transits. Both of these planets orbit M-dwarfs (both approximately M4V stars Cloutier et al. 2021; Berta-Thompson et al. 2015), which are prone to exhibit photospheric heterogeneities like star spots and faculae, which influence the final transmission spectrum (Rackham et al. 2018). However, KELT-11 is not a late-type star but rather a retired A-type. Previous observations of the star also did not suggest significant stellar variability (see Colón et al. 2020, for a discussion of ground-based photometry). *TESS* observations taken in March 2019 and February 2023 also seem to not exhibit any periodic, coherent variability (Colón et al. 2020). The *CHEOPS* observations of KELT-11 b taken during its commissioning in March 2020 showed some variability, possibly due to granulation Benz et al. (2021). The amplitude of the signal is approximately 200 ppm on timescales between 30 minutes and 4 hours. We do not observe the same; on the contrary, our white light curves using

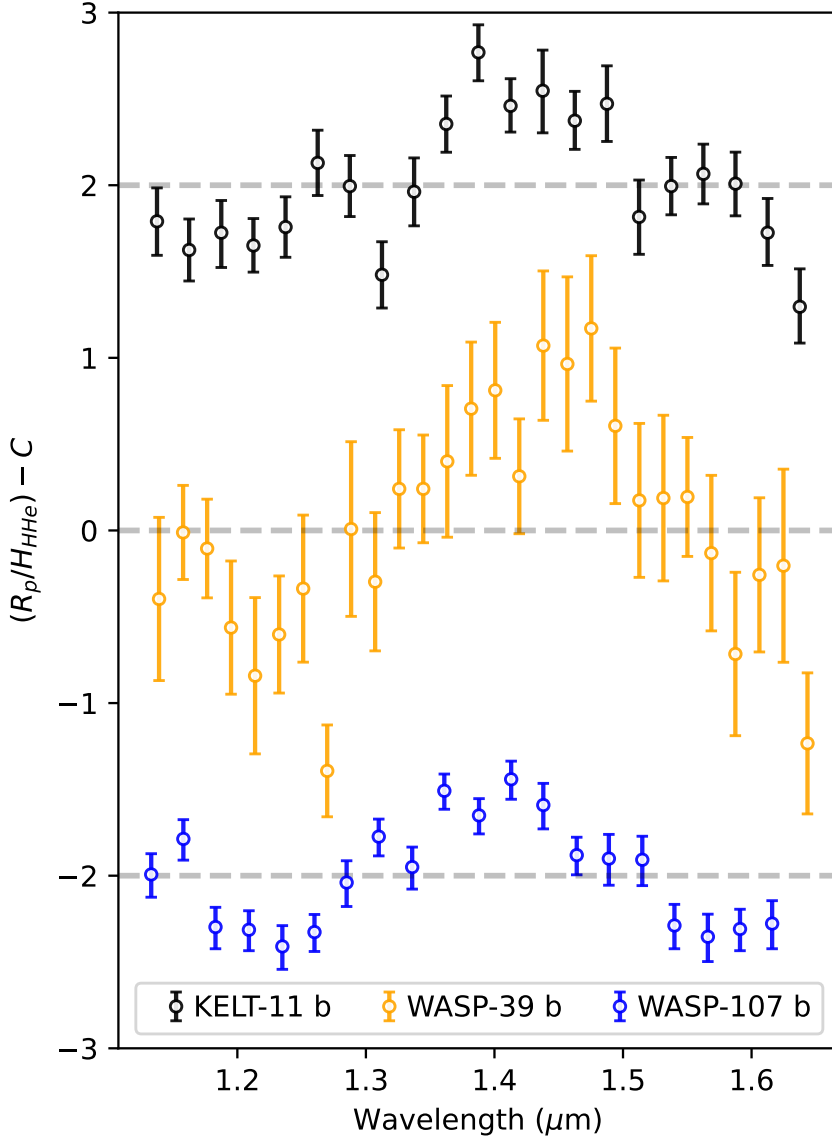


Figure 5.9: Comparison of the G141 transmission spectra of hot, inflated sub-Saturn planets following Colón et al. (2020). The KELT-11 b spectrum in the plot comes from this work, the WASP-39 b spectrum was published in Wakeford et al. (2018), and the WASP-107 b spectrum in Kreidberg et al. (2018b). We divided the planetary radius by the scale height ($H = \frac{k_B T_{\text{eq}}}{\mu g}$), assuming a molecular weight of $\mu = 2.3$ g/mol (see Crossfield & Kreidberg 2017; Colón et al. 2020). To guide the eye, we show the mean for each planet as a horizontal line. All planets exhibit the well-known water absorption feature around $1.4 \mu\text{m}$. We shifted the spectra by a constant C , for visualization purposes.

the G102 and G141 grism data seem stable and have high precision. Our Allan deviation plots (see Fig. 5.17) hint that we are not dominated by correlated noise from unaccounted instrumental systematics or stellar variability.

5.5 Summary

In this work, we have analyzed the *HST*/WFC3 data of KELT-11 b. Here, we summarize our main findings:

- The unusual shape of the *HST*/WFC3 G141 grism changes significantly when not using the `divide-white` technique, which assumes that the systematics have the same shape across the whole detector. We determine that `divide-white` is not adequate for this dataset because the systematic noise varies with wavelength. This should be taken into consideration for the analysis of other earlier type star WFC3 NIR data, where the stellar flux strongly varies with wavelength.
- Our G102 and G141 white light curves do not show any star spot crossing events or other forms of variability. We archive a precise white light curve with a root-mean-square (rms) of 71.6 ppm (for G102) and 37.6 ppm (for G141) for the residuals.
- Our G102 transmission spectrum of KELT-11 b reveals diminished transit depths at shorter wavelengths, likely attributed to contamination by faculae on the stellar photosphere during the time of observations. While this phenomenon has been previously observed in late-type stars like GJ 1132 and GJ 1214, it represents a novel observation for an earlier-type star like KELT-11.

In the future, using *JWST* to observe KELT-11 b presents a significant opportunity to probe its C/O ratio and provide crucial insights into the formation pathways of these inflated sub-Saturns. Additionally, KELT-11 b's high equilibrium temperature, low density, and bright host star make it an optimal target for atmospheric studies using *JWST*'s transmission spectroscopy, making it one of the most observable planets to date.

Acknowledgements

This research is based on observations made with the NASA/ESA Hubble Space Telescope obtained from the Space Telescope Science Institute, which is operated by the Association of Universities for Research in Astronomy, Inc., under NASA contract NAS 5-26555. These observations are associated with programs #15255 and #15926.

This research has made use of the NASA Exoplanet Archive, which is operated by the California Institute of Technology, under contract with the National Aeronautics and Space Administration under the Exoplanet Exploration Program.

We gratefully acknowledge the packages and tools that made this work possible: **batman** (Kreidberg 2015), **PACMAN** (Zieba & Kreidberg 2022), **dynesty** (Speagle 2020; Kozlov et al. 2023b; Skilling 2004, 2006; Higson et al. 2019), **numpy** (Harris et al. 2020), **matplotlib** (Hunter 2007a), **astropy** (Astropy Collaboration et al. 2013, 2018, 2022).

Appendix

5.A Best fitting white light curve model

In order to find the two models that describe each of our datasets the best, we use the Bayesian Information Criterion (BIC; Schwarz 1978). The BIC is commonly used in exoplanet science for model selection. It measures how well a given model describes the data depending on the number of free parameters in the model and the amount of data points. It is defined as:

$$\text{BIC} = -2\mathcal{L}_{\max} + k \ln(N), \quad (5.4)$$

where k is the number of free parameters in the model, N is the number of data points, and \mathcal{L}_{\max} is the maximum likelihood given by:

$$\mathcal{L}_{\max} = -\frac{1}{2} \sum_i \left[\left(\frac{\text{data}_i - \text{model}_i}{\text{err}_i} \right)^2 + \ln(2\pi \text{err}_i^2) \right], \quad (5.5)$$

with data_i being the measured flux, err_i its uncertainty, and model_i the flux predicted by the model. From Equation 5.4 we can conclude that the preferred model is the one with the lower BIC value. It penalizes model complexity (high k) to avoid overfitting and penalizes models that do not fit the data well (low \mathcal{L}_{\max}).

For each of the models we tested, we used the dynamic nested sampling code **dynesty** (Speagle 2020; Koposov et al. 2023a) to estimate the free parameters and their uncertainties. We used the following setup for all of our runs: `nlive_init=1000`, `dlogz_init=0.0001`, `nlive_batch=100`, and `maxbatch=100`⁷.

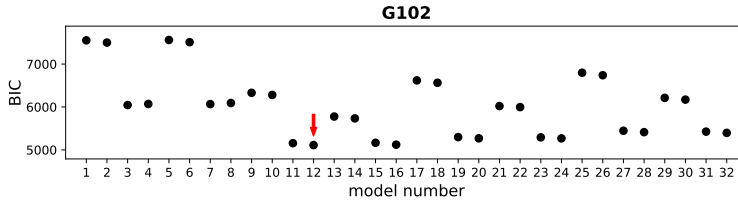


Figure 5.10: The Bayesian Information Criterion (BIC) for each model fitted to the G102 data. The model numbers are explained in Table 5.7. The red arrow marks the model with the lowest BIC.

⁷The various arguments are explained in **dynesty**'s documentation: https://dynesty.readthedocs.io/en/latest/api.html#dynesty.dynamicsampler.DynamicSampler.run_nested

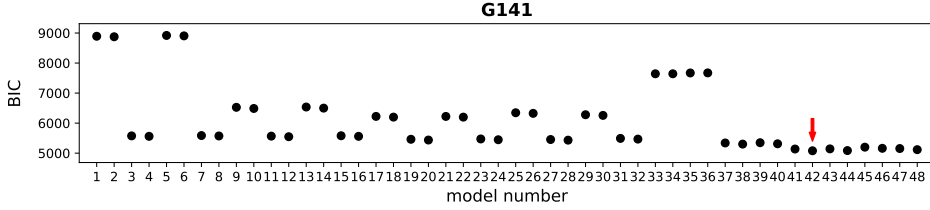


Figure 5.11: The Bayesian Information Criterion (BIC) for each model fitted to the G141 data. The model numbers are explained in Table 5.8. The red arrow marks the model with the lowest BIC.

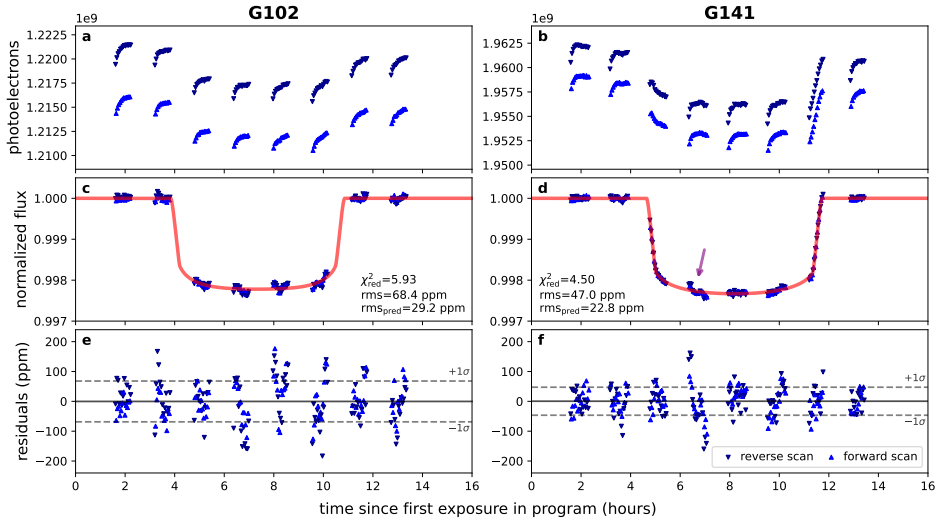


Figure 5.12: Best white light curve fits for the G102 and G141 observations when only removing the first orbit.

Table 5.7: All 32 white light curve fits run on the G102 dataset. The fit with the lowest Bayesian Information Criterion (BIC) is marked in bold. M_i : model number used in Figure 5.10, “visit model”: function from Equation 5.3 used to model the visit-long systematics, “rem. orbits”: lists which orbit was removed when performing the fit (e.g., “1,2” corresponds to the removal of the first and second orbit), LD: linear limb-darkening (1) or two parameter limb darkening (2) following Kipping (2013), “ r_3 ”: “Y” if the delay function was used in the fit, or “N” if not, “ $N_{f.p.}$ ”: number of free parameters in the fit, rms (ppm): the root-mean-square of the residuals in parts-per-million (ppm), $\times\text{phot.}$: the factor by which the rms of the residuals is above the photon limit, χ^2 : the chi-squared, $\chi^2_{\text{red.}}$: the reduced chi-squared, BIC: the Bayesian Information Criterion, ΔBIC : the difference between the respective BIC (BIC_i) and the lowest BIC in the list (BIC_{\min}) (so: $\Delta\text{BIC} = \text{BIC}_i - \text{BIC}_{\min}$), and $\log \mathcal{Z}$ the final evidence outputted by **dynesty**. The predicted rms in the case of photon-noise-limited observations for G102 was 29.2 ppm.

M_i	visit model	rem. orbits	LD	r_3	$N_{f.p.}$	rms (ppm)	$\times\text{phot.}$	χ^2	$\chi^2_{\text{red.}}$	BIC	ΔBIC	$\log \mathcal{Z}$	$\Delta \log \mathcal{Z}$
1	lin.	1	1	N	11	111.7	3.8	2936.9	15.54	7553.2	2441.6	-2700.9	-393.9
2	lin.	1	2	N	12	110.6	3.8	2879.8	15.32	7501.4	2389.8	-2699.9	-393.0
3	lin.	1,2	1	N	11	98.6	3.4	2000.4	12.20	6045.4	933.8	-2350.8	-43.9
4	lin.	1,2	2	N	12	99.0	3.4	2019.9	12.39	6070.2	958.5	-2349.9	-43.0
5	lin.	1	1	Y	12	111.8	3.8	2940.2	15.64	7561.8	2450.1	-2701.7	-394.7
6	lin.	1	2	Y	13	110.7	3.8	2883.5	15.42	7510.4	2398.7	-2702.4	-395.5
7	lin.	1,2	1	Y	12	99.0	3.4	2016.8	12.37	6067.1	955.4	-2355.9	-48.9
8	lin.	1,2	2	Y	13	99.5	3.4	2036.5	12.57	6091.9	980.3	-2353.9	-47.0
9	quad.	1	1	N	12	85.2	2.9	1708.8	9.09	6330.4	1218.7	-2658.8	-351.8
10	quad.	1	2	N	13	83.8	2.9	1653.6	8.84	6280.5	1168.9	-2658.3	-351.3
11	quad.	1,2	1	N	12	73.3	2.5	1105.7	6.78	5155.9	44.3	-2310.1	-3.2
12	quad.	1,2	2	N	13	71.6	2.5	1056.3	6.52	5111.6	0.0	-2306.9	0.0
13	quad.	1	1	Y	13	69.9	2.4	1150.2	6.15	5777.1	665.5	-2624.8	-317.8
14	quad.	1	2	Y	14	68.4	2.3	1102.1	5.93	5734.3	622.7	-2621.0	-314.0
15	quad.	1,2	1	Y	13	73.4	2.5	1110.2	6.85	5165.6	53.9	-2313.2	-6.3
16	quad.	1,2	2	Y	14	71.8	2.5	1061.0	6.59	5121.5	9.9	-2311.0	-4.0

Table 5.7: Continued.

17	exp.	1	1	N	12	92.2	3.2	1998.3	10.63	6619.9	1508.3	-2671.0	-364.1
18	exp.	1	2	N	13	90.7	3.1	1936.9	10.36	6563.8	1452.2	-2671.9	-364.9
19	exp.	1,2	1	N	12	77.8	2.7	1247.1	7.65	5297.3	185.6	-2317.7	-10.8
20	exp.	1,2	2	N	13	76.8	2.6	1213.8	7.49	5269.1	157.5	-2317.9	-10.9
21	exp.	1	1	Y	13	77.0	2.6	1394.4	7.46	6021.3	909.7	-2642.6	-335.6
22	exp.	1	2	Y	14	76.2	2.6	1364.9	7.34	5997.1	885.5	-2640.0	-333.1
23	exp.	1,2	1	Y	13	77.5	2.7	1236.2	7.63	5291.6	180.0	-2320.2	-13.2
24	exp.	1,2	2	Y	14	76.6	2.6	1207.0	7.50	5267.6	155.9	-2320.3	-13.4
25	log.	1	1	N	12	96.2	3.3	2176.5	11.58	6798.1	1686.5	-2681.0	-374.0
26	log.	1	2	N	13	94.8	3.2	2113.0	11.30	6739.9	1628.2	-2679.4	-372.4
27	log.	1,2	1	N	12	82.3	2.8	1395.7	8.56	5445.9	334.3	-2325.4	-18.5
28	log.	1,2	2	N	13	81.2	2.8	1357.5	8.38	5412.8	301.2	-2323.1	-16.2
29	log.	1	1	Y	13	82.1	2.8	1585.1	8.48	6212.1	1100.4	-2651.4	-344.5
30	log.	1	2	Y	14	80.9	2.8	1539.7	8.28	6171.9	1060.2	-2647.1	-340.2
31	log.	1,2	1	Y	13	81.6	2.8	1370.0	8.46	5425.4	313.7	-2324.6	-17.6
32	log.	1,2	2	Y	14	80.6	2.8	1336.0	8.30	5396.5	284.9	-2322.7	-15.8

Table 5.8: All 32 white light curve fits run on the G141 dataset. Parameters like in Table 5.7. The predicted rms in the case of photon-noise-limited observations for G141 was 22.8 ppm.

M_i	visit model	rem. orbits	LD	r_3	$N_{f.p.}$	rms (ppm)	\times phot.	χ^2	$\chi^2_{red.}$	BIC	Δ BIC	$\log \mathcal{Z}$	$\Delta \log \mathcal{Z}$
1	lin.	1	1	N	11	92.3	4.0	3647.8	17.21	8892.4	3812.4	-3073.4	-557.0
2	lin.	1	2	N	12	92.0	4.0	3625.9	17.19	8875.9	3795.9	-3074.4	-558.0

Table 5.8: Continued.

3	lin.	1,2	1	N	11	52.7	2.3	1030.1	5.66	5575.4	495.5	-2564.0	-47.6
4	lin.	1,2	2	N	12	52.2	2.3	1009.7	5.58	5560.3	480.4	-2565.5	-49.1
5	lin.	1	1	Y	12	92.5	4.1	3669.5	17.39	8919.4	3839.4	-3078.8	-562.4
6	lin.	1	2	Y	13	92.3	4.0	3649.9	17.38	8905.3	3825.3	-3078.8	-562.4
7	lin.	1,2	1	Y	12	52.9	2.3	1036.1	5.72	5586.7	506.8	-2569.7	-53.3
8	lin.	1,2	2	Y	13	52.4	2.3	1016.9	5.65	5572.8	492.8	-2569.4	-53.0
9	quad.	1	1	N	12	54.6	2.4	1276.4	6.05	6526.3	1446.4	-2972.9	-456.5
10	quad.	1	2	N	13	53.7	2.4	1232.7	5.87	6488.1	1408.1	-2970.2	-453.8
11	quad.	1,2	1	N	12	52.4	2.3	1016.1	5.61	5566.8	486.8	-2570.5	-54.1
12	quad.	1,2	2	N	13	51.7	2.3	991.9	5.51	5547.8	467.8	-2572.5	-56.1
13	quad.	1	1	Y	13	54.7	2.4	1280.8	6.10	6536.2	1456.2	-2976.4	-460.0
14	quad.	1	2	Y	14	53.8	2.4	1238.6	5.93	6499.4	1419.4	-2972.9	-456.5
15	quad.	1,2	1	Y	13	52.6	2.3	1023.9	5.69	5579.8	499.8	-2577.8	-61.4
16	quad.	1,2	2	Y	14	51.9	2.3	999.2	5.58	5560.4	480.4	-2577.4	-61.0
17	exp.	1	1	N	12	47.7	2.1	974.2	4.62	6224.2	1144.2	-2942.9	-426.5
18	exp.	1	2	N	13	47.0	2.1	944.8	4.50	6200.1	1120.1	-2941.5	-425.1
19	exp.	1,2	1	N	12	49.6	2.2	911.5	5.04	5462.1	382.1	-2560.6	-44.2
20	exp.	1,2	2	N	13	48.8	2.1	881.0	4.89	5436.9	356.9	-2559.8	-43.4
21	exp.	1	1	Y	13	47.5	2.1	967.8	4.61	6223.1	1143.1	-2947.5	-431.1
22	exp.	1	2	Y	14	46.8	2.1	939.1	4.49	6199.9	1119.9	-2941.9	-425.5
23	exp.	1,2	1	Y	13	49.8	2.2	916.8	5.09	5472.7	392.7	-2565.7	-49.3
24	exp.	1,2	2	Y	14	48.9	2.1	885.8	4.95	5447.0	367.0	-2564.0	-47.6
25	log.	1	1	N	12	50.6	2.2	1095.6	5.19	6345.5	1265.6	-2953.6	-437.2
26	log.	1	2	N	13	50.0	2.2	1069.9	5.10	6325.3	1245.3	-2953.6	-437.2

Table 5.8: Continued.

27	log.	1,2	1	N	12	49.4	2.2	903.7	4.99	5454.3	374.3	-2557.6	-41.2
28	log.	1,2	2	N	13	48.7	2.1	877.0	4.87	5432.9	352.9	-2557.6	-41.2
29	log.	1	1	Y	13	48.9	2.1	1024.1	4.88	6279.5	1199.5	-2945.1	-428.7
30	log.	1	2	Y	14	48.3	2.1	996.8	4.77	6257.6	1177.6	-2942.8	-426.4
31	log.	1,2	1	Y	13	50.3	2.2	935.7	5.20	5491.6	411.7	-2560.5	-44.1
32	log.	1,2	2	Y	14	49.5	2.2	906.7	5.07	5467.8	387.8	-2559.2	-42.8
33	lin.	1,5	1	N	11	91.4	4.0	3097.6	17.02	7643.0	2563.0	-2666.2	-149.8
34	lin.	1,5	2	N	12	91.3	4.0	3092.6	17.09	7643.3	2563.3	-2667.8	-151.4
35	lin.	1,5	1	Y	12	91.7	4.0	3119.9	17.24	7670.6	2590.7	-2670.1	-153.7
36	lin.	1,5	2	Y	13	91.7	4.0	3116.8	17.32	7672.8	2592.8	-2671.8	-155.4
37	quad.	1,5	1	N	12	46.1	2.0	789.0	4.36	5339.7	259.7	-2551.2	-34.8
38	quad.	1,5	2	N	12	45.0	2.0	750.6	4.15	5301.4	221.4	-2546.9	-30.5
39	quad.	1,5	1	Y	13	46.2	2.0	792.2	4.40	5348.2	268.2	-2555.6	-39.2
40	quad.	1,5	2	Y	14	45.0	2.0	750.8	4.20	5312.1	232.1	-2551.6	-35.2
41	exp.	1,5	1	N	12	39.8	1.7	586.9	3.24	5137.7	57.7	-2525.5	-9.1
42	exp.	1,5	2	N	13	37.6	1.6	524.0	2.91	5080.0	0.0	-2516.4	0.0
43	exp.	1,5	1	Y	13	39.8	1.7	586.9	3.26	5142.9	62.9	-2527.0	-10.6
44	exp.	1,5	2	Y	14	37.6	1.6	525.4	2.94	5086.6	6.7	-2517.7	-1.3
45	log.	1,5	1	N	12	41.8	1.8	648.7	3.58	5199.4	119.5	-2531.5	-15.1
46	log.	1,5	2	N	13	40.4	1.8	605.8	3.37	5161.7	81.8	-2525.7	-9.3
47	log.	1,5	1	Y	13	40.2	1.8	598.3	3.32	5154.3	74.3	-2522.6	-6.2
48	log.	1,5	2	Y	14	38.7	1.7	555.3	3.10	5116.5	36.5	-2517.9	-1.5

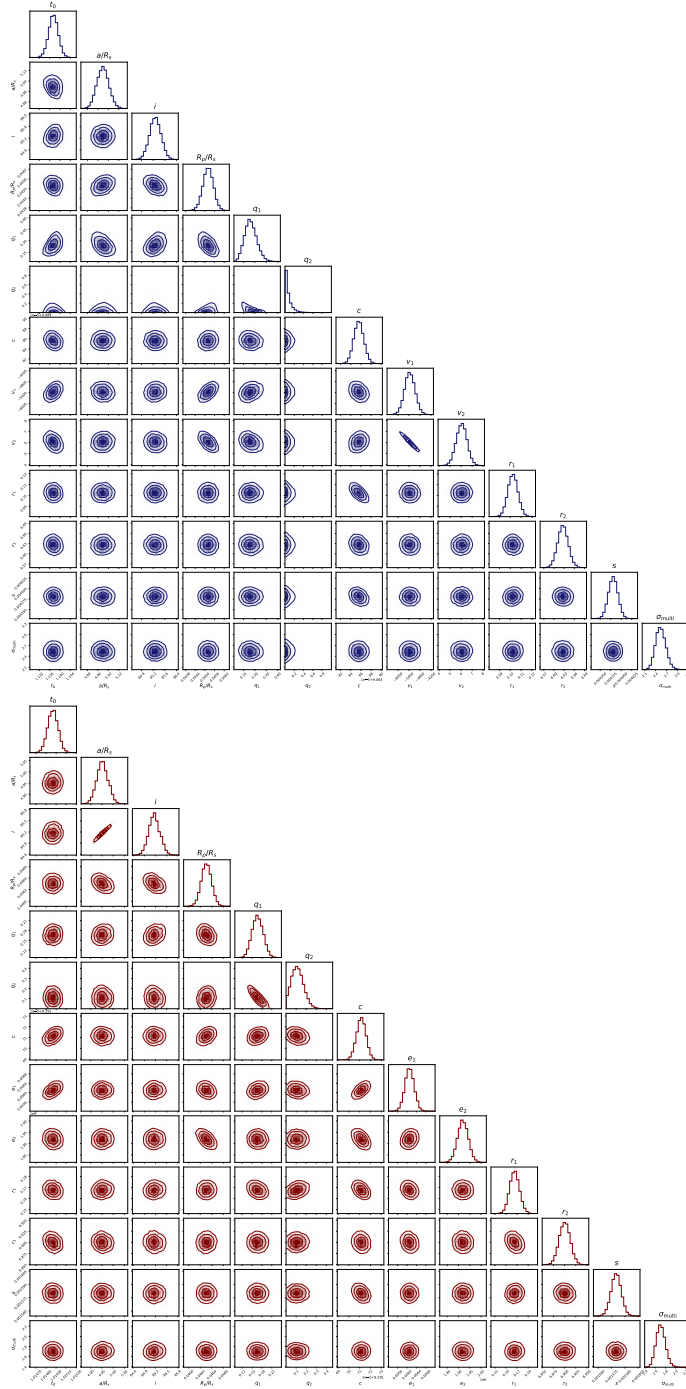


Figure 5.13: Corner plots for the white light curve fits based on the G102 and G141 data sets on the left and right sides, respectively.

5.B Spectroscopic light curve fits

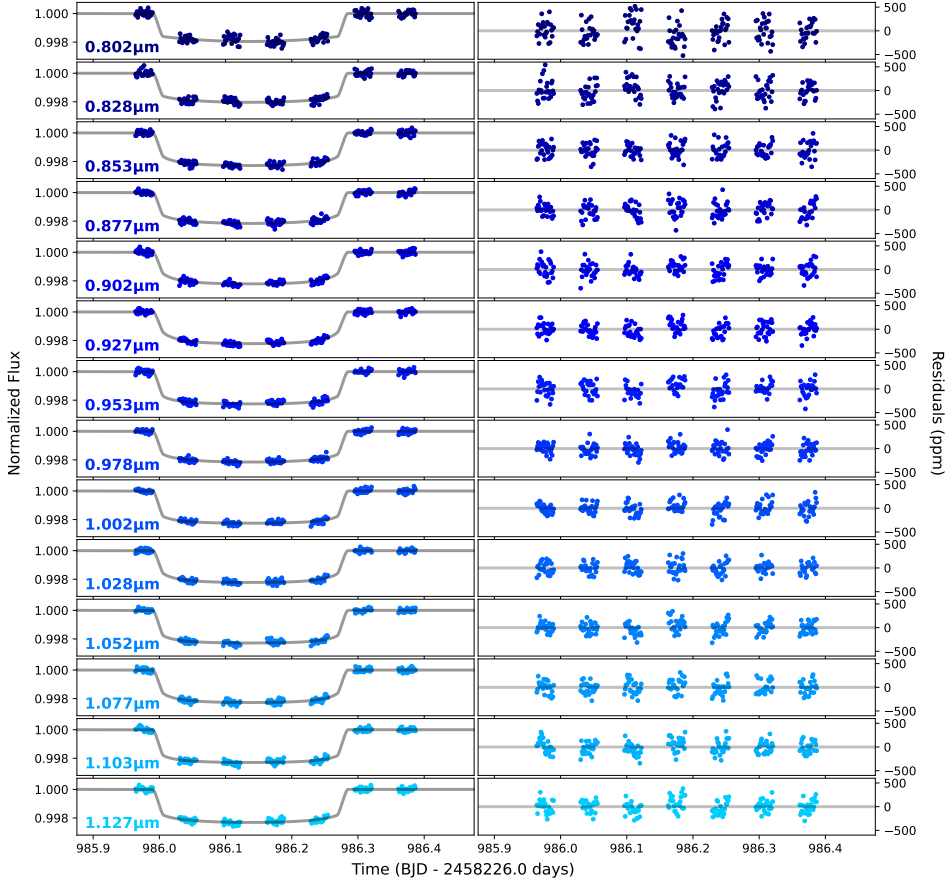


Figure 5.14: All spectroscopic light curve fits for the G102 data. The left column shows the best-fitting transit model to the light curve with the systematics removed. The right column shows the residuals of our best light curve fit.

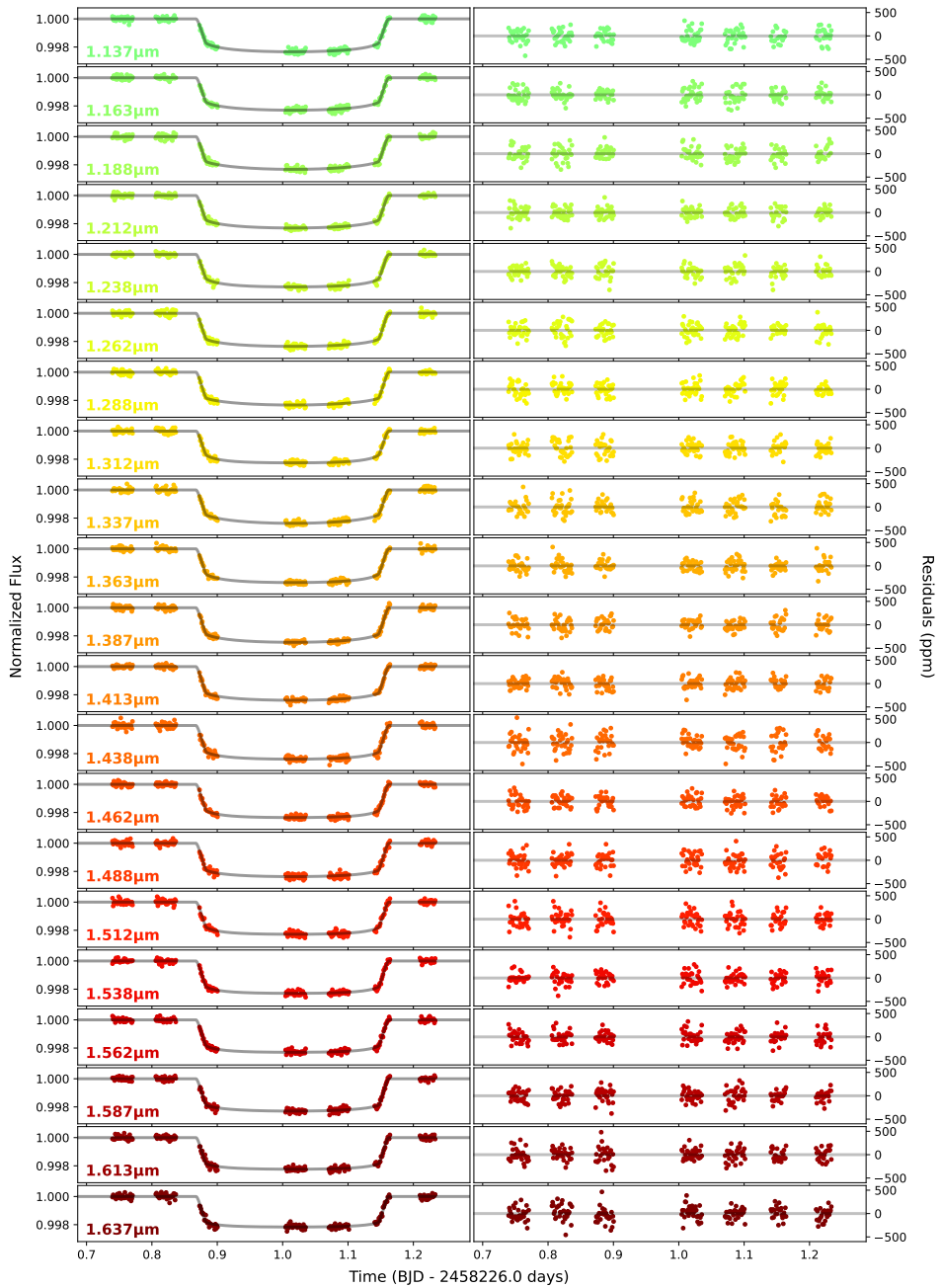


Figure 5.15: Same as Figure 5.14 but for the G141 data.

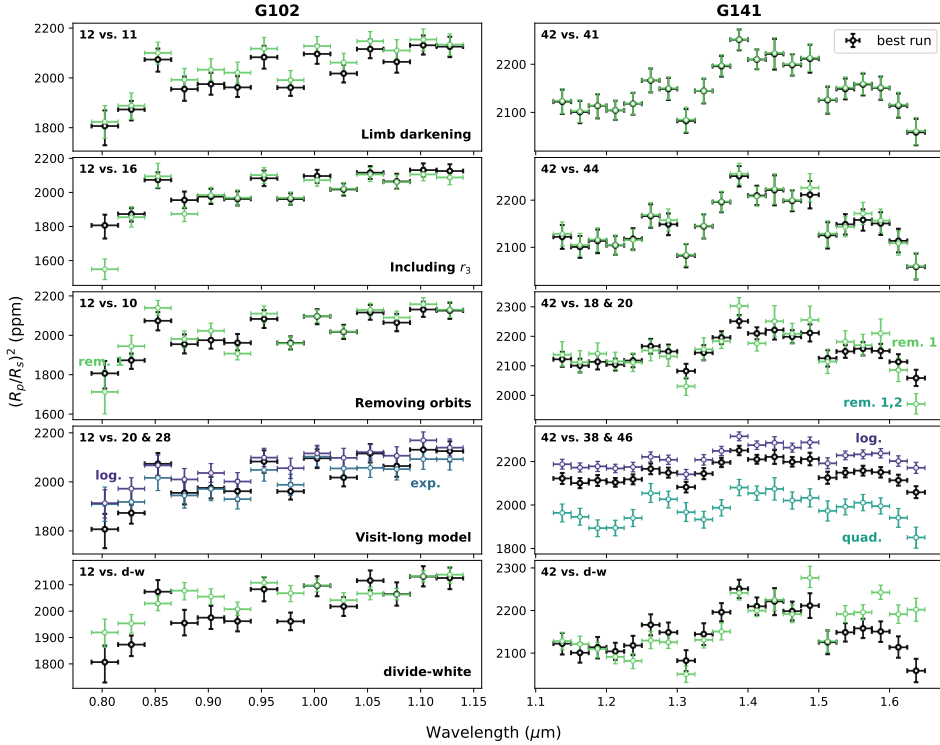


Figure 5.16: Plot showing how different model assumptions change the transmission spectrum for the G102 data (left column) and for the G141 data (right column). The top left of each subplot lists the specific models shown following the model number M_i in Table 5.7 (for G102) and Table 5.8 (for G141). The last row compares our best run (black), with a **divide-white** run. The transit depth remains fairly flat on the red edge for the **divide-white** G141 transmission spectrum, like in Colón et al. (2020) (see Fig. 5.7).

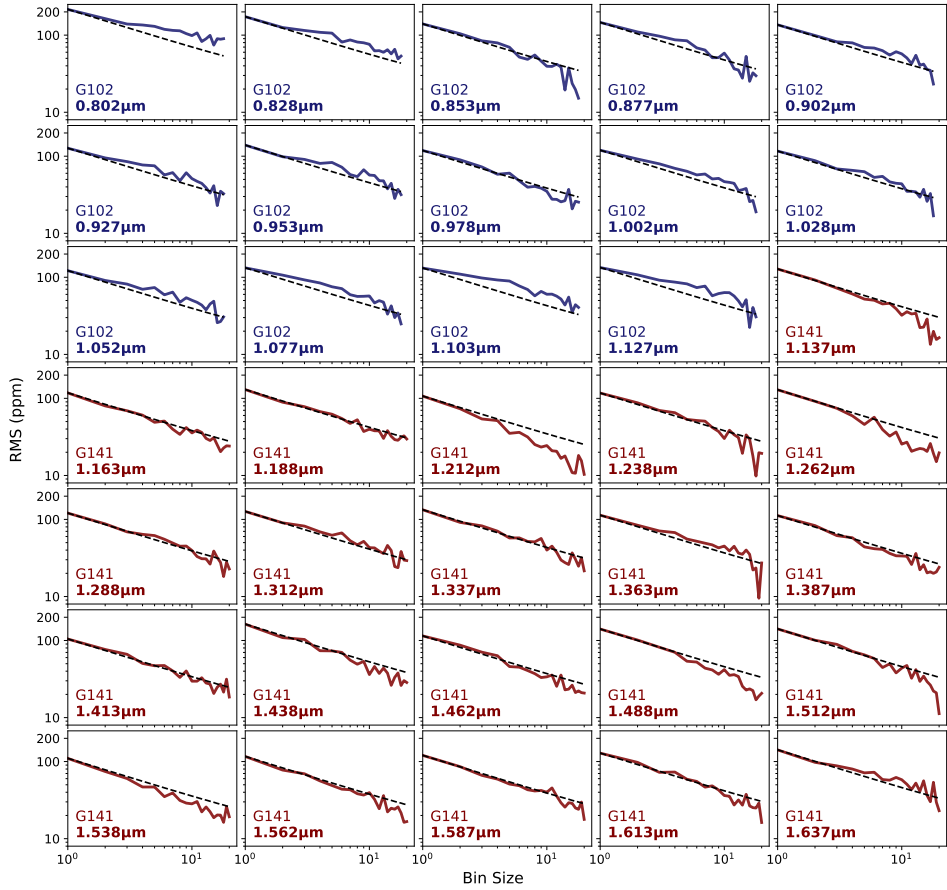


Figure 5.17: Allan deviation plots for all spectroscopic light curve fits.

Table 5.9: Various properties of the spectroscopic light curve fits. The predicted rms in the case of photon-noise-limited observations is $\text{rms}_{\text{pred.}}$. σ_{multi} is the uncertainty-multiplier factor described in Section 5.3.1. Other parameters (rms, $\times_{\text{phot.}}$, χ^2 , and $\chi_{\text{red.}}^2$) are explained in Table 5.7. q_1 and q_2 are the parameters of the quadratic limb darkening law following the Kipping (2013) parameterization. We used q_1 and q_2 to derive the two parameters u_1 and u_2 from the popular quadratic limb darkening law.

λ_{mid} (μm)	rms	$\text{rms}_{\text{pred.}}$	$\times_{\text{phot.}}$	χ^2	$\chi_{\text{red.}}^2$	σ_{multi}	q_1	q_2	u_1	u_2
G102										
0.802	215.4	190.2	1.13	224	1.36	1.27	$0.06^{+0.05}_{-0.03}$	$0.89^{+0.08}_{-0.14}$	$0.39^{+0.10}_{-0.12}$	$-0.17^{+0.06}_{-0.05}$
0.828	173.3	153.7	1.13	223	1.35	1.26	$0.11^{+0.07}_{-0.06}$	$0.42^{+0.21}_{-0.21}$	$0.27^{+0.09}_{-0.10}$	$0.05^{+0.18}_{-0.12}$
0.853	139.7	135.2	1.03	187	1.13	1.06	$0.26^{+0.11}_{-0.09}$	$0.12^{+0.18}_{-0.08}$	$0.12^{+0.13}_{-0.08}$	$0.39^{+0.16}_{-0.22}$
0.877	146.1	123.7	1.18	244	1.48	1.24	$0.21^{+0.10}_{-0.09}$	$0.26^{+0.23}_{-0.16}$	$0.23^{+0.11}_{-0.13}$	$0.21^{+0.22}_{-0.21}$
0.902	135.9	113.5	1.20	251	1.52	1.24	$0.38^{+0.16}_{-0.14}$	$0.09^{+0.11}_{-0.06}$	$0.11^{+0.09}_{-0.07}$	$0.50^{+0.18}_{-0.21}$
0.927	126.9	108.0	1.17	242	1.46	1.23	$0.45^{+0.13}_{-0.14}$	$0.07^{+0.11}_{-0.05}$	$0.09^{+0.11}_{-0.07}$	$0.58^{+0.14}_{-0.22}$
0.953	139.1	104.1	1.34	312	1.89	1.36	$0.20^{+0.08}_{-0.07}$	$0.10^{+0.12}_{-0.07}$	$0.08^{+0.08}_{-0.06}$	$0.35^{+0.12}_{-0.15}$
0.978	118.3	100.9	1.17	241	1.46	1.20	$0.20^{+0.13}_{-0.09}$	$0.21^{+0.27}_{-0.16}$	$0.19^{+0.12}_{-0.13}$	$0.25^{+0.24}_{-0.24}$
1.002	119.4	99.3	1.20	253	1.53	1.24	$0.15^{+0.07}_{-0.07}$	$0.11^{+0.18}_{-0.08}$	$0.09^{+0.09}_{-0.06}$	$0.30^{+0.12}_{-0.18}$
1.028	116.3	98.0	1.19	246	1.49	1.23	$0.29^{+0.10}_{-0.10}$	$0.06^{+0.12}_{-0.05}$	$0.07^{+0.09}_{-0.05}$	$0.47^{+0.12}_{-0.19}$
1.052	121.7	98.6	1.23	267	1.61	1.28	$0.18^{+0.08}_{-0.07}$	$0.08^{+0.14}_{-0.06}$	$0.07^{+0.09}_{-0.05}$	$0.35^{+0.12}_{-0.16}$
1.077	132.5	99.3	1.33	311	1.89	1.38	$0.28^{+0.10}_{-0.10}$	$0.07^{+0.12}_{-0.05}$	$0.08^{+0.09}_{-0.06}$	$0.46^{+0.12}_{-0.19}$
1.103	131.5	101.4	1.30	294	1.78	1.33	$0.15^{+0.09}_{-0.07}$	$0.11^{+0.18}_{-0.08}$	$0.09^{+0.09}_{-0.06}$	$0.30^{+0.15}_{-0.18}$
1.127	133.6	103.8	1.29	290	1.76	1.37	$0.15^{+0.12}_{-0.09}$	$0.27^{+0.47}_{-0.20}$	$0.21^{+0.14}_{-0.14}$	$0.18^{+0.27}_{-0.29}$
G141										
1.137	127.8	115.5	1.11	236	1.29	1.14	$0.19^{+0.04}_{-0.03}$	$0.26^{+0.17}_{-0.14}$	$0.23^{+0.12}_{-0.12}$	$0.21^{+0.15}_{-0.15}$
1.163	117.6	113.1	1.04	209	1.14	1.07	$0.16^{+0.03}_{-0.03}$	$0.31^{+0.18}_{-0.15}$	$0.25^{+0.11}_{-0.11}$	$0.15^{+0.14}_{-0.14}$

Table 5.9: Continued.

1.188	129.8	109.6	1.18	271	1.48	1.22	$0.13^{+0.03}_{-0.03}$	$0.46^{+0.22}_{-0.19}$	$0.34^{+0.11}_{-0.13}$	$0.03^{+0.16}_{-0.14}$
1.212	106.8	107.5	0.99	190	1.04	1.02	$0.16^{+0.03}_{-0.03}$	$0.31^{+0.16}_{-0.14}$	$0.25^{+0.10}_{-0.11}$	$0.15^{+0.14}_{-0.13}$
1.238	117.1	105.9	1.11	236	1.29	1.14	$0.19^{+0.03}_{-0.03}$	$0.15^{+0.14}_{-0.10}$	$0.13^{+0.10}_{-0.08}$	$0.30^{+0.11}_{-0.13}$
1.262	129.0	105.9	1.22	286	1.56	1.25	$0.13^{+0.03}_{-0.03}$	$0.30^{+0.20}_{-0.16}$	$0.22^{+0.12}_{-0.11}$	$0.15^{+0.14}_{-0.15}$
1.288	120.6	105.2	1.15	254	1.39	1.18	$0.11^{+0.03}_{-0.02}$	$0.43^{+0.23}_{-0.19}$	$0.28^{+0.11}_{-0.12}$	$0.05^{+0.15}_{-0.14}$
1.312	126.8	104.0	1.22	287	1.57	1.25	$0.20^{+0.03}_{-0.03}$	$0.07^{+0.09}_{-0.05}$	$0.06^{+0.08}_{-0.05}$	$0.39^{+0.06}_{-0.10}$
1.337	133.3	103.8	1.28	318	1.74	1.32	$0.16^{+0.03}_{-0.03}$	$0.43^{+0.20}_{-0.18}$	$0.34^{+0.12}_{-0.12}$	$0.05^{+0.15}_{-0.15}$
1.363	113.3	104.1	1.09	229	1.25	1.12	$0.19^{+0.03}_{-0.03}$	$0.17^{+0.13}_{-0.10}$	$0.15^{+0.10}_{-0.09}$	$0.29^{+0.11}_{-0.12}$
1.387	112.0	105.8	1.06	216	1.18	1.09	$0.15^{+0.03}_{-0.03}$	$0.31^{+0.17}_{-0.14}$	$0.24^{+0.10}_{-0.10}$	$0.15^{+0.13}_{-0.13}$
1.413	104.4	106.3	0.98	186	1.02	1.01	$0.12^{+0.02}_{-0.02}$	$0.31^{+0.17}_{-0.15}$	$0.21^{+0.10}_{-0.10}$	$0.13^{+0.12}_{-0.12}$
1.438	162.7	107.6	1.51	442	2.41	1.56	$0.13^{+0.03}_{-0.03}$	$0.20^{+0.21}_{-0.14}$	$0.15^{+0.13}_{-0.10}$	$0.22^{+0.12}_{-0.16}$
1.462	114.5	108.1	1.06	217	1.19	1.09	$0.15^{+0.02}_{-0.02}$	$0.09^{+0.11}_{-0.06}$	$0.07^{+0.08}_{-0.05}$	$0.32^{+0.06}_{-0.09}$
1.488	140.7	110.2	1.28	315	1.72	1.31	$0.10^{+0.03}_{-0.03}$	$0.26^{+0.24}_{-0.17}$	$0.17^{+0.12}_{-0.11}$	$0.15^{+0.13}_{-0.15}$
1.512	141.1	111.3	1.27	310	1.69	1.30	$0.16^{+0.03}_{-0.03}$	$0.09^{+0.12}_{-0.06}$	$0.07^{+0.08}_{-0.05}$	$0.32^{+0.07}_{-0.11}$
1.538	109.9	112.2	0.98	185	1.01	1.01	$0.14^{+0.02}_{-0.02}$	$0.09^{+0.10}_{-0.06}$	$0.06^{+0.07}_{-0.05}$	$0.30^{+0.06}_{-0.09}$
1.562	116.3	115.0	1.01	198	1.08	1.04	$0.13^{+0.02}_{-0.02}$	$0.08^{+0.11}_{-0.06}$	$0.06^{+0.07}_{-0.04}$	$0.30^{+0.06}_{-0.09}$
1.587	120.2	117.8	1.02	201	1.10	1.05	$0.09^{+0.02}_{-0.02}$	$0.28^{+0.23}_{-0.16}$	$0.17^{+0.11}_{-0.10}$	$0.14^{+0.12}_{-0.14}$
1.613	128.6	119.7	1.07	223	1.22	1.10	$0.10^{+0.02}_{-0.02}$	$0.14^{+0.17}_{-0.10}$	$0.09^{+0.09}_{-0.06}$	$0.23^{+0.08}_{-0.11}$
1.637	141.6	123.3	1.15	255	1.39	1.18	$0.08^{+0.02}_{-0.02}$	$0.07^{+0.10}_{-0.05}$	$0.04^{+0.05}_{-0.03}$	$0.25^{+0.05}_{-0.07}$

6

THE β PICTORIS B HILL SPHERE TRANSIT CAMPAIGN - II. SEARCHING FOR THE SIGNATURES OF THE β PICTORIS EXOPLANETS THROUGH TIME DELAY ANALYSIS OF THE δ SCUTI PULSATIONS

Sebastian Zieba, Konstanze Zwintz, Matthew Kenworthy, Daniel Hey, Simon J. Murphy, Rainer Kuschnig, Lyu Abe, Abdelkrim Agabi, Djamel Mekarnia, Tristan Guillot, François-Xavier Schmider, Philippe Stee, Yuri De Pra, Marco Buttu, Nicolas Crouzet, Samuel Mellon, Jeb Bailey III, Remko Stuik, Patrick Dorval, Geert-Jan J. Talens, Steven Crawford, Eric Mamajek, Iva Laginja, Michael Ireland, Blaine Lomberg, Rudi Kuhn, Ignas Snellen, Paul Kalas, Jason J. Wang, Kevin B. Stevenson, Ernst de Mooij, Anne-Marie Lagrange, Sylvestre Lacour, Mathias Nowak, Paul A. Strøm, Zhang Hui, and Lifan Wang
Accepted in A&A, 2024.

Abstract

The β Pictoris system is the closest known stellar system with directly detected gas giant planets, an edge-on circumstellar disc, and evidence of falling sublimating bodies and transiting exocomets. The inner planet, β Pictoris c, has also been indirectly detected with radial velocity (RV) measurements. The star is a known δ Scuti pulsator, and the long-term stability of these pulsations opens up the possibility of indirectly detecting the gas giant planets through time delays of the pulsations due to a varying light travel time. We search for phase shifts in the δ Scuti pulsations consistent with the known planets β Pictoris b and c and carry out an analysis of the stellar pulsations of β Pictoris over a multi-year timescale. We used photometric data collected by the BRITe-Constellation, bRing, ASTEP, and TESS to derive a list of the strongest and most significant δ Scuti pulsations. We carried out an analysis with the open-source python package `maelstrom` to study the stability of the pulsation modes of β Pictoris in order to determine the long-term trends in the observed pulsations. We did not detect the expected signal for β Pictoris b or β Pictoris c. The expected time delay is 6 seconds for β Pictoris c and 24 seconds for β Pictoris b. With simulations, we determined that the photometric noise in all the combined data sets cannot reach the sensitivity needed to detect the expected timing drifts. An analysis of the pulsational modes of β Pictoris using `maelstrom` showed that the modes themselves drift on the timescale of a year, fundamentally limiting our ability to detect exoplanets around β Pictoris via pulsation timing.

6.1 Introduction

β Pictoris is a nearby southern hemisphere star visible with the naked eye for which δ Scuti-like pulsations were discovered by Koen (2003). The planetary-mass companion β Pictoris b was detected using the VLT/NaCo instrument with direct imaging (Lagrange et al. 2009b, 2010). Evidence of a second planet in the β Pictoris system was published by Lagrange et al. (2019b) using the radial velocity (RV) method and recently independently confirmed by Nowak et al. (2020) and Lagrange et al. (2020) using VLTI/GRAVITY observations.

The lifetime and frequency stability of δ Scuti pulsations make them astronomical “stellar clocks,” and therefore, they are great targets for applying timing techniques (Compton et al. 2016). The common orbital motion of a star together with a companion around the barycenter of a system results in a periodic early or late arrival of the stellar pulsational signals. This principle led to the first detection of planets orbiting a pulsar outside the Solar System (Wolszczan & Frail 1992; Wolszczan 1994). The periodic variation of the arrival times can be seen as either a frequency modulation (FM; Shibahashi & Kurtz 2012; Shibahashi et al. 2015) or a phase modulation (PM; Murphy et al. 2014; Murphy & Shibahashi 2015; Murphy et al. 2016b). The latter perspective works better for companions in wider orbits.

By applying the PM method on Kepler data, Murphy et al. (2016a) discovered a massive planet ($m \sin i \approx 12M_J$) with an orbital period of about 840 days around a δ Scuti star. In addition to the discovery of this planet, the PM method has led to the detection of 341 binaries and hundreds of more candidates (Murphy et al. 2018). Furthermore, it has provided us with the eccentricity, period, and mass function of these companions orbiting stars, just as the RV method does (e.g. Nesvold & Kuchner 2015). Applying the same method to pulsating stars observed by the TESS mission will lead to many more binary systems with full orbital solutions.

In this work, we use the data collected by the TESS satellite in its primary mission and data collected by the Hill sphere¹ transit campaign, which was an international effort of space-based (e.g. through the BRITE-Constellation) and ground-based (e.g. through bRing, ASTEP) observations that searched for signatures of material around the giant planet β Pictoris b (Kalas et al. 2019; Kenworthy 2017). We analyzed this photometric data by searching for phase variations (and therefore time delays) caused by orbital motion in the pulsational signals. β Pictoris was observed for approximately four months from October 2018 to February 2019 during the primary mission of TESS. A second visit occurred during TESS’ extended mission from November 2020 to February 2021 (see Table 6.3 for a summary of all visits).

In Section 6.2, we describe the properties of the different components in the β Pictoris system. Section 6.3 has a summary of all observational instruments and a frequency analysis for the photometry collected by TESS. The theory and equations for this paper can be found in Section 6.4, and our results and conclusions

¹The Hill sphere is the region around a planet where masses, such as moons and planetary rings, are gravitationally bound to the planet.

follow in Sections 6.5 and 6.6.

6.2 The β Pictoris system

β Pictoris (HD 39060; HR 2020) is one of the most studied and intriguing star-planet systems. The Infrared Astronomical Satellite (IRAS) discovered an infrared excess (Aumann et al. 1984) for this bright and close southern star that was attributed to the presence of a circumstellar disc. This disc was first imaged by Smith & Terrile (1984) and clearly showed the edge-on geometry of this system. The gas and dust in this disc is mostly “second generation,” that is, constantly replenished by collisions of comets and asteroids (Lagrange et al. 2000). A warp in this disc (Augereau et al. 2001; Mouillet et al. 1997; Nesvold & Kuchner 2015) and signatures of evaporating exocomets (also called falling evaporating bodies, or FEBs) in spectroscopy (Ferlet et al. 1987; Beust & Morbidelli 2000) were attributed to an exoplanet orbiting the star interacting dynamically with its environment (for more information on exocomets observed around β Pictoris detected in photometry, see Zieba et al. 2019; Strøm et al. 2020; Pavlenko et al. 2022; Lecavelier des Etangs et al. 2022).

6.2.1 The star

Koen (2003) discovered δ Scuti-type pulsations at the millimagnitude level originating from β Pictoris. Further analysis by Mékarnia et al. (2017), Zwintz et al. (2019), and Zieba et al. (2019) showed dozens of additional frequencies between 20 and 80 cycles per day. An asteroseismic large spacing, $\Delta\nu$, has been measured for β Pictoris (Bedding et al. 2020), which might facilitate a precise asteroseismic age in the future. The pulsations also induce intrinsic variations in the RV at $\lesssim 1 \text{ km s}^{-1}$ peak to peak (Lagrange et al. 2009a, 2012; Galland et al. 2006), which hampers the search for planets with the RV method in this system. A selection of the fundamental properties of the star β Pictoris are listed in Table 6.1.

6.2.2 The planets: β Pictoris b and c

The warp of the inner disc of β Pictoris observed by the Hubble Space Telescope and in ground-based observations was one of the indirect lines of evidence for a massive substellar companion orbiting the star (Burrows et al. 1995; Mouillet et al. 1997; Heap et al. 2000; Golimowski et al. 2006). Signatures of infalling exocomets in the spectra of the star also needed a “perturber” to scatter them onto eccentric inner system-bearing orbits. The planet, β Pictoris b, was then discovered using the VLT/NaCo instrument data in 2003 (Lagrange et al. 2009b) and was later confirmed by Lagrange et al. (2010). A transit-like event was observed in 1981 and attributed to a planet (Lecavelier Des Etangs et al. 1995). However, a better orbit determination with the VLT/SPHERE instrument ruled out β Pictoris b as the cause of that event (Lagrange et al. 2019a). Using data from the Gemini Planet Imager, Wang et al. (2016) were able to rule out a transit of the planet β Pictoris b during the conjunction in 2017 at a 10σ level. However, a Hill sphere transit was

Table 6.1: Various stellar parameters of the star β Pictoris.

Parameter	Value	Reference
RA (J2000.0)	05h 47m 17.09s	1
DEC (J2000.0)	-51h 03m 59.41s	1
V (mag)	3.86	2
TESS (mag)	3.696	1
age (Myr)	23 ± 3	3
parallax (mas)	50.93 ± 0.15	4,5,6
Distance (pc)	19.63 ± 0.06	4,5,6
Spectral class	A6V	7
Radius (R_{\odot})	1.497 ± 0.025	8
Mass (M_{\odot})	$1.75^{+0.03}_{-0.02}$	9
Teff (K)	8090 ± 59	8

References. (1) Stassun et al. (2019); (2) Cousins (1971); (3) Mamajek & Bell (2014); (4) Gaia Collaboration et al. (2016); (5) Gaia Collaboration et al. (2023); (6) Lindegren et al. (2021); (7) Gray et al. (2006); (8) Zwintz et al. (2019); (9) Lacour et al. (2021).

Table 6.2: Various parameters of the planets β Pictoris b and c based on Lacour et al. (2021).

Parameter	Unit	β Pictoris b	β Pictoris c
Mass	M_J	$11.90^{+2.93}_{-3.04}$	$8.89^{+0.75}_{-0.75}$
a	au	$9.93^{+0.03}_{-0.03}$	$2.68^{+0.02}_{-0.02}$
e	—	$0.103^{+0.003}_{-0.003}$	$0.32^{+0.02}_{-0.02}$
i	$^{\circ}$	$89.00^{+0.00}_{-0.01}$	$88.95^{+0.09}_{-0.10}$
$\varpi^{(a)}$	$^{\circ}$	$199.3^{+2.8}_{-3.1}$	$66.0^{+1.8}_{-1.7}$
$\tau^{(b)}$	—	$0.719^{+0.008}_{-0.010}$	$0.724^{+0.006}_{-0.006}$
P	years	$23.61^{+0.09}_{-0.09}$	3.34 ± 0.04
P	days	8623^{+31}_{-32}	1221 ± 15
$t_p^{(c)}$	MJD	65243	59888

Notes.

^(a) The argument of periastron ϖ reported in Lacour et al. (2021) follows the definition in Blunt et al. (2020) and therefore refers to the orbit of the companion and not to the star. In this paper, however, we refer to the orbit of the star when we use ϖ .

^(b) reference epoch MJD 59000 (31 May 2020).

^(c) derived from τ .

predicted for the time between late 2017 and early 2018 (Lecavelier des Etangs & Vidal-Madjar 2016; Wang et al. 2016). Various observational campaigns were initiated by PicSat (Nowak et al. 2018; Menegaldo et al. 2022); bRing (Kenworthy 2017); and the BRITE-Constellation (Weiss et al. 2014) in order to photometrically observe possible material around the planet; however, there was no significant detection (Kenworthy et al. 2021). The mass and the orbital solution of the outer planet β Pictoris b are listed in Table 6.2.

Evidence of an additional planet in the β Pictoris system was published by Lagrange et al. (2019b). Over 6000 spectra of the star taken between 2003 and 2018 by the HARPS instrument at the ESO La Silla 3.6 m telescope have been analyzed, and they showed a hint of a planetary signal. β Pictoris c was then ultimately directly detected by Nowak et al. (2020) and Lagrange et al. (2020) using VLTI/GRAVITY observations. A list of parameters for the planet can be found in Table 6.2.

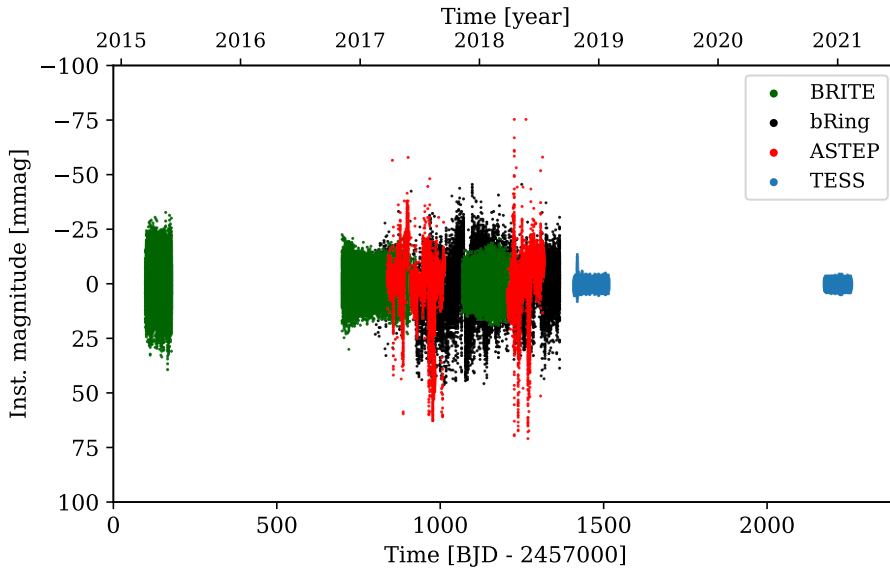


Figure 6.1: Full light curve of all available observations of the star β Pictoris used in this work.

6.3 Observations

Due to the 2017-2018 Hill Sphere Transit of β Pictoris b, an international campaign of space- and ground-based observations was launched in order to search for signatures of material around the giant planet (Kalas et al. 2019; Kenworthy et al. 2021). Table 6.3 summarizes various properties of the different light curves. Changes to those light curves other than the Gaussian high-pass procedure, which is explained in Section 6.A.2, are noted in the following subsections. The data

Table 6.3: Summary of the properties of the various instruments and corresponding light curves.

Observation	Wavelength (nm)	Observation start	Observation end	T (days)	$1/T$ (10^{-3} d^{-1})	$f_{\text{Ny.}}$ (d^{-1})	cadence (s)	DC (%)
BHr	550 – 700	16 March 2015	2 June 2015	78.32	12.77	4167	10.37	6.78
BTr + BHr	550 – 700	4 Nov. 2016	17 June 2017	224.6	4.453	2128	20.30	7.07
BHr	550 – 700	9 Nov. 2017	25 April 2018	167.3	5.976	2128	20.30	7.48
bRing	463 – 639	2 Feb. 2017	1 Sept. 2018	575.5	1.738	135.4	319.1	27.0
ASTEPI7	695 – 844	28 March 2017	14 Sept. 2017	170.0	5.881	495.8	87.13	18.9
ASTEPI8	695 – 844	28 March 2018	15 July 2018	109.3	9.150	502.8	85.92	29.2
TESS	600 – 1000	19 Oct. 2018	1 Feb. 2019	105.2	9.507	360.0	120.0	85.3
TESS	600 – 1000	20 Nov. 2020	8 Feb. 2021	79.8	12.53	360.0	120.0	90.2

Notes.

The term T denotes the time base of the observations, the reciprocal value $1/T$ corresponds to the Rayleigh criterion, $f_{\text{Ny.}}$ is the Nyquist frequency, and DC is the duty cycle. BRITE Lem (BLb) is equipped with a blue filter and observed β Pictoris from December 2016 until June 2017, but due to significantly higher noise in the time series, the data was disregarded from the analysis. See Zwintz et al. (2019) for an analysis of the BLb observations.

provided by BRITE-Constellation was left unchanged. A detailed analysis of the photometry of β Pictoris collected by BRITE-Constellation and bRing was published by Zwintz et al. (2019). As we wanted to measure the periodic motion of a star around a barycenter, we also wanted to correct for the motion the Earth in the Solar System. All the observations in this work were therefore converted to the Barycentric Julian Date in the barycentric dynamical time (BJD_{TDB}) standard using the Python tool BARYCORRPY (Kanodia & Wright 2018), which is based on the IDL code BARYCORR (Wright & Eastman 2014).

6.3.1 BRITE-Constellation

The BRITE-Constellation (Weiss et al. 2014) consists of five nanosatellites collecting photometry for the brightest stars on the sky. In this work, we analyzed data collected by three of the satellites: BRITE-Heweliusz (BHr), BRITE-Toronto (BTr), and BRITE-Lem (BLb). Being in a low-earth orbit, the orbital periods of the satellites are all around 100 minutes. A minimum of 15 minutes per orbit is dedicated to observations. Three different runs were conducted in the constellations around Pictor and Vela, which also included the star β Pictoris. A summary of the durations and various properties of the observations can be found in Table 6.3. The pipeline for the photometry reduction is described in Popowicz et al. (2017). An analysis of all BRITE observations was conducted in Zwintz et al. (2019). For the three runs by BHr, BTr+BHr, and BHr, which all used the red BRITE filter, six, 13, and eight significant frequencies were extracted, respectively. The only run with a blue filter by BLb suffered from higher noise compared to the other BRITE observations. Zwintz et al. (2019) has reported four frequencies in the collected BLb photometry. The blue observations were discarded from this analysis, as the data quality was not good enough to provide additional information.

6.3.2 bRing

The bRing project (which stands for “the β Pictoris b Ring project”) was initiated in order to collect photometry of β Pictoris during the Hill sphere transit of β Pictoris b at the end of 2017 (Stuik et al. 2017). To that end, two stations in South Africa and Australia were built, each consisting of two wide-field cameras. Their design is based on the Multi-Site All-Sky CAmera (MASCARA) (Snellen et al. 2012; Talens et al. 2017). The capability of bRing to monitor bright stars and find previously unknown variables has been shown by Mellon et al. (2019). More information on the observing strategy and design of bRing can be found in Stuik et al. (2017). The reduction pipeline for the MASCARA and bRing instruments is described in Talens et al. (2018). With a passband of 463 – 639 nm, bRing collected the shortest wavelengths of all observatories considered in this work. We expected to see the highest pulsational amplitudes in these data, as β Pictoris is a star of spectral type A6 (Zwintz et al. 2019) and has its energy maximum in the blue optical wavelengths. Due to some evident outliers in the data, one 5σ clip with respect to the median of the data set was applied. This significantly weakened

the one-day aliases in the spectral window. An iterative sigma clipping procedure was not conducted due to noticeable changes in the amplitudes of the pulsations in this case (see Hogg et al. (2010) for a discussion of sigma clipping in order to remove outliers). The observations by bRing were separated into two equally sized segments in order to gain more time delay measurements while also maintaining a precision in frequency and phase comparable to the ASTEP observations. Zwintz et al. (2019) found six significant frequencies in the photometry collected by bRing. All of them are also identified in the data collected by BRITE, ASTEP, and TESS.

6.3.3 ASTEP

The Antarctic Search for Transiting ExoPlanets, or ASTEP, is an automated telescope with an aperture of 40 cm located at the Concordia station at Dome C in Antarctica (Abe et al. 2013; Guillot et al. 2015; Mékarnia et al. 2017). It uses a Sloan i' filter (centered at 763 nm). We only used measurements with a sun elevation lower than -18° . Notably, data points where the centroid of the star did not fall on the central pixel suffer from strong outliers. The removal of these outliers and a 5σ clip with respect to the median weakened aliases significantly but without noticeable changes in the amplitude of the strongest pulsational frequencies. Mékarnia et al. (2017) conducted a frequency analysis of the β Pictoris photometry collected by the ASTEP observatory, and they are consistent with the ones seen in the TESS data.

6.3.4 TESS

The Transiting Exoplanet Survey Satellite (TESS; Ricker et al. 2015) was launched in April 2018 in order to find transiting exoplanets around nearby bright stars. The data of β Pictoris (TIC 270577175, $T = 3.696$ mag) was collected from 19 October 2018 to 1 February 2019 in sectors four through seven and from 20 November 2020 to 8 February 2021 in the sectors 32 through 34. The data for first four sectors were obtained during TESS' primary mission, and data for the three other sectors were obtained approximately two years later as part of the first extended mission. β Pictoris is one of the preselected targets for which short-cadence (2 minutes) data are provided. Due to the high-cadence data, the high photometric precision of TESS, its high duty cycle, and the long baseline, δ Scuti pulsations can be resolved and identified with high precision. The photometric data of β Pictoris as observed by TESS was accessed and modified with the Python package `lightcurve` (Lightcurve Collaboration et al. 2018), which retrieves the data from the MAST archive.² For this analysis, we used the Pre-search Data Conditioning Simple Aperture Photometry (PDCSAP; Smith et al. 2012; Stumpe et al. 2012) light curves, which are produced from the Science Processing Operations Center (SPOC) pipeline (Jenkins et al. 2016; Jenkins 2017; Jenkins et al. 2010). These PDCSAP light curves were corrected for systematics by the SPOC pipeline. We also visually inspected the target pixel files (TPF) in order to rule out various instrumental and astrophysical effects, such as Solar System asteroids or comets

²<https://archive.stsci.edu/tess/>

crossing the field of view. A comparison of the Lomb-Scargle periodogram (Lomb 1976; Scargle 1982) of the raw simple aperture photometry and PDCSAP light curves showed a significant change in the noise at low frequencies. This is due to the systematic effects present in sector four. The lowest noise in the low-frequency range can be found for the PDCSAP light curve with a completely removed fourth sector. This light curve was then used for the main frequency analysis.

The individual sectors were normalized by dividing each of the sectors by their respective median flux, and the sectors were combined into one light curve. Furthermore, every measurement with a non-zero quality flag (see Sect. 9 in the TESS Science Data Products Description Document)³ was removed. Such anomalies as cosmic ray events or instrumental issues were marked by these quality flags.

The frequency analysis was conducted using the Python package `SMURFS` (Müller 2020) and checked with the software package `Period04` (Lenz & Breger 2005). Following Breger et al. (1993), all pulsation frequencies down to a signal-to-noise ratio of four were extracted. The frequency range analyzed is between zero and the Nyquist frequency of 360 cycles per day. Following the procedure described in Zieba et al. (2019), 37 significant p-modes in frequencies ranging from 34 to 76 d⁻¹ were identified. As we are only interested in the strongest pulsational frequencies for this time delay analysis, we did not try to further recover any of the lower amplitude modes. A list of the extracted frequencies can be found in Table 6.5.

6.4 Theory and methodology

In this chapter, we discuss the theory behind time delays and the methods used in order to finally arrive at the time delay plot. Importantly, this plot can be used to search for companions around pulsating stars.

6.4.1 δ Scuti stars

δ Scuti stars can be found at the intersection region between the main sequence and the instability strip on the Hertzsprung-Russell diagram. Thanks to the nearly uninterrupted, high-precision photometry of Kepler’s primary four-year mission, the general understanding of pulsating stars has been revolutionized. δ Scuti stars have masses between approximately 1.5 and 2.5 M_{\odot} . They pulsate in radial and non-radial low-degree, low-order pressure (p) modes that are primarily driven by an opacity mechanism (also called a κ -mechanism) in their HeII zone with contributions from turbulent pressure (Houdek 2000; Antoci et al. 2014) and the edge-bump mechanism (Murphy et al. 2020b). The oscillations have periods between 18 minutes and 8 hours respectively 80 and three cycles per day (Aerts et al. 2010). Linear combinations of those oscillations can, however, create peaks at lower frequencies (Breger & Montgomery 2014). Besides main-sequence and more-evolved stars, δ Scuti pulsations were observed in pre-main-sequence stars, thus giving us the possibility to learn about early stellar evolution (Zwintz et al. 2014; Murphy et al. 2021; Steindl et al. 2022).

³<https://archive.stsci.edu/missions/tess/doc/EXP-TESS-ARC-ICD-TM-0014.pdf>

6.4.2 The ephemeris equation

The search for time delays in certain astrophysical signals requires a (quasi-)periodic process in space. A review on this and the related equations can be found in Hermes (2018). There are different processes that are “clock-like” under the assumption of a closed system, including the exceptionally stable signals of pulsars, the eclipse time of binary stars, or certain pulsating stars, as in our case. Deviations from periodic signals can be used to analyze the spin-down of pulsars or to discover companions around pulsars (Wolszczan & Frail 1992; Wolszczan 1994), eclipsing binaries (Barnes & Moffett 1975), or pulsating stars (Silvotti et al. 2007) (for a general review of pulsating stars in binary systems see Murphy 2018). To do so, one creates O-C (observed minus calculated) diagrams (see e.g. Sterken 2005) in order to search for deviations from the predicted ephemeris in the observations. O-C diagrams work the best if the star is pulsating in only a single mode and if the maxima are narrow and well defined, as they are easy to track in that case. However, these diagrams especially struggle with multi-mode pulsators.

6.4.3 Frequency modulation and phase modulation: The state of the art

Building on the established methods of O-C diagrams, two new and complementary techniques have emerged for finding companions around pulsating stars. The FM method (Shibahashi & Kurtz 2012) searches and analyzes the variations in the frequency of a pulsating star induced by a companion. The periodic FM creates multiples around every pulsation peak in the frequency spectrum. Their frequencies, relative amplitudes, and phases can be used to get a full orbital solution, as described in Shibahashi et al. (2015). The effectiveness of the FM method was validated through a comparison with an eclipsing binary system (Kurtz et al. 2015), and it is best suited for data sets with a baseline that exceeds the orbital period of the companion.

The PM method is more sensitive to companions in wider orbits. It was developed by Murphy et al. (2014), Murphy & Shibahashi (2015), and Murphy et al. (2016b). Compton et al. (2016) showed that δ Scuti stars and white dwarfs are best suited for this method. Its effectiveness was demonstrated by Schmid et al. (2015) by showing the binary nature of KIC10080943 using the PM method and attributing certain pulsations to the corresponding star in the binary due to the antiphase modulation in time delays. Such a system with observable time delays in both components is called a PB2, analogous to spectroscopic terminology, where binary star systems are called SB2s if both stars show observable RVs. Other proof of the functionality of the PM method was shown by Derekas et al. (2019) by comparing the orbital parameters derived from RV with those from PM.

An additional advantage of the PM method is its easier automation for many stars. When applying this method to 2224 main-sequence A/F stars in the four-year main Kepler data, Murphy et al. (2018) were able to find 317 PB1 systems, where only one component is pulsating and showing time delays, and 24 PB2 systems, where two stars are pulsating. It is worth noting here that determining

orbital solutions using spectra and generating RV curves for the same number of stars would be much more time intensive.

Other methods were developed by Koen (2014) and Balona (2014) to search for binary systems by tracing the δ Scuti pulsations of stars. In contrast to the FM and PM methods, these methods are not able to provide a full orbital solution, which is usually gained by analyzing RV curves of spectroscopic binaries.

6.4.4 Time delays

Time delays arise when a signal (in our case always an electromagnetic wave with the propagation velocity defined by the speed of light) has to travel different distances at different epochs. Following Smart (1977) and Balona (2014), the distance r between the pulsating star and the center of gravity of its system can be described by

$$r = \frac{a_1 (1 - e^2)}{1 + e \cos f}, \quad (6.1)$$

where a_1 denotes the semi-major axis of the star, e is its eccentricity, and f is the true anomaly. The distance to the star varies relative to the Earth by

$$z = r \sin(f + \varpi) \sin i, \quad (6.2)$$

with ϖ being the argument of periapsis, that is, the angle between the nodal point and the periapsis,⁴ and i as the inclination of the system.

At this point, Equation 6.1 can be substituted into Equation 6.2. The time delay $\tau = -z/c$ is then completely described by the following equation:

$$\tau(t, \mathbf{x}) = -\frac{a_1 \sin i}{c} (1 - e^2) \frac{\sin f \cos \varpi + \cos f \sin \varpi}{1 + e \cos f}. \quad (6.3)$$

The set $\mathbf{x} = (\Omega = 2\pi/P, a_1 \sin i/c, e, \varpi, t_p)$ in Equation 6.3 includes all of the system-specific parameters needed to describe the time delay for a given time t . The term P is the orbital period of the system, or equivalently $1/P = \nu_{\text{orb}}$ the orbital frequency, and thus Ω is the angular orbital frequency. The projected semi-major axis of the pulsating star is described by $a_1 \sin i$. Dividing this quantity by the speed of light c gives us the size of the orbit for the pulsating star in light seconds. The argument of periapsis is described by ϖ and the time of periapsis passage by t_p . (For a graphical visualization of the orbital parameters, see Murphy & Shibahashi (2015).)

The two trigonometric functions of the true anomaly, $\sin f$ and $\cos f$, can be expressed in terms of series expansions and Bessel functions:

$$\cos f = -e + \frac{2(1 - e^2)}{e} \sum_{n=1}^{\infty} J_n(ne) \cos n\Omega (t - t_p), \quad (6.4)$$

⁴The argument of periapsis is usually denoted with ω . This symbol, however, is used in asteroseismology to denote the angular oscillation frequency. Also, one should not confuse ϖ with the longitude of periapsis, which is the sum of the longitude of the ascending node Ω and the argument of periapsis.

$$\sin f = 2\sqrt{1-e^2} \sum_{n=1}^{\infty} J'_n(ne) \sin n\Omega(t - t_p), \quad (6.5)$$

with $J'_n(x) = dJ_n(x)/dx$ (the derivation of Equation 6.4 and 6.5 can be found in Appendix A of Shibahashi et al. 2015). The changing distances between us and the clock in space are fundamentally connected with varying radial velocities, v_{rad} :

$$v_{\text{rad}} = c \frac{d\tau}{dt}. \quad (6.6)$$

By substituting Equation 6.3 into Equation 6.6, we obtain

$$v_{\text{rad}} = -\frac{\Omega a_1 \sin i}{\sqrt{1-e^2}} [\cos(f + \varpi) + e \cos \varpi]. \quad (6.7)$$

Given Equation 6.6 and the convention that a positive RV corresponds with a receding object and a negative RV with an approaching one, we could deduce the following: a negative time delay is due to an early arrival of the signal, that is, the star is closer to us, and vice versa⁵ (see Table 6.4).

Table 6.4: Sign convention for the RV v_{rad} and the time delays τ .

	positive sign (+)	negative sign (-)
v_{rad}	moving away	approaching
τ	farther away / late arrival	closer / early arrival

One can see in Equations 6.3 and 6.7 that the time delay as well as the RV of a system can be completely described by the orbital parameters. If we obtain those parameters by one method, we can predict what we should observe with the other one. Furthermore, if we generate the time delay plot from our observations, we can apply a chi-squared minimization technique in order to get the parameters in set **x**. This concept was introduced with Murphy & Shibahashi (2015) and is a major improvement to Murphy et al. (2014), where the time delay measurements were numerically differentiated in order to derive the parameters from the obtained RV curve.

Finally, by using two of the derived orbital parameters, $a_1 \sin i/c$ and P_{orb} , we can calculate the mass function $f(m_1, m_2, \sin i)$ for the binary system:

$$f(m_1, m_2, \sin i) := \frac{(m_2 \sin i)^3}{(m_1 + m_2)^2} = \frac{4\pi^2 c^3}{G} v_{\text{orb}}^2 \left(\frac{a_1 \sin i}{c} \right)^3, \quad (6.8)$$

where m_2 is the mass of the (usually non-pulsating) companion and G is the gravitational constant.

⁵This convention for the time delays was established with Murphy & Shibahashi (2015), while Murphy et al. (2014) used reversed signs; their plots are therefore mirrored around the vertical axis.

6.4.5 Phase modulation method: Methodology

Before we could create the time delay plot, we had to analyze the change in the phase of the various pulsation modes with time. The basic equations for that can be found in Murphy et al. (2014) and are summarized in the following. We started by dividing the light curve into n equally sized segments. Then, we calculated the phase in every segment for each frequency. This left us with a series of phases Φ_j for every segment $(1, 2, \dots, n)$ for a fixed frequency ν_j :

$$\Phi_j = [\phi_{1j}, \phi_{2j}, \dots, \phi_{ij}, \dots, \phi_{nj}]. \quad (6.9)$$

Numerically, the phase in a segment is derived by calculating the argument of the Fourier Transformation in the respective segment:

$$\Phi(t; \nu) = \tan^{-1} \left(\frac{\text{Im}(F(t; \nu, \delta t))}{\text{Real}(F(t; \nu, \delta t))} \right), \quad (6.10)$$

where $F(t; \nu, \delta t)$ is the value of the Fourier Transformation of the time series for frequency ν in segment δt .

As phases are frequency dependent, the resulting phase shifts have different amplitudes for different frequencies. To get rid of this effect, we converted them into time delays by first calculating the relative phase shifts:

$$\Delta\phi_{ij} = \phi_{ij} - \bar{\phi}_j, \quad (6.11)$$

with $\bar{\phi}_j$ as the mean phase of frequency ν_j :

$$\bar{\phi}_j = \frac{1}{n} \sum_{i=1}^n \phi_{ij}. \quad (6.12)$$

The time delay τ_{ij} for segment i and frequency ν_j is thus simply the relative phase shift divided by the angular pulsation frequency:

$$\tau_{ij} = \frac{\Delta\phi_{ij}}{2\pi\nu_j}. \quad (6.13)$$

A planet with an orbital frequency of v_{orb} in a circular orbit will induce time delays that can be described by a sine function with phase ψ :

$$\tau(t) = A \sin(2\pi v_{\text{orb}} t + \psi). \quad (6.14)$$

The amplitude A can be simply derived by inserting the center of mass equation $m_1 a_1 = m_2 a_2$ into $\tau = a_1 \sin i / c$:

$$\tau = \frac{a_P \sin i}{c} \frac{M_S}{M_*}, \quad (6.15)$$

with a_S as the semi-major axis of the companion. The terms M_S and M_* are the mass of the companion and the star, respectively. Using Equation 6.15 and the mass of around $1.8 M_\odot$ given in Table 6.1, we could calculate the expected time delay for a given period. This is visualized in Figure 6.2. The time delay is around 24 seconds for β Pictoris b and 6 seconds for β Pictoris c. For comparison, the

smallest time delay detected in the main Kepler data is 7 seconds (Murphy et al. 2016a).

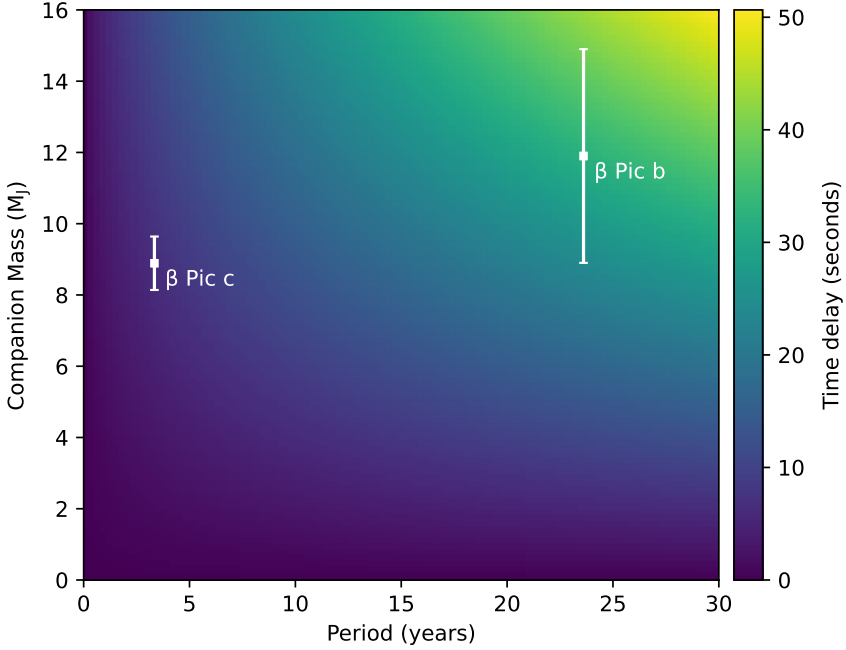


Figure 6.2: Time delays for the β Pictoris system. The colors indicate the expected time delays for an edge-on planet in a circular orbit. The uncertainties in the orbital period for the planets are smaller than the marker size.

For more eccentric orbits, the pulsation time plot is described by a sum of harmonics with amplitudes A_k and phases ϕ_k corresponding to order k :

$$\tau(t) = \sum_{k=1}^N A_k \sin(2\pi k v_{\text{orb}} t + \psi_k). \quad (6.16)$$

The height of the first harmonic relative to the one of the orbital frequency is a measure of the eccentricity. The theory behind this is described in Appendix A of Murphy et al. (2014). A visualization of that can be seen in Figure 6.3. An increase in eccentricity also influences the amplitude of the time delay. This is given by the following equation:

$$\frac{a_1 \sin i}{c} = \frac{(\tau_{\text{max}} - \tau_{\text{min}})}{2} (1 - e^2 \cos^2 \varpi)^{-1/2}. \quad (6.17)$$

The maximum time delay is therefore reached in the case of $\varpi = \pm\pi/2$ or for the simple circular orbit case.

The larger the ratio between the orbital size $a_1 \sin i/c$ and the pulsation period $1/\nu$, the higher the sensitivity of the method (Murphy et al. 2016b).

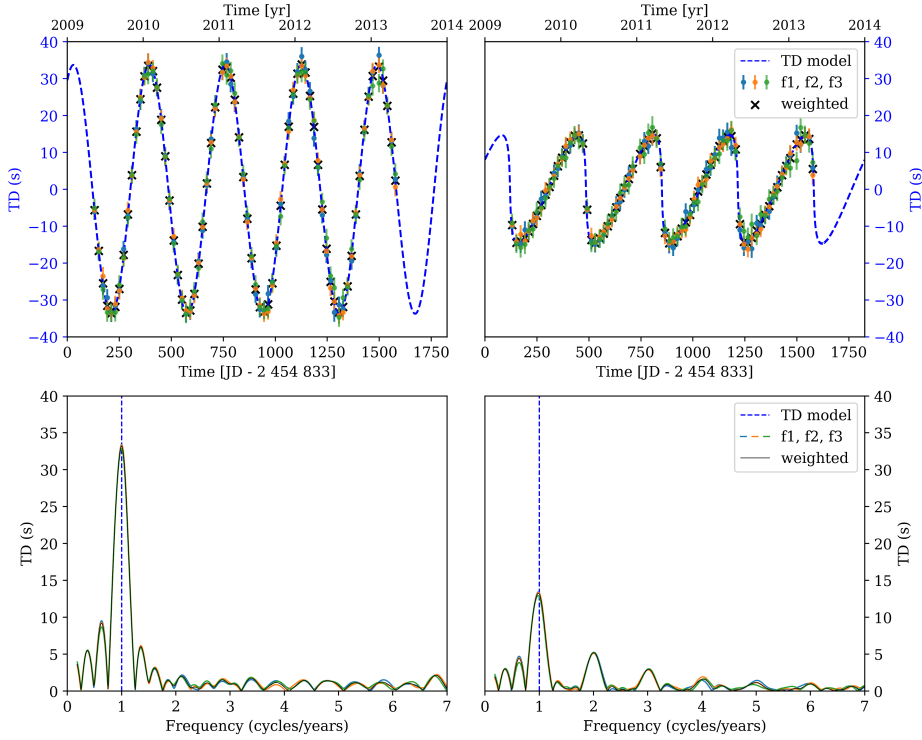


Figure 6.3: Simulation of a companion in a circular ($e = 0$; left column) and eccentric ($e = 0.9$; right column) orbit as if observed by the Kepler Space Telescope. The following parameters were used: $P = 1$ year, $\varpi = 0$, $M_{\text{pulsating}} = 1.8 M_{\odot}$, and $M_{\text{companion}} = 0.1 M_{\odot}$. This led to a semi-amplitude of around 34 seconds in the circular case (using Equation 6.15) and around 15 seconds in the eccentric case (using Equation 6.17). *Upper panel:* Simulated time delay plot. *Lower panel:* Fourier transformation of the time delays. One can clearly see the relative increase of the first harmonic at two cycles/year for the eccentric case.

Due to the size of the segments, one has to make a trade-off between time or frequency resolution. Using a shorter segment size has the advantage of a finer sensitivity at periastron; however, the uncertainties are simultaneously increased because of a poorer frequency resolution in the Fourier transform.

Under the assumption of Gaussian noise, increasing the cadence of an observation by a factor of N decreases the uncertainties in the measured phases by a factor of \sqrt{N} (Murphy 2012). The phase errors also scale inversely with amplitude, which means that the most valuable frequencies are the ones with the highest amplitudes.

6.4.6 Intrinsic amplitude and phase variations

Amplitude modulations in δ Scuti stars have been observed in the past and thoroughly analyzed in the four-year main Kepler data by Bowman et al. (2016). Additionally, due to intrinsic reasons for those modulations (such as the coupling of pulsational modes or pairs of close unresolved frequencies leading to a beating effect), binarity can cause variability.

β Pictoris is known to show amplitude variation in certain pulsational frequencies, as reported by Zwintz et al. (2019) and Mékarnia et al. (2017). However, PMs have not been observed yet (Zwintz et al. 2019).

6.4.7 Light curve reduction

Following Murphy et al. (2016a), unused frequencies were pre-whitened from our light curves, as their presence adds unwanted variance to the data. Furthermore, a high-pass filter was applied to the light curve to remove any remaining instrumental signal and low-frequency oscillations, preserving all content at frequencies above 5 d^{-1} . The effect of a high-pass filter on low frequencies can be seen in Figure 6.4.

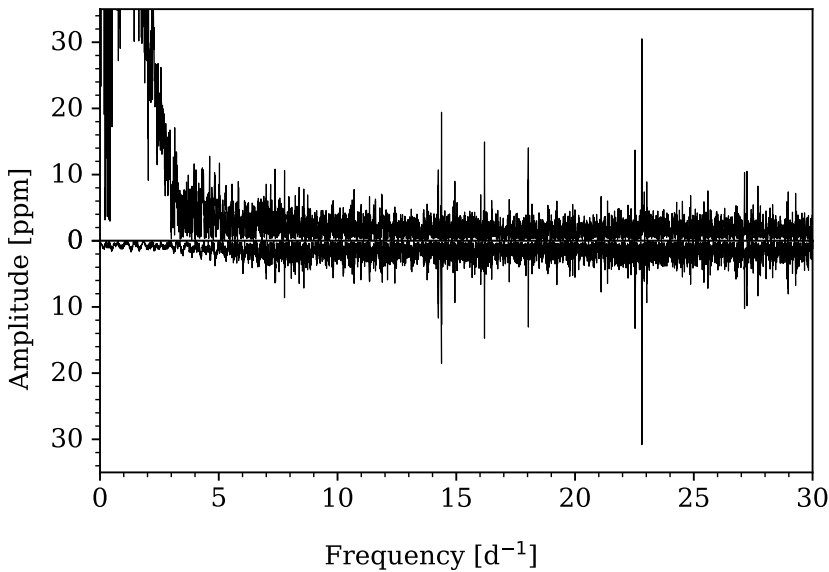


Figure 6.4: Comparison of the amplitude spectra of the “raw” PDCSAP light curve (upper panel) and the Gaussian high-pass filtered light curve (lower panel). The power of the peaks below five d^{-1} are significantly weakened without influencing the δ Scuti pulsations.

6.5 Results

To track the PM over all data sets, we started by determining which frequencies have a signal-to-noise ratio greater than four in all observations. This is the case for the four strongest frequencies in the TESS data (the first four frequencies listed in Table 6.5). The stability of those frequencies over the different observations is analyzed in Section 6.5.1. We then looked at time delay curves created from simulated light curves. For this, the “best-case scenario” of a four-year Kepler observation of β Pictoris is studied in Section 6.5.2. The time delays of the real observations and a comparison to a simulated re-creation can be found in Section 6.5.3. Finally, we analyze the pulsational stability of the δ Scuti pulsations of β Pictoris using TESS data in Section 6.5.5.

6.5.1 Frequency stability between the different observations

As mentioned in Section 6.4.5, the PM method derives a time delay from the observed PM at fixed frequencies. The precision with which pulsational frequencies can be determined depends on the quality of the data (cadence, timebase, precision, etc.). The photometry collected by the TESS mission has the smallest uncertainties in frequency of all data sets (see Fig. 6.5). We therefore used TESS as a “gold standard” for the frequencies used in the PM method. The uncertainties in the frequencies were calculated following Montgomery & Odonoghue (1999). However, as noted in their publication, these errors are a lower limit of the true values. Keeping in mind that the actual error bars are probably bigger, one can see that the frequencies are in agreement with each other across the different data sets (Fig. 6.5).

6.5.2 Simulation based on Kepler data

Figure 6.6 shows the expected time delays for β Pictoris caused by β Pictoris b and β Pictoris c using the full orbital solution given in Table 6.2. The addition of the individual contributions on the phases gives the total time delay curve as seen by the solid line in Figure 6.6.

In order to see how such properties as photometric precision, cadence, and gaps in the observations influence the derived time delays, we simulated light curves of β Pictoris. We used the actual time stamps of the short-cadence observations of Kepler (Borucki et al. 2010), which have a cadence of around one minute. The simulations consist of a multi-sine of the frequencies listed in Table 6.5. Using even more frequencies increases the computational time without influencing the results of the simulations due to their low amplitudes. The time stamps were then modulated by the expected time delay at a given time using Equation 6.3 and assuming a two-planet configuration in this system. Further, Gaussian noise on the order of 30 ppm was added to every data point, which is comparable to the noise floor of TESS. Following the procedure explained in Section 6.4.5, the light curve was separated into 20-day segments, and the time delays were calculated from the phases in every segment with a fixed frequency. Finally, we calculated

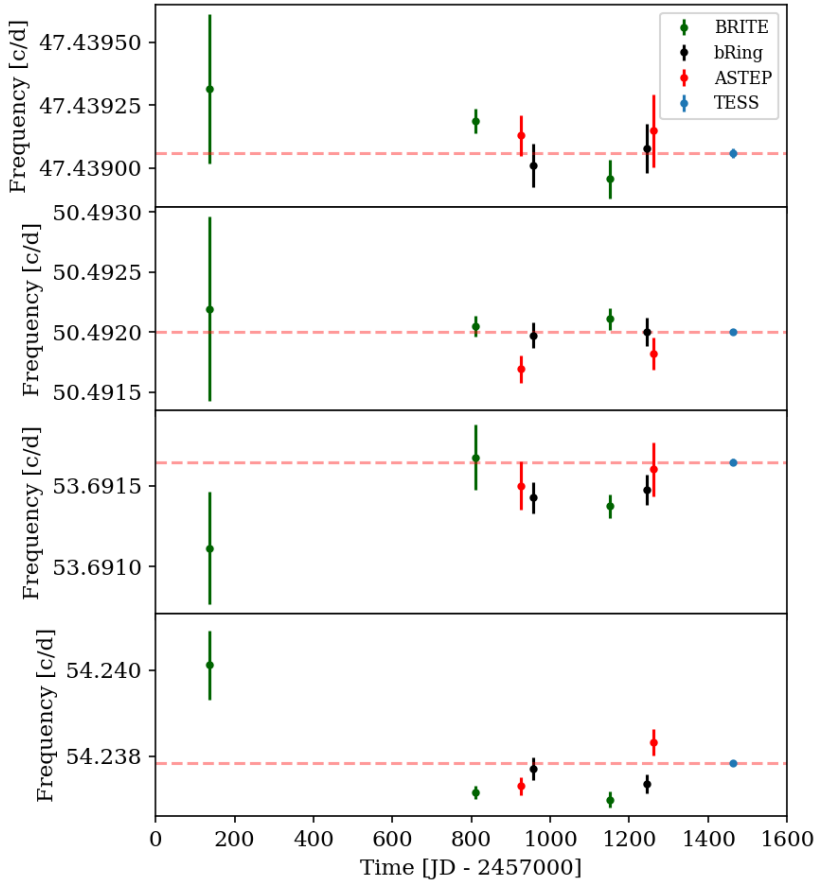


Figure 6.5: Frequencies and their uncertainties over all data sets for the four modes that are visible in all observations from the four different observatories. The dashed red line marks the frequency determined by the TESS mission, which has the smallest uncertainties. The uncertainties were calculated following Montgomery & Odonoghue (1999).

weighted time delay values and their corresponding uncertainties using the first three frequencies with the highest amplitudes.

The first simulation (Fig. 6.7) used the Kepler short-cadence one-minute time stamps. The measured time delays follow the prediction for a two-planet case. Removing every second data point, which effectively reduces the number of measurements by 50%, does not change the result (Fig. 6.8). One can, however, observe a small increase in the uncertainties for the time delays. This is expected, as a decrease of data points by a factor of two increases the uncertainty by a factor of $\sqrt{2}$, assuming Gaussian noise (Murphy 2012). Finally, we induced gaps into the light curve, effectively simulating ground-based observations by having data only

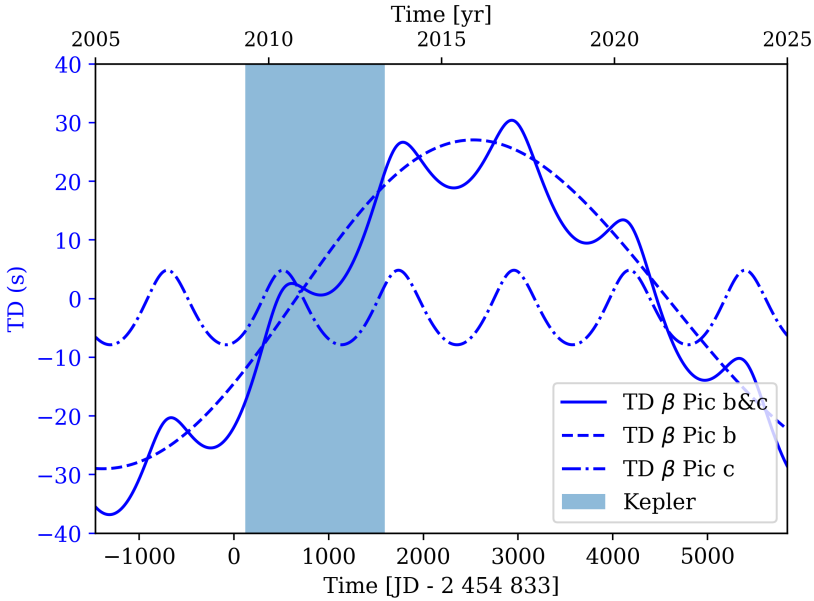


Figure 6.6: Expected time delays for two planets in the β Pictoris system. The dashed line is for β Pictoris b, the dashed-dotted line is for β Pictoris c, and the solid line shows both. The blue shaded region marks the time span of Kepler’s four-year main mission; we note that Kepler did not observe β Pictoris.

for half of the day. Due to a worse spectral window, there are many more peaks present in the amplitude spectrum. These new peaks influence the phases for the observed frequencies, as they cannot be resolved anymore. The scatter in the time delays increases significantly (Fig. 6.9), and one cannot conclusively distinguish between a one-planet solution (only β Pictoris b) or a two-planet solution. A bigger segment size mitigates this effect, as expected by the Rayleigh criterion.

This clearly illustrates that gaps influence the time delays the strongest, as the uncertainties in phase only scale with the square root of the cadence factor. One should also remove identified frequencies that are not used in the time delay analysis to get rid of their aliases.

6.5.3 Time delay analysis of the photometry

Figure 6.10 shows the predicted time delays caused by the planets in the β Pictoris system during the times when the observatories BRITE, ASTEP, bRing, and TESS collected photometry for the star. The available observations have been introduced in Section 6.3. The semi-amplitude of the predicted time delays for β Pictoris b and c is around 24 and 6 seconds, respectively.

As seen in Section 6.5.1, the TESS observations show the smallest uncertainties in frequency and were therefore used as a “gold standard” in this analysis. The

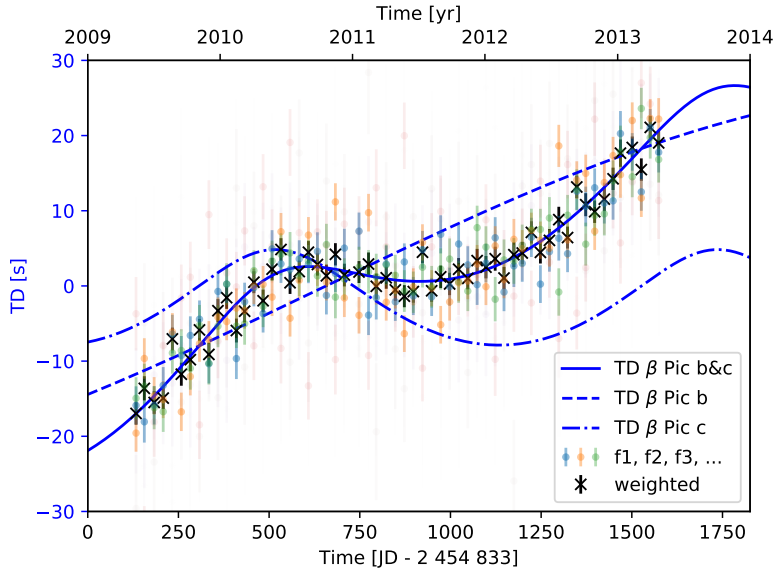


Figure 6.7: Derived time delay curve using 20-day segments by simulating Kepler observations of β Pictoris. Properties of the simulated light curve: one-minute cadence, continuous observations, 20 ppm noise in flux. The strongest frequencies (f_1 , f_2 , f_3 , ...) are shown here with their uncertainties. The weighted average of the measurements is shown in black.

frequency was thus fixed to the TESS values, as the PM method observes the phase shifts at a constant frequency (see Section 6.4.5). The time delay predictions (blue lines in Figure 6.10, 6.11 and 6.12) were also normalized to the midpoint time of TESS. As a time delay is a relative measure and not an absolute one, we set the time delay for TESS to zero. The evaluated time delays shown in Figures 6.11 and 6.12 are therefore relative to the TESS values.

The code used to calculate the time delays was written for this analysis and is heavily based on existing ones, namely `timedelay`⁶ and `maelstrom`⁷ (Hey et al. 2020a). The equations that were needed in order to evaluate the time delays are given in Section 6.4.4 and 6.4.5.

The phases were calculated by subtracting the midpoint time of the full data set. As discussed in Section 6.5.1, there are only four frequencies that are significant in all observations. The phases for each data set were then calculated based on a least-squares routine and their uncertainties from the respective covariance matrices. Equation 6.13 gives the conversion between the phase of a frequency and the respective time delays.

Figure 6.11 shows the derived time delays for the four different frequencies. They are clearly not consistent with each other. As discussed in Section 6.4.6,

⁶<https://github.com/danhey/timedelay>

⁷<https://github.com/danhey/maelstrom>

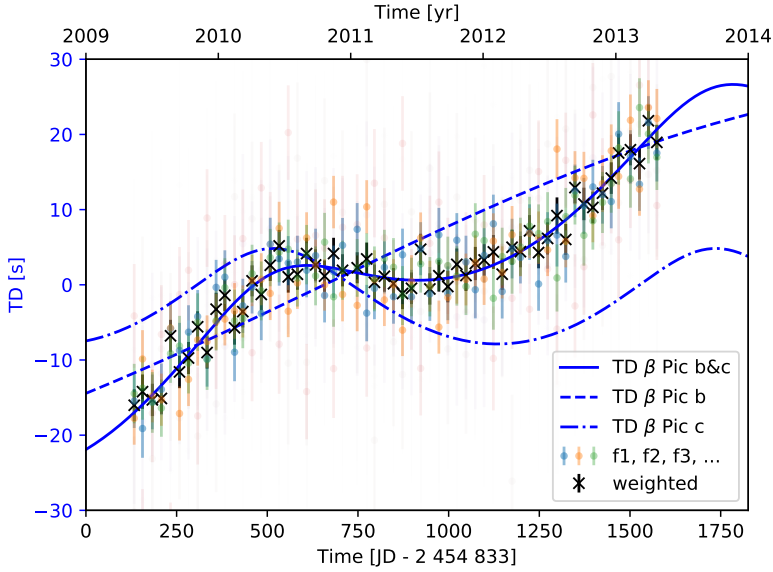


Figure 6.8: Derived time delay curve using 20-day segments by simulating Kepler observations of β Pictoris. Properties of the simulated light curve: two-minute cadence, continuous observations, 20 ppm noise in flux.

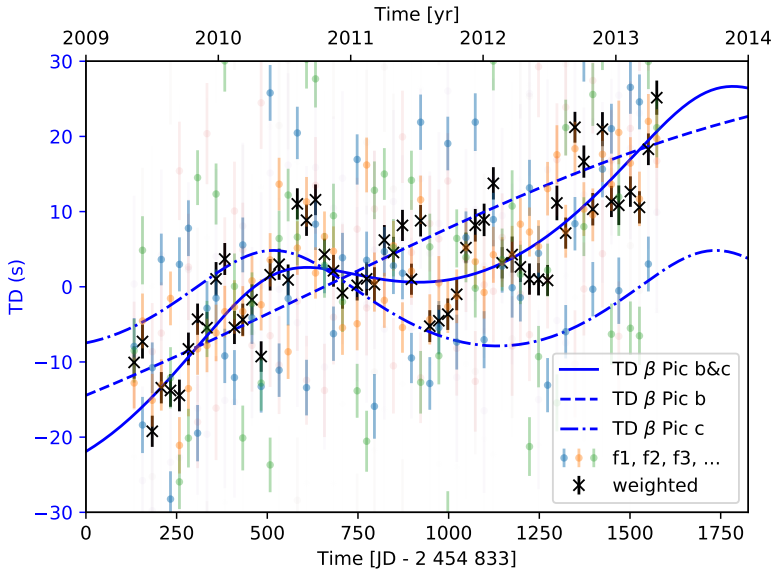


Figure 6.9: Derived time delay curve using 20-day segments by simulating Kepler observations of β Pictoris. Properties of the simulated light curve: one-minute cadence, 0.5-day gaps every day, 20 ppm noise in flux.

this rules out an extrinsic cause for the modulations (e.g., a companion), as all frequencies would show a similar behavior (examples of this are shown in Figure 6.3, 6.7, 6.8 and 6.9). A change in frequency was ruled out in Section 6.5.1. Furthermore, Zwintz et al. (2019) showed no significant phase change for our four frequencies in the BHR 2018 data set (therein, these four frequencies have the designations F8, F11, F13, and F15).

Next, we attempted to reproduce the different data sets as faithfully as possible and compare them with the time delay values shown in Figure 6.11. For that, we first determined the frequency, amplitude, and phase of the four pulsation modes visible in all observations. We calculated the residual noise for the pre-whitened data sets, which was then used to estimate the uncertainties following Montgomery & Odonoghue (1999). As before, we fixed the frequency to the TESS value. As we do not know the exact “true” frequency of the pulsations with infinite precision, we introduced an offset between the true pulsational frequencies and the TESS data set in the simulations. The uncertainty in frequency for these four strongest frequencies is on the order of 10^{-5} d^{-1} (see Table 6.5). This offset explains the linear trend for every frequency that is visible in Figure 6.11. The time delays of the simulated data set are shown in Figure 6.12.

This linear trend was discussed on simulated data in Section 3.2 of Murphy et al. (2016b) and “almost certainly” explains the observed trend in the WASP data of Murphy et al. (2013). A way to correct for it is to evaluate the slope between two maxima or minima of the sinusoidal variations. This is not a possibility in our case, as we would have had to further segment the data sets to identify the position of the maxima or minima, leading to even higher scatter in the phase. The lower panel of Figure 6.11 also shows that the uncertainties in the derived time delays for the data sets other than TESS are too big to differentiate between a one-planet or two-planet scenario, even without this linear trend. We therefore discuss the possibility of a second β Pictoris observation by TESS in the extended mission in the next section.

6.5.4 Detection limits for β Pictoris

Here, we determine the detection limits for companions in the β Pictoris system using the PM method. In a prior study by Hey et al. (2020b), the authors tried to estimate the detection limits of companions around δ Scuti stars. Their approach involved simulating time-series observations of these pulsating stars and adding white noise to the data. This allowed them to find a relationship between the S/N of the stellar pulsations and the observed scatter in the resulting time delay ($a \sin i/c$). The established relationship could be directly converted into a parameter space defining detectable companion masses and their orbital periods. The authors found that the detectability of companions strongly depends on the S/N of the stellar pulsations. Given the comparably low observed S/N of the δ Scuti pulsations observed in β Pictoris and the instability of the pulsational modes, we opted for a more conservative detection limit than what (84th percentile in Hey et al. 2020b) presented in their prior work.

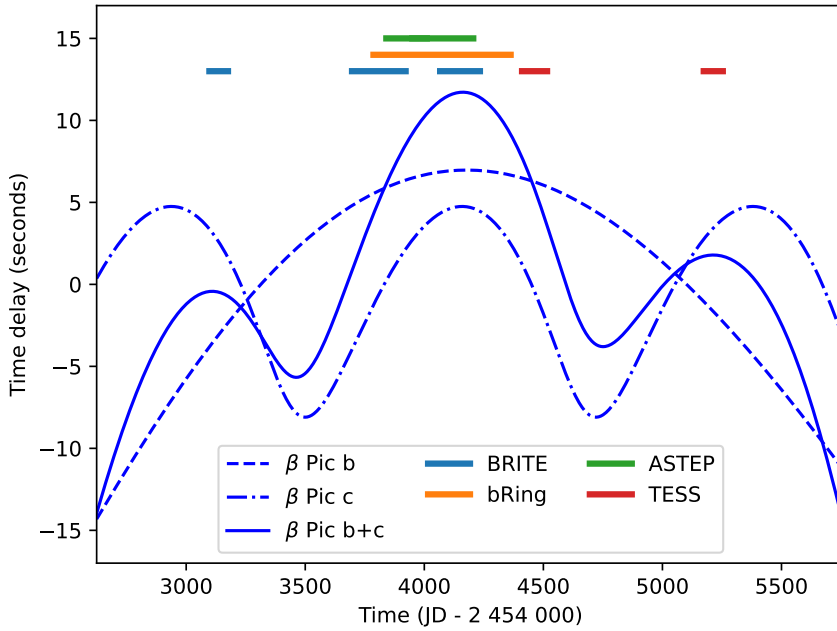


Figure 6.10: Time delay predictions for β Pictoris b (dashed line), c (dashed-dotted line), and both planets (solid line). Times when the star was observed are marked with lines.

Our findings are presented in Figure 6.13. We determined that the intrinsic variability of β Pictoris is too high to detect planet c. The other companion, β Pictoris b, is primarily not detectable at the moment due to the short baseline of observations compared to its long orbital period of approximately 24 years. It is worth noting that these calculations assume that the pulsational modes stay stable during the time of observations. However, we show in Section 6.5.5 by using the TESS data that this assumption is generally not met, with some modes appearing and disappearing during the observations. This further complicates any efforts to detect companions around the star.

6.5.5 Analysis of pulsational stability using TESS data

β Pictoris was observed in seven individual sectors between October 2018 and February 2021 (see Table 6.3). We performed a frequency analysis of these TESS sectors using *maelstrom*. We find that β Pictoris is seemingly undergoing significant frequency and amplitude modulation, which buries any signal induced by planetary companions. The periodograms of the stellar pulsations clearly show significant amplitude modulation by the rotational signal (see Fig. 6.14). We also find that the star is showing modes that are appearing and disappearing on short timescales. Figure 6.15 shows a mode that seems to be just appearing during the second half of the TESS observations. In summary, we find that β Pictoris' modes

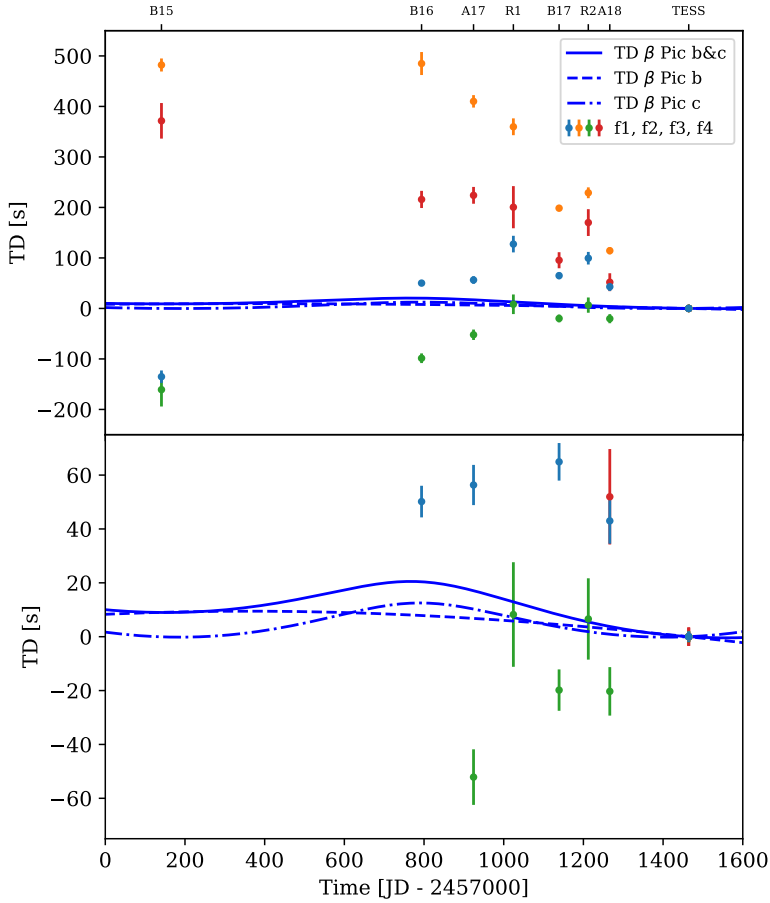


Figure 6.11: Time delay plot calculated from the phases of four different frequencies for all available observations by BRITE, bRing, ASTEP and TESS. Each color represents a frequency (f1, f2, f3, and f4) listed in Table 6.5. The blue lines indicate time delay predictions for β Pictoris b (dashed line), c (dashed, dotted line), and both planets (solid line). The lower panel is a zoom-in of the upper panel. The uncertainties in the time delays were derived from the covariance matrices given by the least-squares procedure, which was used in order to calculate the phases of the respective frequencies. The ticks at the top of the plot denote the various observatories: B15, B16, and B17 for the BRITE observations in the years 2015, 2016, and 2017, respectively; A17 and A18 for the ASTEP observations in 2017 and 2018; and R1 and R2 for the first and second part of the bRing data.

are not stable enough to probe to the necessary phase precision for the planetary companions.

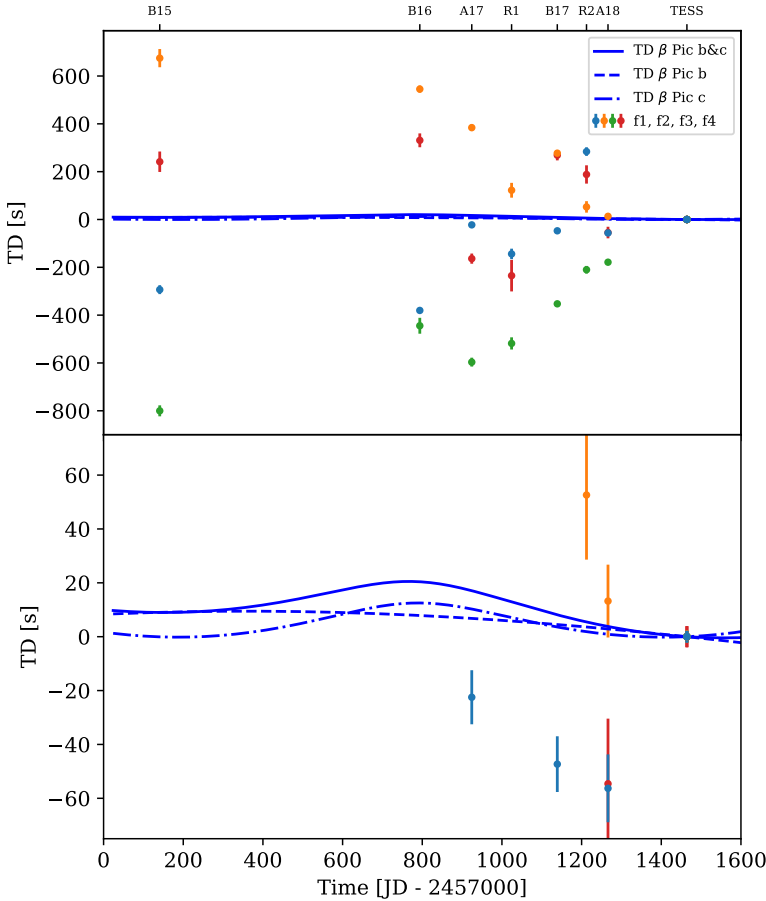


Figure 6.12: Time delay plot for the simulated data set showing a high similarity to the time delays of the real data set presented in Figure 6.12. The colored points represent the simulated time delays for the four strongest pulsational frequencies. The blue lines indicate time delay predictions for β Pictoris b (dashed line), c (dashed-dotted line), and both planets (solid line). The lower panel is a zoom-in of the upper panel. A description of the ticks at the top of the plot can be found in the caption of Figure 6.11.

6.5.6 Comparison to KIC 7917485

Here we compare the β Pictoris system to another A star with a planet detected through pulsation timing, KIC 7917485 (Murphy et al. 2016a), and evaluate the differences between the host stars that have affected the detectability of their corresponding planets. Compared to other Kepler δ Scuti stars, including those with binary star companions, (e.g., Murphy et al. 2018, 2020a), and Murphy et al. (2016a) found that KIC 7917485 had an exceptionally low time delay noise (sixth lowest of the 2040 δ Scuti stars in the Kepler primary mission sample). Similar

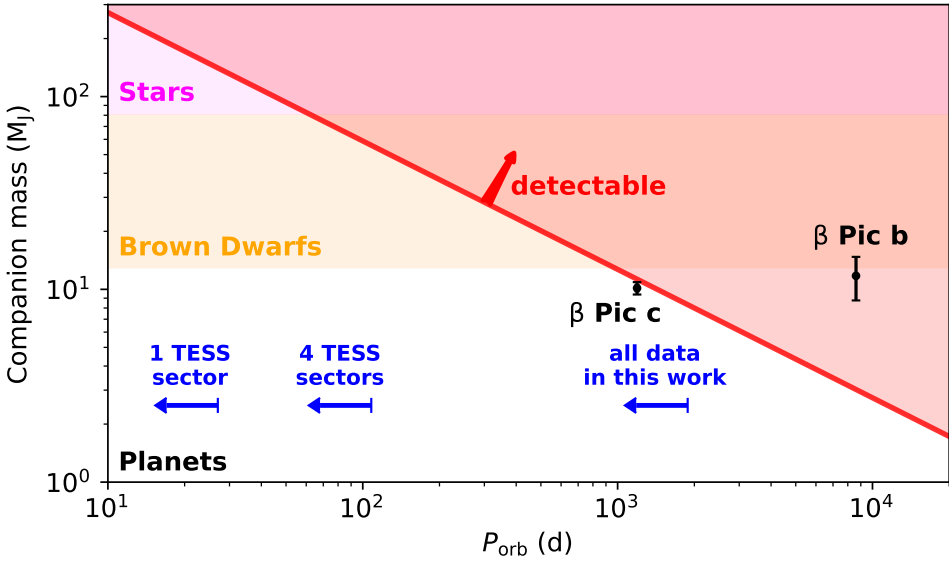


Figure 6.13: Detection limits for the β Pictoris system based on the calculations presented in Hey et al. (2020b) assuming $1.8 M_{\odot}$ for the star and an inclination of 90° for both planets. The detectable parameter space for companions depending on their orbital period P_{orb} and mass is shaded red, assuming β Pictoris is a non-ideal δ Scuti pulsator (see Section 6.5.5 for a discussion on the pulsational modes of β Pictoris as seen by TESS). β Pictoris c is generally not detectable due to the intrinsic noise of the pulsations, and the time delay caused by β Pictoris b has a period that is too long in comparison to the baseline of our observations. The masses corresponding to brown dwarfs ($13 M_J \lesssim M \lesssim 80 M_J$) are shaded in yellow, and the stellar regime ($M > 80 M_J$) is in magenta, with M_J being a Jupiter mass. The figure is adapted from Hey et al. (2020b).

planetary-mass companions might exist around the second and ninth lowest noise stars in the Kepler sample (KIC 9700322 and KIC 8453431). Unlike KIC 7917485, however, the observations of these systems and their potential companions do not cover a full orbital period, thus precluding determination of their orbital parameters.

The additional time-delay jitter seen in β Pictoris might arise from mode interaction or from other effects causing the observed changes in mode amplitude. It is this jitter that hinders the ability to detect planetary-mass objects around pulsating stars. This is comparable to the intrinsic RV jitter of a star, which impacts the ability to detect planets using RV measurements. The intrinsic variability is evident in the δ Scuti pulsations of β Pictoris and generally renders white dwarfs and subdwarfs as less ideal targets for the analysis of their time delays using the PM method (Murphy 2018). This limitation persists despite the high oscillation frequencies exhibited by these pulsating stars that would otherwise make them promising targets for detecting time delays caused by a companion (Compton et al. 2016).

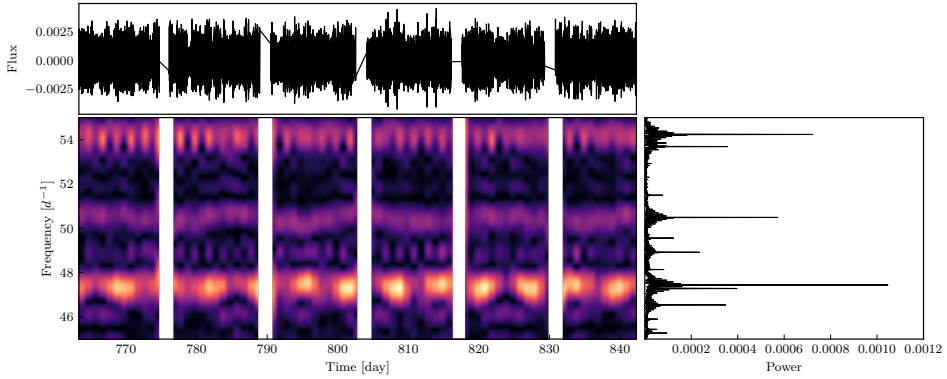


Figure 6.14: Two-dimensional periodogram showing the frequency region between 45 and 55 d^{-1} . One can see that most of the modes are significantly amplitude modulated by the rotational signal. The mode at 54 d^{-1} goes much faster, which is probably due to beating with nearby modes. The mode at 50.5 d^{-1} itself undergoes incoherent FM.

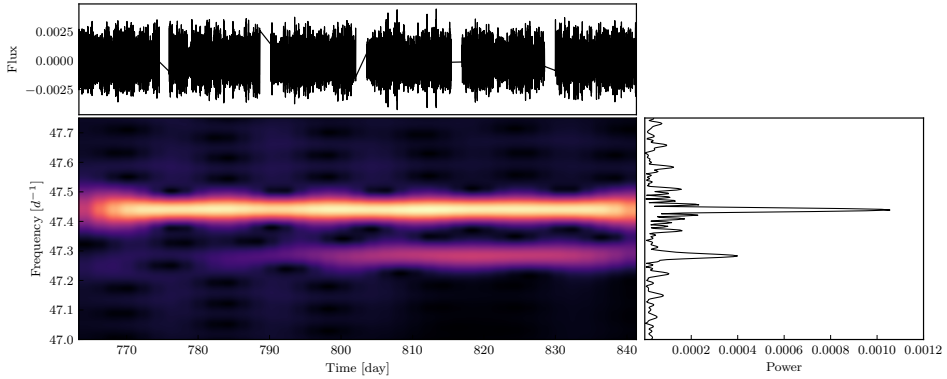


Figure 6.15: Periodogram showing a pulsational mode around 47.3 d^{-1} that is just appearing at the end of the observations.

6.6 Conclusions

In this work, we have analyzed the time delays derived from the phases of the δ Scuti pulsations of β Pictoris. The photometric data of the star were collected over a time period of approximately four years by four different observatories: the BRITE-Constellation, bRing, ASTEP, and TESS. In contrast to previous studies, we did not segment the observations into smaller sets (e.g. ten-day bins). This would have caused high uncertainties in the phases and therefore also in the time delays. Nevertheless, we could not see the influence of β Pictoris b or c in the data due to this time delay scatter. The uncertainty in the pulsational frequencies leads to a linear trend in the time delays and has also been seen in a previous study by Murphy et al. (2013) and in simulations by Murphy et al. (2016b). We performed a

frequency analysis using the open-source tool **maelstrom**. We find that β Pictoris does not have the needed stability to detect planetary companions using the time delay method. The stellar pulsations clearly show strong amplitude modulation caused by the rotational signal and identify modes that seemingly appeared during our observations.

Previous studies have used the PM method on Kepler data, finding many binary star systems (Murphy et al. 2016b, and references therein) and a planet (Murphy et al. 2016a). This work is the first to use the PM method with so many different data sets that have a precision significantly lower than the Kepler mission. However, the PM method remains valuable technique, as it is able to find planets and stars in a parameter space that is poorly covered by other methods, such as the RV method (see e.g. Murphy 2018).

Acknowledgements

This work includes data collected by the TESS mission, which are publicly available from the Mikulski Archive for Space Telescopes (MAST). Funding for the TESS mission is provided by the NASA Explorer Program. This work has made use of data from the European Space Agency (ESA) mission *Gaia* (<https://www.cosmos.esa.int/gaia>), processed by the *Gaia* Data Processing and Analysis Consortium (DPAC, <https://www.cosmos.esa.int/web/gaia/dpac/consortium>). Funding for the DPAC has been provided by national institutions, in particular the institutions participating in the *Gaia* Multilateral Agreement. We made use of the software package **Period04** (Lenz & Breger 2005), the Python programming language (Rossum 1995), and the open-source Python packages **numpy** (van der Walt et al. 2011), **matplotlib** (Hunter 2007b), **astropy** (Astropy Collaboration et al. 2013), **lightkurve** (Lightkurve Collaboration et al. 2018), **timedelay**⁸, **maelstrom**⁹ and **SMURFS** (Müllner 2020). This research has made use of the SIMBAD database, operated at CDS, Strasbourg, France. This research has made use of the NASA Exoplanet Archive, which is operated by the California Institute of Technology, under contract with the National Aeronautics and Space Administration under the Exoplanet Exploration Program. Part of this research was carried out at the Jet Propulsion Laboratory, California Institute of Technology, under a contract with the National Aeronautics and Space Administration (80NM0018D0004). This research has made use of data collected by the BRITE-Constellation satellite mission, designed, built, launched, operated and supported by the Austrian Research Promotion Agency (FFG), the University of Vienna, the Technical University of Graz, the University of Innsbruck, the Canadian Space Agency (CSA), the University of Toronto Institute for Aerospace Studies (UTIAS), the Foundation for Polish Science & Technology (FNiTP MNiSW), and National Science Centre (NCN). The bRing observatory at Siding Springs, Australia was supported by a University of Rochester University Research Award. The field activities at Dome C for ASTEP benefit from the sup-

⁸<https://github.com/danhey/timedelay>

⁹<https://github.com/danhey/maelstrom>

port of the French and Italian polar agencies IPEV and PNRA in the framework of the Concordia station programme. The PicSat team thanks funding from the European Research Council (ERC) under the Horizon 2020 research and innovation programme (Grant agreement No. 639248, LITHIUM). SJM was supported by the Australian Research Council (ARC) through Future Fellowship FT210100485.

Appendix

6.A TESS frequency analysis

6.A.1 Frequency list

Table 6.5: Pulsational frequencies, amplitudes in instrumental millimagnitudes, and normalized flux in parts per million, phases, and signal-to-noise ratio sorted by the pre-whitening sequence.

#	Freq. (d^{-1})	Ampl. (mmag)	Ampl. (ppm)	Phase	S/N
1	47.43895(6)	1.029(9)	948(9)	0.9071(14)	20.6
2	53.69166(7)	0.948(9)	873(9)	0.2782(16)	19.4
3	50.49168(7)	0.926(9)	852(9)	0.5567(16)	23.4
4	54.23716(12)	0.553(9)	509(9)	0.982(3)	22.8
5	39.06315(15)	0.442(9)	407(9)	0.699(3)	22.5
6	46.54259(16)	0.415(9)	382(9)	0.391(4)	18.7
7	48.9192(3)	0.230(9)	212(9)	0.950(6)	17.3
8	43.5283(3)	0.214(9)	197(9)	0.029(7)	19.9
9	47.2853(4)	0.182(9)	168(9)	0.186(8)	16.2
10	57.4525(4)	0.164(9)	151(9)	0.577(9)	18.0
11	34.7605(5)	0.143(9)	131(9)	0.754(10)	23.7
12	38.1297(5)	0.131(9)	121(9)	0.980(11)	20.2
13	45.2698(5)	0.120(9)	110(9)	0.411(12)	12.8
14	51.4969(6)	0.118(9)	109(9)	0.397(13)	14.7
15	47.2686(7)	0.093(9)	85(9)	0.419(16)	12.3
16	50.8310(8)	0.086(9)	79(9)	0.630(17)	12.9
17	49.7131(8)	0.085(9)	78(9)	0.290(17)	11.3
18	53.8545(8)	0.085(9)	78(9)	0.566(17)	9.5
19	44.6833(8)	0.084(9)	77(9)	0.297(18)	11.3
20	65.1356(8)	0.083(9)	76(9)	0.350(18)	17.9
21	43.8292(8)	0.082(9)	76(9)	0.555(18)	16.3
22	49.5595(8)	0.079(9)	73(9)	0.980(19)	13.4
23	42.0365(9)	0.077(9)	71(9)	0.327(19)	11.1
24	54.2269(9)	0.073(9)	67(9)	0.51(2)	10.0

Continued on next page

Table 6.5 – continued from previous page

#	Freq. (d^{-1})	Ampl. (mmag)	Ampl. (ppm)	Phase	S/N
25	41.6498(9)	0.071(9)	65(9)	0.59(2)	13.0
26	48.1381(10)	0.064(9)	59(9)	0.23(2)	11.2
27	45.8998(10)	0.064(9)	59(9)	0.73(2)	12.4
28	50.2689(12)	0.054(9)	50(9)	0.90(3)	12.1
29	75.6780(13)	0.052(9)	48(9)	0.68(3)	12.2
30	58.3469(13)	0.050(9)	46(9)	0.61(3)	11.3
31	45.4375(14)	0.047(9)	44(9)	0.00(3)	12.3
32	54.4625(14)	0.047(9)	43(9)	0.16(3)	8.1
33	53.6827(15)	0.042(9)	39(9)	0.16(3)	7.3
34	53.5521(16)	0.040(9)	37(9)	0.48(4)	7.7
35	42.1735(16)	0.040(9)	37(9)	0.70(4)	9.5
36	58.2515(17)	0.039(9)	36(9)	0.81(4)	10.5
37	42.3963(17)	0.039(9)	36(9)	0.68(4)	11.5

6.A.2 Gaussian high-pass filter

By applying a Gaussian high-pass filter on the TESS light curve (see Fig. 6.16), the long-term variations such as systematics and the exocomets are significantly weakened. At the same time however, the higher frequencies related to the δ Scuti pulsations are preserved.

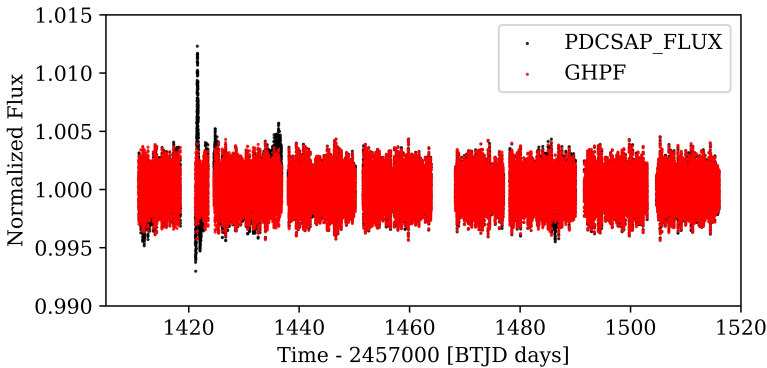


Figure 6.16: Comparison of the PDCSAP light curve (black in the background) and the Gaussian high-pass filter (red dots) of it. The Gaussian high-pass filter clearly shows less long-term variations in the light curve.

BIBLIOGRAPHY

- Abe, L., Gonçalves, I., Agabi, A., et al. 2013, *A&A*, 553, A49
- Acuña, L., Deleuil, M., & Mousis, O. 2023, *A&A*, 677, A14
- Acuña, L., Deleuil, M., Mousis, O., et al. 2021, *A&A*, 647, A53
- Adams, E. R., Jackson, B., Endl, M., et al. 2017, *AJ*, 153, 82
- Adams, F. C. & Laughlin, G. 2006, *ApJ*, 649, 1004
- Aerts, C., Christensen-Dalsgaard, J., & Kurtz, D. W. 2010, *Asteroseismology* (Springer Dordrecht)
- Agol, E., Cowan, N. B., Knutson, H. A., et al. 2010, *ApJ*, 721, 1861
- Agol, E., Dorn, C., Grimm, S. L., et al. 2021, *PSJ*, 2, 1
- Ahrer, E.-M., Stevenson, K. B., Mansfield, M., et al. 2023, *Nature*, 614, 653
- Airapetian, V. S., Barnes, R., Cohen, O., et al. 2020, *International Journal of Astrobiology*, 19, 136
- Alderson, L., Wakeford, H. R., Alam, M. K., et al. 2023, *Nature*, 614, 664
- Allard, F., Allard, N. F., Homeier, D., et al. 2007a, *A&A*, 474, L21
- Allard, N. F., Kielkopf, J. F., & Allard, F. 2007b, *European Physical Journal D*, 44, 507
- Allart, R., Bourrier, V., Lovis, C., et al. 2019, *A&A*, 623, A58
- Alonso, R. 2018, in *Handbook of Exoplanets*, ed. H. J. Deeg & J. A. Belmonte (Springer International Publishing), 40
- Anderson, D. R., Collier Cameron, A., Delrez, L., et al. 2017, *A&A*, 604, A110
- Angelo, I. & Hu, R. 2017, *AJ*, 154, 232
- Antoci, V., Cunha, M., Houdek, G., et al. 2014, *ApJ*, 796, 118
- Arney, G., Meadows, V., Crisp, D., et al. 2014, *Journal of Geophysical Research (Planets)*, 119, 1860
- Astropy Collaboration, Price-Whelan, A. M., Lim, P. L., et al. 2022, *Astrophysical Journal*, 935, 167
- Astropy Collaboration, Price-Whelan, A. M., Sipőcz, B. M., et al. 2018, *AJ*, 156, 123

- Astropy Collaboration, Robitaille, T. P., Tollerud, E. J., et al. 2013, *A&A*, 558, A33
- Atreya, S. K., Crida, A., Guillot, T., et al. 2022, arXiv e-prints, arXiv:2205.06914
- Augereau, J. C., Nelson, R. P., Lagrange, A. M., Papaloizou, J. C. B., & Mouillet, D. 2001, *A&A*, 370, 447
- Aumann, H. H., Gillett, F. C., Beichman, C. A., et al. 1984, *ApJ*, 278, L23
- Auvergne, M., Bodin, P., Boisdard, L., et al. 2009, *A&A*, 506, 411
- Balona, L. A. 2014, *MNRAS*, 443, 1946
- Baraffe, I., Chabrier, G., Allard, F., & Hauschildt, P. H. 1998, *A&A*, 337, 403
- Baraffe, I., Homeier, D., Allard, F., & Chabrier, G. 2015, *A&A*, 577, A42
- Barnes, T. G., I. & Moffett, T. J. 1975, *AJ*, 80, 48
- Barragán, O., Gandolfi, D., Dai, F., et al. 2018, *A&A*, 612, A95
- Barton, E. J., Yurchenko, S. N., & Tennyson, J. 2013, *MNRAS*, 434, 1469
- Batalha, N. E., Mandell, A., Pontoppidan, K., et al. 2017, *PASP*, 129, 064501
- Batalha, N. M., Borucki, W. J., Bryson, S. T., et al. 2011, *ApJ*, 729, 27
- Bean, J. 2012, Revealing the Diversity of Super-Earth Atmospheres, HST Proposal ID 13021. Cycle 20
- Beatty, T. G., Stevens, D. J., Collins, K. A., et al. 2017, *AJ*, 154, 25
- Bedding, T. R., Murphy, S. J., Hey, D. R., et al. 2020, *Nature*, 581, 147
- Bell, T., Ahler, E.-M., Brande, J., et al. 2022, *The Journal of Open Source Software*, 7, 4503
- Bell, T. J., Kreidberg, L., Kendrew, S., et al. 2023a, arXiv e-prints, arXiv:2301.06350
- Bell, T. J., Welbanks, L., Schlawin, E., et al. 2023b, *Nature*, 623, 709
- Benneke, B., Wong, I., Piaulet, C., et al. 2019, *ApJ*, 887, L14
- Benz, W., Broeg, C., Fortier, A., et al. 2021, *Experimental Astronomy*, 51, 109
- Bergfors, C., Brandner, W., Daemgen, S., et al. 2013, *MNRAS*, 428, 182
- Berta, Z. K., Charbonneau, D., Désert, J.-M., et al. 2012, *ApJ*, 747, 35
- Berta-Thompson, Z. K., Irwin, J., Charbonneau, D., et al. 2015, *Nature*, 527, 204
- Beust, H. & Morbidelli, A. 2000, *Icarus*, 143, 170
- Birkby, J. L. 2018, arXiv e-prints, arXiv:1806.04617
- Birkby, J. L., de Kok, R. J., Brogi, M., et al. 2013, *MNRAS*, 436, L35
- Blunt, S., Wang, J. J., Angelo, I., et al. 2020, *AJ*, 159, 89
- Bolmont, E., Selsis, F., Owen, J. E., et al. 2017, *MNRAS*, 464, 3728

- Bonomo, A. S., Dumusque, X., Massa, A., et al. 2023, *A&A*, 677, A33
- Borucki, W. J., Koch, D., Basri, G., et al. 2010, *Science*, 327, 977
- Bourrier, V., Dumusque, X., Dorn, C., et al. 2018, *A&A*, 619, A1
- Bowman, D. M., Kurtz, D. W., Breger, M., Murphy, S. J., & Holdsworth, D. L. 2016, *MNRAS*, 460, 1970
- Brandeker, A., Alibert, Y., Bourrier, V., et al. 2021, Is it raining lava in the evening on 55 Cancri e?, *JWST Proposal. Cycle 1*
- Breger, M. & Montgomery, M. H. 2014, *ApJ*, 783, 89
- Breger, M., Stich, J., Garrido, R., et al. 1993, *A&A*, 271, 482
- Brugger, B., Mousis, O., Deleuil, M., & Deschamps, F. 2017, *ApJ*, 850, 93
- Brugger, B., Mousis, O., Deleuil, M., & Lunine, J. I. 2016, *ApJ*, 831, L16
- Bryson, S., Coughlin, J., Batalha, N. M., et al. 2020, *AJ*, 159, 279
- Burdanov, A., Delrez, L., Gillon, M., & Jehin, E. 2018, in *Handbook of Exoplanets*, ed. H. J. Deeg & J. A. Belmonte (Springer International Publishing), 130
- Burrows, C. J., Krist, J. E., Stapelfeldt, K. R., & WFPC2 Investigation Definition Team. 1995, in *American Astronomical Society Meeting Abstracts*, Vol. 187, *American Astronomical Society Meeting Abstracts*, 32.05
- Bushouse, H., Eisenhamer, J., Dencheva, N., et al. 2022, *JWST Calibration Pipeline*, Zenodo
- Carone, L., Mollière, P., Zhou, Y., et al. 2021, *Astronomy and Astrophysics*, 646, A168
- Castan, T. & Menou, K. 2011, *ApJ*, 743, L36
- Castelli, F. & Kurucz, R. L. 2003, in *Modelling of Stellar Atmospheres*, ed. N. Piskunov, W. W. Weiss, & D. F. Gray, Vol. 210, A20
- Catling, D. C. & Kasting, J. F. 2017, *Exoplanets: Habitability and Characterization* (Cambridge University Press), 422–448
- Chachan, Y. & Stevenson, D. J. 2018, *ApJ*, 854, 21
- Chadney, J. M., Galand, M., Unruh, Y. C., Koskinen, T. T., & Sanz-Forcada, J. 2015, *Icarus*, 250, 357
- Challener, R. C., Harrington, J., Jenkins, J., et al. 2021, *PSJ*, 2, 9
- Chao, K.-H., deGraffenried, R., Lach, M., et al. 2021, *Chemie der Erde / Geochemistry*, 81, 125735
- Charbonneau, D., Allen, L. E., Megeath, S. T., et al. 2005, *ApJ*, 626, 523
- Charbonneau, D., Brown, T. M., Noyes, R. W., & Gilliland, R. L. 2002, *Astrophysical Journal*, 568, 377
- Chiang, E. & Laughlin, G. 2013, *MNRAS*, 431, 3444

- Cloutier, R., Charbonneau, D., Deming, D., Bonfils, X., & Astudillo-Defru, N. 2021, *AJ*, 162, 174
- Colon, K. 2017, The KELT-11b Opportunity: Measuring the Atmospheric Water Abundance for a Sub-Saturn-Mass Planet around a Metal-Rich Star, HST Proposal id.15255. Cycle 25
- Colon, K., Angerhausen, D., Barclay, T., et al. 2019, Testing the Hypothesis of a Low Metallicity Atmosphere for the Extremely Inflated Sub-Saturn-Mass Planet KELT-11b, HST Proposal. Cycle 27, ID. #15926
- Colón, K. D., Kreidberg, L., Welbanks, L., et al. 2020, *AJ*, 160, 280
- Compton, D. L., Bedding, T. R., Murphy, S. J., & Stello, D. 2016, *MNRAS*, 461, 1943
- Cousins, A. W. J. 1971, *Royal Observatory Annals*, 7
- Cowan, N. B. & Agol, E. 2011, *ApJ*, 729, 54
- Cowan, N. B. & Fujii, Y. 2018, in *Handbook of Exoplanets*, ed. H. J. Deeg & J. A. Belmonte (Springer International Publishing), 147
- Crida, A., Ligi, R., Dorn, C., Borsa, F., & Lebreton, Y. 2018a, *Research Notes of the American Astronomical Society*, 2, 172
- Crida, A., Ligi, R., Dorn, C., & Lebreton, Y. 2018b, *ApJ*, 860, 122
- Crosley, M. K. & Osten, R. A. 2018, *ApJ*, 856, 39
- Crossfield, I. J. M. & Kreidberg, L. 2017, *AJ*, 154, 261
- Crossfield, I. J. M., Malik, M., Hill, M. L., et al. 2022, *ApJ*, 937, L17
- Crouzet, N., McCullough, P. R., Deming, D., & Madhusudhan, N. 2014, *ApJ*, 795, 166
- Cubillos, P., Harrington, J., Madhusudhan, N., et al. 2013, *ApJ*, 768, 42
- Cumming, A., Butler, R. P., Marcy, G. W., et al. 2008, *PASP*, 120, 531
- Dai, F., Masuda, K., Winn, J. N., & Zeng, L. 2019, *ApJ*, 883, 79
- Dang, L., Cowan, N. B., Hammond, M., et al. 2021, A Hell of a Phase Curve: Mapping the Surface and Atmosphere of a Lava Planet K2-141b, JWST Proposal. Cycle 1
- Dawson, R. I. & Fabrycky, D. C. 2010, *ApJ*, 722, 937
- Dawson, R. I. & Johnson, J. A. 2018, *ARA&A*, 56, 175
- de Wit, J., Wakeford, H. R., Gillon, M., et al. 2016, *Nature*, 537, 69
- de Wit, J., Wakeford, H. R., Lewis, N. K., et al. 2018, *Nature Astronomy*, 2, 214
- Deibert, E. K., de Mooij, E. J. W., Jayawardhana, R., et al. 2021, *AJ*, 161, 209
- Delrez, L., Gillon, M., Triaud, A. H. M. J., et al. 2018, *MNRAS*, 475, 3577
- Deming, D., Bouwman, J., Dicken, D., et al. 2021, A Time Series Calibration of Medium Resolution Spectroscopy with MIRI, JWST Proposal. Cycle 1, ID. #1556

- Deming, D., Knutson, H., Kammer, J., et al. 2015, *ApJ*, 805, 132
- Deming, D. & Knutson, H. A. 2020, *Nature Astronomy*, 4, 453
- Deming, D., Louie, D., & Sheets, H. 2019, *PASP*, 131, 013001
- Deming, D. & Seager, S. 2017, arXiv e-prints, arXiv:1701.00493
- Deming, D., Seager, S., Richardson, L. J., & Harrington, J. 2005, *Nature*, 434, 740
- Deming, D., Wilkins, A., McCullough, P., et al. 2013, *Astrophysical Journal*, 774, 95
- Deming, D., Wilkins, A., McCullough, P., et al. 2012, in *American Astronomical Society Meeting Abstracts*, Vol. 219, American Astronomical Society Meeting Abstracts #219, 405.05
- Demory, B.-O. 2014, *ApJ*, 789, L20
- Demory, B.-O., Gillon, M., de Wit, J., et al. 2016a, *Nature*, 532, 207
- Demory, B. O., Gillon, M., Deming, D., et al. 2011, *A&A*, 533, A114
- Demory, B.-O., Gillon, M., Madhusudhan, N., & Queloz, D. 2016b, *MNRAS*, 455, 2018
- Derekas, A., Murphy, S. J., Dállya, G., et al. 2019, *MNRAS*, 486, 2129
- Diamond-Lowe, H., Charbonneau, D., Malik, M., Kempton, E. M. R., & Beletsky, Y. 2020, *AJ*, 160, 188
- Domingue, D. L., Koehn, P. L., Killen, R. M., et al. 2007, *Space Sci. Rev.*, 131, 161
- Dong, C., Jin, M., Lingam, M., et al. 2018, *Proceedings of the National Academy of Science*, 115, 260
- Dorn, C., Harrison, J. H. D., Bonsor, A., & Hands, T. O. 2019, *MNRAS*, 484, 712
- Dorn, C., Noack, L., & Rozel, A. B. 2018, *A&A*, 614, A18
- Dressing, C. D. & Charbonneau, D. 2015, *ApJ*, 807, 45
- Ducrot, E., Gillon, M., Delrez, L., et al. 2020, *A&A*, 640, A112
- Ducrot, E., Sestovic, M., Morris, B. M., et al. 2018, *AJ*, 156, 218
- Dumusque, X., Bonomo, A. S., Haywood, R. D., et al. 2014, *ApJ*, 789, 154
- Dyrek, A., Min, M., Decin, L., et al. 2023, arXiv e-prints, arXiv:2311.12515
- Eastman, J. D., Rodriguez, J. E., Agol, E., et al. 2019, arXiv e-prints, arXiv:1907.09480
- Ehrenreich, D., Bourrier, V., Bonfils, X., et al. 2012, *A&A*, 547, A18
- Ehrenreich, D., Bourrier, V., Wheatley, P. J., et al. 2015, *Nature*, 522, 459
- Encrenaz, T. & Coustenis, A. 2018, in *Handbook of Exoplanets*, ed. H. J. Deeg & J. A. Belmonte (Springer International Publishing), 45
- Espinoza, N., Bello-Arufe, A., Buchhave, L. A., et al. 2021, The first near-infrared spectroscopic phase-curve of a super-Earth, JWST Proposal. Cycle 1

- Espinoza, N., Kossakowski, D., & Brahm, R. 2019, *Monthly Notices of the RAS*, 490, 2262
- Essack, Z., Seager, S., & Pajusalu, M. 2020, *ApJ*, 898, 160
- Evans, T. M., Sing, D. K., Wakeford, H. R., et al. 2016, *Astrophysical Journal Letters*, 822, L4
- Fabrycky, D. C. 2010, in *Exoplanets*, ed. S. Seager (University of Arizona Press), 217–238
- Faedi, F., Barros, S. C. C., Anderson, D. R., et al. 2011, *A&A*, 531, A40
- Fazio, G. G., Hora, J. L., Allen, L. E., et al. 2004, *ApJS*, 154, 10
- Fegley, B. & Cameron, A. G. W. 1987, *Earth and Planetary Science Letters*, 82, 207
- Feinstein, A. D., Radica, M., Welbanks, L., et al. 2023, *Nature*, 614, 670
- Ferlet, R., Hobbs, L. M., & Madjar, A. V. 1987, *A&A*, 185, 267
- Fischer, D. A. 2018, arXiv e-prints, arXiv:1807.11925
- Fischer, D. A., Marcy, G. W., Butler, R. P., et al. 2008, *ApJ*, 675, 790
- Fischer, D. A. & Valenti, J. 2005, *ApJ*, 622, 1102
- Fleming, D. P., Barnes, R., Luger, R., & VanderPlas, J. T. 2020, *ApJ*, 891, 155
- Foreman-Mackey, D. 2016, *The Journal of Open Source Software*, 1, 24
- Foreman-Mackey, D., Hogg, D. W., Lang, D., & Goodman, J. 2013a, *Publications of the ASP*, 125, 306
- Foreman-Mackey, D., Hogg, D. W., Lang, D., & Goodman, J. 2013b, *PASP*, 125, 306
- Foreman-Mackey, D., Luger, R., Agol, E., et al. 2021a, *The Journal of Open Source Software*, 6, 3285
- Foreman-Mackey, D., Luger, R., Agol, E., et al. 2021b, *exoplanet: Gradient-based probabilistic inference for exoplanet data & other astronomical time series*, Zenodo
- Fortney, J. J. 2005, *MNRAS*, 364, 649
- Fortney, J. J., Mordasini, C., Nettelmann, N., et al. 2013, *ApJ*, 775, 80
- Fraine, J., Deming, D., Benneke, B., et al. 2014, *Nature*, 513, 526
- France, K., Loyd, R. O. P., Youngblood, A., et al. 2016, *ApJ*, 820, 89
- Fulton, B. J., Petigura, E. A., Howard, A. W., et al. 2017, *AJ*, 154, 109
- Gaia Collaboration, Prusti, T., de Bruijne, J. H. J., et al. 2016, *A&A*, 595, A1
- Gaia Collaboration, Vallenari, A., Brown, A. G. A., et al. 2023, *A&A*, 674, A1
- Galland, F., Lagrange, A. M., Udry, S., et al. 2006, *A&A*, 447, 355
- Garcia, L. J., Moran, S. E., Rackham, B. V., et al. 2022, *A&A*, 665, A19

- Gelman, A. & Rubin, D. B. 1992, *Statist. Sci.*, 7, 457
- Gelman, A. & Rubin, D. B. 1992, *Statistical Science*, 7, 457
- Giacobbe, P., Brogi, M., Gandhi, S., et al. 2021, *Nature*, 592, 205
- Gillon, M., Deming, D., Demory, B. O., et al. 2010, *A&A*, 518, A25
- Gillon, M., Demory, B. O., Madhusudhan, N., et al. 2014, *A&A*, 563, A21
- Gillon, M., Ducrot, E., Agol, E., et al. 2023, TRAPPIST-1 Planets: Atmospheres Or Not?, JWST Proposal. Cycle 2, ID. #3077
- Gillon, M., Jehin, E., Lederer, S. M., et al. 2016, *Nature*, 533, 221
- Gillon, M., Meadows, V., Agol, E., et al. 2020, in *Bulletin of the American Astronomical Society*, Vol. 52, 0208
- Gillon, M., Triaud, A. H. M. J., Demory, B.-O., et al. 2017, *Nature*, 542, 456
- Gillon, M., Triaud, A. H. M. J., Fortney, J. J., et al. 2012, *A&A*, 542, A4
- Golimowski, D. A., Ardila, D. R., Krist, J. E., et al. 2006, *AJ*, 131, 3109
- Gray, R. O., Corbally, C. J., Garrison, R. F., et al. 2006, *AJ*, 132, 161
- Greene, T. P., Bell, T. J., Ducrot, E., et al. 2023, arXiv e-prints, arXiv:2303.14849
- Guillot, T., Abe, L., Agabi, A., et al. 2015, *Astronomische Nachrichten*, 336, 638
- Günther, M. N. & Daylan, T. 2019, *allesfitter: Flexible star and exoplanet inference from photometry and radial velocity*, *Astrophysics Source Code Library*, record ascl:1903.003
- Günther, M. N. & Daylan, T. 2021, *Astrophysical Journal, Supplement*, 254, 13
- Guo, X., Crossfield, I. J. M., Dragomir, D., et al. 2020, *AJ*, 159, 239
- Hammond, M. & Pierrehumbert, R. T. 2017, *ApJ*, 849, 152
- Hapke, B. 1977, *Physics of the Earth and Planetary Interiors*, 15, 264
- Hapke, B. 2001, *JGR*, 106, 10039
- Hapke, B. 2002, *Icarus*, 157, 523
- Hapke, B. 2012, *Theory of Reflectance and Emittance Spectroscopy*, 2nd edn. (Cambridge: Cambridge University Press)
- Harrington, J., Luszcz, S., Seager, S., Deming, D., & Richardson, L. J. 2007, *Nature*, 447, 691
- Harris, C. R., Millman, K. J., van der Walt, S. J., et al. 2020, *Nature*, 585, 357
- Heap, S. R., Lindler, D. J., Lanz, T. M., et al. 2000, *ApJ*, 539, 435
- Hebb, L., Collier-Cameron, A., Loeillet, B., et al. 2009, *ApJ*, 693, 1920
- Hermes, J. J. 2018, *Timing by Stellar Pulsations as an Exoplanet Discovery Method* (Springer Cham), 6

- Hey, D., Murphy, S., Foreman-Mackey, D., et al. 2020a, *The Journal of Open Source Software*, 5, 2125
- Hey, D. R., Murphy, S. J., Foreman-Mackey, D., et al. 2020b, *AJ*, 159, 202
- Higson, E., Handley, W., Hobson, M., & Lasenby, A. 2019, *Statistics and Computing*, 29, 891
- Hilbert, B. 2008, WFC3 TV3 Testing: IR Channel Nonlinearity Correction, Instrument Science Report WFC3 2008-39, 14 pages
- Hirschmann, M. M. 2000, *Geochemistry, Geophysics, Geosystems*, 1, 1042
- Hogg, D. W., Bovy, J., & Lang, D. 2010, arXiv e-prints, arXiv:1008.4686
- Horne, K. 1986, *Publications of the ASP*, 98, 609
- Houdek, G. 2000, in *Astronomical Society of the Pacific Conference Series*, Vol. 210, *Delta Scuti and Related Stars*, ed. M. Breger & M. Montgomery, 454
- Howell, S. B., Sobek, C., Haas, M., et al. 2014, *PASP*, 126, 398
- Hu, R., Brandeker, A., Damiano, M., et al. 2021, Determining the Atmospheric Composition of the Super-Earth 55 Cancri e, JWST Proposal. Cycle 1
- Hu, R., Demory, B.-O., Seager, S., Lewis, N., & Showman, A. P. 2015, *ApJ*, 802, 51
- Hu, R., Ehlmann, B. L., & Seager, S. 2012, *ApJ*, 752, 7
- Huitson, C. M., Sing, D. K., Pont, F., et al. 2013, *Monthly Notices of the RAS*, 434, 3252
- Hunter, J. D. 2007a, *Computing in Science and Engineering*, 9, 90
- Hunter, J. D. 2007b, *Computing in Science and Engineering*, 9, 90
- Husser, T. O., Wende-von Berg, S., Dreizler, S., et al. 2013, *Astronomy and Astrophysics*, 553, A6
- Ingalls, J. G., Krick, J. E., Carey, S. J., et al. 2012, in *Society of Photo-Optical Instrumentation Engineers (SPIE) Conference Series*, Vol. 8442, *Space Telescopes and Instrumentation 2012: Optical, Infrared, and Millimeter Wave*, ed. M. C. Clampin, G. G. Fazio, H. A. MacEwen, & J. Oschmann, Jacobus M., 84421Y
- Ito, Y., Ikoma, M., Kawahara, H., et al. 2015, *ApJ*, 801, 144
- Iyer, A. R., Line, M. R., Muirhead, P. S., Fortney, J. J., & Gharib-Nezhad, E. 2023, *ApJ*, 944, 41
- Jackson, B., Stark, C. C., Adams, E. R., Chambers, J., & Deming, D. 2013, *ApJ*, 779, 165
- Jenkins, J. M. 2017, *Kepler Data Processing Handbook: Overview of the Science Operations Center*, Tech. rep., NASA Ames Research Center
- Jenkins, J. M., Caldwell, D. A., Chandrasekaran, H., et al. 2010, *ApJ*, 713, L87
- Jenkins, J. M., Twicken, J. D., McCauliff, S., et al. 2016, in *Society of Photo-Optical Instrumentation Engineers (SPIE) Conference Series*, Vol. 9913, *Software and Cyberinfrastructure for Astronomy IV*, 99133E

- Johnstone, C. P., Güdel, M., Brott, I., & Lüftinger, T. 2015, *A&A*, 577, A28
- Jontof-Hutter, D. 2019, *Annual Review of Earth and Planetary Sciences*, 47, 141
- JWST Transiting Exoplanet Community Early Release Science Team, Ahrer, E.-M., Alderson, L., et al. 2023, *Nature*, 614, 649
- Kalas, P., Zwintz, K., Kenworthy, M., et al. 2019, in *American Astronomical Society Meeting Abstracts*, Vol. 233, American Astronomical Society Meeting Abstracts #233, 218.03
- Kane, S. R., Roettenbacher, R. M., Unterborn, C. T., Foley, B. J., & Hill, M. L. 2020, *PSJ*, 1, 36
- Kanodia, S. & Wright, J. T. 2018, *Barycorrpy: Barycentric velocity calculation and leap second management*
- Kass, R. E. & Raftery, A. E. 1995, *Journal of the American Statistical Association*, 90, 773
- Kasting, J. F., Whitmire, D. P., & Reynolds, R. T. 1993, *Icarus*, 101, 108
- Keles, E., Mallonn, M., Kitzmann, D., et al. 2022, *MNRAS*, 513, 1544
- Keller, L. P. & Berger, E. L. 2017, in *Asteroids, Comets, Meteors (ACM) 2017 Meeting*, Montevideo
- Kenworthy, M. 2017, *Nature Astronomy*, 1, 0099
- Kenworthy, M. A., Mellon, S. N., Bailey, J. I., et al. 2021, *A&A*, 648, A15
- Kipping, D. & Jansen, T. 2020, *Research Notes of the American Astronomical Society*, 4, 170
- Kipping, D. M. 2013, *MNRAS*, 435, 2152
- Kite, E. S., Fegley, Bruce, J., Schaefer, L., & Gaidos, E. 2016, *ApJ*, 828, 80
- Kite, E. S., Manga, M., & Gaidos, E. 2009, *ApJ*, 700, 1732
- Knutson, H. A., Benneke, B., Deming, D., & Homeier, D. 2014, *Nature*, 505, 66
- Knutson, H. A., Charbonneau, D., Allen, L. E., et al. 2007, *Nature*, 447, 183
- Koen, C. 2003, *MNRAS*, 341, 1385
- Koen, C. 2014, *MNRAS*, 444, 1486
- Koll, D. D. B., Malik, M., Mansfield, M., et al. 2019a, *ApJ*, 886, 140
- Koll, D. D. B., Malik, M., Mansfield, M., et al. 2019b, *ApJ*, 886, 140
- Königl, A., Giacalone, S., & Matsakos, T. 2017, *ApJ*, 846, L13
- Kopal, Z. 1954, *MNRAS*, 114, 101
- Koposov, S., Speagle, J., Barbary, K., et al. 2023a, *joshspeagle/dynesty: v2.1.0*, Zenodo
- Koposov, S., Speagle, J., Barbary, K., et al. 2023b, *joshspeagle/dynesty: v2.1.2*, Zenodo

- Kopparapu, R. K., Ramirez, R., Kasting, J. F., et al. 2013, *ApJ*, 765, 131
- Kopparapu, R. K., Ramirez, R. M., SchottelKotte, J., et al. 2014, *ApJ*, 787, L29
- Kreidberg, L. 2015, *PASP*, 127, 1161
- Kreidberg, L. 2018, in *Handbook of Exoplanets*, ed. H. J. Deeg & J. A. Belmonte (Springer International Publishing), 100
- Kreidberg, L., Agol, E., Bolmont, E., et al. 2021a, Hot Take on a Cool World: Does Trappist-1c Have an Atmosphere?, JWST Proposal. Cycle 1, ID. #2304
- Kreidberg, L., Bean, J. L., Désert, J.-M., et al. 2014a, *Nature*, 505, 69
- Kreidberg, L., Bean, J. L., Désert, J.-M., et al. 2014b, *Astrophysical Journal Letters*, 793, L27
- Kreidberg, L., Hu, R., Kite, E. S., et al. 2021b, A Search for Signatures of Volcanism and Geodynamics on the Hot Rocky Exoplanet LHS 3844b, JWST Proposal. Cycle 1
- Kreidberg, L., Koll, D. D. B., Morley, C., et al. 2019a, *Nature*, 573, 87
- Kreidberg, L., Line, M. R., Bean, J. L., et al. 2015, *ApJ*, 814, 66
- Kreidberg, L., Line, M. R., Parmentier, V., et al. 2018a, *Astronomical Journal*, 156, 17
- Kreidberg, L., Line, M. R., Thorngren, D., Morley, C. V., & Stevenson, K. B. 2018b, *ApJ*, 858, L6
- Kreidberg, L. & Loeb, A. 2016, *ApJ*, 832, L12
- Kreidberg, L., Lopez, E., Cowan, N., et al. 2018c, Taking the Temperature of a Lava Planet, Spitzer Proposal
- Kreidberg, L., Luger, R., & Bedell, M. 2019b, *Astrophysical Journal Letters*, 877, L15
- Kunimoto, M. & Matthews, J. M. 2020, *AJ*, 159, 248
- Kurtz, D. W., Hambleton, K. M., Shibahashi, H., Murphy, S. J., & Prša, A. 2015, *MNRAS*, 446, 1223
- Kurucz, R. L. 1992, *Rev. Mexicana Astron. Astrofis.*, 23, 45
- Kurucz, R. L. 1993, SYNTHE spectrum synthesis programs and line data
- Lacour, S., Wang, J. J., Rodet, L., et al. 2021, *A&A*, 654, L2
- Lagage, P.-O. & Bouwman, J. 2017, Thermal emission from Trappist1-b, JWST Proposal. Cycle 1, ID. #1279
- Lagrange, A. M., Backman, D. E., & Artymowicz, P. 2000, in *Protostars and Planets IV*, ed. V. Mannings, A. P. Boss, & S. S. Russell, 639
- Lagrange, A. M., Boccaletti, A., Langlois, M., et al. 2019a, *A&A*, 621, L8
- Lagrange, A. M., Bonnefoy, M., Chauvin, G., et al. 2010, *Science*, 329, 57
- Lagrange, A. M., De Bondt, K., Meunier, N., et al. 2012, *A&A*, 542, A18

- Lagrange, A. M., Desort, M., Galland, F., Udry, S., & Mayor, M. 2009a, *A&A*, 495, 335
- Lagrange, A. M., Gratadour, D., Chauvin, G., et al. 2009b, *A&A*, 493, L21
- Lagrange, A. M., Meunier, N., Rubini, P., et al. 2019b, *Nature Astronomy*, 421
- Lagrange, A.-M., Rubini, P., Nowak, M., et al. 2020, *A&A*
- Lanotte, A. A., Gillon, M., Demory, B. O., et al. 2014, *A&A*, 572, A73
- Lecavelier des Etangs, A., Cros, L., Hébrard, G., et al. 2022, *Scientific Reports*, 12, 5855
- Lecavelier Des Etangs, A., Deleuil, M., Vidal-Madjar, A., et al. 1995, *A&A*, 299, 557
- Lecavelier Des Etangs, A., Pont, F., Vidal-Madjar, A., & Sing, D. 2008, *A&A*, 481, L83
- Lecavelier des Etangs, A. & Vidal-Madjar, A. 2016, *A&A*, 588, A60
- Lee, E. J. & Chiang, E. 2017, *ApJ*, 842, 40
- Léger, A., Grasset, O., Fegley, B., et al. 2011, *Icarus*, 213, 1
- Léger, A., Rouan, D., Schneider, J., et al. 2009, *A&A*, 506, 287
- Lellouch, E. 2018, in *Handbook of Exoplanets*, ed. H. J. Deeg & J. A. Belmonte (Springer International Publishing), 47
- Lenz, P. & Breger, M. 2005, *Communications in Asteroseismology*, 146, 53
- Lichtenberg, T., Schaefer, L. K., Nakajima, M., & Fischer, R. A. 2023, in *Astronomical Society of the Pacific Conference Series*, Vol. 534, *Protostars and Planets VII*, ed. S. Inutsuka, Y. Aikawa, T. Muto, K. Tomida, & M. Tamura, 907
- Liddle, A. R. 2007, *MNRAS*, 377, L74
- Lightkurve Collaboration, Cardoso, J. V. d. M., Hedges, C., et al. 2018, *Lightkurve: Kepler and TESS time series analysis in Python*, *Astrophysics Source Code Library*
- Lim, O., Benneke, B., Doyon, R., et al. 2023, *ApJ*, 955, L22
- Lincowski, A. P. 2020, PhD thesis, University of Washington, Seattle
- Lincowski, A. P., Meadows, V. S., Crisp, D., et al. 2018, *ApJ*, 867, 76
- Lindgren, L., Klioner, S. A., Hernández, J., et al. 2021, *A&A*, 649, A2
- Lithwick, Y., Xie, J., & Wu, Y. 2012, *ApJ*, 761, 122
- Lomb, N. R. 1976, *Astrophysics and Space Science*, 39, 447
- Lopez, E. D. 2017, *MNRAS*, 472, 245
- Lopez, E. D. & Fortney, J. J. 2014, *ApJ*, 792, 1
- Louden, T. & Kreidberg, L. 2018, *MNRAS*, 477, 2613

- Luger, R., Agol, E., Foreman-Mackey, D., et al. 2019, *Astronomical Journal*, 157, 64
- Luger, R. & Barnes, R. 2015, *Astrobiology*, 15, 119
- Lundkvist, M. S., Kjeldsen, H., Albrecht, S., et al. 2016, *Nature Communications*, 7, 11201
- Lust, N. B., Britt, D., Harrington, J., et al. 2014, *PASP*, 126, 1092
- Lustig-Yaeger, J., Fu, G., May, E. M., et al. 2023, arXiv e-prints, arXiv:2301.04191
- Lyu, X., Koll, D. D. B., Cowan, N. B., et al. 2023, arXiv e-prints, arXiv:2310.01725
- Madhusudhan, N. 2019, *ARA&A*, 57, 617
- Malavolta, L., Mayo, A. W., Loudon, T., et al. 2018, *AJ*, 155, 107
- Malik, M., Grosheintz, L., Mendonça, J. M., et al. 2017, *The Astronomical Journal*, 153, 56
- Malik, M., Kempton, E. M. R., Koll, D. D. B., et al. 2019a, *ApJ*, 886, 142
- Malik, M., Kitzmann, D., Mendonça, J. M., et al. 2019b, *The Astronomical Journal*, 157, 170
- Mallama, A., Wang, D., & Howard, R. A. 2002, *Icarus*, 155, 253
- Mamajek, E. E. & Bell, C. P. M. 2014, *MNRAS*, 445, 2169
- Mandel, K. & Agol, E. 2002, *ApJ*, 580, L171
- Mann, A. W., Dupuy, T., Kraus, A. L., et al. 2019, *ApJ*, 871, 63
- Mansfield, M., Kite, E. S., Hu, R., et al. 2019, *ApJ*, 886, 141
- Marcq, E. 2012, *Journal of Geophysical Research (Planets)*, 117, E01001
- Marcq, E., Salvador, A., Massol, H., & Davaille, A. 2017, *Journal of Geophysical Research (Planets)*, 122, 1539
- May, E. M. & Stevenson, K. B. 2020, *AJ*, 160, 140
- Mayor, M. & Queloz, D. 1995, *Nature*, 378, 355
- Mayorga, L. C., Jackiewicz, J., Rages, K., et al. 2016, *AJ*, 152, 209
- McArthur, B. E., Endl, M., Cochran, W. D., et al. 2004, *ApJ*, 614, L81
- McCullough, P. & MacKenty, J. 2012, *Considerations for using Spatial Scans with WFC3*, Space Telescope WFC Instrument Science Report
- McCullough, P. R., Crouzet, N., Deming, D., & Madhusudhan, N. 2014, *ApJ*, 791, 55
- McDonald, G. D., Kreidberg, L., & Lopez, E. 2019, *ApJ*, 876, 22
- McEwen, A. S., Keszthelyi, L., Spencer, J. R., et al. 1998, *Science*, 281, 87
- Meadows, V. S. & Crisp, D. 1996, *JGR*, 101, 4595
- Meier Valdés, E. A., Morris, B. M., Demory, B. O., et al. 2023, *A&A*, 677, A112

- Mékarnia, D., Chapellier, E., Guillot, T., et al. 2017, *A&A*, 608, L6
- Mellon, S. N., Mamajek, E. E., Stuik, R., et al. 2019, *ApJS*, 244, 15
- Mendonça, J. M., Malik, M., Demory, B.-O., & Heng, K. 2018, *AJ*, 155, 150
- Menegaldo, C. G., de O. Fialho, F., Janot-Pacheco, E., Pait, F. M., & Lapeyrère, V. 2022, *PASP*, 134, 034501
- Mercier, S. J., Dang, L., Gass, A., Cowan, N. B., & Bell, T. J. 2022, *AJ*, 164, 204
- Miguel, Y., Kaltenegger, L., Fegley, B., & Schaefer, L. 2011, *ApJ*, 742, L19
- Mikal-Evans, T., Sing, D. K., Barstow, J. K., et al. 2022, *Nature Astronomy*, 6, 471
- Modirrousta-Galian, D., Ito, Y., & Micela, G. 2021, *Icarus*, 358, 114175
- Mollière, P., van Boekel, R., Dullemond, C., Henning, T., & Mordasini, C. 2015, *ApJ*, 813, 47
- Mollière, P., Wardenier, J. P., van Boekel, R., et al. 2019, *A&A*, 627, A67
- Montgomery, M. H. & Odonoghue, D. 1999, *Delta Scuti Star Newsletter*, 13, 28
- Moore, K. & Cowan, N. B. 2020, *MNRAS*, 496, 3786
- Mordasini, C., van Boekel, R., Mollière, P., Henning, T., & Benneke, B. 2016, *ApJ*, 832, 41
- Morley, C. V., Kreidberg, L., Rustamkulov, Z., Robinson, T., & Fortney, J. J. 2017, *ApJ*, 850, 121
- Moroz, V. I., Ekonomov, A. P., Moshkin, B. E., et al. 1985, *Advances in Space Research*, 5, 197
- Morris, B. M., Delrez, L., Brandeker, A., et al. 2021, *A&A*, 653, A173
- Mouillet, D., Larwood, J. D., Papaloizou, J. C. B., & Lagrange, A. M. 1997, *MNRAS*, 292, 896
- Mousis, O., Deleuil, M., Aguichine, A., et al. 2020, *ApJ*, 896, L22
- Mugnai, L. V., Modirrousta-Galian, D., Edwards, B., et al. 2021, *Astronomical Journal*, 161, 284
- Müllner, M. 2020, *MarcoMuellner/SMURFS*, Zenodo
- Murphy, S. J. 2012, *MNRAS*, 422, 665
- Murphy, S. J. 2018, *arXiv e-prints*, arXiv:1811.12659
- Murphy, S. J., Barbara, N. H., Hey, D., Bedding, T. R., & Fulcher, B. D. 2020a, *MNRAS*, 493, 5382
- Murphy, S. J., Bedding, T. R., & Shibahashi, H. 2016a, *ApJ*, 827, L17
- Murphy, S. J., Bedding, T. R., Shibahashi, H., Kurtz, D. W., & Kjeldsen, H. 2014, *MNRAS*, 441, 2515
- Murphy, S. J., Joyce, M., Bedding, T. R., White, T. R., & Kama, M. 2021, *MNRAS*, 502, 1633

- Murphy, S. J., Moe, M., Kurtz, D. W., et al. 2018, *MNRAS*, 474, 4322
- Murphy, S. J., Pigulski, A., Kurtz, D. W., et al. 2013, *MNRAS*, 432, 2284
- Murphy, S. J., Saio, H., Takada-Hidai, M., et al. 2020b, *MNRAS*, 498, 4272
- Murphy, S. J. & Shibahashi, H. 2015, *MNRAS*, 450, 4475
- Murphy, S. J., Shibahashi, H., & Bedding, T. R. 2016b, *MNRAS*, 461, 4215
- National Academies of Sciences, Engineering, and Medicine. 2021, *Pathways to Discovery in Astronomy and Astrophysics for the 2020s*
- Nesvold, E. R. & Kuchner, M. J. 2015, *ApJ*, 798, 83
- Nguyen, T. G., Cowan, N. B., Banerjee, A., & Moores, J. E. 2020, *MNRAS*, 499, 4605
- Nguyen, T. G., Cowan, N. B., Pierrehumbert, R. T., Lupu, R. E., & Moores, J. E. 2022, *MNRAS*, 513, 6125
- Nikolov, N., Sing, D. K., Pont, F., et al. 2014, *MNRAS*, 437, 46
- Nowak, M., Lacour, S., Crouzier, A., et al. 2018, in *Society of Photo-Optical Instrumentation Engineers (SPIE) Conference Series*, Vol. 10698, *Space Telescopes and Instrumentation 2018: Optical, Infrared, and Millimeter Wave*, ed. M. Lystrup, H. A. MacEwen, G. G. Fazio, N. Batalha, N. Siegler, & E. C. Tong, 1069821
- Nowak, M., Lacour, S., Lagrange, A.-M., et al. 2020, *A&A*
- Odert, P., Leitzinger, M., Guenther, E. W., & Heinzel, P. 2020, *MNRAS*, 494, 3766
- Parmentier, V. & Crossfield, I. J. M. 2018, in *Handbook of Exoplanets*, ed. H. J. Deeg & J. A. Belmonte (Springer International Publishing), 116
- Paudel, R. R., Gizis, J. E., Mullan, D. J., et al. 2018, *ApJ*, 858, 55
- Pavlenko, Y., Kulyk, I., Shubina, O., et al. 2022, *A&A*, 660, A49
- Pepper, J., Rodriguez, J. E., Collins, K. A., et al. 2017, *AJ*, 153, 215
- Perez, F. & Granger, B. E. 2007, *Computing in Science and Engineering*, 9, 21
- Petigura, E. A., Marcy, G. W., Winn, J. N., et al. 2018, *AJ*, 155, 89
- Petrovich, C., Deibert, E., & Wu, Y. 2019, *AJ*, 157, 180
- Piaulet, C., Benneke, B., Rubenzahl, R. A., et al. 2021, *AJ*, 161, 70
- Pinhas, A., Rackham, B. V., Madhusudhan, N., & Apai, D. 2018, *MNRAS*, 480, 5314
- Polyanskiy, M. N. 2016, *Refractive index database*, <https://refractiveindex.info>, accessed on 2022-06-23
- Pont, F., Knutson, H., Gilliland, R. L., Moutou, C., & Charbonneau, D. 2008, *MNRAS*, 385, 109
- Pont, F., Zucker, S., & Queloz, D. 2006, *MNRAS*, 373, 231

- Popowicz, A., Pigulski, A., Bernacki, K., et al. 2017, *A&A*, 605, A26
- Pu, B. & Lai, D. 2019, *MNRAS*, 488, 3568
- Quanz, S. P., Absil, O., Benz, W., et al. 2022a, *Experimental Astronomy*, 54, 1197
- Quanz, S. P., Ottiger, M., Fontanet, E., et al. 2022b, *A&A*, 664, A21
- Rackham, B., Espinoza, N., Apai, D., et al. 2017, *ApJ*, 834, 151
- Rackham, B. V., Apai, D., & Giampapa, M. S. 2018, *ApJ*, 853, 122
- Rackham, B. V., Espinoza, N., Berdyugina, S. V., et al. 2023, *RAS Techniques and Instruments*, 2, 148
- Rasmussen, K. C., Currie, M. H., Hagee, C., et al. 2023, *AJ*, 166, 155
- Raymond, S. N., Quinn, T., & Lunine, J. I. 2004, *Icarus*, 168, 1
- Redfield, S., Endl, M., Cochran, W. D., & Koesterke, L. 2008, *ApJ*, 673, L87
- Ricker, G. R., Winn, J. N., Vanderspek, R., et al. 2014, in *Society of Photo-Optical Instrumentation Engineers (SPIE) Conference Series*, Vol. 9143, *Space Telescopes and Instrumentation 2014: Optical, Infrared, and Millimeter Wave*, ed. J. Oschmann, Jacobus M., M. Clampin, G. G. Fazio, & H. A. MacEwen, 914320
- Ricker, G. R., Winn, J. N., Vanderspek, R., et al. 2015, *Journal of Astronomical Telescopes, Instruments, and Systems*, 1, 014003
- Rigby, J., Perrin, M., McElwain, M., et al. 2023, *PASP*, 135, 048001
- Roberge, A. & Seager, S. 2018, in *Handbook of Exoplanets*, ed. H. J. Deeg & J. A. Belmonte (Springer International Publishing), 98
- Robinson, T. D. 2017, *ApJ*, 836, 236
- Robinson, T. D. & Crisp, D. 2018, *JQSRT*, 211, 78
- Robinson, T. D., Meadows, V. S., Crisp, D., et al. 2011, *Astrobiology*, 11, 393
- Roettenbacher, R. M. & Kane, S. R. 2017, *ApJ*, 851, 77
- Rogers, L. A. 2015, *ApJ*, 801, 41
- Rossi, F. & Pascale, J. 1985, *PRA*, 32, 2657
- Rossum, G. 1995, *Python Reference Manual*, Tech. rep., Centrum voor Wiskunde en Informatica (CWI), Amsterdam, The Netherlands, The Netherlands
- Rouan, D., Deeg, H. J., Demangeon, O., et al. 2011, *ApJ*, 741, L30
- Rustamkulov, Z., Sing, D. K., Mukherjee, S., et al. 2023, *Nature*, 614, 659
- Ryabchikova, T., Piskunov, N., Kurucz, R. L., et al. 2015, *Physica Scripta*, 90, 054005
- Sanchis-Ojeda, R., Rappaport, S., Winn, J. N., et al. 2014, *ApJ*, 787, 47
- Sanchis-Ojeda, R., Rappaport, S., Winn, J. N., et al. 2013, *ApJ*, 774, 54
- Scargle, J. D. 1982, *ApJ*, 263, 835

- Schaefer, L. & Fegley, B. 2004, *Icarus*, 169, 216
- Schaefer, L. & Fegley, B. 2009, *ApJ*, 703, L113
- Schaefer, L. & Fegley, B. 2010, *Icarus*, 208, 438
- Schaefer, L., Wordsworth, R. D., Berta-Thompson, Z., & Sasselov, D. 2016, *ApJ*, 829, 63
- Schmid, V. S., Tkachenko, A., Aerts, C., et al. 2015, *A&A*, 584, A35
- Schwarz, G. 1978, *Annals of Statistics*, 6, 461
- Seager, S. 2010, *Exoplanet Atmospheres: Physical Processes* (Princeton University Press)
- Selsis, F., Wordsworth, R. D., & Forget, F. 2011, *A&A*, 532, A1
- Sheets, H. A. & Deming, D. 2014, *ApJ*, 794, 133
- Sheets, H. A. & Deming, D. 2017, *AJ*, 154, 160
- Shibahashi, H. & Kurtz, D. W. 2012, *MNRAS*, 422, 738
- Shibahashi, H., Kurtz, D. W., & Murphy, S. J. 2015, *MNRAS*, 450, 3999
- Showman, A. P., Cooper, C. S., Fortney, J. J., & Marley, M. S. 2008, *ApJ*, 682, 559
- Showman, A. P., Fortney, J. J., Lian, Y., et al. 2009, *ApJ*, 699, 564
- Showman, A. P. & Polvani, L. M. 2011, *ApJ*, 738, 71
- Silvotti, R., Schuh, S., Janulis, R., et al. 2007, *Nature*, 449, 189
- Sing, D. K., Désert, J. M., Fortney, J. J., et al. 2011a, *A&A*, 527, A73
- Sing, D. K., Fortney, J. J., Nikolov, N., et al. 2016, *Nature*, 529, 59
- Sing, D. K., Pont, F., Aigrain, S., et al. 2011b, *MNRAS*, 416, 1443
- Singh, V., Bonomo, A. S., Scandariato, G., et al. 2022, *A&A*, 658, A132
- Skilling, J. 2004, in *American Institute of Physics Conference Series*, Vol. 735, *Bayesian Inference and Maximum Entropy Methods in Science and Engineering: 24th International Workshop on Bayesian Inference and Maximum Entropy Methods in Science and Engineering*, ed. R. Fischer, R. Preuss, & U. V. Toussaint, 395–405
- Skilling, J. 2006, *Bayesian Analysis*, 1, 833
- Smart, W. M. 1977, *Textbook on Spherical Astronomy*, 6th edn. (Cambridge University Press)
- Smith, B. A. & Terrile, R. J. 1984, *Science*, 226, 1421
- Smith, J. C., Stumpe, M. C., Van Cleve, J. E., et al. 2012, *Publications of the Astronomical Society of the Pacific*, 124, 1000

- Smith, R. M., Zavodny, M., Rahmer, G., & Bonati, M. 2008, in Society of Photo-Optical Instrumentation Engineers (SPIE) Conference Series, Vol. 7021, High Energy, Optical, and Infrared Detectors for Astronomy III, ed. D. A. Dorn & A. D. Holland, 70210J
- Snellen, I., de Kok, R., Birkby, J. L., et al. 2015, *A&A*, 576, A59
- Snellen, I. A. G., Albrecht, S., de Mooij, E. J. W., & Le Poole, R. S. 2008, *A&A*, 487, 357
- Snellen, I. A. G., de Kok, R. J., le Poole, R., Brogi, M., & Birkby, J. 2013, *ApJ*, 764, 182
- Snellen, I. A. G., Stuik, R., Navarro, R., et al. 2012, in Society of Photo-Optical Instrumentation Engineers (SPIE) Conference Series, Vol. 8444, Proc. SPIE, 84440I
- Sotin, C., Grasset, O., & Mocquet, A. 2007, *Icarus*, 191, 337
- Spake, J. J., Sing, D. K., Evans, T. M., et al. 2018, *Nature*, 557, 68
- Speagle, J. S. 2020, *MNRAS*, 493, 3132
- Stamnes, K., Tsay, S. C., Jayaweera, K., & Wiscombe, W. 1988, *Applied Optics*, 27, 2502
- Stamnes, K., Tsay, S. C., Wiscombe, W., & Laszlo, I. 2000, DISORT, a general-purpose Fortran program for discrete-ordinate-method radiative transfer in scattering and emitting layered media: documentation of methodology., <ftp://climate.gsfc.nasa.gov/pub/wiscombe/MultipleScatt/>
- Stassun, K. G., Oelkers, R. J., Paegert, M., et al. 2019, *AJ*, 158, 138
- Steindl, T., Zwintz, K., & Müllner, M. 2022, *A&A*, 664, A32
- Sterken, C. 2005, in Astronomical Society of the Pacific Conference Series, Vol. 335, The Light-Time Effect in Astrophysics: Causes and cures of the O-C diagram, ed. C. Sterken, 3
- Stetson, P. B. 1987, *PASP*, 99, 191
- Stevenson, K. B., Bean, J. L., Seifahrt, A., et al. 2014a, *AJ*, 147, 161
- Stevenson, K. B., Désert, J.-M., Line, M. R., et al. 2014b, *Science*, 346, 838
- Stevenson, K. B., Harrington, J., Fortney, J. J., et al. 2012, *ApJ*, 754, 136
- Stock, J. W., Kitzmann, D., Patzer, A. B. C., & Sedlmayr, E. 2018, *Monthly Notices of the Royal Astronomical Society*, 479, 865
- Strøm, P. A., Bodewits, D., Knight, M. M., et al. 2020, *PASP*, 132, 101001
- STScI Development Team. 2013, pysynphot: Synthetic photometry software package
- Stuik, R., Bailey, J. I., Dorval, P., et al. 2017, *A&A*, 607, A45
- Stumpe, M. C., Smith, J. C., Van Cleve, J. E., et al. 2012, *Publications of the Astronomical Society of the Pacific*, 124, 985
- Sulis, S., Dragomir, D., Lendl, M., et al. 2019, *A&A*, 631, A129

- Swain, M., Deroo, P., Tinetti, G., et al. 2013, *Icarus*, 225, 432
- Talens, G. J. J., Albrecht, S., Spronck, J. F. P., et al. 2017, *A&A*, 606, A73
- Talens, G. J. J., Deul, E. R., Stuik, R., et al. 2018, *A&A*, 619, A154
- Tamburo, P., Mandell, A., Deming, D., & Garhart, E. 2018, *AJ*, 155, 221
- Teachey, A. & Kipping, D. M. 2018, *Science Advances*, 4, eaav1784
- Ter Braak, C. J. F. 2006, *Statistics and Computing*, 16, 239
- Thorngren, D. P., Fortney, J. J., Murray-Clay, R. A., & Lopez, E. D. 2016, *ApJ*, 831, 64
- Tilley, M. A., Segura, A., Meadows, V., Hawley, S., & Davenport, J. 2019, *Astrobiology*, 19, 64
- Tsai, S.-M., Lee, E. K. H., Powell, D., et al. 2023, *Nature*, 617, 483
- Tsiaras, A., Rocchetto, M., Waldmann, I. P., et al. 2016a, *ApJ*, 820, 99
- Tsiaras, A., Waldmann, I. P., Rocchetto, M., et al. 2016b, *Astrophysical Journal*, 832, 202
- Untertorn, C. T., Desch, S. J., Hinkel, N. R., & Lorenzo, A. 2018, *Nature Astronomy*, 2, 297
- Valencia, D., Ikoma, M., Guillot, T., & Nettelmann, N. 2010, *A&A*, 516, A20
- Valsecchi, F., Rappaport, S., Rasio, F. A., Marchant, P., & Rogers, L. A. 2015, *ApJ*, 813, 101
- van der Walt, S., Colbert, S. C., & Varoquaux, G. 2011, *Computing in Science and Engineering*, 13, 22
- Van Eylen, V., Agentoft, C., Lundkvist, M. S., et al. 2018, *MNRAS*, 479, 4786
- Van Grootel, V., Fernandes, C. S., Gillon, M., et al. 2018, *ApJ*, 853, 30
- Vanderburg, A., Becker, J. C., Buchhave, L. A., et al. 2017, *AJ*, 154, 237
- Vanderburg, A. & Johnson, J. A. 2014, *PASP*, 126, 948
- Vanderburg, A., Latham, D. W., Buchhave, L. A., et al. 2016, *ApJS*, 222, 14
- Vanderspek, R., Huang, C. X., Vanderburg, A., et al. 2019, *ApJ*, 871, L24
- Vidal-Madjar, A., Lecavelier des Etangs, A., Désert, J. M., et al. 2003, *Nature*, 422, 143
- Virtanen, P., Gommers, R., Oliphant, T. E., et al. 2020, *Nature Methods*, 17, 261
- Wakeford, H. R., Sing, D. K., Deming, D., et al. 2018, *AJ*, 155, 29
- Wakeford, H. R., Sing, D. K., Kataria, T., et al. 2017, *Science*, 356, 628
- Wallace, L., Bernath, P., Livingston, W., et al. 1995, *Science*, 268, 1155
- Wang, H. S., Liu, F., Ireland, T. R., et al. 2019, *MNRAS*, 482, 2222
- Wang, J., Mawet, D., Ruane, G., Hu, R., & Benneke, B. 2017, *AJ*, 153, 183

- Wang, J. J., Graham, J. R., Pueyo, L., et al. 2016, *AJ*, 152, 97
- Weiss, L. M. & Marcy, G. W. 2014, *ApJ*, 783, L6
- Weiss, W. W., Rucinski, S. M., Moffat, A. F. J., et al. 2014, *Publications of the Astronomical Society of the Pacific*, 126, 573
- Welbanks, L., Madhusudhan, N., Allard, N. F., et al. 2019, *ApJ*, 887, L20
- Wilson, D. J., Froning, C. S., Duvvuri, G. M., et al. 2021, *ApJ*, 911, 18
- Winn, J. N. 2010, in *Exoplanets*, ed. S. Seager (University of Arizona Press), 55–77
- Winn, J. N., Holman, M. J., Bakos, G. Á., et al. 2007, *AJ*, 134, 1707
- Winn, J. N., Holman, M. J., Torres, G., et al. 2008, *ApJ*, 683, 1076
- Winn, J. N., Matthews, J. M., Dawson, R. I., et al. 2011, *ApJ*, 737, L18
- Winn, J. N., Sanchis-Ojeda, R., & Rappaport, S. 2018, *NAR*, 83, 37
- Winn, J. N., Sanchis-Ojeda, R., Rogers, L., et al. 2017, *AJ*, 154, 60
- Wolfgang, A. & Lopez, E. 2015, *ApJ*, 806, 183
- Wolszczan, A. 1994, *Science*, 264, 538
- Wolszczan, A. & Frail, D. A. 1992, *Nature*, 355, 145
- Wordsworth, R. 2015, *ApJ*, 806, 180
- Wordsworth, R. & Kreidberg, L. 2022, *ARA&A*, 60, 159
- Wright, J. T. & Eastman, J. D. 2014, *PASP*, 126, 838
- Wright, J. T., Marcy, G. W., Howard, A. W., et al. 2012, *ApJ*, 753, 160
- Wright, N. J., Newton, E. R., Williams, P. K. G., Drake, J. J., & Yadav, R. K. 2018, *MNRAS*, 479, 2351
- Yee, J. C., Fazio, G. G., Benjamin, R., et al. 2017, arXiv e-prints, arXiv:1710.04194
- Zeng, L., Jacobsen, S. B., Sasselov, D. D., et al. 2019, *Proceedings of the National Academy of Science*, 116, 9723
- Zhang, M., Dai, F., Hu, R., Knutson, H. A., & Lam, K. 2021a, The First and Only Multi-wavelength Map of an Ultra-short-period sub-Earth, JWST Proposal. Cycle 1
- Zhang, M., Knutson, H. A., Wang, L., Dai, F., & Barragán, O. 2022, *AJ*, 163, 67
- Zhang, M., Knutson, H. A., Wang, L., et al. 2021b, *AJ*, 161, 181
- Zhang, Z., Zhou, Y., Rackham, B. V., & Apai, D. 2018, *AJ*, 156, 178
- Zhou, Y., Apai, D., Lew, B. W. P., & Schneider, G. 2017, *Astronomical Journal*, 153, 243
- Zhu, W. & Dong, S. 2021, *ARA&A*, 59, 291
- Zieba, S., Hu, R., Kreidberg, L., et al. 2023a, The search for regolith on the airless exoplanet LHS 3844 b, JWST Proposal. Cycle 2, ID. #4008

- Zieba, S. & Kreidberg, L. 2022, *The Journal of Open Source Software*, 7, 4838
- Zieba, S., Kreidberg, L., Ducrot, E., et al. 2023b, *Nature*, 620, 746
- Zieba, S., Zilinskas, M., Kreidberg, L., et al. 2022, *A&A*, 664, A79
- Zieba, S., Zwintz, K., Kenworthy, M. A., & Kennedy, G. M. 2019, *A&A*, 625, L13
- Zilinskas, M., Miguel, Y., Lyu, Y., & Bax, M. 2021, *MNRAS*, 500, 2197
- Zilinskas, M., van Buchem, C., Miguel, Y., et al. 2022, arXiv e-prints, arXiv:2202.04759
- Zwintz, K., Fossati, L., Ryabchikova, T., et al. 2014, *Science*, 345, 550
- Zwintz, K., Reese, D. R., Neiner, C., et al. 2019, *A&A*, 627, A28

ENGLISH SUMMARY

“Where Do We Come From? What Are We? Where Are We Going?” The study of planets inside and outside of our solar system is integral to answering these fundamental questions of humanity. Astronomy as a whole is shedding light on the diversity of the cosmos and our place in it. In my field of research, we do this by characterizing planets outside our solar system, so-called exoplanets. By learning about their formation, evolution, composition, and habitability, we ultimately learn about our origins, the future of our own planet, and its uniqueness. The holy grail of exoplanet research is ultimately to determine whether the Earth and life as we know it are rare or ubiquitous. Scientists will argue when we will finally find an “Earth-twin” that could host life as we know it, but we have surely never been that close to reaching this goal.

It is remarkable how much we have learned about these distant worlds in just a few decades: Since the first discovery of exoplanets in the 1990s, we know of more than 5,500 planets at the moment. Ground and space-based telescopes and instruments were built to discover these planets. Typically, however, we cannot see the exoplanet directly. They are too close to their host stars, which are orders of magnitude brighter. Therefore, it is still a challenge to spatially resolve planets around their stars. More often, we observe the combined light from both sources — the star and the planet — which can provide us with a whole range of planetary properties, from fundamental ones like their size and mass up to characteristics like their atmospheric composition, their heat redistribution, or their reflectivity. NASA launched space missions, such as the Kepler Space Telescope in 2009 and the Transiting Exoplanet Survey Satellite (TESS) in 2018, to discover these distant worlds and measure their sizes. These telescopes utilized a technique called the “transit method,” which relies on the system architecture to be edge-on, so that the planet would occult — or “transit” — their host star periodically. During such a transit, the exoplanet covers the stellar disk as seen from the Earth, leading to an observed decrease in flux. This method has been the most successful one up to now, caused by the simple scalability of the problem: one just has to point a sensitive telescope up to the sky and record the brightness of stars in the field of view over time to discover new planets. A different technique called the radial velocity method can then provide us with the planetary masses. From the measured radii and masses, we derive the planet’s bulk density, which informs us about its composition: A planet with a big iron core will have a higher density than one that is dominated by silicates with a small core. The majority of rocky exoplanets are Earth-like in composition, meaning around 30% iron and 70% “rocks” or

silicates. Planets bigger than 1.6 times the Earth's radius are expected to have retained a hydrogen atmosphere with a significant amount of their mass in gas form. These planets are also expected to have molten surfaces, as the pressure strongly increases with decreasing altitude. Once you reach the surface, the temperature will be too high to host a solid, unmolten surface. This is typically why we do not consider these bigger worlds to be rocky.

However, despite measuring the densities of rocky planets and learning about their bulk compositions, we still do not know much about the composition of small planet atmospheres and how often these worlds hold onto them. The "Great Observatories," which were launched by NASA between 1990 and 2003, included two space telescopes that would ultimately become the workhorse facilities for the characterization of transiting exoplanets over the last decade: The Hubble Space Telescope was launched in 1990 aboard Space Shuttle Discovery with an aperture of 2.4 meters, and the Spitzer Space Telescope in 2003 with an 85 cm mirror. In space, telescopes avoid contamination by the thermal infrared background of the Earth, which makes precise infrared observations possible. Although both telescopes were never designed to study exoplanets, clever data processing routines and, in the case of Hubble, upgrades during the Hubble servicing missions led to the atmospheric characterization of many Jupiter-sized and also smaller exoplanets.

After the Spitzer Space Telescope was shut off in January 2020, the exoplanet community lost the capability to observe exoplanets in transmission or emission in the infrared at wavelengths greater than 2 microns from space. This was a big loss, as molecules we are interested in finding in the atmosphere of other planets, such as water (H_2O) or carbon dioxide (CO_2), have features in the infrared. The strong absorption of carbon dioxide was noted by the astrophysicist and science communicator Carl Sagan, when he testified before Congress in 1985 on climate change. The following is a direct quote from Carl Sagan when he addressed the Congress members during the hearing:

"The air between us is transparent, except in Los Angeles and places of that sort. In the ordinary visible part of the spectrum, we can see each other. But if our eyes were sensitive at, say, 15 microns in the infrared, we could not see each other. The air would be black between us. And that's because, in this case, carbon dioxide. Carbon dioxide is very strongly absorbing at 15 microns. And other wavelengths in the infrared. Likewise, there are parts of the infrared spectrum where water vapor absorbs, where we could not see each other if we were only as far apart as we are in this room."

The search for atmospheres on rocky exoplanets containing molecules like water, carbon dioxide, or oxygen requires a precise infrared telescope. Thankfully, after many delays, JWST was launched on Christmas Day 2021, providing scientists again with the capability to study planets in these infrared wavelengths with unprecedented precision. Its groundbreaking precision is due to many factors, like a large collecting area of 6.5 meters and the thermal stability of the telescope. JWST therefore gives us for the first time the possibility to search for high-mean-molecular-weight atmospheres made of carbon dioxide (CO_2), oxygen (O_2), and

nitrogen (N_2) on temperate rocky worlds.

There are generally two techniques to study the atmospheres of transiting exoplanets. The first one, occurs during a transit and is therefore called transmission spectroscopy: when a planet occults its host star from our view as the observer, a part of the starlight will travel through the atmosphere of the planet, if there is any. Certain wavelengths will be absorbed by the constituents of the atmosphere. These missing wavelengths are then observed by us, and we can deduce the elements and molecules that make up the gas shell around the planet. The other method to characterize the atmospheres of exoplanets occurs approximately half an orbit after the transit when the planet disappears behind its host star; we call that an “eclipse.” During the eclipse itself, we only observe the stellar light. Any flux emitted by the planet is hidden by the star. However, right before and after the planet hides behind its star, we observe the emission coming from the dayside of the planet. From this peek-a-boo game with the planet, we measure an emission spectrum — the method is therefore called emission spectroscopy — and we can detect elements or molecules in the atmosphere of the planet or directly study its surface. When we study the emission coming from not only the dayside of the planet but from the other sides of the planet during the orbit of the planet around its host star, we observe a so-called phase curve. These kinds of observations can then inform us about global processes like heat transport due to winds in the planet’s atmosphere.

K2 and Spitzer phase curves of the rocky ultra-short-period planet K2-141 b hint at a tenuous rock vapor atmosphere

In Chapter 2, we observed such a phase curve for a lava exoplanet called K2-141 b using Spitzer. These lava planets are characterized by their really short orbital periods and very hot daysides. With an orbital period of just 7 hours, the planet is so strongly irritated by its star that the average dayside temperature is above 2000 Kelvin. That is enough to melt the rocks on the planet’s surface, leading to a dayside magma ocean, and potentially to a thin rock vapor atmosphere caused by the evaporation of rocks. The latter is especially interesting, as the study of the evaporated atmosphere might eventually tell us about the composition of the planet’s surface. In my work, I combined previously taken Kepler observations of K2-141 b with new Spitzer data. The Spitzer Space Telescope stared at the star for about 70 hours, leading to the observation of 10 continuous orbits of the planet. Combining the data taken by Kepler in the optical with the Spitzer infrared observations, we tentatively attribute the deep eclipse observed by Kepler to such a rock vapor atmosphere. However, only follow-up will reveal the true nature of the planet. Thankfully, JWST observations of the planet were already taken, and the interpretation is currently underway. Due to its wavelength coverage and precision, JWST will improve our understanding of lava planet atmospheres.

PACMAN: A pipeline to reduce and analyze Hubble Wide Field Camera 3 IR Grism data

In Chapter 3, I present a publicly available tool for astronomers to access and process exoplanet observations taken by one of the instruments on the Hubble Space

Telescope. The original code has been used in many publications over the past decade and is now made available for everyone under the name PACMAN. Hubble's Wide Field Camera 3 (WFC3) instrument was installed during a servicing mission in 2009. The spectral range of WFC3 notably picks up molecular infrared absorption from water, which allowed for the successful detection of water in the atmospheres of over a dozen exoplanets. However, analyzing Hubble data presents challenges, with different pipelines producing conflicting results in the literature in the past. To ensure research reproducibility, it's good scientific practice for the software used in data reduction and analysis to be open-source. This approach makes it easier to compare different pipelines and lowers the barriers for newcomers entering the field of exoplanet atmospheres. The source code of PACMAN and examples on how to use the code to get a transmission or emission spectrum of an exoplanet can therefore be found online.

No thick carbon dioxide atmosphere on the rocky exoplanet TRAPPIST-1 c

In Chapter 4, we published one of the first results of JWST, shedding light on a rocky exoplanet and offering insights into its atmospheric makeup. Over the past decades, our understanding of exoplanets has expanded significantly, revealing that small planets are quite common throughout the Milky Way. It's estimated that around 20 to 50% of stars may host a planet similar in size to Earth. By measuring the densities of these exoplanets, we infer that they typically possess a rocky composition similar to our own planet. However, our knowledge regarding the atmospheric composition of these terrestrial planets remains limited, and we're still uncertain how often rocky planets hold onto their atmospheres. Thanks to the capabilities of JWST, we now have the capability to search for more Earth-like atmospheres composed of molecules such as carbon dioxide, oxygen, and nitrogen. Of particular interest for astronomers is a system called TRAPPIST-1. This nearby, small star hosts seven transiting terrestrial planets, offering possibilities for studying small planets with a whole range of temperatures. Among these planets, three orbit in the region around the star where the temperatures might be suited for liquid water on the planet's surface, known as the habitable zone. Because of the star's proximity, small size, and relatively low temperature, the planets are ideal candidates for atmospheric follow-up characterization. This provides us with a unique opportunity to search for atmospheres on small planets outside the Solar System. It's worth noting that small stars like TRAPPIST-1 are the most common type of stars in the Milky Way. Hence, finding out if planets orbiting small stars can retain their atmospheres is currently one of the main open questions in the field of exoplanets. If we find that planets orbiting these stars indeed retained substantial atmospheres throughout their existence, then this would offer hopeful indications for the potential habitability of the numerous rocky planets hosted by small stars. But if we find that planets around small stars are devoid of atmospheres, it might suggest that stars similar to the Sun offer a more favorable environment for the emergence of life. To make a step forward in solving these open questions, we observed four eclipses of the exoplanet TRAPPIST-1 c with the Mid-Infrared Instrument (MIRI) aboard JWST. In our observations, we leveraged the strong absorption of CO₂ at 15 microns (as noted in the quote by Carl Sagan

above) to search for an atmosphere on TRAPPIST-1 c. We do not detect a strong absorption caused by CO₂, leading us to exclude certain atmospheric scenarios, particularly those that are dominated by CO₂. Instead, our findings are more consistent with thinner atmospheres or bare-rock surfaces. For instance, we can confidently rule out an atmosphere on TRAPPIST-1 c, which resembles that of a badly ventilated room, i.e., CO₂ concentrations of 1000 ppm at sea level. Interestingly, TRAPPIST-1 c, which lies outside of the star's habitable zone, is similar in size, mass, and irradiation to Venus. One of the main scientific discoveries of this chapter is that, unlike Venus, the planet lacks a high-pressure atmosphere that is primarily made of carbon dioxide. This is the first study to characterize an exoplanet that resembles Venus or is reasonably comparable to Earth. Its findings will help understand the origin and evolution of rocky planets orbiting small stars, thereby guiding future studies of these systems.

A Hubble WFC3 infrared look at the transmission spectrum of the hot, inflated sub-Saturn KELT-11 b

In Chapter 5, we utilize the open-source pipeline PACMAN presented in Chapter 3 to analyze Hubble observations of a hot Jupiter exoplanet KELT-11b and learn about its atmospheric properties. Thanks to the planet's short orbital period and high equilibrium temperature, it's a great target for atmospheric studies. We looked at the stellar light as the planet passed in front of its star and analyzed how it changed as a function of wavelength and time. We found that a commonly used method to analyze the spectra of transiting exoplanets taken by Hubble might not always be accurate. Our observed planetary transmission spectrum also hinted at potential contamination from the star itself. Surface features on the star, such as stellar spots, can influence the spectrum — a phenomenon commonly observed in smaller, cooler stars but less expected in larger stars like our Sun. Our study underscores the importance of robust data reduction and a thorough interpretation of the planetary transmission spectrum, even for high signal-to-noise targets like hot Jupiters. Failure to consider contamination from the host star could lead to misinterpretations, attributing atmospheric features to the planet that actually originate from molecules in the stellar atmosphere.

The β Pictoris b Hill Sphere Transit Campaign - II. Searching for the signatures of the β Pictoris exoplanets through time delay analysis of the δ Scuti pulsations

Finally, in Chapter 6, we study a nearby planetary system called β Pictoris. The system stands out as the closest stellar system where we've directly spotted gas giant planets, along with an intriguing edge-on circumstellar disk and signs of transiting exocomets. We investigated the stellar pulsations of the star in order to see the signatures of the known planets, β Pictoris b and c, and also search for still unknown companions. A star and its planets are always orbiting a common center of mass, which leads to a small periodic change in distance between us and the host star. By measuring the arrival time of the stellar pulsations, we could detect periodic early or late arrivals, hinting at companions, which change the light travel time of the signals. We analyzed photometric data from various ground- and space-based observatories to study the pulsations' stability. We did not detect

the signals for the planets due to the high noise in the data. Our analysis also suggests that the star's pulsations themselves drift over time, making it challenging to detect exoplanets through pulsation timing for stars like β Pictoris. While we couldn't see the signatures of the planets using this method, our study sheds light on the limitations and potential of pulsation timing in exoplanet detection.

Previous observations of rocky exoplanets with the Hubble Space Telescope or the Spitzer Space Telescope were primarily able to rule out hydrogen-dominated atmospheric compositions. However, thanks to the remarkable capabilities of JWST, we now have the opportunity to explore more realistic, Earth-like atmospheres on temperate rocky worlds. The frequency and conditions under which these small worlds maintain atmospheres remain uncertain. If we discover that planets orbiting small stars are devoid of atmospheres, it may suggest that Sun-like stars offer a more favorable environment for life to emerge. In any case, the forthcoming discoveries with JWST will mark a crucial milestone in our understanding of the atmospheres, surfaces, and potential habitability of rocky planets. While detecting biosignatures on observable exoplanets with JWST may require quite some luck and observational time, the prospects look promising in the coming decades with the advent of the ELTs and potential future missions like the Habitable Worlds Observatory (HWO) and ESA's Large Interferometer For Exoplanets (LIFE) mission. Ultimately, the most robust method to determine whether a terrestrial exoplanet harbors an atmosphere is to study its thermal emission, reflected light, or transmission spectrum. So let's aim our observatories at rocky planets and embark on this journey of discovery!

NEDERLANDSE SAMENVATTING

“Waar komen we vandaan? Wie zijn wij? Waar gaan we heen?” De studie van planeten binnen en buiten ons zonnestelsel is een integraal onderdeel van het beantwoorden van deze fundamentele vragen van de mensheid. De astronomie als geheel werpt licht op de diversiteit van de kosmos en onze plaats daarin. In mijn onderzoeksveld doen we dit door planeten buiten ons zonnestelsel, zogenaamde exoplaneten, te karakteriseren. Door meer te weten te komen over hun vorming, evolutie, samenstelling en bewoonbaarheid, komen we uiteindelijk meer te weten over onze oorsprong, de toekomst van onze eigen planeet en het unieke karakter ervan. De heilige graal van het exoplaneetonderzoek is uiteindelijk te bepalen of de aarde en het leven zoals wij dat kennen zeldzaam is of juist vaak voorkomt. Wetenschappers zullen erover twisten wanneer we eindelijk een “aardetweeling” zullen vinden die het leven zoals wij dat kennen zou kunnen huisvesten, maar we zijn zeker nog nooit zo dicht bij het bereiken van dit doel geweest.

Het is opmerkelijk hoeveel we in slechts een paar decennia hebben geleerd over deze verre werelden: Sinds de eerste ontdekking van exoplaneten in de jaren negentig zijn er op dit moment meer dan 5.500 planeten bekend. Telescopen en instrumenten op de grond en in de ruimte zijn gebouwd om deze planeten te ontdekken. Meestal kunnen we de exoplaneet echter niet rechtstreeks zien. Ze bevinden zich te dicht bij hun moedersterren, die ordes van grootte helderder zijn. Daarom is het nog steeds een uitdaging om planeten rond hun sterren ruimtelijk op te lossen. Vaak observeren we het gecombineerde licht van beide bronnen — de ster en de planeet — dat ons een hele reeks eigenschappen van planeten kan geven, van fundamentele zoals hun grootte en massa tot kenmerken zoals hun atmosferische samenstelling, hun warmtedistributie of hun reflectiviteit. NASA lanceerde ruimtemissies zoals de Kepler Space Telescope in 2009 en de Transiting Exoplanet Survey Satellite (TESS) in 2018 om deze verre werelden te ontdekken en hun grootte te meten. Deze telescopen maakten gebruik van een techniek die de “transitmethode” wordt genoemd. Deze techniek is gebaseerd op de architectuur van het systeem, zodat de planeet regelmatig voor zijn moederster langsgaat en daarbij de ster verduisterd — we spreken ook wel van een “overgang” of “transit”. Tijdens zo’n overgang bedekt de exoplaneet de sterschijf gezien vanaf de aarde, wat leidt tot een waargenomen afname van de flux. Deze methode is tot nu toe het meest succesvol geweest, omdat het probleem eenvoudig op te lossen is: je hoeft alleen maar een gevoelige telescoop naar de hemel te richten en de helderheid van sterren in het beeldveld in de loop van de tijd te registreren om nieuwe planeten te ontdekken. Een andere techniek, de radiële snelheidsmethode, kan ons dan de

massa's van de planeten geven. Uit de gemeten stralen en massa's leiden we de bulkdichtheid van de planeet af, die ons informatie geeft over de samenstelling: Een planeet met een grote ijzeren kern zal een hogere dichtheid hebben dan een planeet die wordt gedomineerd door silicaten met een kleine kern. De meeste rotsachtige exoplaneten hebben een samenstelling die lijkt op die van de aarde, dat wil zeggen ongeveer 30% ijzer en 70% "rotsen" of silicaten. Planeten die groter zijn dan 1,6 keer de straal van de aarde hebben naar verwachting een waterstofatmosfeer met een aanzienlijk deel van hun massa in gasvorm. Er wordt ook verwacht dat deze planeten gesmolten oppervlakken hebben, omdat de druk sterk toeneemt met afnemende hoogte. Zodra je het oppervlak bereikt, zal de temperatuur te hoog zijn om een vast, ongesmolten oppervlak te herbergen. Dit is typisch de reden waarom we deze grotere werelden niet als rotsachtig beschouwen.

Maar ondanks dat we de dichtheden van rotsachtige planeten meten en meer te weten komen over hun bulksamenstellingen, weten we nog steeds niet veel over de samenstelling van de atmosferen van kleine planeten en hoe vaak deze werelden die vasthouden. De Grote Observatoria, die tussen 1990 en 2003 door de NASA werden gelanceerd, omvatten twee ruimtetelescopen die in het afgelopen decennium uiteindelijk het werkpaard zouden worden voor de karakterisering van transiterende exoplaneten: De Hubble ruimtetelescoop werd in 1990 gelanceerd aan boord van Space Shuttle Discovery met een opening van 2,4 meter en de Spitzer ruimtetelescoop in 2003 met een spiegel van 85 cm. In de ruimte vermijden telescopen vervuiling door de thermisch-infrarode achtergrond van de aarde, waardoor nauwkeurige infraroodwaarnemingen mogelijk zijn. Hoewel beide telescopen nooit zijn ontworpen om exoplaneten te bestuderen, hebben slimme gegevensverwerkingsroutines en, in het geval van Hubble, upgrades tijdens de Hubble-onderhoudsmisssies geleid tot de atmosferische karakterisering van veel exoplaneten ter grootte van Jupiter en ook kleinere exoplaneten.

Nadat de Spitzer ruimtetelescoop in januari 2020 werd uitgeschakeld, verloor de exoplaneetgemeenschap de mogelijkheid om exoplaneten in transmissie of emissie in het infrarood bij golflengten van meer dan 2 micron vanuit de ruimte waar te nemen. Dit was een groot verlies, omdat moleculen waarin we geïnteresseerd zijn in de atmosfeer van andere planeten, zoals water (H_2O) of koolstofdioxide (CO_2), kenmerken hebben in het infrarood. De sterke absorptie van koolstofdioxide werd opgemerkt door de astrofysicus en wetenschapscommunicator Carl Sagan, toen hij in 1985 voor het Congres getuigde over klimaatverandering. Het volgende is een citaat van Carl Sagan toen hij de leden van het Congres toesprak tijdens de hoorzitting:

"De lucht tussen ons is transparant, behalve in Los Angeles en dat soort plaatsen. In het gewone zichtbare deel van het spectrum kunnen we elkaar zien. Maar als onze ogen gevoelig zouden zijn voor bijvoorbeeld 15 micron in het infrarood, dan zouden we elkaar niet kunnen zien. De lucht tussen ons zou zwart zijn. En dat komt, in dit geval, door koolstofdioxide. Kooldioxide is zeer sterk absorberend bij 15 micron. En andere golflengten in het infrarood. Zo zijn er ook delen van het infraroodspectrum waar waterdamp absorbeert, waar we elkaar niet zouden kunnen zien als we maar zo ver uit elkaar waren als in deze

kamer.”

De zoektocht naar rotsachtige exoplaneetatmosferen met moleculen als water, kooldioxide of zuurstof vereist een nauwkeurige infraroodtelescoop. Gelukkig werd JWST na veel vertragingen gelanceerd op eerste kerstdag 2021, waardoor wetenschappers weer de mogelijkheid hebben om planeten in deze infrarode golflengten met ongekeende precisie te bestuderen. De baanbrekende precisie is te danken aan vele factoren, zoals een grote spiegel van 6,5 meter en de thermische stabiliteit van de telescoop. JWST geeft ons daarom voor het eerst de mogelijkheid om te zoeken naar atmosferen met een hoog moleculair gewicht van kooldioxide (CO_2), zuurstof (O_2) en stikstof (N_2) op gematigde rotsachtige werelden.

Er zijn over het algemeen twee technieken om de atmosferen van transiterende exoplaneten te bestuderen. De eerste vindt plaats tijdens een overgang en wordt daarom transmissiespectroscopie genoemd: wanneer een planeet vanuit ons gezichtspunt als waarnemer voor de star langs trekt, reist een deel van het sterlicht door de atmosfeer van de planeet, als die er is. Bepaalde golflengten worden geabsorbeerd door de bestanddelen van de atmosfeer. Deze ontbrekende golflengten worden dan door ons waargenomen en we kunnen daaruit afleiden uit welke elementen en moleculen de gasschil rond de planeet bestaat. De andere methode om de atmosferen van exoplaneten te karakteriseren vindt ongeveer een halve baan na de overgang plaats, wanneer de planeet achter zijn moederster verdwijnt; we noemen dat een “eclips”. Tijdens de eclips zelf observeren we alleen het stellare licht. Alle flux die de planeet uitzendt, wordt verduisterd door de ster. Vlak voor en nadat de planeet zich achter zijn ster verbergt, nemen we echter de emissie waar die van de dagzijde van de planeet komt. Van dit kiekeboe-spel met de planeet meten we een emissiespectrum — de methode wordt daarom emissiespectroscopie genoemd — en kunnen we elementen of moleculen in de atmosfeer van de planeet detecteren of direct het oppervlak bestuderen. Als we de emissie bestuderen die niet alleen van de dagzijde van de planeet komt, maar ook van de andere zijden van de planeet tijdens de baan van de planeet rond zijn moederster, nemen we een zogenaamde fasekromme waar. Dit soort waarnemingen kan ons dan informeren over globale processen zoals warmtetransport door winden in de atmosfeer van de planeet.

K2- en Spitzer-fasekrommen van de rotsachtige ultrakorte-periodeplaneet K2-141 b wijzen op een ijle rotsdampatmosfeer.

In hoofdstuk 2 hebben we met Spitzer zo’n fasekromme waargenomen voor een lava-exoplaneet genaamd K2-141 b. Deze lavaplaneten worden gekenmerkt door hun zeer korte omlooptijden en zeer hete dagzijden. Met een omlooptijd van slechts 7 uur wordt de planeet zo sterk verhit door zijn ster dat de gemiddelde dagkanttemperatuur boven de 2000 Kelvin ligt. Dat is genoeg om de rotsen op het oppervlak van de planeet te smelten, wat leidt tot een magma-oceaan op de dagzijde en mogelijk tot een dunne atmosfeer van rotsdamp door de verdamping van rotsen. Vooral dat laatste is interessant, omdat de studie van de verdampte atmosfeer ons uiteindelijk meer zou kunnen vertellen over de samenstelling van het oppervlak van de planeet. In mijn werk heb ik eerdere Kepler-waarnemingen van K2-141 b gecombineerd met nieuwe Spitzer-gegevens. De Spitzer ruimtete-

lescoop heeft ongeveer 70 uur naar de ster gekeken, waardoor 10 ononderbroken banen van de planeet zijn waargenomen. Door de optische gegevens van Kepler te combineren met de infraroodwaarnemingen van Spitzer, kunnen we de diepe eclips die Kepler heeft waargenomen voorzichtig toeschrijven aan een dergelijke rotsdampatmosfeer. Maar alleen vervolgwaarnemingen kunnen de ware aard van de planeet onthullen. Gelukkig zijn er al JWST-waarnemingen van de planeet gedaan en wordt er momenteel gewerkt aan de interpretatie ervan. Dankzij zijn golflengtebereik en precisie zal JWST ons begrip van de atmosferen van lavaplaneten verbeteren.

PACMAN: een pijplijn voor het verkleinen en analyseren van Hubble Wide Field Camera 3 IR Grism-gegevens

In hoofdstuk 3 presenteer ik een algemeen beschikbaar hulpmiddel waarmee astronomen exoplaneetwaarnemingen van een van de instrumenten van de Hubble ruimtetelescoop kunnen bekijken en verwerken. De oorspronkelijke code is de afgelopen tien jaar in veel publicaties gebruikt en is nu voor iedereen beschikbaar onder de naam PACMAN. Het Wide Field Camera 3-instrument (WFC3) van de Hubble-ruimtetelescoop werd in 2009 tijdens een onderhoudsmisatie geïnstalleerd. Het spectrale bereik van WFC3 pikt met name moleculaire infraroodabsorptie van water op, waardoor met succes water in de atmosferen van meer dan een dozijn exoplaneten kon worden gedetecteerd. Het analyseren van Hubble-gegevens brengt echter uitdagingen met zich mee, waarbij verschillende pijplijnen in het verleden in de literatuur tegenstrijdige resultaten hebben opgeleverd. Om ervoor te zorgen dat het onderzoek reproduceerbaar is, is het een goede wetenschappelijke gewoonte dat de software die wordt gebruikt voor gegevensreductie en -analyse open-source is. Deze aanpak maakt het gemakkelijker om verschillende pijplijnen te vergelijken en verlaagt de drempel voor nieuwkomers op het gebied van exoplaneetatmosferen. De broncode van PACMAN en voorbeelden van hoe je de code kunt gebruiken om een transmissie- of emissiespectrum van een exoplaneet te verkrijgen, zijn daarom online te vinden.

Geen dikke kooldioxideatmosfeer op de rotsachtige exoplaneet TRAPPIST-1 c

In hoofdstuk 4 hebben we een van de eerste resultaten van JWST gepubliceerd, die licht werpt op een rotsachtige exoplaneet en inzicht geeft in de samenstelling van zijn atmosfeer. In de afgelopen decennia is ons begrip van exoplaneten aanzienlijk toegenomen en is duidelijk geworden dat kleine planeten veel voorkomen in de Melkweg. Geschat wordt dat ongeveer 20 tot 50% van de sterren een planeet herbergt die qua grootte vergelijkbaar is met de aarde. Door de dichtheid van deze exoplaneten te meten, leiden we af dat ze meestal een rotsachtige samenstelling hebben die vergelijkbaar is met die van onze eigen planeet. Onze kennis over de samenstelling van de atmosfeer van deze aardse planeten blijft echter beperkt en we weten nog steeds niet zeker hoe vaak rotsachtige planeten hun atmosfeer vasthouden. Dankzij de mogelijkheden van JWST hebben we nu de mogelijkheid om te zoeken naar meer aardachtige atmosferen die bestaan uit moleculen zoals kooldioxide, zuurstof en stikstof. Bijzonder interessant voor astronomen is een systeem dat TRAPPIST-1 heet. Deze nabije, kleine ster herbergt zeven transiterende

aardse planeten, wat mogelijkheden biedt voor het bestuderen van kleine planeten met een heel scala aan temperaturen. Van deze planeten draaien er drie in het gebied rond de ster waar de temperatuur geschikt zou kunnen zijn voor vloeibaar water op het oppervlak van de planeet, de zogenaamde bewoonbare zone. Vanwege de nabijheid van de ster, de kleine omvang en de relatief lage temperatuur zijn de planeten ideale kandidaten voor atmosferische follow-up karakterisering. Dit biedt ons een unieke kans om te zoeken naar atmosferen op kleine planeten buiten het zonnestelsel. Het is noemenswaardig dat kleine sterren zoals TRAPPIST-1 het meest voorkomende type sterren in de Melkweg zijn. Daarom is het momenteel een van de belangrijkste open vragen op het gebied van exoplaneten om uit te vinden of planeten rond kleine sterren hun atmosfeer kunnen behouden. Als we erachter komen dat planeten rond deze sterren inderdaad gedurende hun hele bestaan een substantiële atmosfeer hebben behouden, dan zou dit hoopvolle aanwijzingen bieden voor de mogelijke bewoonbaarheid van de vele rotsachtige planeten rond kleine sterren. Maar als we ontdekken dat planeten rond kleine sterren geen atmosfeer hebben, zou dat erop kunnen wijzen dat sterren die op de zon lijken een gunstiger omgeving bieden voor het ontstaan van leven. Om een stap voorwaarts te zetten in het oplossen van deze open vragen, hebben we vier verduisteringen van de exoplaneet TRAPPIST-1 c geobserveerd met het Mid-Infrarood Instrument (MIRI) aan boord van JWST. In onze waarnemingen hebben we gebruik gemaakt van de sterke absorptie van CO₂ bij 15 micron (zoals vermeld in het citaat van Carl Sagan hierboven) om te zoeken naar een atmosfeer op TRAPPIST-1 c. We zien geen sterke absorptie van CO₂ bij 15 micron. We detecteren geen sterke absorptie veroorzaakt door CO₂, waardoor we bepaalde atmosferische scenario's uitsluiten, met name scenario's die worden gedomineerd door CO₂. In plaats daarvan komen onze bevindingen meer overeen met dunnere atmosferen of kale rotsoppervlakken. We kunnen bijvoorbeeld met zekerheid een atmosfeer op TRAPPIST-1 c uitsluiten die lijkt op die van een slecht geventileerde kamer, dat wil zeggen CO₂-concentraties van 1000 ppm op zeeniveau. Het is interessant dat TRAPPIST-1 c, dat buiten de bewoonbare zone van de ster ligt, qua grootte, massa en straling vergelijkbaar is met Venus. Een van de belangrijkste wetenschappelijke ontdekkingen van dit hoofdstuk is dat de planeet, in tegenstelling tot Venus, geen hogedruk-atmosfeer heeft die voornamelijk uit kooldioxide bestaat. Dit is de eerste studie die een exoplaneet karakteriseert die op Venus lijkt of redelijk vergelijkbaar is met de aarde. De bevindingen zullen bijdragen aan een beter begrip van het ontstaan en de evolutie van rotsachtige planeten die rond kleine sterren draaien en zo richting geven aan toekomstige studies van deze systemen.

Een Hubble WFC3-infraroodblik op het transmissiespectrum van de hete, opgeblazen sub-Saturn KELT-11 b

In hoofdstuk 5 gebruiken we de open-source pijplijn PACMAN uit hoofdstuk 3 om Hubble-waarnemingen van de hete Jupiter-exoplaneet KELT-11 b te analyseren en meer te weten te komen over zijn atmosferische eigenschappen. Dankzij de korte omlooptijd van de planeet en de hoge evenwichtstemperatuur is het een geweldig doelwit voor atmosferisch onderzoek. We keken naar het stellaire licht toen de planeet voor zijn ster langsging en analyseerden hoe het veranderde als functie van de

golflengte en de tijd. We ontdekten dat een veelgebruikte methode om de spectra van transiterende exoplaneten te analyseren, die door Hubble is gemaakt, niet altijd nauwkeurig is. Het door ons waargenomen transmissiespectrum van de planeten wees ook op mogelijke vervuiling door de ster zelf. Oppervlakte-eigenschappen van de ster, zoals stellaire vlekken, kunnen het spectrum beïnvloeden — een verschijnsel dat vaak wordt waargenomen bij kleinere, koelere sterren, maar minder wordt verwacht bij grotere sterren zoals onze zon. Onze studie onderstreept het belang van robuuste datareductie en een grondige interpretatie van het planetaire transmissiespectrum, zelfs voor doelen met een hoog signaal-ruisverhouding zoals hete Jupiters. Als er geen rekening wordt gehouden met vervuiling door de moederster, kan dit leiden tot verkeerde interpretaties, waarbij atmosferische kenmerken aan de planeet worden toegeschreven die eigenlijk afkomstig zijn van moleculen in de stellaire atmosfeer.

De β Pictoris b Hill Sphere Transit Campagne - II. Zoeken naar de signatures van de β Pictoris exoplaneten door tijdsvertraginganalyse van de δ Scuti pulsaties

Tot slot bestuderen we in hoofdstuk 6 een nabijgelegen planetenstelsel genaamd β Pictoris. Het systeem valt op als het dichtstbijzijnde stersysteem waar we direct gasreuzenplaneten hebben waargenomen, samen met een schijf die we van opzij zien en tekenen van transiterende exokometen. We hebben de stertrillingen van de ster onderzocht om de signatures van de bekende planeten, β Pictoris b en c, te zien en ook om te zoeken naar nog onbekende begeleiders. Een ster en zijn planeten draaien altijd rond een gemeenschappelijk massamiddelpunt, wat leidt tot een kleine periodieke verandering in de afstand tussen ons en de ster. Door de aankomsttijd van de stellaire pulsaties te meten, zouden we periodieke vroege of late aankomsten kunnen detecteren, wat wijst op begeleiders die de lichtreistijd van de signalen veranderen. We analyseerden fotometrische gegevens van verschillende observatoria op de grond en in de ruimte om de stabiliteit van de pulsaties te bestuderen. We hebben de signalen van de planeten niet kunnen detecteren vanwege de hoge ruis in de gegevens. Onze analyse suggereert ook dat de pulsaties van de ster zelf in de loop van de tijd veranderen, waardoor het voor sterren als β Pictoris een uitdaging is om exoplaneten te detecteren aan de hand van pulsatie-timing. Hoewel we met deze methode de signatures van de planeten niet konden zien, werpt onze studie licht op de beperkingen en mogelijkheden van pulsatie-timing bij het detecteren van exoplaneten.

Eerdere waarnemingen van rotsachtige exoplaneten met de Hubble-ruimtetelescoop of de Spitzer-ruimtetelescoop waren voornamelijk in staat om door waterstof gedomineerde atmosferische samenstellingen uit te sluiten. Dankzij de opmerkelijke mogelijkheden van JWST hebben we nu echter de mogelijkheid om meer realistische, aardachtige atmosferen op gematigde rotsachtige werelden te onderzoeken. Het is nog onzeker hoe vaak en onder welke omstandigheden deze kleine werelden hun atmosferen behouden. Als we ontdekken dat planeten rond kleine sterren geen atmosfeer hebben, kan dat erop wijzen dat zonachtige sterren een gunstigere omgeving bieden voor het ontstaan van leven. In elk geval zullen de komende ontdekkingen met JWST een cruciale mijlpaal zijn in ons begrip van de

atmosferen, oppervlakken en mogelijke bewoonbaarheid van rotsachtige planeten. Hoewel het detecteren van biosignalen op waarneembare exoplaneten met JWST heel wat geluk en observatietijd kan vergen, zien de vooruitzichten er veelbelovend uit in de komende decennia met de komst van de ELT's en mogelijke toekomstige missies zoals het Habitable Worlds Observatory (HWO) en ESA's Large Interferometer For Exoplanets (LIFE) missie. Uiteindelijk is de meest robuuste methode om te bepalen of een aardse exoplaneet een atmosfeer heeft, het bestuderen van de thermische emissie, het gereflecteerde licht of het transmissiespectrum. Dus laten we onze observatoria richten op rotsachtige planeten en beginnen aan deze ontdekkingsreis!

DEUTSCHE ZUSAMMENFASSUNG

„Woher kommen wir? Wer sind wir? Wohin gehen wir?“ Die Erforschung der Planeten innerhalb und außerhalb unseres Sonnensystems ist ein wesentlicher Bestandteil zur Beantwortung dieser grundlegenden Fragen der Menschheit. Die Astronomie als Ganzes beleuchtet die Vielfalt des Kosmos und unseren Platz darin. In meinem Forschungsbereich tun wir dies, indem wir Planeten außerhalb unseres Sonnensystems, so genannte Exoplaneten, charakterisieren. Indem wir etwas über ihre Entstehung, Entwicklung, Zusammensetzung und Bewohnbarkeit erfahren, lernen wir letztlich etwas über unseren Ursprung, die Zukunft unseres eigenen Planeten und seine Einzigartigkeit. Der heilige Gral der Exoplanetenforschung besteht letztlich darin, festzustellen, ob die Erde und das Leben, wie wir es kennen, selten oder allgegenwärtig sind. Die Wissenschaftler werden sich darüber streiten, wann wir endlich einen „Erd-Zwilling“ finden werden, der Leben, wie wir es kennen, beherbergen könnte, aber so nah waren wir diesem Ziel sicher noch nie.

Es ist bemerkenswert, wie viel wir in nur wenigen Jahrzehnten über diese fernen Welten gelernt haben: Seit der ersten Entdeckung von Exoplaneten in den 1990er Jahren sind uns derzeit mehr als 5 500 Planeten bekannt. Es wurden boden- und weltraumgestützte Teleskope und Instrumente gebaut, um diese Planeten zu entdecken. In der Regel können wir die Exoplaneten jedoch nicht direkt sehen. Sie sind zu nahe an ihren Wirtsternen, die um Größenordnungen heller sind. Daher ist es immer noch eine Herausforderung, Planeten um ihre Sterne herum räumlich aufzulösen. Häufiger beobachten wir das kombinierte Licht beider Quellen — des Sterns und des Planeten —, das uns eine ganze Reihe von Planeteneigenschaften liefern kann, von grundlegenden Eigenschaften wie Größe und Masse bis hin zu Merkmalen wie der atmosphärischen Zusammensetzung, der Wärmeverteilung oder dem Reflexionsvermögen. Die NASA hat Weltraummissionen wie das Kepler-Weltraumteleskop im Jahr 2009 und den Transiting Exoplanet Survey Satellite (TESS) im Jahr 2018 gestartet, um diese fernen Welten zu entdecken und ihre Größe zu messen. Diese Teleskope nutzten eine Technik, die als „Transitmethode“ bezeichnet wird und die darauf beruht, dass das System so ausgerichtet ist, dass der Planet seinen Wirtstern in regelmäßigen Abständen verdeckt — oder „transitiert“. Während eines solchen Transits verdeckt der Exoplanet von der Erde aus gesehen die Sternscheibe, was zu einer beobachteten Abnahme des Lichtstroms führt. Diese Methode war bisher die erfolgreichste, was auf die einfache Skalierbarkeit des Problems zurückzuführen ist: Man muss nur ein empfindliches Teleskop auf den Himmel richten und die Helligkeit der Sterne im Sichtfeld im Laufe der Zeit aufzeichnen, um neue Planeten zu entdecken. Eine andere Technik, die Radi-

algeschwindigkeitsmethode, kann uns dann die Planetenmassen liefern. Aus den gemessenen Radien und Massen können wir die durchschnittliche Dichte des Planeten ableiten, die uns Aufschluss über seine Zusammensetzung gibt: Ein Planet mit einem großen Eisenkern hat eine höhere Dichte als ein Planet, der von Silikaten dominiert wird und einen kleinen Kern hat. Die meisten felsigen Exoplaneten haben eine erdähnliche Zusammensetzung, d. h. sie bestehen zu etwa 30 % aus Eisen und zu 70 % aus „Gestein“ oder Silikaten. Bei Planeten, die größer als das 1,6-fache des Erdradius sind, wird davon ausgegangen, dass sie eine Wasserstoffatmosphäre bewahrt haben und ein erheblicher Teil ihrer Masse in Gasform vorliegt. Diese Planeten dürften auch geschmolzene Oberflächen haben, da der Druck mit abnehmender Höhe stark zunimmt. Sobald man die Oberfläche erreicht, ist die Temperatur zu hoch, um eine feste, ungeschmolzene Oberfläche zu haben. Dies ist der Grund, warum wir diese größeren Welten nicht als felsig betrachten.

Doch obwohl wir die Dichte von Gesteinsplaneten messen und ihre Zusammensetzung kennen, wissen wir immer noch nicht viel über die Zusammensetzung der Atmosphären von Kleinplaneten und darüber, wie oft diese Welten Atmosphären beibehalten. Zu den "Great Observatories", die von der NASA zwischen 1990 und 2003 in Betrieb genommen wurden, gehörten zwei Weltraumteleskope, die im letzten Jahrzehnt zu den wichtigsten Geräten für die Charakterisierung von transitierenden Exoplaneten wurden: Das Hubble-Weltraumteleskop wurde 1990 an Bord des Space Shuttle Discovery mit einer Öffnung von 2,4 Metern gestartet, das Spitzer-Weltraumteleskop 2003 mit einem 85-cm-Spiegel. Im Weltraum vermeiden die Teleskope die Kontamination durch den thermischen Infrarot-Hintergrund der Erde, was präzise Infrarotbeobachtungen ermöglicht. Obwohl beide Teleskope nie für die Erforschung von Exoplaneten konzipiert waren, konnten dank ausgeklügelter Datenverarbeitungsroutinen und — im Falle von Hubble — durch Nachrüstungen während der Hubble-Wartungsmissionen viele Exoplaneten von Jupitergröße und auch kleinere Exoplaneten atmosphärisch charakterisiert werden.

Nachdem das Spitzer-Weltraumteleskop im Januar 2020 abgeschaltet wurde, verlor die Exoplanetengemeinschaft die Möglichkeit, Exoplaneten in Transmission oder Emission im Infraroten bei Wellenlängen von mehr als 2 Mikrometern vom Weltraum aus zu beobachten. Dies war ein großer Verlust, da Moleküle wie Wasser (H_2O) oder Kohlenstoffdioxid (CO_2), an denen wir in der Atmosphäre anderer Planeten interessiert sind, charakteristische Merkmale im Infraroten aufweisen. Die starke Absorption von Kohlenstoffdioxid wurde von dem Astrophysiker und Wissenschaftskommunikator Carl Sagan erwähnt, als er 1985 vor dem Kongress über den Klimawandel aussagte. Es folgt ein direktes Zitat von Carl Sagan, als er sich während der Anhörung an die Kongressmitglieder wandte:

„Die Luft zwischen uns ist durchsichtig, außer in Los Angeles und anderen Orten dieser Art. Im normalen sichtbaren Teil des Spektrums können wir uns gegenseitig sehen. Aber wenn unsere Augen empfindlich wären, sagen wir, bei 15 Mikrometern im Infraroten, könnten wir einander nicht sehen. Die Luft zwischen uns wäre schwarz. Und das liegt in diesem Fall am Kohlenstoffdioxid. Kohlenstoffdioxid absorbiert sehr stark bei 15 Mikrometern. Und auch bei anderen Wellenlängen im Infraroten. Ebenso gibt es Bereiche des Infrarotspektrums, in denen

Wasserdampf absorbiert, in denen wir uns nicht sehen könnten, wenn wir so weit voneinander entfernt wären, wie wir es in diesem Raum sind.“

Die Suche nach Atmosphären auf felsigen Exoplaneten, die Moleküle wie Wasser, Kohlendioxid oder Sauerstoff enthalten, erfordert ein präzises Infrarotteleskop. Glücklicherweise wurde das JWST nach vielen Verzögerungen am Weihnachtstag 2021 gestartet und bietet den Wissenschaftlern nun wieder die Möglichkeit, Planeten in diesen Infrarot-Wellenlängen mit noch nie dagewesener Präzision zu untersuchen. Seine bahnbrechende Präzision ist auf viele Faktoren zurückzuführen, wie z. B. einen großen Spiegeldurchmesser von 6,5 Metern und die thermische Stabilität des Teleskops. JWST gibt uns daher zum ersten Mal die Möglichkeit, auf gemäßigten felsigen Welten nach Atmosphären mit einem hohen mittleren Molekulargewicht aus Kohlenstoffdioxid (CO_2), Sauerstoff (O_2) und Stickstoff (N_2) zu suchen.

Es gibt im Allgemeinen zwei Techniken zur Untersuchung der Atmosphären von transitierenden Exoplaneten. Die erste Methode, die während eines Transits zum Einsatz kommt, wird Transmissionsspektroskopie genannt: Wenn ein Planet seinen Wirtsstern aus unserer Sicht als Beobachter verdeckt, durchdringt ein Teil des Sternenlichts die Atmosphäre des Planeten, falls es eine gibt. Bestimmte Wellenlängen werden dabei von den Bestandteilen der Atmosphäre absorbiert. Diese fehlenden Wellenlängen werden dann von uns beobachtet, und wir können auf die Elemente und Moleküle schließen, aus denen die Gashölle um den Planeten besteht. Die andere Methode zur Charakterisierung der Atmosphären von Exoplaneten findet etwa eine halbe Umlaufbahn nach dem Transit statt, wenn der Planet hinter seinem Wirtsstern verschwindet; wir nennen das eine „Bedeckung“. Während der Bedeckung selbst beobachten wir nur das Licht des Sterns. Der vom Planeten ausgesandte Lichtstrom wird durch den Stern verdeckt. Unmittelbar bevor und nachdem sich der Planet hinter seinem Stern versteckt, beobachten wir jedoch die Emission, die von der Tagseite des Planeten ausgeht. Anhand dieses Guck-guck-Spieles mit dem Planeten messen wir ein Emissionsspektrum — die Methode wird daher als Emissionsspektroskopie bezeichnet — und können Elemente oder Moleküle in der Atmosphäre des Planeten nachweisen oder direkt seine Oberfläche untersuchen. Wenn wir die Emissionen untersuchen, die nicht nur von der Tagseite des Planeten, sondern auch von den anderen Seiten des Planeten während der Umlaufbahn des Planeten um seinen Wirtsstern ausgehen, beobachten wir eine so genannte Phasenkurve. Diese Art von Beobachtungen kann uns dann Aufschluss über globale Prozesse wie den Wärmetransport durch die Winde in der Planetenatmosphäre geben.

K2- und Spitzer-Phasenkurven des ultrakurzperiodischen Gesteinsplaneten K2-141 b deuten auf eine dünne Gesteinsdampfatmosphäre hin

In Kapitel 2 haben wir mit Spitzer eine solche Phasenkurve für einen Lava-Exoplaneten namens K2-141 b beobachtet. Diese Lavaplaneten zeichnen sich durch sehr kurze Umlaufzeiten und sehr heiße Tagessseiten aus. Bei einer Umlaufzeit von nur 7 Stunden wird der Planet von seinem Stern so stark aufgeheizt, dass die durchschnittliche Tagessseitentemperatur bei über 2000 Kelvin liegt. Das reicht

aus, um das Gestein auf der Planetenoberfläche zu schmelzen, was zu einem tageseitigen Magmaocean und möglicherweise zu einer dünnen Gesteinsdampf-atmosphäre führt, die durch die Verdampfung von Gestein entsteht. Letzteres ist besonders interessant, da die Untersuchung der verdampften Atmosphäre möglicherweise Aufschluss über die Zusammensetzung der Planetenoberfläche geben könnte. In meiner Arbeit habe ich frühere Kepler-Beobachtungen von K2-141 b mit neuen Spitzer-Daten kombiniert. Das Weltraumteleskop Spitzer hat den Stern etwa 70 Stunden lang beobachtet und dabei 10 kontinuierliche Umläufe des Planeten erfasst. Durch die Kombination der optischen Daten von Kepler mit den Infrarotbeobachtungen von Spitzer können wir die von Kepler beobachtete tiefe Bedeckung vorläufig auf eine solche Gesteinsdampf-atmosphäre zurückführen. Die wahre Beschaffenheit des Planeten kann jedoch nur durch weitere Beobachtungen festgestellt werden. Glücklicherweise wurden bereits JWST-Beobachtungen des Planeten durchgeführt, und die Auswertung ist derzeit im Gange. Aufgrund seiner Wellenlängenabdeckung und Präzision wird JWST unser Verständnis der Atmosphären von Lavaplaneten verbessern.

PACMAN: Eine Pipeline zur Reduzierung und Analyse von Hubble Wide Field Camera 3 IR Grism Daten

In Kapitel 3 stelle ich ein öffentlich zugängliches Werkzeug vor, mit dem Astronomen auf Exoplanetenbeobachtungen zugreifen und diese verarbeiten können, die von einem der Instrumente des Hubble-Weltraumteleskops aufgenommen wurden. Der ursprüngliche Code wurde in den letzten zehn Jahren in vielen Publikationen verwendet und ist nun unter dem Namen PACMAN für jedermann zugänglich. Das Hubble-Instrument Wide Field Camera 3 (WFC3) wurde während einer Wartungsmission im Jahr 2009 installiert. Der Spektralbereich der WFC3 erfasst vor allem die molekulare Infrarotabsorption von Wasser, was den erfolgreichen Nachweis von Wasser in den Atmosphären von über einem Dutzend Exoplaneten ermöglichte. Die Analyse von Hubble-Daten stellt jedoch eine Herausforderung dar, da verschiedene Codes (auch: Pipelines) in der Vergangenheit zu widersprüchlichen Ergebnissen in der Literatur geführt haben. Um die Reproduzierbarkeit von Forschungsergebnissen zu gewährleisten, ist es gute wissenschaftliche Praxis, die für die Datenreduktion und -analyse verwendeten Programme als Open-Source-Software anzubieten. Dieser Ansatz erleichtert den Vergleich verschiedener Pipelines und senkt die Hürden für Neulinge auf dem Gebiet der Exoplanetenatmosphären. Der Quellcode von PACMAN und Beispiele für die Verwendung des Codes, um ein Transmissions- oder Emissionsspektrum eines Exoplaneten zu erhalten, sind daher online zu finden.

Keine dicke Kohlenstoffdioxidatmosphäre auf dem felsigen Exoplaneten TRAPPIST-1 c

In Kapitel 4 haben wir eines der ersten Ergebnisse von JWST veröffentlicht, das einen felsigen Exoplaneten analysiert und Einblicke in seine atmosphärische Beschaffenheit bietet. In den letzten Jahrzehnten hat sich unser Verständnis von Exoplaneten erheblich erweitert und gezeigt, dass kleine Planeten in der Milchstraße recht häufig sind. Man schätzt, dass etwa 20 bis 50 % der Sterne einen

Planeten von ähnlicher Größe wie die Erde beherbergen. Die Messung der Dichte dieser Exoplaneten lässt den Schluss zu, dass sie in der Regel eine ähnliche Gesteinszusammensetzung wie unser eigener Planet aufweisen. Unser Wissen über die atmosphärische Zusammensetzung dieser terrestrischen Planeten ist jedoch nach wie vor begrenzt, und wir wissen immer noch nicht, wie oft Gesteinsplaneten ihre Atmosphären behalten. Dank der Fähigkeiten von JWST können wir nun nach weiteren erdähnlichen Atmosphären suchen, die aus Molekülen wie Kohlenstoffdioxid, Sauerstoff und Stickstoff bestehen. Von besonderem Interesse für die Astronomen ist ein System namens TRAPPIST-1. Dieser nahe gelegene, kleine Stern beherbergt sieben transitierende terrestrische Planeten, was uns die Möglichkeit bietet, kleine Planeten mit einer ganzen Reihe von Temperaturen zu untersuchen. Von diesen Planeten kreisen drei in der Region um den Stern, in der die Temperaturen für flüssiges Wasser auf der Planetenoberfläche geeignet sein könnten, der so genannten bewohnbaren Zone. Aufgrund der Nähe des Sterns, der geringen Größe und der relativ niedrigen Temperatur sind die Planeten ideale Kandidaten für eine Charakterisierung der Atmosphäre. Dies bietet uns eine einzigartige Gelegenheit, nach Atmosphären auf kleinen Planeten außerhalb des Sonnensystems zu suchen. Es ist erwähnenswert, dass kleine Sterne wie TRAPPIST-1 die häufigste Art von Sternen in der Milchstraße sind. Daher ist die Frage, ob Planeten, die kleine Sterne umkreisen, ihre Atmosphären behalten können, derzeit eine der wichtigsten offenen Fragen auf dem Gebiet der Exoplaneten. Wenn wir herausfinden, dass Planeten, die diese Sterne umkreisen, tatsächlich während ihrer gesamten Existenz eine beträchtliche Atmosphäre behalten haben, wäre dies ein hoffnungsvoller Hinweis auf die mögliche Bewohnbarkeit der zahlreichen Gesteinsplaneten, die von kleinen Sternen beherbergt werden. Wenn wir jedoch feststellen, dass Planeten um kleine Sterne keine Atmosphären haben, könnte dies darauf hindeuten, dass sonnenähnliche Sterne eine günstigere Umgebung für die Entstehung von Leben bieten. Um bei der Lösung dieser offenen Fragen einen Schritt weiterzukommen, haben wir mit dem Mid-Infrared Instrument (MIRI) an Bord des JWST vier Bedeckungen des Exoplaneten TRAPPIST-1 c beobachtet. Bei unseren Beobachtungen nutzten wir die starke Absorption von CO_2 bei 15 Mikrometern (wie in dem obigen Zitat von Carl Sagan erwähnt), um nach einer Atmosphäre auf TRAPPIST-1 c zu suchen. Wir können keine starke Absorption durch CO_2 feststellen, was uns dazu veranlasst, bestimmte atmosphärische Szenarien auszuschließen, insbesondere solche, die von CO_2 dominiert werden. Stattdessen stimmen unsere Ergebnisse eher mit dünneren Atmosphären oder blankem Gesteinsoberflächen überein. So können wir zum Beispiel eine Atmosphäre auf TRAPPIST-1 c, die der eines schlecht belüfteten Raumes ähnelt, d.h. CO_2 -Konzentrationen von 1000 ppm auf Meereshöhe, sicher ausschließen. Interessanterweise ist TRAPPIST-1 c, der außerhalb der bewohnbaren Zone des Sterns liegt, in Bezug auf Größe, Masse und Sterneinstrahlung ähnlich wie die Venus. Eine der wichtigsten wissenschaftlichen Entdeckungen dieses Kapitels ist, dass der Planet im Gegensatz zur Venus keine Hochdruckatmosphäre hat, die hauptsächlich aus Kohlenstoffdioxid besteht. Dies ist die erste Studie zur Charakterisierung eines Exoplaneten, der der Venus ähnelt oder mit der Erde einigermaßen vergleichbar ist. Die Ergebnisse werden dazu beitragen, den Ursprung und die Entwicklung von Gesteinsplaneten, die kleine Sterne umkreisen,

zu verstehen, und so die künftige Erforschung dieser Systeme leiten.

Ein Hubble WFC3-Infrarot-Blick auf das Transmissionsspektrum des heißen, aufgeblähten Sub-Saturns KELT-11 b

In Kapitel 5 verwenden wir die in Kapitel 3 vorgestellte Open-Source-Pipeline PACMAN, um Hubble-Beobachtungen des heißen Jupiter-Exoplaneten KELT-11 b zu analysieren und mehr über seine atmosphärischen Eigenschaften zu erfahren. Dank der kurzen Umlaufzeit des Planeten und seiner hohen Gleichgewichtstemperatur ist er ein hervorragendes Ziel für Atmosphärenstudien. Wir haben uns das Sternenlicht angesehen, als der Planet vor seinem Stern vorbeizog, und analysiert, wie es sich in Abhängigkeit von der Wellenlänge und der Zeit verändert. Wir fanden heraus, dass eine übliche Methode zur Analyse der Spektren von transitierenden Exoplaneten, die von Hubble aufgenommen wurden, möglicherweise nicht immer zuverlässig ist. Das von uns beobachtete Transmissionsspektrum des Planeten deutete auch auf eine mögliche Kontamination durch den Stern selbst hin. Oberflächenmerkmale des Sterns, wie stellare Flecken, können das Spektrum beeinflussen — ein Phänomen, das häufig bei kleineren, kühleren Sternen beobachtet wird, bei größeren Sternen wie unserer Sonne jedoch weniger zu erwarten ist. Unsere Studie unterstreicht die Bedeutung einer robusten Datenreduktion und einer gründlichen Interpretation des Transmissionsspektrums von Planeten, selbst bei Zielen mit hohem Signal-Rausch-Verhältnis wie heißen Jupitern. Wird die Kontamination durch den Wirtstern nicht berücksichtigt, könnte dies zu Fehlinterpretationen führen, die dem Planeten atmosphärische Merkmale zuschreiben, die eigentlich von Molekülen in der Sternatmosphäre stammen.

Die β Pictoris b Hill Sphere Transit-Kampagne - II. Suche nach den Signaturen der β Pictoris-Exoplaneten durch Zeitverzögerungsanalyse der δ Scuti-Pulsationen

In Kapitel 6 schließlich untersuchen wir ein nahe gelegenes Planetensystem namens β Pictoris. Dieses System ist das nächstgelegene Sternsystem, in dem wir direkt Gasriesenplaneten entdeckt haben, zusammen mit einer faszinierenden zirkumstellaren Scheibe und Anzeichen von transitierenden Exokometen. Wir haben die stellaren Pulsationen des Sterns untersucht, um die Signaturen der bekannten Planeten β Pictoris b und c zu erkennen und auch nach noch unbekannten Begleitern zu suchen. Ein Stern und seine Planeten umkreisen immer einen gemeinsamen Schwerpunkt, was zu einer kleinen periodischen Abstandsänderung zwischen uns und dem Wirtstern führt. Durch die Messung der Ankunftszeit der Sternpulsationen könnten wir periodisch verfrühte oder verspätete Ankünfte feststellen, die auf Begleiter hinweisen, die die Lichtlaufzeit der Signale verändern. Wir analysierten photometrische Daten von verschiedenen boden- und weltraumgestützten Observatorien, um die Stabilität der Pulsationen zu untersuchen. Aufgrund des starken Rauschens in den Daten konnten wir die Signale der Planeten nicht erkennen. Unsere Analyse deutet auch darauf hin, dass die Pulsationen des Sterns selbst im Laufe der Zeit driften, was es schwierig macht, Exoplaneten anhand der Pulsationszeiten von Sternen wie β Pictoris zu entdecken. Obwohl wir mit dieser Methode die Signaturen der Planeten nicht sehen konnten, wirft unsere Studie ein Licht auf die Grenzen und Möglichkeiten der Pulsationszeitmessung bei der

Entdeckung von Exoplaneten.

Frühere Beobachtungen felsiger Exoplaneten mit dem Hubble Space Telescope oder dem Spitzer Space Telescope konnten in erster Linie eine von Wasserstoff dominierte Zusammensetzung der Atmosphäre ausschließen. Dank der bemerkenswerten Fähigkeiten von JWST haben wir nun jedoch die Möglichkeit, realistischere, erdähnliche Atmosphären auf gemäßigten felsigen Welten zu finden. Die Häufigkeit und die Bedingungen, unter denen diese kleinen Welten Atmosphären besitzen, sind nach wie vor ungewiss. Wenn wir feststellen, dass Planeten, die kleine Sterne umkreisen, keine Atmosphären haben, könnte dies darauf hindeuten, dass sonnenähnliche Sterne eine günstigere Umgebung für die Entstehung von Leben bieten. In jedem Fall werden die bevorstehenden Entdeckungen mit JWST einen entscheidenden Meilenstein in unserem Verständnis der Atmosphären, Oberflächen und der potenziellen Bewohnbarkeit von Gesteinsplaneten darstellen. Auch wenn die Entdeckung von Biosignaturen auf beobachtbaren Exoplaneten mit JWST eine Menge Glück und Beobachtungszeit erfordert, sind die Aussichten für die kommenden Jahrzehnte mit dem Aufkommen der ELTs und potenziellen zukünftigen Missionen wie dem Habitable Worlds Observatory (HWO) und der ESA-Mission Large Interferometer For Exoplanets (LIFE) vielversprechend. Die zuverlässigste Methode, um festzustellen, ob ein terrestrischer Exoplanet eine Atmosphäre besitzt, ist die Untersuchung seiner Wärmeemission, seines reflektierten Lichts oder seines Transmissionsspektrums. Richten wir also unsere Observatorien auf Gesteinsplaneten und begeben wir uns auf diese Entdeckungsreise!

PUBLICATIONS

Lead Author

Transiting exocomets detected in broadband light by TESS in the β Pictoris system.
S. Zieba, K. Zwintz, M. Kenworthy, et al., 2019, A&A, 625, L13.

K2 and Spitzer phase curves of the rocky ultra-short-period planet K2-141 b hint at a tenuous rock vapor atmosphere.
S. Zieba, M. Zilinskas, L. Kreidberg, et al., 2022, A&A, 664, A79.

PACMAN: A pipeline to reduce and analyze Hubble Wide Field Camera 3 IR Grism data.
S. Zieba, L. Kreidberg, 2022, JOSS, 7, 4838.

No thick carbon dioxide atmosphere on the rocky exoplanet TRAPPIST-1 c.
S. Zieba, L. Kreidberg, E. Ducrot, et al., 2023, Nature, 620, 746.

The β Pictoris b Hill Sphere Transit Campaign sphere transit campaign II. Searching for the signatures of the β Pictoris exoplanets through time delay analysis of the δ Scuti pulsations.
S. Zieba, K. Zwintz, M. Kenworthy, et al., 2024, accepted in A&A.

Contributor

Revisiting the pulsational characteristics of the exoplanet host star β Pictoris.
K. Zwintz, D. Reese, C. Neiner, et al. [including **S. Zieba**], 2019, A&A, 627, A28.

An unusually large gaseous transit in a debris disc.
D. Iglesias, J. Olofsson, A. Bayo, et al. [including **S. Zieba**], 2019, MNRAS, 490, 5218.

The First Habitable-zone Earth-sized Planet from TESS. I. Validation of the TOI-700 System.
E. Gilbert, T. Barclay, J. Schlieder, et al. [including **S. Zieba**], 2020, AJ, 160, 116.

The First Habitable-zone Earth-sized Planet from TESS. II. Spitzer Confirms TOI-700 d.

J. Rodriguez, A. Vanderburg, **S. Zieba**, et al., 2020, AJ, 160, 117.

Exocomets from a Solar System Perspective.

P. Strøm, D. Bodewits, M. Knight, et al. [including **S. Zieba**], 2020, PASP, 132, 101001.

Observability of evaporating lava worlds.

M. Zilinskas, C. van Buchem, Y. Miguel, et al. [including **S. Zieba**], 2022, A&A, 661, A126.

A Transmission Spectrum of the Sub-Earth Planet L98-59 b in 1.1-1.7 μm .

M. Damiano, R. Hu, T. Barclay, et al. [including **S. Zieba**], 2022, AJ, 164, 225.

Eureka!: An End-to-End Pipeline for JWST Time-Series Observations.

T. Bell, E. Ahrer, J. Brande, et al. [including **S. Zieba**], 2022, JOSS, 7, 4503.

Identification of carbon dioxide in an exoplanet atmosphere.

JWST Transiting Exoplanet Community Early Release Science Team, E. Ahrer, L. Alderson, et al. [including **S. Zieba**], 2023, Nature, 614, 649.

*Early Release Science of the exoplanet WASP-39b with JWST NIRC*am*.*

E. Ahrer, K. Stevenson, M. Mansfield, et al. [including **S. Zieba**], 2023, Nature, 614, 653.

Early Release Science of the exoplanet WASP-39b with JWST NIRSpec PRISM.

Z. Rustamkulov, D. Sing, S. Mukherjee, et al. [including **S. Zieba**], 2023, Nature, 614, 659.

Photochemical Hazes Dramatically Alter Temperature Structure and Atmospheric Circulation in 3D Simulations of Hot Jupiters.

M. Steinrueck, T. Koskinen, P. Lavvas, et al. [including **S. Zieba**], 2023, ApJ, 951, 117.

CHEOPS's hunt for exocomets: photometric observations of 5 Vul.

I. Rebollido, **S. Zieba**, D. Iglesias, et al., 2023, MNRAS, 523, 1441.

A reflective, metal-rich atmosphere for GJ 1214b from its JWST phase curve.

E. Kempton, M. Zhang, J. Bean, et al. [including **S. Zieba**], 2023, Nature, 620, 67.

Potential Atmospheric Compositions of TRAPPIST-1 c Constrained by JWST/MIRI Observations at 15 μm .

A. Lincowski, V. Meadows, **S. Zieba**, et al., 2023, ApJL, 955, L7.

Characterization of K2-167 b and CALM, a new stellar activity mitigation method.
Z. de Beurs, A. Vanderburg, E. Thygesen, et al. [including **S. Zieba**], 2024, MNRAS, 529, 1047.

Nightside clouds and disequilibrium chemistry on the hot Jupiter WASP-43b.
T. Bell, N. Crouzet, P. Cubillos, et al. [including **S. Zieba**], 2024, Nat Astron.

CURRICULUM VITAE

I was born in Grödig, a suburb of Salzburg city, Austria, in June 1995. The town rests at the foot of the Berchtesgaden Alps, with the majestic Untersberg straddling the border between Salzburg and Bavaria. It's also home to the Mozartkugeln confection manufacturer, Mirabell. Even now, after all these years, both the mountains and Mozartkugeln still bring me joy. At the age of six, my family relocated from Grödig to Plainfeld, a small town 12 kilometers east of Salzburg city. There, I attended the “Volkschule Plainfeld” as my primary school. Later, at ten, I embarked on the path of grammar school at the “Privatgymnasium Herz-Jesu-Missionare” in Salzburg. It was here that I translated Latin and Greek texts into German and developed a keen interest in astronomy. During this period, I also fondly recall giving outreach talks on exoplanets.

After turning 18, I left Salzburg and moved to Innsbruck to study physics there. I was truly spoiled, moving from one picturesque city to the next one. After making my way through lectures on for example classical mechanics, optics, and quantum theory, I completed my bachelor project under the supervision of Professor Norbert Przybilla in 2017. I didn't hesitate and immediately continued my academic journey also at the University of Innsbruck with a Master's degree. Having to make a decision on my specialization within physics, I decided on the “in-depth study” of astro- and particle physics. Ultimately, I worked together with Professor Konstanze Zwintz and was co-supervised by Professor Matthew Kenworthy. During this time, with the help of my co-authors, I ended up discovering comets around a different star. Before working on that paper, I didn't even know that “exocomets” were a thing in the first place.

I then started my PhD in January 2020, with the joint Max Planck Institute for Astronomy and Leiden University affiliation, under the supervision of Professor Laura Kreidberg and my Leiden supervisor, Professor Ignas Snellen. Before moving to Heidelberg in August 2020, I spent the first 2 months of my PhD in Leiden, then 3 months in Boston, and finally 2 additional months in Innsbruck. What followed were 4 years of analyzing Spitzer, Kepler, Hubble, and JWST data to learn more about the atmospheres and surfaces of exoplanets. During this time I was privileged to attend many conferences at various places around the world, including Las Vegas, New Zealand, Oxford, Zürich, and Los Angeles. At every one of these conferences, I got to meet new friends and see old ones again.

During my PhD in 2023, I got two JWST observational programs accepted as principal investigator (PI) to further investigate rocky exoplanet atmospheres and study the transition between small planets and larger ones that have signif-

icant envelopes. In 2023, I had the opportunity to work with JWST data when one of Laura's programs was accepted in Cycle 1 to observe the rocky exoplanet TRAPPIST-1 c. We ended up publishing our results in the journal *Nature* in June of 2024. This was followed by an intense time of finishing my thesis and applying for postdoc positions. Ultimately, I was awarded the prestigious Hubble Fellowship to continue my research at the Center for Astrophysics (CfA) in Boston. Later in 2024, I will be relocating to Boston to begin this position there.

ACKNOWLEDGEMENTS

Here, I would like to express my deep gratitude to the many people whose unwavering support and encouragement have been so important throughout my journey to receiving my doctorate degree.

I have to start my acknowledgments with my math and astronomy teacher from grammar school, Herbert. Even though I already had a big interest in astronomy at this age, I might not have gotten that interested in exoplanets if it weren't for you, suggesting I prepare a presentation on these distant worlds. The field has for sure moved on a lot since the discovery of the "Earth-like" planets like Gliese 581 c, and I still remember preparing PowerPoint presentations on that planet for the group. Astronomy ended up being "my thing back in school, and your support was surely a big part of that. Thank you.

After finishing school in Salzburg, I studied in Innsbruck. I highly appreciate the supervision of my master's thesis supervisor, Konstanze, who guided me throughout this first scientific journey. My interest in trying to get as much information as possible from simple measurements of light over time has surely come from the work with you in your group. I also wanna acknowledge Matt who was a great co-supervisor on this Master's thesis project. The exocomet discovery in the TESS data was surely an incredibly exciting time in my Master's and also came with some sleepless nights. I'm glad I could work together with you both and that I had your guidance during my project. Also, thank you, Matt, for the continued motivation you gave me to finish the Master thesis paper which is now a chapter in this thesis. After the exocomet discovery, I was able to travel to Leiden for a workshop. There, I finally met Matt in person, and also Ignas, who ultimately ended up being my PhD promotor. I enjoyed every conversation we had, Ignas, especially important to me was the first one, which ultimately led to me getting in touch with Laura.

When friends or collaborators ask me how Laura is as a supervisor, I can only talk about her in the best way possible. Laura, you've been incredibly supportive in every way during my journey as a PhD student. You are kind, humble, and you are able to communicate complicated topics really well. Whoever I met at conferences could only confirm that you've been the nicest to everyone. You also always had lots of time for me throughout my whole PhD to discuss the progress I have made over the past few days or the setbacks I had. I appreciate the time you invested in me, and I hope we get to continue working together in the future.

My time as a student at the MPIA started out rough with lockdowns, but I really enjoyed every time I was able to be together with my generation of MPIA

students, especially Eric, Evert, Verena, and Nico. Our skiing trips and other outdoor adventures were surely lots of fun! The Austrian apres-ski music was obviously another highlight of these trips! I am really glad I eventually ended up in an office at the MPIA with a really nice atmosphere. One of my main motivations to go to work every day was being back in this office and getting to talk with my besties, Marten and Molly. I surely enjoyed the pool games we had in our default place, Metropol, with the usual drink, Bananenweizen. Also, I will surely miss banana juice abroad. Marten, I indeed enjoyed the Stargate-related discussions we had. We should still give that presentation on the inner workings of the Stargate system! The chess ark we had was also a highlight, but I just cannot keep up with your Elo. Molly, I think there's still enough space on the office walls for us to do dozens more Taylor Swift quizzes. It's getting so hard, though; Taylor is too productive. I'm really lucky to have had someone in the office I could always chat with about Taylor-related updates. And boy there were a lot during my PhD. Talking about Taylor, I obviously want to say how much fun it is to be part of her fandom and enjoy the great music she makes. I also loved our trip to Minehead, where I realized that the UK is not exclusively grey and rainy. Also loved that apple juice I had there! Finally, I also really enjoyed my encounters with any of the other students or postdocs in Heidelberg who I got to meet during my PhD like Max, Selina, Lucian, Glen, Liang, Alex, Callie, Steve, Jonas, and Paul.

Despite my Leiden affiliation, I did not get to be in Leiden that often. But my PhD started off with working together with the Leiden-based Lava planet expert Yamila and her student Mantas. I really appreciate your kindness, Yamila, and your scientific input on the various papers and proposals we have worked on. It was always nice to meet you whenever I was in Leiden or we attended the same conference. Mantas, every time we got to get together in person was a blast! I also wanna acknowledge the rest of the Leiden core gang, Amy and Chris. I think there has been no conference in the past few years without at least one of you guys, Amy, Chris, and Mantas. Amy, the skiing trip was lots of fun, and thanks for proofreading some Dutch stuff for me. After all these Duolingo lessons, I still don't know much more than "boterham." We should also visit our friend Prune again in Copenhagen! Chris, thanks for borrowing me your colorful jacket after I lost mine in Zürich. I can't wait to sing Angels by the late great Robbie Williams again with you. I think we get better every time. I also got to briefly meet some other Leiden folks like Lucie, Thijs, Louis, Dario, and Chloe. Every encounter with you guys was also really nice.

My time in my mid-twenties was made so much better by my girlfriend, Brianna. It's funny how we first met in Boston the first time I visited the US and now I'm going back to start my fellowship there. I still remember it all too well when we could finally meet up again in Toronto after some pandemic-related restrictions were lifted. That city was surely barren cold with all that wind and I still remember the first fall of snow, and how it glistened as it fell. What followed was just a great time with your support in every single way. You've made me a better person over the past few years, and I am looking forward to being less long-distance in the next few years. You mean so much to me. Hope you know that. It was also nice to get to meet everyone else in the Zawadzki Family, namingly Craig, Lori, Chelsea,

Poe, and Piper. It was delightful to get to know all of you over the past years. I also enjoyed getting to know Brianna's friends, like Michael, Arvind, Steve, and Josie, every time I visited central Pennsylvania.

Last but certainly not least, I want to express my heartfelt gratitude to my family—my mom, Margo, my dad, Georg, and my brother, Peter — who have supported me my whole life. It's undeniable that my passion for astronomy and science fiction was ignited by my mom, who introduced me to TV shows like Star Trek TNG, DS9, Voyager, and Stargate. My mom was always there to help me, like when she supported me in translating ancient Greek texts for my homework. I also owe my love for skiing to my parents, and I cherish the hope of continuing our mountain adventures together in the future! Thanks, Dad, for driving so far every once in a while just to get us some perogies and other foods all the way from Poland. Thanks, Peter, for being there in Innsbruck with me. I'm still impressed by some of these long bike rides you did in Tyrol. Thanks to everyone in my family. I cannot express how much you mean to me.

Everyone I've listed here has supported me in one way or another. For that, I want to say a deep thank you from my heart — or, as we would say where I'm from, *dankschee fia ois!*

